Early breast anomalies detection with microwave and ultrasound modalities

Yingying Qin

université PARIS-SACLAY

Détection précoce d'anomalies du sein à l'aide de modalités microondes et ultrasonores

Early breast anomalies detection with microwave and ultrasound modalities

Thèse de doctorat de l'Université Paris-Saclay

École doctorale n° 580, Sciences et technologies de l'information et de la communication (STIC)
Spécialité de doctorat : Traitement du signal et des images
Unité de recherche : Université Paris-Saclay, ENS Paris-Saclay, CNRS, Systèmes et Applications des Technologies de l'Information et de l'Energie
91190 Gif-sur-Yvette, France
Référent : Ecole Normale Supérieure Paris-Saclay

Thèse présentée et soutenue à Paris-Saclay, le 28 septembre 2021, par

Yingying QIN

Composition du jury

Florence Tupin Professeure,Télécom Paris Tech, Institut Polytechnique de Paris	Présidente
Oliver Dorn Senior Lecturer, The University of Manchester	Rapporteur & Examinateur
Joe LoVetri Professor, University of Manitoba	Rapporteur & Examinateur
Martina Teresa Bevacqua Assistant-Professor, Mediterranean University of Reggio Calabria	Examinatrice
Sébastien Bourguignon Maître de conférences, Ecole Centrale de Nantes	Examinateur
Sylvie Le Hegarat-Mascle Professeure, Université Paris-Saclay	Examinatrice
Florence Tupin Professeure,Télécom Paris Tech, Institut Polytechnique de Paris	Examinatrice
Thomas Rodet Professeur, Ecole Normale Supérieure Paris-Saclay	Directeur de thèse
Dominique Lesselier Directeur de recherche émérite, CNRS	Co-encadrant
Marc Lambert Chargé de recherche, CNRS	Invité

Thèse de doctorat

NNT: 2021UPASG058

Contents

List of Figures

List of Tables

Notation

Quantities concerning configuration:

- N_i: number of incidences
- N_r: number of receivers
- N_f: number of frequencies
- N_x, N_y: number of pixels in x and y directions
- M: number of pixels, $M = N_x \times N_y$
- $\mathcal{D}$: domain of interest
- $\mathcal{S}$: exterior line (circle) of measurement

Variables related to physical quantities:

- ϵ_r: complex relative permittivity
- ϵ_0: relative permittivity in free space
- σ: conductivity
- μ: permeability
- c: speed of sound
- α: attenuation
- α_0: attenuation coefficient at 1 MHz
- k: wavenumber
- k_b: wavenumber in background
- f: frequency
- ω: angular frequency
- χ: contrast, discrete form $\boldsymbol{\chi}$, $M \times 1$ vector, can either be dielectric contrast $\boldsymbol{\chi}^{\text{em}}$ or acoustic contrast $\boldsymbol{\chi}^{\text{ac}}$, $\mathbf{X} = \text{diag}(\boldsymbol{\chi})$
- F^i: incident field, discrete form $\mathbf{F^i}$, $M \times N_i \times N_f$ matrix, can either be electric field $\mathbf{E^i}$ or pressure field $\mathbf{P^i}$
- F^s: scattered field, discrete form $\mathbf{F^s}$, $M \times N_r \times N_f$ matrix, can either be electric field $\mathbf{E^s}$ or pressure field $\mathbf{P^s}$
- F^t: total field, discrete form $\mathbf{F^t}$, $M \times N_i \times N_f$ matrix, can either be electric field $\mathbf{E^t}$ or pressure field $\mathbf{P^t}$
- J: contrast source, discrete form $\mathbf{J}$, $M \times N_i \times N_f$ matrix

Operators and functions

- $g(\cdot, \cdot)$: two-dimensional scalar Green's function
- $g_{3D}(\cdot, \cdot)$: three-dimensional scalar Green's function
- $\text{J}_1(\cdot)$: 1st-kind Bessel function
- $\text{H}_n^{(1)}(\cdot)$: 1st-kind nth-order Hankel function
- $G_d(\cdot)$: Mapping from $\mathcal{D}$ to $\mathcal{D}$
- $G_s(\cdot)$: Mapping from $\mathcal{D}$ to $\mathcal{S}$
- $Q(\cdot)$: optimization criterion

- $< \cdot, \cdot >$ inner product
- $\mathbf{X}^T$: transpose of $\mathbf{X}$
- $\mathbf{X}^\dagger$: conjugate transpose of $\mathbf{X}$
- $\overline{\mathbf{x}}$: conjugate of $\mathbf{x}$
- $.\times$: pointwise product
- ∇: gradient
- $\nabla\times$: curl
- $\nabla\cdot$: divergence
- ∇^2: Laplace operator

Others:

- $\mathbf{G_d}$: Discretization of G_d, $M \times M$ matrix
- $\mathbf{G_s}$: Discretization of G_s, $N_s \times M$ matrix
- $\mathbf{D_1}$, $\mathbf{D_2}$, $\mathbf{D_3}$, $\mathbf{D_4}$: $M \times M$ matrices to calculate difference in horizontal, vertical and two diagonal directions
- $\mathbf{I_{(M)}}$: $(M \times M)$ identity matrix
- $\mathbf{b}_1$, $\mathbf{b}_2$, $\mathbf{b}_3$, $\mathbf{b}_4$: edge variables in different directions
- $\mathbf{g}_x^{(n)}$: gradient with respect to variable x at nth iteration
- $\mathbf{v}_x$: search direction for updating the variable x

Acknowledgements

How time flies! I have lived in France for three years and have finished my PhD study. Here I would like to dedicate this thesis to all those who have offered me support and help during these three years.

First, I would like to express my deep gratitude to my supervisor, Professor Thomas Rodet for his constant encouragement and illuminating instruction. He is nice and patient to give me time to get used to life in France and to learn from the beginning. He also provided me with much useful guidance, from how to use the software for writing, how to give a presentation, to how to do research. He gave me many novel and practical ideas based on which we were able to develop our algorithms and go further.

I would also express my sincere appreciation to my co-advisor, Dr. Dominique Lesselier. He cared about my study and my life, providing me with quite essential books and materials that helped me to get into the field of inverse problem and imaging. He also offered me opportunities to attend international conferences and to communicate with other scientists all over the world, which has broadened my academic view.

I would also like to thank Dr. Marc Lambert. To start is always tough and it was his code that showed me how to represent the quantities in the problem and that gave me guidance for coding. He also offered his nice suggestions and support to me, which made me confident.

I also thank the referees of my thesis, Dr. Oliver Dorn and Professor Joe LoVetri, and the examiners of my Ph.D. defense, Dr. Martina Teresa Bevacqua, Dr. Sébastien Bourguignon, Professor Sylvie Le Hegarat-Mascle and Professor Florence Tupin. They have spent time in reading my manuscript and given detailed comments and suggestions which will definitely improve the work.

I would like to thank my Chinese friends and colleagues in France, in China, in Singapore, and elsewhere: Dr. Peipei Ran and Yarui Zhang, whom I have worked with and who have helped me a lot with my life in France; Dr. Zicheng Liu and Dr. Yu Zhong, who have given me many nice suggestions on my work; Yusheng Lin and Song Zang, my colleagues at SATIE, who have helped me to get familiar with the laboratory.

My sincere thank also goes to my colleagues in ENS Paris-Saclay and CentraleSupélec: Tristan Duchenne, Thomas Cuidu, and many others, who have given me much convenience and support for my life and work.

My great appreciation goes to my family for their support and love. They have cared about my life and study and they always encouraged me to go ahead. I would also thank my brother who made me more confident in myself since he often asked me questions about his homework. It is a pity that they could not travel around France during my PhD study. I hope the world can get normal soon.

All in all, I am lucky to have been a PhD student in SATIE and L2S. This will be a precious experience in my life.

Chapter 1

Introduction et résumé en français

Le cancer du sein est des plus fréquents chez les femmes. La détection précoce d'une petite tumeur peut cependant améliorer le traitement et aider au pronostic. Chaque modalité d'imagerie dédiée au cancer du sein possède ses avantages et ses limites. En pratique, deux ou plusieurs modalités sont souvent utilisées pour un diagnostic plus précis.

Dans cette thèse, nous étudions la combinaison de deux modalités à faible coût et non ionisantes, un système basé sur les micro-ondes et un système basé sur les ultrasons. Ce choix se justifie car ces systèmes sont complémentaires en terme d'information : les ultrasons fournissent des détails structurels avec une relative haute résolution, mais offrent un faible contraste, et les micro-ondes délivrent un contraste élevé entre un tissu sain et un tissu tumoral, mais le font au prix d'une résolution faible. Le but est donc de tirer le maximum de ces deux modalités afin d'obtenir des images possédant à la fois une haute résolution et un fort contraste pour les tissus tumoraux afin de pouvoir effectuer la détection précoce de tumeurs ainsi qu'indiqué.

De plus, nous allons utiliser des systèmes de mesure où l'on n'applique pas de contraintes sur le sein, contrairement à la mammographie, par exemple, et où la géométrie de mesure ne dépendra pas de l'opérateur, contrairement entre autre à l'échographie classique.

Nous allons donc avoir deux systèmes qui vont reposer sur la diffraction des ondes qu'elles soient électromagnétiques ou mécaniques. En terme méthodologique il nous faudra résoudre deux problèmes dits de diffraction inverse. Dans un tel cadre, nous avons un ensemble de paramètres caractéristiques décrivant l'objet d'intérêt tels les propriétés diélectriques en micro-ondes et les paramètres acoustiques en ultrasons, liés à un ensemble d'observables, tels le champ électrique diffracté ou/et le champ de pression, par un opérateur direct modélisant mathématiquement le principe de formation des données collectées.

A partir de l'état d'objet connu, déterminer les observables est un problème direct, notre objectif étant quant à lui de trouver une solution avec des observations données, sachant que nous connaissons l'opérateur direct. Un tel problème est un problème inverse. Il est généralement mal posé au sens d'Hadamard, et des techniques appropriées doivent être appliquées si nous voulons obtenir une solution tant stable que robuste.

Les méthodes tomographiques sur la base desquelles nous développons nos algorithmes d'imagerie sont très étudiées dorénavant. De telles méthodes peuvent en effet récupérer la distribution des paramètres à l'intérieur de la région d'intérêt et être utilisées comme ici à la fois pour l'imagerie par micro-ondes et par ultrasons.

Pour décrire le processus brièvement, nous pouvons dire qu'une source émet des ondes et les champs diffractés par l'objet sont collectés par des récepteurs placés à l'extérieur de cet objet. Cette procédure est répétée avec les sources placées à des positions différentes. En dehors du caractère mal-posé venant de la diffraction multiple, le problème de diffraction inverse est non linéaire, en particulier pour un diffracteur de fort contraste. Nous énumérons ci-après trois types de méthodes, déterministe traditionnelle, bayésienne et la méthode basée sur l'apprentissage automatique.

Méthodes déterministes : Le problème est généralement transformé en un problème d'optimisation. Pour obtenir le contraste, on minimise les moindres carrés entre champ diffracté mesuré et champ obtenu à partir de l'opérateur direct, qui est dans ce cas non linéaire. Ces méthodes peuvent ensuite être classées en méthodes non itératives et méthodes itératives :

- Les méthodes non itératives peuvent donner le résultat en peu de temps, mais ne sont généralement valides que lorsque certaines approximations sont pertinentes, telles l'approximation de Born (BA ou Born Approximation) et celle de Rytov (RA ou Rytov Approximation). La méthode de rétro-propagation (BP ou Back Propagation) décompose quant à elle le problème inverse en plusieurs problèmes linéaires et chaque problème peut être résolu sans itération. De telles méthodes, appropriées pour les diffracteurs dits faibles, ne peuvent pas être appliquées à des situations complexes en pratique, mais elles peuvent fournir une première hypothèse pour les méthodes itératives, et elles sont souvent utilisées à cette fin.

- Les méthodes itératives permettent d'obtenir des résultats de meilleurs qualité, les principales sont listées ci-dessous :

  - La méthode de la série de Born (Born Séries Method) utilise BA afin d'obtenir une estimation initiale du champ à l'intérieur de l'objet et du contraste, puis résout le problème de manière itérative. Dans la méthode itérative de Born (BIM ou Born Iterative Method), avec le contraste initial, un champ d'ordre supérieur peut être obtenu en résolvant le problème direct et ce champ est utilisé pour mettre à jour le contraste en minimisant l'écart entre le champ diffracté mesuré et le champ calculé. Cette procédure est poursuivie jusqu'à ce qu'un critère d'arrêt soit satisfait.
  - La méthode itérative de Born distordue (DBIM ou Distorted Born Iterative Method) implique quant à elle que le problème soit linéarisé à chaque itération. La différence entre l'arrière-plan (background) actuel et le vrai diffracteur est mise à jour. La fonction de Green inhomogène est appliquée et mise à jour à chaque itération en fonction de l'arrière-plan actuel dans DBIM tandis que dans la méthode itérative de Born variationnelle (VBIM ou Variational Born Iterative Method) la fonction de Green reste inchangée.
  - La méthode du gradient modifié (MGM ou Modified Gradient Method) traite pour sa part l'équation d'état comme régularisateur. Les champs et le contraste sont mis à jour à chaque itération en minimisant le coût fonctionnel de sorte que le problème de transfert soit évité, c'est-à-dire d'éviter de mener une inversion de matrice pour résoudre le problème direct non linéaire.
  - Suivant la même idée, la méthode d'inversion de source de contraste (CSI ou Contrast Source Inversion) implique des équations intégrales. On prend en compte une nouvelle paramétrisation avec l'estimation des sources de courants induits et celle du contraste. De plus, on considère que ces paramètres sont indépendants. Un algorithme d'optimisation alterné est utilisé alors afin de mettre à jour le contraste et la source.
  - La méthode d'optimisation basée sur le sous-espace (SOM ou Subspace Optimization Method) est également conduite avec des équations intégrales de type source. Sur la base d'une décomposition en valeurs singulières tronquée des courants induits, en analysant les propriétés spectrales de la fonction de Green multipliée par le champ diffracté, tandis que la partie tronquée est obtenue par optimisation.
  - Une décomposition similaire est appliquée à la carte du courant associé au champ total à l'intérieur de la région d'intérêt dans la méthode TSOM (ou Two-Fold Subspace Optimization Method). Compte tenu de la relation entre fonctions de Fourier et fonctions singulières d'un opérateur intégral, des bases de Fourier discrètes sont utilisées pour construire le sous-espace et l'algorithme de transformée de Fourier rapide (FFT) est utilisé pour optimiser

les inconnues. La méthode correspondante, FFT-TSOM, atteint une complexité de calcul inférieure à celle de la méthode TSOM car la décomposition en vecteurs singuliers est calculée de manière rapide à l'aide des FFT.

Méthodes basées sur l'inférence bayésienne : Au-delà des méthodes déterministes ci-dessus, les problèmes de diffraction inverse peuvent être résolus dans un cadre bayésien : l'information provenant des données et les hypothèses que l'on fait sur les inconnues sont modélisées mathématiquement par des probabilités.

La règle de Bayes exprime la distribution *a posteriori* en fonction de la vraisemblance et de la distribution *a priori*. La loi *a posteriori* permet de rassembler toutes les informations que l'on connaît sur l'inconnue, celle qui vient des hypothèses *a priori* et celle qui vient des données mesurées. Il est généralement malaisé d'obtenir une expression analytique de cette distribution *a posteriori*, en particulier il est souvent très difficile de calculer sa fonction de partition (facteur de normalisation).

La loi *a posteriori* permet de connaître la probabilité de toutes les solutions possibles. Afin de mener une estimation à bien et de retenir une seule solution nous devons effectuer de l'estimation ponctuelle. Cela veut dire choisir uniquement un point de la distribution. Les estimateurs ponctuels les plus rencontrés sont le Maximum *A Posteriori* (MAP) et l'espérance *a posteriori* (PM : Posterior Mean). L'estimateur du maximum *a posteriori* est le plus répandu, car il revient à un problème d'optimisation, il permet d'avoir la solution la plus probable et nous n'avons pas besoin de connaître la fonction de partition pour le calculer. Le second estimateur ponctuel est l'espérance *a posteriori* ; il possède des propriétés de robustesse car il minimise l'erreur quadratique moyenne. Par contre, pour le calculer, on est souvent tenu de passer par une approximation stochastique. Il s'agit des méthodes d'échantillonnage, telles que les méthodes de Monte Carlo par chaînes de Markov (MCMC ou Monte Carlo Markov Chain). Ces méthodes consistent à générer une série d'échantillons qui converge vers la distribution de la loi souhaitée. Pour ce faire, on peut utiliser les approches de Hasting Metropolis qui permettent d'éviter de connaître explicitement la fonction de partition.

Mais il existe d'autres méthodes d'approximation analytique, cette fois, qui peuvent être utilisées. Ces approches sont moins répandues que la précédente. Il y a tout d'abord l'approximation de Laplace qui approche la distribution *a posteriori* par une gaussienne de moyenne égale au maximum de la loi. Une autre approche analytique a été introduite dans le domaine de la physique statistique sous le nom de l'approximation en champ moyen. Le principe est d'approcher la loi *a posteriori* par une loi plus simple, séparable. On procède ensuite à une optimisation variationnelle afin de trouver la loi la plus proche de la loi *a posteriori* au sens de la divergence de Kullback Leiber. Le caractère bayésien de cette approche associée à l'optimisation variationnelle lui a donné son nom d'approche bayésienne variationnelle ou d'approximation bayésienne variationnelle.

Un des intérêts des approches bayésiennes est que l'on peut définir des approches non supervisées, c'est-à-dire des approches ou l'on n'a pas besoin de régler des paramètres pour que la méthode fournisse de bons résultats. En effet, dans les approches classiques de régularisation il faut régler un paramètre qui est un compromis entre le terme d'attache aux données (la proximité de la solution par rapport aux données) et le terme de régularisation (qui empêche d'avoir des solutions qui amplifient le bruit présent dans les données). La qualité de la solution est donc très dépendante du réglage de ce paramètre. De plus, la valeur de ce paramètre varie fortement en fonction de la dimension relative des données et des inconnues ainsi qu'en fonction du rapport signal à bruit présent dans les données. La formalisation bayésienne permet de déterminer que ce paramètre de réglage correspond au rapport entre la variance de la vraisemblance et la variance de la loi *a priori*. L'approche bayésienne en introduisant une loi non informative sur ces variances que l'on appelle les hyperparamètres permet de conduire une estimation conjointe des inconnues et de ces hyperparamètres. Ces hyperparamètres sont appelés des variables cachées et comme l'on estime des paramètres des lois qui modélisent les inconnues on note ces approches comme étant bayésiennes hiérarchiques.

Approches par apprentissage automatique : Les réseaux de neurones étaient déjà utilisés pour résoudre des problèmes de diffraction inverse au siècle dernier. Mais récemment, en raison du succès des méthodes par apprentissage profond dans la reconnaissance vocale, les tâches de vision par ordinateur, e.g., reconnaissance d'images, segmentation, détection d'objets, etc., ces approches ont été utilisées dans le cadre de l'inversion du problème de diffraction.

Parmi ces méthodes nous nous focaliserons sur les réseaux de neurones convolutifs (CNN ou Convolutional Neural Networks). Ceux-ci sont très populaires car ils possèdent une forte capacité de modélisation locale avec peu de paramètres. Alliés aux capacités de calcul croissantes, les CNN peuvent produire la carte du diffracteur, point seulement quelques caractéristiques de l'objet, et ils sont donc largement utilisés pour l'imagerie quantitative.

Les CNN peuvent être exécutés en combinaison avec des algorithmes d'inversion traditionnels, la structure des CNN étant généralement basée sur le U-Net.

Une méthode de rétropropagation peut ainsi fournir l'entrée d'une cascade de réseaux CNN résiduels multicouches à valeurs complexes afin d'obtenir une meilleure reconstruction du contraste. Ou l'on peut partir de la majeure partie du courant de contraste obtenu à partir du champ diffracté et le champ total correspondant en entrée.

Résolution d'un problème d'inversion en utilisant l'information provenant de plusieurs modalités

Puisque le problème inverse est, rappelons-le, mal posé, l'information provenant des seules données ne suffit pas pour obtenir une reconstruction acceptable. Nous devons introduire de l'information, par exemple à l'aide de régularisation. Mais il est souvent préférable d'avoir une autre source plus pertinente que les hypothèses générales effectuées lors de la régularisation. Ainsi, les informations spécifiques provenant d'autres modalités d'imagerie peuvent être très utiles pour obtenir plus d'information sur l'objet recherché. Comme les différentes modalités ne fournissent pas les mêmes grandeurs physiques de l'objet, nous devons effectuer de la fusion d'information afin de tirer partie de ces modalités.

Cette fusion peut se faire après le processus d'imagerie pour produire un résultat plus informatif et aider au diagnostic. Dans un tel cadre, une procédure de recalage est nécessaire afin d'aligner spatialement les images (cibles) avec une autre (référence), avant d'opérer la fusion d'images.

Le recalage est généralement considéré lui-même comme un problème d'optimisation pour trouver une transformation paramétrique sur des images cibles en maximisant la similarité entre images transformées et image de référence. Les images peuvent être fusionnées par de simples opérations pixel par pixel, telles que la moyenne des pixels correspondants des images d'entrée ou la sélection des valeurs maximales ou minimales des pixels correspondants.

La fusion d'images provenant de différentes modalités a été largement étudiée et possède de nombreuses applications telles que la fusion X et ultrasons, la fusion MRI (ou Magnetic Resonance Imaging) et ultrasons, et la mammographie et MRI. Notons que chaque modalité d'imagerie a ses inconvénients qui peuvent affecter la qualité de l'image. Pour notre part, nous nous concentrons sur la fusion reconstruction d'image. Il s'agit de reconstruire conjointement les images des deux modalités pour les informations portées par les deux modalités permettant de lever les indéterminations liées à l'inversion.

Fusion successive : La fusion peut alors être réalisée successivement, le résultat de reconstruction d'une modalité fournissant une connaissance préalable de l'objet pour l'inversion via l'autre modalité. Les informations structurelles peuvent être extraites des images fournies par la modalité de plus haute résolution en tant qu'informations préalables, sous la forme de limites tissulaires indiquant les emplacements des discontinuités ou des régions tissulaires indiquant si deux pixels sont du même type de tissu. Ces informations peuvent alors être utilisées dans le terme de régularisation, soit être incorporées dans un cadre bayésien, soit fournir une meilleure initialisation de la distribution des paramètres.

Dans la littérature, les applications de ces méthodes se trouvent principalement dans le domaine de l'imagerie médicale et en particulier dans le problème de la reconstruction des images par émission de positon (PET : Positon Emission Tomography). En effet, cette modalité est relativement basse résolution et la connaissance de l'atténuation des tissus permet d'obtenir de meilleures reconstructions. Dans ce cadre, des informations anatomiques provenant d'autres modalités comme l'IRM ou la tomodensitométrie peuvent naturellement être incorporées en cadre bayésien. A titre d'exemple, les limites horizontales et verticales dérivées de l'IRM pour la reconstruction d'images fonctionnelles peuvent l'être afin qu'une régularisation introduisant de la douceur dans l'image soit uniquement imposée là où il n'y a pas de sauts importants. Des variables modélisant les frontières des organes issues des images MRI ou TDM sont introduites. On utilise pour cela une loi *a priori* conditionnelle sur l'image PET par rapport à ces variables de frontière. Un seuil concernant les probabilités des limites dans les deux modalités est utilisé pour déterminer si une arête peut être négligée ou doit être améliorée.

Dans la tomographie optique de diffusion des travaux ont modifié le paramètre de régularisation des zones qui étaient identifiées comme des tumeurs à l'aide d'une radiographie mammaire.

Dans le cas de la reconstruction de données pour la tomographie proche infrarouge (NIR ou Near Infrared Tomography), les images IRM ont permis de déterminer le maillage d'éléments finis qui permet de définir plus précisément la paramétrisation de la solution dans une géométrie plus proche de la réalité.

Enfin, dans le domaine de l'imagerie micro-onde, des approches existent qui sont basées sur des algorithmes de mesure de retard (Delay and Sum ou DAS), approches comparables à celles des systèmes échographiques. Des informations issues d'imagerie IRM sont utilisées afin de segmenter l'image en nombre fini de tissus, ce qui permet de tenir compte des retards spécifiques de chaque tissu, et comme cela d'améliorer la qualité de la reconstruction.

Fusion reconstruction conjointe : L'inversion conjointe est un autre moyen de faire de la fusion d'information en présence de données multimodales. Les relations physiques entre différents paramètres peuvent ainsi être incorporées dans le processus d'inversion. En géophysique, les liens pétrophysiques entre vitesse sismique et résistivité sont largement étudiés et utilisés pour améliorer les résultats de l'inversion.

Une autre approche consiste à imposer une similarité structurelle aux deux images reconstruites. Les données mesurées par les différentes modalités sont issues du même objet. Nous n'avons pas forcément les mêmes valeurs car les propriétés physiques mesurées ne sont pas les mêmes, mais par contre ces images partagent la même morphologie. En particulier, les frontières entre les différents matériaux ou tissus sont localisées au même endroit. Le domaine où nous avons trouvé le plus de travaux est en géologie. Dans ce cadre, il a été proposé d'introduire le gradient croisé. Il est défini comme le produit extérieur des gradients de différents paramètres, afin de forcer les paramètres à changer dans la même direction. La reconstruction conjointe favorise donc les solutions où les deux images partagent des gradients dans l'image de même direction mais pas forcément de même norme.

Analyse de l'état de l'art

Nous avons vu que chaque modalité d'imagerie avait des qualités et des défauts. Par exemple, le contraste de la mammographie est faible et la qualité de l'imagerie fortement liée à la densité mammaire. L'IRM mammaire est coûteux et de faible spécificité. En fait, il est très difficile d'améliorer le résultat de l'imagerie avec une seule modalité impliquée, comme il a été souligné plus haut. La multi-modalité apporte plus d'informations et les performances sont améliorées.

Nous voulons dans cette thèse utiliser deux modalités dans le but d'un dispositif de contrôle en routine du cancer du sein. De plus, nous ne voulons pas contraindre le sein (évitant la compression de la mamographie) pendant l'acquisition. Il nous faut donc des modalités de mesure relativement peu coûteuses et qui puissent faire l'acquisition quasi simultanément pour s'affranchir du problème

de recalage. Enfin, il faut que ces modalités soient complémentaires en terme d'informations. C'est pourquoi nous avons choisi les modalité micro-ondes et ultrasons. Ces deux modalités ont besoin d'un milieu de couplage, aussi on imagine un dispositif où la patiente s'allonge sur une table percée, et son sein baigne dans un bol contenant un liquide de couplage, plus les capteurs micro-ondes et ultrasonores. De plus, nous allons choisir comme information pour relier les reconstructions des modalités les frontières des différents tissus. Enfin, nous allons présenter dans cette thèse quatre approches originales, la première est basée sur une fusion séquentielle de l'information, et les trois autres sont basées sur une fusion reconstruction conjointe. Ces approches utiliseront des approches d'optimisation, des approches d'apprentissage par réseau de neurones profond et des approches bayésiennes afin d'avoir un algorithme non supervisé.

Plan du manuscrit : Le manuscrit est structuré comme suit : Ce chapitre présente la motivation et le contexte du travail, y compris modalités d'imagerie et leurs avantages et limites, les problèmes inverses et les algorithmes d'inversion. Des méthodes de fusion sont également introduites. Puis suivent les chapitres en anglais, comme suit.

- Le chapitre 2 introduit le challenge posé et les solutions existantes ou devant être développées.
- Le chapitre 3 fournit les détails de la modélisation avancée du problème.
- Le chapitre 4 examine en détail l'état de l'art des algorithmes d'inversion et des algorithmes d'inversion conjointe.
- Le chapitre 5 décrit l'imagerie par micro-ondes avec des informations sur les limites antérieures de l'imagerie ultra-sonore.
- Le chapitre 6 s'attache à l'inversion conjointe des données micro-ondes et ultra-sonores avec estimation de la limite tissulaire via régularisation préservant les bords.
- Le chapitre 7 considère la construction d'un réseau de neurones convolutifs pour l'imagerie avec données acoustiques et micro-ondes en entrée.
- Le chapitre 8 s'intéresse à une méthode bayésienne avec des arêtes comme variables cachées et estimation conjointe des hyperparamètres.
- Le chapitre 9 est de conclusion et perspectives.
- Les références suivent puis la liste des publications et communications associées à ce travail, mais aussi d'autres travaux réalisés en collaboration.

Partie originale de ce travail de thèse

Avant de conclure cette section française du manuscrit de thèse, attardons nous et en partie revenons sur les avancées de ce travail. Nous avons donc investigué la faisabilité de la détection précoce de tumeurs du sein via modalités micro-ondes et ultrasonores. Les méthodes proposées sont basées sur l'hypothèse que les distributions des paramètres acoustiques et électriques partagent la même structure, qui est déterminée par les types de tissus. Deux classes d'approches ont alors été considérées.

Première approche : La permière approche consiste en une méthode de fusion successive. La reconstruction d'une modalité fournit des informations préalables pour l'inversion avec l'autre modalité.

Nous avons reconstruit une image de discontinuités à partir de données ultrasonores. Cela est similaire au balayage en mode B, seul le temps de parcours de l'impulsion est enregistré et utilisé pour déterminer la distance entre point de réflexion et transducteur, la vitesse du son étant supposée constante. La reconstruction des données micro-ondes est effectuée en utilisant un terme de régularisation introduisant de la douceur. Cette régularisation est proche de celle de Tikhonov sur les différences premières avec paramètre supplémentaire binaire (0 ou 1) pour indiquer si frontière au niveau des tissus ou non. En son absence, une régularisation est imposée de sorte que deux pixels adjacents tendent à posséder des paramètres similaires. Sinon, la valeur est 0 et la discontinuité est autorisée. Et cette approche est codée dans le cadre d'une approche de linéarisation successive au cours des itérations.

Seconde approche : La seconde approche est basée sur de la fusion conjointe où données acoustiques et micro-ondes sont inversées simultanément.

Une inversion conjointe avec régularisation préservant les bords est proposée. La méthode de reconstruction avec préservation des frontières des tissus est basée sur la dualité. C'est une approche semi-quadratique, dont le principe est le suivant : afin de préserver les frontières on introduit une régularisation non quadratique. Et par dualité on introduit des variables auxiliaires permettant d'avoir un problème quadratique de connaissance des variables auxiliaires et d'optimisation séparable.

Premier bénéfice, on remplace un problème non quadratique et non séparable par deux problèmes liés plus simples car l'un est quadratique et l'autre est séparable. L'autre bénéfice de ce choix est que ces variables auxiliaires qui décrivent les frontières vont nous servir à faire le lien entre nos deux problèmes de reconstruction. Ces variables de bord sont continues entre 0 et 1. Une valeur approchant 1 correspond à une discontinuité qui doit être préservée, tandis qu'une valeur proche de 0 signifie que les petites variations seront lissées.

Cette régularisation est intégrée dans la méthode d'inversion par contraste de source (CSI) et imposée aux paramètres acoustiques et électriques tandis que les variables de bord sont partagées. Nous avons combiné les méthodes d'optimisation utilisées en CSI et la régularisation préservant les bords, une minimisation alternée étant utilisée pour mettre à jour les paramètres de la source acoustique, puis du contraste acoustique, puis les variables de bord, puis la source de courant induit, et enfin le contraste micro-onde.

Troisième approche : Notre troisième approche est basée sur les réseaux de neurones convolutifs (CNN). Les différents flux ont été conçus afin de gérer des données provenant de différentes modalités et les cartes de caractéristiques ont donc été fusionnées après plusieurs couches de sorte que les informations des ultrasons et des micro-ondes soient correctement combinées.

Après apprentissage du réseau sur la base d'apprentissage, le réseau produit les paramètres acoustiques et électriques afin de donner les images de reconstruction. Le lien entre les deux modalités s'effectue au travers de la production d'une segmentation commune. La structure commune du sein fournit des informations supplémentaires au réseau pour apprendre la cartographie des données aux paramètres physiques. Cet apprentissage multitâche peut aider à la formation du réseau et améliorer la capacité de généralisation.

De plus, un travail important sur le choix des paramètres définis comme les entrées du réseau a été effectué, afin que le temps de calcul demeure raisonnable. La similarité structurelle est un bon choix à cet effet puisque les paramètres sont liés au type de tissu. Les informations de structure basées sur le bord ou sur la région peuvent être utilisées. Si informations de région choisies, une segmentation de l'image est généralement nécessaire tandis que la limite peut être obtenue plus facilement. En revanche, CNN apprend lui-même la cartographie, permettant d'intégrer les informations sur la région.

Quatrième approche : La quatrième approche vise à obtenir les mêmes résultats que la seconde, mais sans le besoin de régler des hyperparamètres. En effet, cette seconde approche nécessite le réglage de nombreux paramètres afin que la méthode fonctionne correctement. En particulier, il y a des paramètres de compromis entre l'information provenant de la régularisation et l'information provenant des données. De plus, il faut avoir une idée de l'amplitude des discontinuités présentes dans l'image pour corriger le paramètre de régularisation et normaliser la variable auxiliaire entre 0 et 1.

Pour ce faire, nous avons utiliisé une approche bayésienne hiérarchique. Cette approche détermine s'il y a présence de discontinuités en utilisant une variable binaire de Bernouilli commune aux deux modalités. Enfin, il est procédé à l'estimation conjointe d'un grand nombre de variables. Pour cela, nous avons utilisé une approche bayésienne variationnelle pour que les dépendances des hyperparamètres soient simplifiées et que l'on puisse avoir des solutions calculables. Nous estimons donc des lois de probabilité pour toutes les variables estimées et nous le faisons à partir d'un algorithme de minimisation alternée.

Chapter 2

Introduction

Breast cancer is one of the most common cancers among women worldwide and a leading cause for mortality. It is estimated that in 2020, breast cancer results in the most new cases among all cancers, with more than 2.26 million women diagnosed with it and becomes the most life-threatening cancer in females with approximately 700.000 deaths [1].

Early detection of small breast tumor can help prevent metastasis and improve the treatment performance. By identifying a tumor in early stages of 0 or I means that the tumor is noninvasive, smaller than 20 mm in greatest dimension, no evidence of distant metastases and no lymph node metastases [2]. Many researches have reported a decreasing survival rate as the tumor size increases [3, 4]. Thus it is of great concern to develop imaging techniques to detect tumors at an early stage.

2.1 Breast imaging

Here we introduce some noninvasive breast imaging technologies for breast screening and tumor detection.

Mammography

Mammography is the most common breast screening modality and the gold standard method to detect early-stage breast tumors before physical symptoms develop. It projects low-dose X-rays through the compressed breast to form an image based on the absorption of photons by the structure. Mammography can provide images with high resolution, yet the contrast is low. In [5], a slight difference in X-ray attenuation between glandular and tumorous tissue is reported. The sensitivity (true positive rate) of mammography is relatively low, estimated at 78%, and it is quite related to the breast density. The value drops to only 48% in women with extremely dense breasts [6]. Patients may also suffer from the potential ionizing radiation and uncomfortable examination.

Digital breast tomosynthesis (DBT)

DBT or three-dimensional (3D) mammography combined with two-dimensional digital mammography is widely used now for breast screening and diagnosis [7]. In a DBT system, a series of 2D projections by x-ray are acquired at different angles by moving the x-ray tube along a small arc and will be used to reconstruct the 3D structure of the breast. Several studies have shown that combined DBT and digital mammography can improve the sensitivity and specificity (true negative) rates [8, 9]. Though DBT may improve the cancer detection performance, some research shows that cancers detected by DBT tend to be less aggressive [10, 11] leading to problem of overdiagnosis. Besides, the radiation dose is slightly higher than mammography.

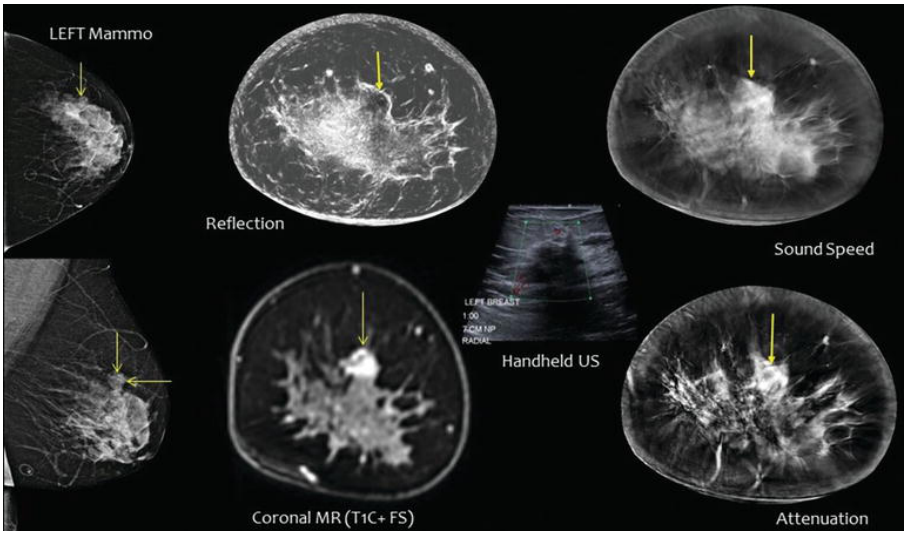

Figure 2.1: Comparison between images of mammography (left), MRI (middle bottom) and ultrasound (middle top and right), with arrows pointing to an IDC (invasive ductal carcinoma).

Magnetic Resonance Imaging (MRI)

Breast MRI is recommended as an adjunct tool to mammography to detect and stage breast tumor and other abnormalities [12]. During the MRI examination, the patient is placed in a strong magnetic field and radio frequency signals are applied to create detailed images of the interior of the breast. MRI yields high-resolution images and ensures high sensitivity, regardless of the breast density [13]. Compared with mammography, MRI is painless and nonionizing. However, MRI is expensive for a general population and it is difficult to distinguish between cancer and benign disease, resulting in a false positive result and low specificity [14, 15].

Breast Ultrasound (US)

Ultrasound, cost effective and safe, is usually used to supplement mammography, particularly for women with dense breasts. Breast ultrasound can be used in various ways. Sonography is the most common form in breast diagnosis [16], which can be applied with a hand-held transducer which transmits high-frequency sound waves and receives echos from tissues at different depths along the propagation path. The strength and the time of the echos from different directions are recorded to form an image. Since pulse transmission and reception can be ended in less than a millisecond, real-time imaging can be achieved. Though it improves the sensitivity [17], the hanheld feature and small aperture make it highly operator-dependent and difficult to image the whole breast. Automated breast ultrasound (ABUS) [18] has been developed to reduce operator-dependence and increase the view field. However, it has the same issue as high false-positive rates with hand-held ultrasound.

Apart from sonography, other imaging techniques have been investigated and developed, like Doppler Ultrasound [19], elastography [20] and so on. Among them, ultrasound tomography is a promising technique for tissue-specific imaging and characterization. It images the breast in a quantitative manner by reconstructing tissue parameters, such as speed of sound and attenuation. Experiments [21] have shown a coronal and an axial resolution at about 0.7 mm and 2.5 mm, while for MRI, the resolutions are 1.6 mm and 0.8 mm. The main problem for such imaging techniques is the low contrast since the acoustic properties of normal and tumorous tissues are quite similar [22].

Figure 2.1 shows images obtained from different imaging modalities of a given breast [21]. It can be seen that all the three modalities have a high resolution, The contrast is high in MRI image while it is relatively low in mammogram and ultrasound images.

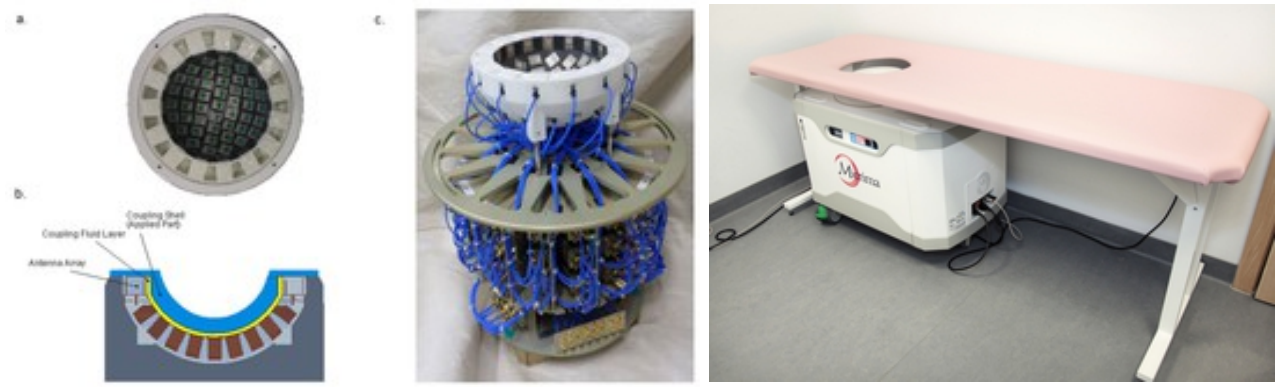

Figure 2.2: Antenna array (left) and the whole system (right) for radar microwave imaging.

Microwave Imaging (MI)

Microwave imaging is an emerging technique and has been a research interest since a decade and more. Microwaves are electromagnetic waves with frequency ranging from 300 MHz and 300 GHz. The wavelength of microwave in free space is between 1 m and 1 mm, accordingly it has a similar dimension to potential anomalies in the human body. The breast is relatively translucent to microwaves such it is not difficult to obtain information from the inside of the breast, however, the resolution is limited [23].

Cancer detection via microwave imaging is based on the difference in the dielectric properties, permittivity and conductivity, between normal and malignant tissue types. Several researchers have studied the electrical properties of healthy tissues and tumorous tissue [24–27]. Many studies have reported a high contrast in the properties between different tissue types over the microwave frequencies.

Microwave can be passive or active. Passive imaging methods [28, 29] try to detect tumors by finding the regions with increased temperature. Active methods mean to illuminate the breast and analyze the scattered and attenuated waves to form an image. Active imaging methods can be classified into two classes, radar-based techniques and tomographic ones. Radar-based approaches [30–33] use ultra-wideband signals for adequate signal penetration and reach a satisfactory resolution as well. One could refer to Figure 2.2 for an example of system for radar microwave imaging [34]. Such methods produce qualitative images indicating the locations of strongly scattering objects within the breast and usually give less detailed information. In contrast, tomographic methods [35–37] are aimed at recovering the distribution of the dielectric parameters inside the breast with narrowband microwave signals and they show promising results for tumor detection.

From the introduction above, it can be seen that each imaging modality has its own advantages and limitations. In practice, two or more modalities are employed for a more accurate diagnosis. In this thesis, we try to combine two low-cost and nonionizing modalities, microwave and ultrasound since they can yield complementary information, i.e., ultrasound can provide structural details of high resolution but with low contrast, while microwave has a high contrast between normal and tumorous tissue but the resolution is low, in the process of imaging to produce images with high resolution and high contrast for early-stage tumor detection. Next, we will introduce the existing methods for tomographic imaging and fusion methods for multimodalities.

2.2 Inverse problem

In this thesis, we focus on tomographic methods to image the breast and try to solve an inverse scattering problem. In such a framework, we have a set of characteristic parameters x, describing the object of interest such as the dielectric properties in microwave and acoustic parameters in ultrasound, linked to a set of observables y, such as the scattered electric field or pressure field, by a forward

operator $\mathcal{A}$ which is a mathematical model of the law of nature. From the known object state x to calculate y is a forward (direct) problem, whereas our aim is to find a solution x with observations y given the relation $\mathcal{A}$. Such a problem is an inverse one, usually ill-posed, and suitable techniques must be applied to find a stable and reasonable solution.

2.2.1 Ill-posedness and regularization

Let us consider a linear case with

$$y = \mathcal{A}(x) \tag{2.1}$$

where y represents the collected data and x the unknown parameters. A problem is well-posed in the sense of Hadamard if all the following conditions are satisfied:

- The solution x^* of equation $y = \mathcal{A}(x)$ exists.
- The solution x^* is unique.
- The solution depends continuously on the data, which means a small perturbation of data y causes a small perturbation on the solution.

If one or more conditions do not hold, the problem is called ill-posed. Typically we need to discretize the equation to solve it numerically and the problem becomes $\mathbf{y} = \mathbf{A}\mathbf{x}$ with $\mathbf{x} \in \mathcal{R}^M$, $\mathbf{y} \in \mathcal{R}^N$ and $\mathbf{A} \in \mathcal{R}^{N\times M}$, the instability can be observed by the ill-conditioned matrix $\mathbf{A}$. $\mathbf{A}$ has a high condition number which is calculated as the ratio of the largest and smallest singular values. With such a matrix, a small error in data $\mathbf{y}$ will lead to high difference in the result while the error caused by noise is inevitable.

As the inverse problem is ill-posed, to invert the problem directly results into unstable and unreliable models. A technique to overcome this difficulty is regularization where a family of well-posed problems which approximate the original inverse problem is considered instead of the original ill-posed one. Usually a least square solution is sought as

$$\mathbf{x} = \text{argmin}_x \|\mathbf{y} - \mathbf{A}\mathbf{x}\|^2 \tag{2.2}$$

which has a solution as $\mathbf{x} = (\mathbf{A}^T\mathbf{A})^{-1}\mathbf{A}^T\mathbf{y}$. However, since $\mathbf{A}$ is ill-conditioned, the solution is not stable. It is of interest to operate a Singular Value Decomposition (SVD) on $\mathbf{A}$ for analysis as $\mathbf{A} = \mathbf{U}\mathbf{\Sigma}\mathbf{V}^T$, where $\mathbf{U}$ and $\mathbf{V}$ are composed of left singular vectors $\mathbf{u}_n$ and right singular vectors $\mathbf{v}_m$, $\mathbf{\Sigma}$ is a $N \times M$ matrix with diagonal elements being the singular values σ_i. Application of SVD yields the solution as $\mathbf{x} = \sum_i \frac{1}{\sigma_i}(\mathbf{u}_i^T\mathbf{y})\mathbf{v}_i$. It can be clearly seen that a small singular value σ_i will amplify the noise in $\mathbf{y}$ and leads to high error. A natural idea is that we can cut off the terms corresponding to the small singular values and the solution becomes $\mathbf{x} = \sum_i^\lambda \frac{1}{\sigma_i}(\mathbf{u}_i^\dagger\mathbf{y})\mathbf{v}_i$. This method is called truncated SVD (TSVD) and an integral λ plays a role of regularization parameter. Yet, the computation burden is high for a large dimensional problem.

In practice, we most often attempt to minimize a modified cost function where, apart from the least square of data misfit, a regularization term is incorporated, as

$$Q(\mathbf{x}) = \|\mathbf{A}\mathbf{x} - \mathbf{y}\|^2 + \lambda Q_{reg}(\mathbf{x}) \tag{2.3}$$

The regularization parameter $\lambda > 0$ controls the trade-off between stability and accuracy. This parameter must be carefully chosen, if it is too small, the approximate solution is unstable, whereas if it is too large the approximate solution will be too far from the original one.

Within such a scheme, various regularization techniques have been proposed to stabilize the solution or to introduce prior information. Next we introduce some regularization techniques widely used in inverse scattering.

The Tikhonov regularization [38], much applied to ill-posed problems, e.g., [39] for references and perspectives, minimizes the distance between the parameter or its derivatives and a prior model. Such a regularization is as an example usually employed in the Distorted Born Iterative Method (DBIM) to stablize the inversion process.

A quadratic criterion can be applied to smooth the gradients at all pixels, yet the edges will be smoothed and cannot be preserved. In edge-preserving regularization, usually a nonquadratic function [40–42] is introduced to less severely penalize a large gradient to preserve edges. Duality between nonquadratic criterion and a half-quadratic (HQ) criterion with additional variables is observed, first with binary edge variables [43, 44], then generalized to continuous ones [45, 46]. Such a regularization has been applied to solve the inverse scattering problem [47].

Some other functions are also aimed at edge preserving. Total variation (TV) [48] is proposed to remove small-scale noise in an image while trying to preserve discontinuities. It is incorporated in the inverse scattering problem as a penalty term to enhance the performance of modified gradient method. In [49], TV as an additional constraint and as a multiplicative constraint is applied. A weighted L2 TV as a multiplicative regularization is proposed in [50] where different weights based on the current gradients are assigned to each pixel and such strategy is much used in inverse scattering problems.

Some Adaptive Discontinuity models are investigated, such as Huber function [51, 52], which contains a quadratic function for variables under the threshold to smooth noise and a linear function for jump above the threshold thus the discontinuity is penalized less severely abou1993nd can be preserved.

Value picking (VP) [53] regularization, a nonspatially structured approach, can be also applied for piece-wise constant profiles. The contrasts are constrained to some certain values and small variations are eliminated.

2.2.2 Inverse scattering methods

In this section, we discuss the tomographic methods based on which we develop our imaging algorithms. Such methods can retrieve the distribution of the parameters inside the region of interest and can be used for both microwave and ultrasound imaging. Usually a source emits waves and the fields scattered by the object are collected by receivers placed outside the object. This procedure is repeated with the other sources placed at different positions. As is well-known, ill-posedness and nonlinearity plague the inverse scattering problem, especially (but not only) for a scatterer with a high contrast. Here we list three types of methods, namely traditional deterministic method, Bayesian method, and machine-learning-based method.

Traditional deterministic methods

In deterministic methods the problem is usually cast into an optimization problem to get the contrast by minimizing a least square misfit between the measured scattered field and the field obtained from an analytical model. These methods can then be classified into two classes, noniterative and iterative methods.

Noniterative methods can give the result in a short time but usually they are valid only when some approximations are assumed such as the Born Approximation (BA) and the Rytov Approximation (RA). The Back-propagation (BP) method decomposes the inverse problem into several linear problems and each problem can be solved without iteration. Such methods, valid for weak scatterers, cannot be applied to complex situations in practice but can give an initial guess for iterative methods.

The Born series method uses BA to get an initial guess of the field inside the object and the contrast and then solves the problem in an iterative way. In the Born iterative method (BIM) [54], with the initial contrast, a field of higher order can be obtained by solving the forward problem and this field is used to update the contrast by minimizing the discrepancy between measured scattered field and the calculated one. Such procedure is continued until a stopping criterion is satisfied. The Distorted Born

Iterative Method (DBIM) —already mentioned in the above— is developed [55] where the problem is linearized at each iteration. The difference between the current background and the true scatterer is updated. The inhomogeneous Green's function is applied and updated at each iteration based on the current background in DBIM while in the Variational Born Iterative Method (VBIM) [56] the Green's function is kept unchanged.

The Modified Gradient Method (MGM) [57] treats the state equation (which describes the wavefield-scatterer interaction inside the domain of interest containing the breast, see next chapter for more detail) as a regularizer. Both the fields and the contrast are updated in each iteration by minimizing the cost functional so as the forward problem is avoided. Based on the same idea, the Contrast Source Inversion (CSI) method is developed [58]. It involves source-type integral equations and contrast source is regarded as an independent parameter. Alternate optimization is used to update the contrast and the contrast source.

Subspace-based Optimization Method (SOM) [59] is also performed with source-type integral equations. Based on TSVD, the main part of the contrast current is determined by analyzing the spectral properties of the Green's function mapping from the contrast current to the scattered fields directly, while the ambiguous part is obtained by an optimization method. Further, a similar decomposition is applied to the mapping from the current to the total field inside the region of interest in the twofold SOM (TSOM) [60]. Considering the relation between Fourier functions and singular functions of an integral operator, discrete Fourier bases are used to construct the subspace and fast Fourier Transform (FFT) algorithm is used to optimize the unknowns. With such an idea, FFT-TSOM [61] achieves a lower computational complexity than the TSOM since the singular vector decomposition (SVD) is avoided for one matrix.

Bayesian methods

Except the above deterministic methods, inverse scattering problems can also be solved in a Bayesian framework. Bayes' rule gives the distribution of parameter $\mathbf{x}$ given the measured data $\mathbf{y}$ as $p(\mathbf{x}|\mathbf{y}) = p(\mathbf{y}|\mathbf{x})p(\mathbf{x})/p(\mathbf{y})$, where $p(\mathbf{x}|\mathbf{y})$ is the posterior distribution, $p(\mathbf{y}|\mathbf{x})$ is the likelihood, $p(\mathbf{x})$ is the prior density of $\mathbf{x}$ and $p(\mathbf{y})$ does not depend on parameters and plays role of a normalization constant. To find the posterior distribution is usually challenging, especially for high-dimensional data. Point estimators, such as maximum a posteriori (MAP) and posterior mean (PM), can be used to get the estimation of the object. Another group of methods tries to find an approximation of the true posterior density. Markov-Chain Monte-Carlo (MCMC) techniques [62] generate a series of samples which converges towards the distribution of the desired law and calculate the empirical mean. Variational Bayesian (VB) approach [63] is another way which approximates the joint posterior distribution with independent separable distributions.

Usually hyperparameters $\boldsymbol{\theta}$ are involved in the prior distribution of the object and the likelihood. These hyperparameters can be fixed while it is also possible to insert them into a Bayesian framework. In the latter case, additional probability distribution is assigned to them and thus a hierarchical Bayesian model is constructed.

In [64], Gaussian distributions are assigned for the real and imaginary parts of the data error separately and a uniform law is applied to the relative permittivity. Maximum likelihood is used to get the solution for microwave imaging with experimental data. Markov Random Field model is widely used in Bayesian methods. Total variation prior can be employed to preserve edges. In [65] such prior is used to get a high-resolution image from a set of low-resolution images with VBA method. Markov Random Field (MRF) where the pixels and their neighbors are modeled are widely considered. If their difference is penalized in a square form, we can get a Gaussian MRF (GMRF). In [66], such a model is used separately for real and imaginary parts of the contrast and MAP estimation is employed to find the solution. GMRF is generalized with power in the potential function ranging between 1 and 2 in [41] and solved with MAP estimation. Some other models use MRF together with hidden variables.

Auxiliary edge variables are introduced for image restoration [43, 67]. In [68], a Gauss-Markov field is used to model the contrast and hidden variables indicating the material class of the pixels are introduced with Potts-Markov field. The posterior mean is estimated with Gibbs sampling. The same prior is also used in [69, 70] for microwave breast imaging with VBA to get the estimation results.

Machine-learning-based method

Machine learning-based inversion algorithms are intensively investigated nowadays, as reviewed as of lately in [71]. Shallow neural networks have been used in inverse scattering problems since the last century. In [72], a one-hidden-layer network is designed to predict the parameters of the circular cylindric scatterer, including the coordinate of the center, the radius and the permittivity of the scatterer, given the scattered field as the input. In [73], a support vector machine is used to approximate the function from the scattered field to the parameters of the scatterer. Earlier work focuses on the estimation of few parameters of the object, such as location and permittivity and so on. Similar works can also be found in [74, 75].

Recently, due to the success of deep learning method in speech recognition, computer vision tasks, such as image recognition [76, 77], segmentation [78, 79], object detection [80, 81] and so on, inversion methods based on deep learning have attracted quite a lot of attention Among all deep learning techniques, convolutional neural networks (CNNs) are the most popular.

Indeed, CNN has strong local modeling capability with few parameters. With the increasing computation ability, CNN can output the scatterer map, not only few characteristics of the object, thus it is widely used for quantitative imaging.

In [82], a CNN structure is designed to use the measured fields as the input and to predict the scatterer map directly. In [83], a two-step method is proposed with a complex-valued CNN to get the initial contrasts of the scatterers from the measured data and then another CNN based on U-Net [79] is to refine this result. CNN can also be run in combination with traditional inversion algorithms. In [84], CNN is to estimate the total contrast current given the part in signal space calculated similarly to SOM as the input, then the noise subspace component of the contrast current and the contrast are optimized iteratively. Other strategies use CNN to refine the obtained results obtained from some conventional algorithms. Similar with [83], in such a method, the structure of CNN is usually based on U-Net. In [85], the result of a backpropagation method is the input of a cascade of multi-layer complex-valued residual CNN networks in order to get a better reconstruction of the contrast. In [86], with the major part of the contrast current obtained from the scattered field and the corresponding total field as the input, the contrast current is predicted. In [87], a U-Net based network is trained to enhance the reconstruction result from CSI where ultrasound prior information is incorporated for microwave imaging and in [88], a 3D CNN is designed for a 3D case, 3D also dealt with in [89] wherein a stage 1 involves a phaseless bulk-parameter inference neural network that recovers geometry and permittivity of the breast fibroglandular region, those bulk parameters being used for calibration and prior for a full phase contrast source inversion at stage 2. We should also cite [90] where a convolutional neural network is trained based on the input of the quantitative ultrasonic compressibility, reconstructed using a linearized inverse scattering algorithm, and the output of the true quantitative dielectric properties corresponding to the same numerical phantom.

2.3 Imaging with multi-modality

As it is described that the inverse problem is ill-posed since only limited data can be collected, thus regularization with additional information is introduced. However, the structure and the parameter values vary from person to person, so it is difficult to find *a priori* information suitable for all patients. Thus, model-specific information from other imaging modalities can be very useful to gain more information.

Information from different modalities can be combined after the imaging process to produce a more informative result and to help the diagnosis. In such a framework, a registration procedure is needed to make the (target) images spatially aligned with another one (reference image) and then image fusion can be operated [91]. Registration is usually considered as an optimization problem to find a parametric transformation on target images by maximizing the similarity between the transformed images and the reference image. The images can be fused by simple pixel-by-pixel operations, such as averaging the corresponding pixels of the input images or selecting the maximum or minimum values of the corresponding pixels.

Apart from this direct fusion, some transform domains can be used to perform fusion such as intensity-hue-saturation (IHS) color space [92] and principal component space [93]. Fusion can be also achieved on multi-scale representations of the original images, such as discrete wavelet transform [94], curvelet transform [95] and contourlet transform [96].

The fusion of images from different modalities —run independently or not, in the same conditions of the imaged structure or not, with the challenge of registration if that structure has been changed by constraints of experiments, like, typically, compression— has been widely investigated and has many applications such as US-X-ray fusion [97], MRI-US fusion [98, 99] and mammography-MRI [100, 101]. Note that each imaging modality has its drawbacks which may duly affect the imaging quality. Our focus is on the fusion during the imaging process to remedy limitations of each modality and to alleviate the ill-posedness of the inverse problem by introducing more information. With this strategy, imaging with fusion can be classified into two classes, sequential inversion and joint inversion.

2.3.1 Sequential inversion

Fusion can be achieved by successive imaging with the reconstruction result of one modality providing prior knowledge of the object for the inversion of another modality. The structural information can be extracted from images provided by the high-resolution modality as prior information, in the form of tissue boundaries indicating the locations of discontinuities or tissue regions showing if two pixels are of the same tissue type.

Some researches use high-resolution prior information to enhance the imaging quality of Positron Emission Tomography (PET). As an example, in [102], MRI-derived horizontal and vertical boundaries are incorporated into a Bayesian framework for image reconstruction so that smoothness is easily broken on the locations where significant boundaries occur. In [103], boundaries given in MR or Computed Tomography (CT) are incorporated by a weighted line site method as the prior for line process in PET reconstruction. A threshold regarding probabilities of the boundaries in both modalities is used to determine whether an edge can be neglected or should be enhanced. In [104], a region-labeling approach is proposed with higher prior probabilities assigned to image segmentations more nearly to anatomical regions.

The results of Diffuse Optical Tomography (DOT) can be improved with other modalities also. In [105], a smaller regularization parameter is distributed in a Tikhonov regularization scheme to pixels identified as part of tumor from X-ray images in DOT breast imaging. In [106], the structural information is extracted from MRI and Finite Element Method (FEM) based on the geometries is applied in DOT. In [107, 108], high-resolution images are segmented into major tissue types. Prior probability density is formulated with a mean value assigned to each region.

It is also intensively investigated for microwave. High-resolution images from other modalities are segmented into different regions and a regularization term is proposed to limit the variation in each region. Such soft prior methods are applied in [109–112]. Hard prior where the parameters within each region are strictly the same is also developed [111]. In such methods, only a few number of values need to be reconstructed. In [113], a dual-modality breast imaging method is proposed. An ultrasound image is obtained by Delay and Sum (DAS) algorithm and then K-means method is applied to segment the image into sub-images representing different tissues. Dielectric parameter values are assigned for

different pixels based on the tissue clusters, which gives more accurate tissue-specific time-delays in DAS algorithm for microwave imaging. Last, the clustered ultrasound image and microwave image are added to form a more representative image. In [114], the structural information is extracted from US reconstruction with the K-means clustering algorithm. Tissue permittivity values are assigned to these regions to form an inhomogeneous background and assist the EM reconstruction by the FEM-CSI algorithm.

2.3.2 Joint inversion

Joint inversion is another way for information fusion where multimodal data are inverted simultaneously.

Physical relations between different parameters can be incorporated in the inversion process to achieve joint inversion. In geophysics, petrophysical links between the seismic velocity and resistivity are widely investigated and applied for inversion [115, 116].

Another way to perform joint inversion is to impose structural similarity. The measured data of multi-modalities are the responses of the same object with identical structure, thus the inversions should find solutions with consistent structure.

In [117], a joint inversion algorithm is proposed for seismic and electrical tomography. Apart from the data misfits, a regularization term is added representing the differences in the normalized structure curvatures between different parameters. The model curvatures are obtained by Laplacian operator and a nonlinear amplitude gain control function is used to normalize them to decrease the influence of the amplitudes and to focus on the locations of the discontinuities. In [118], a structure operator is defined where the curvature of the model is measured by thresholding and evaluating with a polynomial function. Joint inversion is carried out by minimizing the difference in the structure of the models subject to fitting the data.

In [119], cross-gradient is proposed as the outer product of the gradients of different parameters. It is employed to force the parameters to change into the same direction. This method is widely used in geophysics, in [120, 121] as a constraint and in [122–125] as a regularization term. In [126], Joint Total Variation for joint inversion is considered by coupling spatial gradients of both parameters through the square root function as an additional regularization term. In [127], a regularization operator based on weighted L2 total variation is proposed with the weighting coefficients related to the gradients of another modality to exchange information between EM and US inversion. Refer again to [90] as well.

2.4 Objective and outline

From the introduction above, we can see that every imaging modality has its drawbacks. For example, the contrast of mammography is low and the imaging quality is heavily related to the breast density; breast MRI is expensive and has low specificity. It is very difficult to improve the imaging result with only a single modality involved. Instead, with multimodality involved to image the same object, more information can be obtained and the performance can be enhanced. Here we choose microwave and ultrasound for tumor detection, since they are both low-cost, noninvasive and safe, furthermore, they provide complementary information, i.e., ultrasound can provide high-resolution but low-contrast images while microwave imaging has a high contrast but a low resolution. By combining these two modalities, we have the chance to obtain images with both high contrast and high resolution. Since the measured data of the two modalities are the reflection of the same breast with the same tissue distribution, we can use the structure to achieve fusion of these modalities as the properties usually have a small variation in the same tissue but a relatively large one inter-tissues. This structure can be represented by the boundary to show the discontinuity of parameters or by regions to give the information that whether two pixels should have similar parameters or not. To summarize, this thesis investigates breast imaging with both acoustic and electromagnetic data, from boundary information

from ultrasound images as prior in microwave imaging to the case where boundary is jointly estimated in the inversion process. Further, several techniques are employed to get rid of the problem of the choice of hyperparameters, with convolutional neural networks to learn the mapping from data to the parameter distribution and Bayesian method to jointly estimate the hyperparameters.

The thesis is structured as follows:

- This Chapter 2 (here) introduces the motivation and background of the work, including the current imaging modalities and their advantages and limitations, inverse problems and the inversion algorithms. Fusion methods are also introduced.
- In Chapter 3, the details of the forward modeling of the problem, from wave equation to the specific two-dimensional case, are given.
- In Chapter 4, the state of art of inversion algorithms and joint inversion algorithms is considered in detail.
- In Chapter 5, microwave imaging with prior boundary information from ultrasound imaging is described.
- In Chapter 6, joint inversion of electromagnetic and acoustic data with estimation of tissue boundary based on edge-preserving regularization is proposed.
- In Chapter 7, a convolutional neural network is constructed for imaging with both acoustic and electromagnetic data input.
- In Chapter 8, a Bayesian method is proposed with edges as hidden variables and to joint estimation of the hyperparameters.
- In Chapter 9 the proposed algorithms are summarized and some perspectives given.
- The list of references follows as usual.
- Then, a summary of the dissemination linked to the present work and co-operative ones led on superresolution in the diagnostic of a dielectric micro-structure is given.

Chapter 3

Forward problem

3.1 Introduction

An inverse problem is a flip side of some direct problem, or forward problem, which treats the transformation of known causes into effects that are determined by some specified model of a natural process [128]. Here the forward problem gives the physical relation between the known object and the measured scattered fields. In contrast, given the scattered field, to find the physical properties of the object is an inverse problem.

3.2 Electromagnetics

Very many textbooks exist on electromagnetics which one can easily refer to, so thereafter only elements of interest to the analysis are shown. Maxwell's equations read as

$$\nabla \times \vec{E}(\mathbf{r},t) = -\frac{\partial}{\partial t}\vec{B}(\mathbf{r},t) \tag{3.1a}$$

$$\nabla \times \vec{H}(\mathbf{r},t) = \frac{\partial}{\partial t}\vec{D}(\mathbf{r},t) + \vec{J}_i(\mathbf{r},t) + \vec{J}_c(\mathbf{r},t) \tag{3.1b}$$

$$\nabla \cdot \vec{D}(\mathbf{r},t) = \rho_e(\mathbf{r},t) \tag{3.1c}$$

$$\nabla \cdot \vec{B}(\mathbf{r},t) = 0 \tag{3.1d}$$

where $\vec{E} = E_x\vec{x} + E_y\vec{y} + E_z\vec{z}$ and $\vec{H} = H_x\vec{x} + H_y\vec{y} + H_z\vec{z}$ are the electric and magnetic field strength, respectively, $\vec{D}$ the electric displacement, $\vec{B}$ the magnetic flux density, $\vec{J}_i$ the electric current density of the source, $\vec{J}_c$ the conduction electric current density and ρ_e the electric charge density. They are all real functions of position and time.

Considering time-harmonic dependency $e^{-i\omega t}$ and constitutive relations for a linear isotropic at-rest homogeneous medium

$$\vec{D}(\mathbf{r}) = \epsilon\vec{E}(\mathbf{r}) \tag{3.2a}$$

$$\vec{B}(\mathbf{r}) = \mu\vec{H}(\mathbf{r}) \tag{3.2b}$$

$$\vec{J}_c(\mathbf{r}) = \sigma\vec{E}(\mathbf{r}) \tag{3.2c}$$

with $\epsilon = \epsilon_0\epsilon_r$ the permittivity ($\epsilon_0 = 8.854 \times 10^{-12}$ Farad/meter is the permittivity in free space and ϵ_r is the relative permittivity), $\mu = \mu_0\mu_r$ the permeability ($\mu_0 = 4\pi \times 10^{-7}$ Henry/meter is the permeability in free space) and σ the conductivity (σ=0 Siemens/meter in free space) —dispersive models (Debye) of permittivity, not limited as here to a static conductivity, will be considered in the

numerical examples, yet this changes little at this stage of the exposé. Relations between $\vec{E}$ and $\vec{H}$ are as

$$\nabla \times \vec{E}(\mathbf{r}) = i\omega\mu\vec{H}(\mathbf{r}) \tag{3.3}$$

$$\nabla \times \vec{H}(\mathbf{r}) = -i\omega(\epsilon + i\frac{\sigma}{\omega})\vec{E}(\mathbf{r}) + \vec{J}_i(\mathbf{r}) \tag{3.4}$$

By eliminating $\vec{H}$ we obtain the wave equation for the electric field $\vec{E}(\mathbf{r})$ as

$$\nabla \times \nabla \times \vec{E}(\mathbf{r}) - k^2\vec{E}(\mathbf{r}) = i\omega\mu\vec{J}_i(\mathbf{r}) \tag{3.5}$$

where $k^2 = \omega^2\mu\epsilon_0(\epsilon_r + i\frac{\sigma}{\omega\epsilon_0})$. From now on, we define $\epsilon_r + i\frac{\sigma}{\omega\epsilon_0}$ as the complex relative permittivity, and simply represent it as ϵ_r.

To determine $\vec{E}$ from a given source $\vec{J}$, we introduce the dyadic Green's function $\overline{\overline{G}}$, which satisfies

$$\nabla \times \nabla \times \overline{\overline{G}}(\mathbf{r}, \mathbf{r}') - k^2\overline{\overline{G}}(\mathbf{r}, \mathbf{r}') = \overline{\overline{I}}\delta(\mathbf{r} - \mathbf{r}') \tag{3.6}$$

where $\overline{\overline{I}}$ is a unit dyad and can be represented by a unit diagonal matrix. The dyadic Green's function characterizes the response at $\mathbf{r} = (x, y, z)$ produced by a point source at $\mathbf{r}' = (x', y', z')$. It can be expressed in terms of scalar Green's function $g_{3D}(\mathbf{r}, \mathbf{r}')$ as

$$\overline{\overline{G}}(\mathbf{r}, \mathbf{r}') = \left[\overline{\overline{I}} + \frac{1}{k^2}\nabla\nabla\right] g_{3D}(\mathbf{r}, \mathbf{r}') \tag{3.7}$$

where $g_{3D}(\mathbf{r}, \mathbf{r}')$ satisfies the differential equation

$$\left(\nabla^2 + k^2\right) g_{3D}(\mathbf{r}, \mathbf{r}') = -\delta(\mathbf{r} - \mathbf{r}') \tag{3.8}$$

and has the solution

$$g_{3D}(\mathbf{r}, \mathbf{r}') = \frac{e^{ik|\mathbf{r}-\mathbf{r}'|}}{4\pi|\mathbf{r} - \mathbf{r}'|} \tag{3.9}$$

when the Sommerfeld radiation condition

$$\lim_{r\to\infty} r\left[\frac{\partial g_{3D}(\mathbf{r}, \mathbf{r}')}{\partial r} - ikg_{3D}(\mathbf{r}, \mathbf{r}')\right] = 0 \tag{3.10}$$

is applied with $r = |\mathbf{r}|$. In that framework, the electric field can be expressed as

$$\vec{E}(\mathbf{r}) = i\omega\mu \iiint \overline{\overline{G}}(\mathbf{r}, \mathbf{r}')\vec{J}(\mathbf{r}')d^3\mathbf{r}' \tag{3.11}$$

From now, let us consider a scattering problem involving a non-magnetic linear isotropic (possibly) inhomogeneous scatterer with complex permittivity $\epsilon(\mathbf{r}) = \epsilon_0\epsilon_r(\mathbf{r})$ and constant magnetic permeability $\mu(\mathbf{r}) = \mu_0$ located within a non-magnetic linear isotropic homogeneous background medium, the latter assumed with constant complex permittivity $\epsilon(\mathbf{r}) = \epsilon_0\epsilon_b$ and magnetic permeability $\mu(\mathbf{r}) = \mu_0$.

Hypothesizing a source outside the scatterer, the fields $\vec{E}$ and $\vec{H}$ can be decomposed into two parts, the incident fields $\vec{E}^i$ and $\vec{H}^i$ produced by the primary source when the scatterer is absent and the scattered fields $\vec{E}^s$ and $\vec{H}^s$ due to the scatterer, and we have $\vec{E} = \vec{E}^i + \vec{E}^s$, $\vec{H} = \vec{H}^i + \vec{H}^s$. So,

$$\nabla \times \vec{E}^i(\mathbf{r}) = i\omega\mu_0\vec{H}^i(\mathbf{r}) \tag{3.12}$$

$$\nabla \times \vec{H}^i(\mathbf{r}) = -i\omega\epsilon_0\epsilon_b\vec{E}^i(\mathbf{r}) \tag{3.13}$$

and the total fields $\vec{E}$ and $\vec{H}$ read as

$$\nabla \times \vec{E}(\mathbf{r}) = i\omega\mu_0 \vec{H}(\mathbf{r}) \tag{3.14}$$

$$\nabla \times \vec{H}(\mathbf{r}) = -i\omega\epsilon_0\epsilon_r(\mathbf{r})\vec{E}(\mathbf{r}) \tag{3.15}$$

Comparing the above equations,

$$\nabla \times \vec{E}^s(\mathbf{r}) = i\omega\mu_0 \vec{H}^s(\mathbf{r}) \tag{3.16}$$

$$\nabla \times \vec{H}^s(\mathbf{r}) = -i\omega\epsilon_0\epsilon_b \vec{E}^s(\mathbf{r}) - i\omega\epsilon_0(\epsilon_r(\mathbf{r}) - \epsilon_b)\vec{E}(\mathbf{r}) \tag{3.17}$$

Thus the solution to the scattered field is

$$\vec{E}^s(\mathbf{r}) = i\omega\mu_0 \iiint \overline{\overline{G}}(\mathbf{r}, \mathbf{r}')(-i\omega\epsilon_0(\epsilon_r(\mathbf{r}') - \epsilon_b)\vec{E}(\mathbf{r}'))d^3\mathbf{r}' \tag{3.18}$$

emphasizing that, for convenience in terms of not manipulating too many subscripts, the dyadic Green's function $\overline{\overline{G}}$ involved here (and its scalar counterpart g) is as previously defined yet with k now identified to $k_b = \omega\sqrt{\mu_0\epsilon_b}$, i.e., with respect to the exterior medium.

In this thesis, we focus on the algorithmics, thus a two-dimensional case is considered to reduce computational complexity, but the algorithm could be generalized to a three-dimensional case. In the 2D case, all physical parameters are assumed invariant into the z direction. The field can be regarded as a superposition of transverse electric (TE) and transverse magnetic (TM) parts. In the TE case, the electric field is transverse to the z-axis and only has x- and y-components, whereas in the TM case, the magnetic field is transverse to the z-axis. Here a TM case is the one considered and the electric field has a z component only. Thus, the vector integral equation becomes scalar as

$$E_z^s(\mathbf{r}) = i\omega\mu_0 \iint g(\mathbf{r}, \mathbf{r}')(-i\omega\epsilon_0(\epsilon_r(\mathbf{r}') - \epsilon_b)E(\mathbf{r}'))d^2\mathbf{r}' \tag{3.19}$$

where $g(\mathbf{r}, \mathbf{r}')$ is the 2D scalar Green's function, considered from now on. For simplicity, the subscript 'z' is discarded in the following description.

3.3 Acoustics

Regarding acoustic waves, it seems an agreed assumption to treat the soft breast, as is studied in this work, as a fluid medium that supports only compressional waves. In addition, variations of density in the media involved are neglected, so a further simplified mathematical setting. Accordingly, the wave equation [129] is given by

$$\nabla^2 p(\mathbf{r}, t) - \frac{1}{c^2}\frac{\partial^2 p(\mathbf{r}, t)}{\partial t^2} = 0 \tag{3.20}$$

The pressure p is obtained by linearization of the equations for the motion of fluids. c is the local speed of sound. The pressure is a scalar and we consider a two-dimensional case directly. For time-harmonic acoustic waves of the form $p(\mathbf{r}, t) = \Re\{P(\mathbf{r})e^{-i\omega t}\}$, we have the following equation

$$\nabla^2 P(\mathbf{r}) + \frac{\omega^2}{c^2}P(\mathbf{r}) = 0 \tag{3.21}$$

Following the same procedure as with the EM case, for a scattering problem, the pressure $P = P^i + P^s$. The incident field has a homogeneous background as described above, while for the total field P we have

$$\nabla^2 P(\mathbf{r}) + \frac{\omega^2}{[c(\mathbf{r})]^2}P(\mathbf{r}) = 0 \tag{3.22}$$

So,

$$\nabla^2 P^s(\mathbf{r}) + \frac{\omega^2}{c_b^2} P^s(\mathbf{r}) = -\omega^2 (\frac{1}{c^2} - \frac{1}{c_b^2}) P(\mathbf{r}) \tag{3.23}$$

Denote $k = \dfrac{\omega}{c}$ as the wavenumber in the acoustic case, the scattered field is

$$P^s(\mathbf{r}) = \iint g(\mathbf{r}, \mathbf{r}')(k^2 - k_b^2) P(\mathbf{r}') \tag{3.24}$$

the Green's function being, as noted in the above, valued for k_b.

If we consider a lossy medium, the wavenumber can be written as

$$k = \frac{\omega}{c} + i\alpha(\omega) \tag{3.25}$$

where $\alpha(\omega) = \alpha_0 (2\pi\omega)^n$ is the frequency-dependent attenuation coefficient and the power n in soft tissue is studied experimentally and usually is between 0 and 2. Note that here we insert the attenuation parameter in the same way as [130], yet there are other choices. We also assume that the dispersion effect can be neglected and thus the speed of sound is frequency-independent within the frequency band of our interest.

3.4 Forward model

In this work a two-dimensional case with transverse magnetic (TM) polarization is considered. In the two-dimensional case, all physical parameters are assumed invariant in the z direction. Time-harmonic waves are assumed with time dependence $\exp(-i\omega t)$ for both acoustic and electromagnetic cases. The modeled breast is located inside a domain of interest (DoI) $\mathcal{D}$. The known background medium is characterized by its complex relative permittivity ϵ_b, permeability μ_b, and wavenumber $k_b^{\text{em}} = \omega\sqrt{\epsilon_0 \epsilon_b \mu_b}$ in electromagnetics, and its speed of sound c_b, attenuation α_b, and wavenumber $k_b^{\text{ac}} = \omega/c_b + i\alpha_b$ in acoustics. Magnetic permeability is taken constant within the DoI. The unknown parameters are the complex relative permittivity $\epsilon_r(\mathbf{r}) = \epsilon_r'(\mathbf{r}) + i\epsilon_r''(\mathbf{r})$, the sound speed $c(\mathbf{r})$ and the attenuation $\alpha(\mathbf{r})$. For each imaging modality, N_i ideal (line) sources emit the incident wave successively with the resulting scattered field collected by N_r ideal (line) receivers evenly located at $\mathbf{r}_v'$, $v = 1, 2, \ldots, N_r$ on a circle $\mathcal{S}$. Each source illuminates the DoI and scattered fields are collected by all.

As the introduction of previous sections, when a two-dimensional case is considered, the wave equations for electromagnetic and acoustic cases are the same. Here we use F to represent the field, which can be the electric field E or the pressure field P. The forward problem involves two integral equations: the first one is the Lippmann-Schwinger equation (state equation) which describes the wave-scatterer interaction inside the DoI, the second one is the data equation which describes the scattered field produced due to the presence of the object. For the pth incidence, we have

$$F_p^t(\mathbf{r}) = F_p^i(\mathbf{r}) + \int_{\mathcal{D}} (k^2(\mathbf{r}') - k_b^2) g(\mathbf{r}, \mathbf{r}') F_p^t(\mathbf{r}') \, \mathrm{d}\mathbf{r}', \mathbf{r} \in \mathcal{D} \tag{3.26}$$

$$F_p^s(\mathbf{r}) = \int_{\mathcal{D}} (k^2(\mathbf{r}') - k_b^2) g(\mathbf{r}, \mathbf{r}') F_p^t(\mathbf{r}') \, \mathrm{d}\mathbf{r}', \mathbf{r} \in \mathcal{S} \tag{3.27}$$

where $F^i(\mathbf{r})$ is the incident field and $F^t(\mathbf{r})$ the total field, representing the field inside $\mathcal{D}$, with the object absent or present, respectively. F^s is the scattered field collected by the receivers. The two-dimensional scalar Green's function is $g(\mathbf{r}, \mathbf{r}') = \frac{i}{4} \mathrm{H}_0^{(1)}(k_b|\mathbf{r} - \mathbf{r}'|)$ with $\mathrm{H}_0^{(1)}$ 1st-kind 0th-order Hankel function. Denote the contrast as

$$\chi(\mathbf{r}) = \frac{k^2(\mathbf{r}) - k_b^2}{k_b^2} \tag{3.28}$$

and integral operators

$$G_d[x](\mathbf{r}) = k_b^2 \int_{\mathcal{D}} g(\mathbf{r}, \mathbf{r}') x(\mathbf{r}') \, \mathrm{d}\mathbf{r}', \mathbf{r} \in \mathcal{D} \tag{3.29}$$

$$G_s[x](\mathbf{r}) = k_b^2 \int_{\mathcal{D}} g(\mathbf{r}, \mathbf{r}') x(\mathbf{r}') \, \mathrm{d}\mathbf{r}', \mathbf{r} \in \mathcal{S} \tag{3.30}$$

The equations above simplify into

$$F_p^t(\mathbf{r}) = F_p^i(\mathbf{r}) + G_d[\chi F_p^t](\mathbf{r}), \mathbf{r} \in \mathcal{D} \tag{3.31}$$

$$F_p^s(\mathbf{r}) = G_s[\chi F_p^t](\mathbf{r}), \mathbf{r} \in \mathcal{S} \tag{3.32}$$

Denote the contrast source as

$$J_p(\mathbf{r}) = \chi(\mathbf{r}) F_p^t(\mathbf{r}) \tag{3.33}$$

By multiplying the contrast χ on both sides of Equation (3.31) we can get the source-type integral equation as

$$J_p(\mathbf{r}) = \chi(\mathbf{r}) F_p^i(\mathbf{r}) + G_d[J_p](\mathbf{r}), \mathbf{r} \in \mathcal{D} \tag{3.34}$$

$$F_p^s(\mathbf{r}) = G_s[J_p](\mathbf{r}), \mathbf{r} \in \mathcal{S} \tag{3.35}$$

3.5 Discrete model

To handle the problem numerically, discrete forms of the equations have to be derived, here via a standard pulse-basis point-matching Method of Moments (MoM). The DoI is discretized into $M = N_x \times N_y$ subwavelength cells with centers at $\mathbf{r}_m$, $m = 1, 2, \ldots, M$. The dielectric properties are considered homogeneous in each cell. Every square cell is approximated by a small disk with same area and with equivalent radius R whether needed. The equations above become

$$\mathbf{F}_p^{\mathbf{t}} = \mathbf{F}_p^{\mathbf{i}} + \mathbf{G_d} \mathbf{X} \mathbf{F}_p^{\mathbf{t}} \tag{3.36}$$

$$\mathbf{F}_p^{\mathbf{s}} = \mathbf{G_s} \mathbf{X} \mathbf{F}_p^{\mathbf{t}} \tag{3.37}$$

$\mathbf{X}$ is a $M \times M$ diagonal matrix with $\mathrm{diag}(\mathbf{X}) = \boldsymbol{\chi} = [\chi(\mathbf{r}_1), \chi(\mathbf{r}_2), \ldots, \chi(\mathbf{r}_M)]^T$. $\mathbf{F}_p^{\mathbf{t}}$ and $\mathbf{F}_p^{\mathbf{i}}$ are $M \times 1$ vectors with $\mathbf{F}_p^{\mathbf{t/i}} = [F_p^{t/i}(\mathbf{r}_1), F_p^{t/i}(\mathbf{r}_2), \ldots, F_p^{t/i}(\mathbf{r}_M)]^T$. $\mathbf{F}_p^{\mathbf{s}}$ is a $N_r \times 1$ vector as $\mathbf{F}_p^{\mathbf{s}} = [F_p^s(\mathbf{r}'_1), F_p^s(\mathbf{r}'_2), \ldots, F_p^s(\mathbf{r}'_{N_r})]^T$. The $M \times M$ matrix $\mathbf{G_d}$ is

$$\mathbf{G_d}(m, m') = \begin{cases} \dfrac{ik_b\pi R}{2} \mathrm{J}_1(k_b R) \mathrm{H}_0^{(1)}(k_b |\mathbf{r}_m - \mathbf{r}_{m'}|), m \neq m' \\ \dfrac{ik_b\pi R}{2} \mathrm{H}_1^{\{1\}}(k_b R) - 1, \text{otherwise} \end{cases} \tag{3.38}$$

where J_1 is the 1st-kind Bessel function and $\mathrm{H}_1^{(1)}$ the 1st-kind 1st-order Hankel function. The $N_r \times M$ matrix $\mathbf{G_s}$ is

$$\mathbf{G_s}(v, m) = \frac{ik_b\pi R}{2} \mathrm{J}_1(k_b R) \mathrm{H}_0^{(1)}(k_b |\mathbf{r}'_v - \mathbf{r}_m|) \tag{3.39}$$

Similarly, we can discretize the source-type integral equations as follows:

$$\mathbf{J}_p = \mathbf{X} \mathbf{F}_p^{\mathbf{i}} + \mathbf{X} \mathbf{G_d} \mathbf{J}_p \tag{3.40}$$

$$\mathbf{F}_p^{\mathbf{s}} = \mathbf{G_s} \mathbf{J}_p \tag{3.41}$$

where $\mathbf{J}_p$ is $M \times 1$ vector with $\mathbf{J}_p = [J_p(\mathbf{r}_1), J_p(\mathbf{r}_2), \ldots, J_p(\mathbf{r}_M)]$ and likewise for $\mathbf{F}_p^{\mathbf{i}}$.

3.6 Solution to forward problem for simulation

Given the Equation (3.36), the total field can be calculated as

$$\mathbf{F^t} = (\mathbf{I} - \mathbf{G_d X})^{-1} \mathbf{F^i} \tag{3.42}$$

where $\mathbf{I}$ is the identity matrix. When $\mathbf{F^t}$ is obtained, the scattered field $\mathbf{F^s}$ can be calculated directly with Equation (3.37). The matrix $\mathbf{I} - \mathbf{G_d X}$ has a dimension of $M \times M$ and it is quite time-consuming to compute the inverse. Thus we use an iterative method to solve the problem based on source-type equations. With the Equation (3.40), we construct an optimization problem which minimizes $Q_{cur}(\mathbf{J}_1, \mathbf{J}_2, \ldots, \mathbf{J}_{N_i}) = \sum_p \|\mathbf{J}_p - \mathbf{X F^i}_p - \mathbf{X G_d J}_p\|^2$. Here, the conjugate gradient method with Polak-Ribière search direction is employed for optimization. The contrast source is updated as

$$\mathbf{J}_p^{(n)} = \mathbf{J}_p^{(n-1)} + \beta^{(n)} \mathbf{v}_{J_p}^{(n)} \tag{3.43}$$

with the search direction

$$\mathbf{v}_{J_p}^{(n)} = \begin{cases} -\mathbf{g}_{J_p}^{(n)} + \dfrac{\Re < \mathbf{g}_{J_p}^{(n)}, \mathbf{g}_{J_p}^{(n)} - \mathbf{g}_{J_p}^{(n-1)} >}{< \mathbf{g}_{J_p}^{(n-1)}, \mathbf{g}_{J_p}^{(n-1)} >} \mathbf{v}_{J_p}^{(n-1)}, n > 1 \\ -\mathbf{g}_{J_p}^{(n)}, n = 1 \end{cases} \tag{3.44}$$

Note that here we follow [49] to take the real part of $< \mathbf{g}_{J_p}^{(n)}, \mathbf{g}_{J_p}^{(n)} - \mathbf{g}_{J_p}^{(n-1)} >$. Letting the conjugate transpose of $\mathbf{X}$ be $\mathbf{X}^\dagger$, the gradient of Q_{cur} with respect to $\mathbf{J}_p$ at the nth iteration is

$$\mathbf{g}_{J_p}^{(n)} = \mathbf{o}_p^{(n-1)} - \mathbf{G_d^\dagger} \left(\mathbf{X o}_p^{(n-1)} \right) \tag{3.45}$$

with $\mathbf{o}_p^{(n-1)} = \mathbf{J}_p^{(n-1)} - \mathbf{X E^i}_p - \mathbf{X G_d J}_p^{(n-1)}$ and the step size $\beta^{(n)}$ is

$$\beta^{(n)} = \frac{-\sum_p < \mathbf{g}_{J_p}^{(n)}, \mathbf{v}_{J_p}^{(n)} >}{\sum_p \|\mathbf{v}_{J_p}^{(n)} - \mathbf{X G_d v}_{J_p}^{(n)}\|^2} \tag{3.46}$$

Matrix-vector products can be calculated with Fast Fourier Transform (FFT) implemented to reduce the computation complexity. The algorithm to solve the forward problem described is summarized below.

Algorithm 1 Iterative method to solve forward problem

Input: incident field $\mathbf{F^i}_p$, $p = 1, \ldots, N_i$, contrast $\mathbf{X}$
Calculate: $\mathbf{G_d}$ and $\mathbf{G_s}$ with Equation (3.38) and (3.39)
Initialization: $\mathbf{J}_p^{(0)} = \mathbf{X F^i}_p$
repeat
  Update $\mathbf{J}_p$ with Equation (3.43), (3.44) and (3.45)
until a stopping criterion is satisfied
Calculate: $\mathbf{F^s}_p$ with Equation (3.41)
Output: $\mathbf{F^s}$

3.7 Breast models

Lazebnik *et al.* [131, 132] have conducted a large study on the dielectric properties of normal and malignant breast tissues at microwave frequency, from 0.5 to 20 GHz and fitted one-pole Cole-Cole

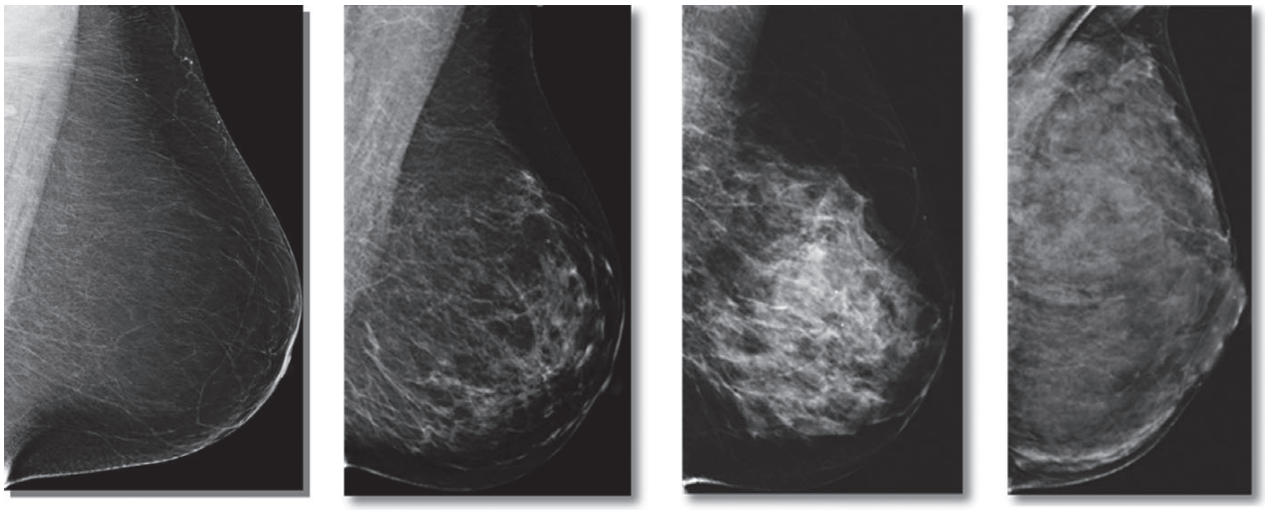

Figure 3.1: Breasts classified into different classes, from left to right: almost entirely fatty, scattered fibroglandular tissue, heterogeneously dense breast and extremely dense tissue (sagittal slices).

model for each sample. Based on such research results, an on-line breast phantom repository has been built by the University of Wisconsin Computational Electromagnetics (UWCEM) Laboratory. Shea *et al.* [133] have fitted a single-pole Debye model for these models over the frequency range 0.5 to 3.5 GHz. Since our operating frequency falls in this region, we use the parameters provided in [133] and breast phantoms in the UWCEM repository to build the models for the microwave case considered in our work. Acoustic parameters are assigned to the models based on the tissue type of each pixel.

3.7.1 Realistic breast models

The UWCEM breast phantom repository provides anatomically realistic numerical breast phantoms derived from MRI images of healthy breasts [134, 135]. Each phantom includes a roughly 1.5-mm-thick skin layer and each voxel is 0.5 mm × 0.5 mm × 0.5 mm. The phantoms in the repository are classified into four classes vs. the radiographic density defined by the American College of Radiology [136], namely almost entirely fatty, scattered fibroglandular tissue, heterogeneously dense breast, and extremely dense tissue. Figure 3.1, extracted from [2], shows images of breasts in these classes.

Since dense breasts have a higher risk for breast cancers [137], we focus on the breast phantoms categorized into the last two classes, Class 3 and 4. A Class 2 phantom is also used in the numerical experiment, yet with no tumor and overall is less investigated. Our models are (coronal) slices along s1 axis (perpendicular to the chest wall, corresponding to z axis) and the chest wall is not included, thus they contain skin, fibroconnective/glandular, transitional, fatty tissues. Here we show some breast models used in this thesis.

Figure 3.2 shows the model categorized into Class 2. This model is from the breast phantom (ID 070604, slice s1=150). In this model, there is more adipose tissue than fibroglandular tissue and no tumor is added. We see also the heterogeneity in fatty and glandular tissues.

Figure 3.3 shows the models from Class 3. These two models are obtained from the same breast phantom (ID 080304, slice s1=150) but with different synthetic tumors. The two tumors are at same position, (1.2 cm, −0.5 cm). The one in the left model has a regular shape and a radius of 5 mm while the one in the right model is irregular-shaped and its largest dimension is no more than 12 mm.

A Class 4 model with an irregular-shaped tumor is shown in Figure 3.4. It is derived from phantom (ID 012304, slice s1=100). A tumor is added in the glandular part at (1.8 cm,1.2 cm) with largest dimension no more than 12 mm.

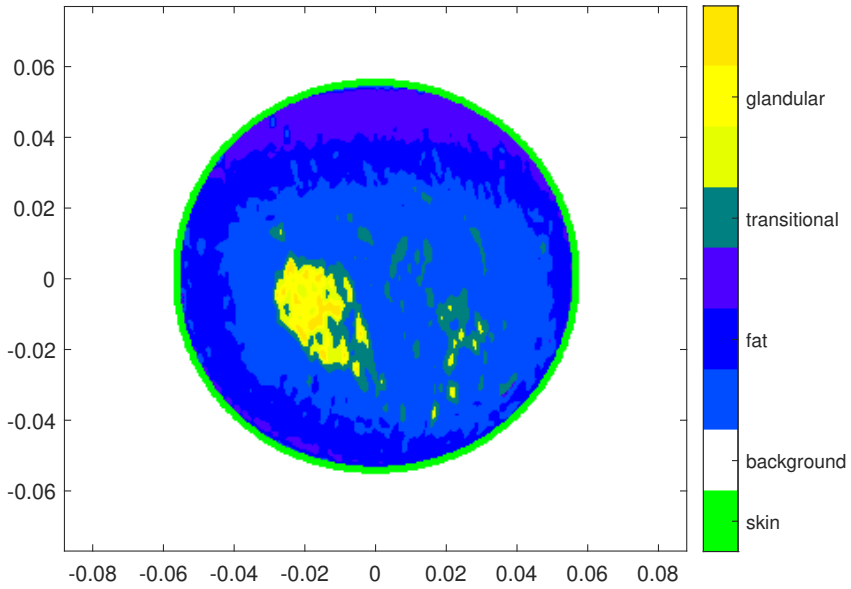

Figure 3.2: A Class 2 model.

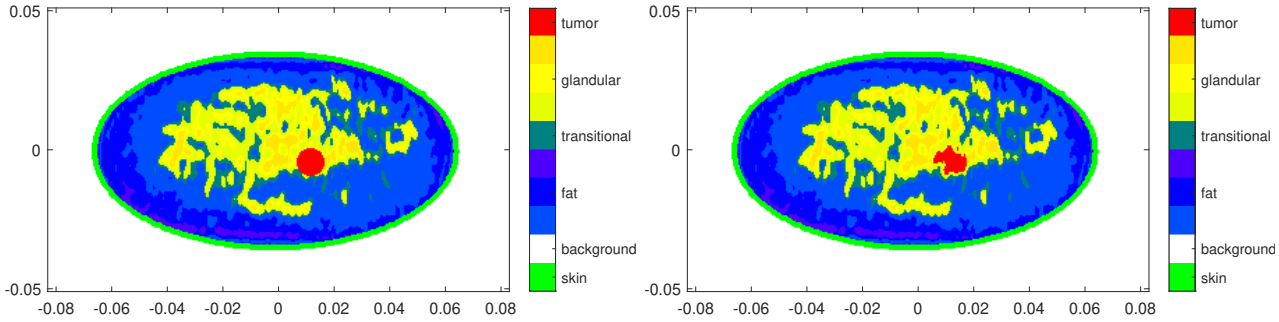

Figure 3.3: Two Class 3 models with a synthetic tumor.

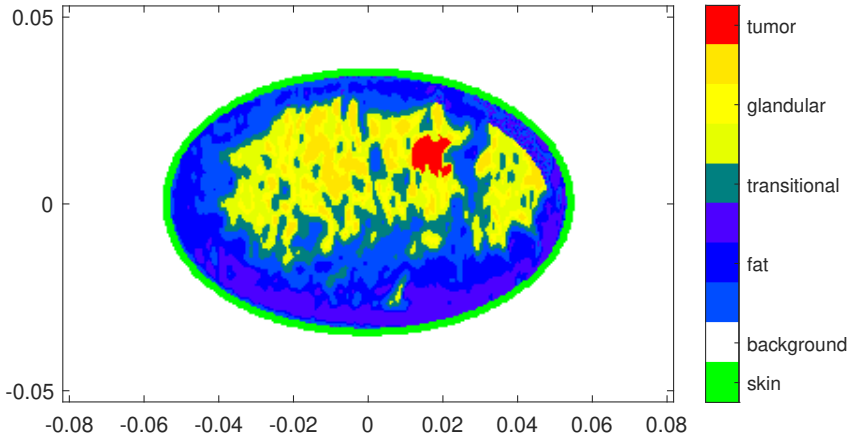

Figure 3.4: A Class 4 model with a synthetic tumor.

With these breast models, dielectric and acoustic parameters are set based on the tissue type. For the microwave case, the first-order Debye model is used to assign a complex relative permittivity to different tissue types as

$$\epsilon_r = \epsilon_\infty + \frac{\Delta\epsilon}{1 - i\omega\tau} + i\frac{\sigma_s}{\omega\epsilon_0} \tag{3.47}$$

with ϵ_∞ the relative permittivity at high frequency, $\Delta\epsilon$ the dispersion amplitude, σ_s the static conductivity and τ the relaxation time. Parameters for normal breast tissues in the breast phantoms are from [133] and listed in Table 3.1 with τ =15 ps constant for all the tissues.

Table 3.1: Debye parameters valid from 0.5 to 3.5 GHz

Tissue type	ε_∞	$\Delta\varepsilon$	σ_s
Adipose tissue (minimum)	2.28	0.141	0.0023
Adipose tissue (25th)	2.74	1.33	0.0207
Adipose tissue (50th)	3.11	1.70	0.0367
Adipose tissue (75th)	4.09	3.54	0.0842
Fibroglandular tissue (25th)	16.8	19.9	0.461
Fibroglandular tissue (50th)	17.5	31.6	0.720
Fibroglandular tissue (75th)	18.6	35.6	0.817
Fibroglandular tissue (maximum)	29.1	38.1	1.38
Skin tissue	15.3	24.8	0.741

For the acoustic case, we assume that pixels in the same tissue type have same acoustic parameters. These values are from [138, 139] and listed in Table 3.2. Note that the type "transitional" is not listed but an average value of fatty and glandular tissues is assigned to it.

Table 3.2: Acoustic sound speed in m/s and attenuation in dB/MHz/cm, and relative dielectric permittivity ϵ_r at 1 GHz, for different tissues.

Tissue/Media	sound speed c	attenuation α_0	permittivity ϵ_r
skin	1615	0.35	$39.8816 + 15.6363i$
fatty	1478	0.48	$4.7950 + 0.8185i$
glandular	1510	0.75	$48.8218 + 15.8941i$
tumor	1548	1.45	$56.2672 + 17.9652i$

A synthetic tumor is added into each model and its relative permittivity is chosen as the 75th percentile curve in [131] and the acoustic parameter is from [139].

3.7.2 Synthetic breast model

Apart from the above complicated realistic breast phantoms, a simple synthetic breast model is also designed to validate the algorithm and to help the analysis. This model consists of skin, fatty, fibroconnective/glandular and tumorous tissues. Each tissue type has regular shape and uniform dielectric property, as shown in Figure 3.5. The skin thickness is 2 mm and the tumor is of 6 mm-diameter. In this model, the DoI is 0.1 m $\times$ 0.1 m-sized.

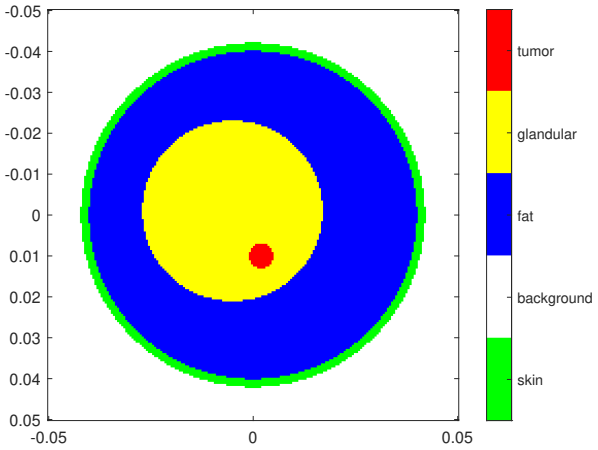

Figure 3.5: A synthetic breast model.

Acoustic parameters of tissue types are the same as with realistic phantoms. The dielectric parameters of fatty and glandular tissues are chosen as the 50th percentile values in Table 3.1. The parameters of the tumor is chosen from [133]. Table 3.2 lists the complex relative permittivity of each tissue type.

Chapter 4

Inversion Algorithms

This chapter focuses on the techniques and algorithms related to our work which consists of four parts. First we will present the basics of convolutional neural networks based on which we will construct a network to fuse the two modalities. Then we introduce the edge-preserving regularization with application of half-quadratic criterion based on which a joint inversion algorithm is developed. Next we will focus on the state-of-the-art approaches for joint inversion and last the inverse scattering algorithms are described.

4.1 Basics of convolutional neural network

In the past decade, different forms of neural networks have been developed, from perceptrons and shallow neural networks to deep belief networks, convolutional neural networks, recurrent neural networks and so on, to solve more complicated problems. Recently, deep learning techniques with deep networks have been a big success in many tasks and have been used also in inverse scattering problem. Among these network structures, CNN is most widely used in this problem. CNN is a data-driven method which requires a large number of training samples and the performance of the network is heavily dependent on the quality and quantity of the training data. Under a supervised-learning scheme, training samples (pairs of input and ideal output) are fed into the network to find proper parameters. These pairs can be measured scattered field and the contrast map, first estimation of the contrast and the real contrast map, estimation of the contrast current and the real one, and many other choices.

Similar with traditional neural networks, a convolutional neural network is stacked by layers with different functions. Figure 4.1, extracted from [140], shows a typical CNN structure used for image recognition. There are some commonly-used layers. The convolutional layer with nonlinear activation

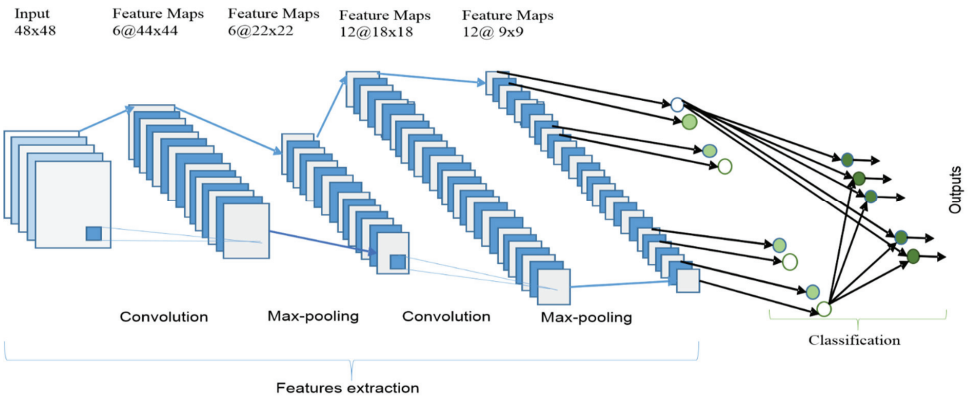

Figure 4.1: A typical CNN structure in image recognition task.

will extract features from the input and sometimes pooling layers are used to reduce the size of the feature maps. Usually the combination of above layers are repeated several times to get a stronger modeling capacity. Batch normalization is a technique widely used to help training. With a loss function defined at the last layer measuring the discrepancy between the predicted output and the given true value, such as least square for regression problem and softmax cross-entropy loss for multiclass classification problem, the parameters are updated in an iterative way by minimizing the loss function. Once the network is well trained, it has the ability to map from the input to output.

4.1.1 Layers of CNN

In this section, several kinds of layers are introduced, as used later in the CNN structure design in our algorithm.

Convolutional layer

A convolutional layer consists of a number of kernels (filters) performing convolution on the input data. A convolutional kernel operates on a local receptive field with the same size of the kernel (such as $3 \times 3 \times C$ where C is usually determined as the number of channels of the input data), computing the dot product between the weight of the kernels and the entries in the receptive field and adding a bias, then it slides over the whole input image. In this way, a two-dimensional map is formed with each element being the convolved result of a certain region by this kernel. Stacking the maps for all kernels along the depth dimension (channel) forms the final output of the convolutional layer. The learnable parameters include the weights and bias for each kernel. The output of kernel k with weight W and bias b is

$$y_{i,j} = \sum_{h,w,c} W_{h,w,c} x_{s_i+h,s_j+w,c} + b \tag{4.1}$$

This is quite different from the fully-connected layers in traditional neural networks where the receptive field of each neuron is the entire previous layer. Such local-connectivity and weight-sharing mechanism can decrease the number of trainable parameters and improve generalization. An example of convolutional layer is shown in Figure 4.2.

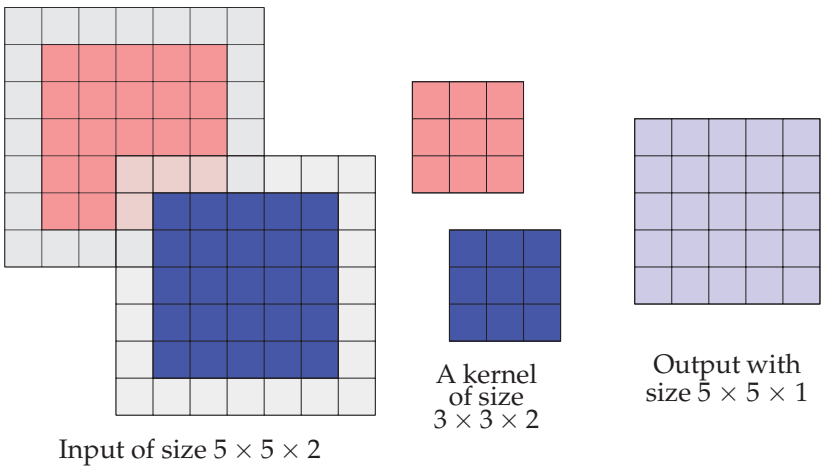

Figure 4.2: Example of convolutional layer: input data is of size $5 \times 5 \times 2$, zero-padding (gray region) is used to keep the size unchanged, a kernel of size $3 \times 3 \times 2$ operates on the input data with stride 1 and generates an output with size $5 \times 5 \times 1$. K kernels will generate an output with size $5 \times 5 \times K$.

Activation layer

Convolution is a linear operation and nonlinear activation is needed to add nonlinearity in the network. In machine learning, the activation function usually are chosen as sigmoid function $f(x) = 1/(1+e^{-x})$ or tanh function $f(x) = (e^x - e^{-x})/(e^x + e^{-x})$. They are saturated functions: the outputs of the sigmoid function are bounded in (0, 1) while for tanh function the output values are between -1 and 1. A drawback of these functions is that when the input is too large or too small, the gradient is too small to contribute in the update of the parameters. This leads to the problem of vanishing gradient especially for deep networks. To overcome this difficulty, rectified linear unit (ReLU) [141] is proposed with activation function $f(x) = \max(0, x)$. Given a positive input, the gradient is a constant 1 which can resolve the vanishing gradient effect. Meanwhile, ReLU is easy to compute and can help accelerate the convergence. However, when $x < 0$, the derivative is zero and the relative weights might not be updated any more. To solve this problem, variants of ReLU focused on the negative part have been proposed such as Leaky ReLU [142] where a fixed small slop is set and parametric ReLU [143] in which the slope for negative input is learnable.

Batch Normalization

Batch normalization (BN) [144] is a widely-used technique in CNN which can enable faster and more stable training. It is proposed to reduce internal covariate shift referred to the change in the distribution of layer inputs caused by updates to the preceding layers which may hinder training. Consider the input x with a size $N \times H \times W \times C$, where N is the number of samples, H and W the height and width of the input map and C the channel number which is the number of kernels of the previous layer. The mean and variance data along the channel c are calculated as

$$\mu_c = \frac{1}{NHW} \sum_n \sum_{h,w} x_{n,h,w,c} \tag{4.2}$$

$$\sigma_c^2 = \frac{1}{NHW} \sum_n \sum_{h,w} (x_{n,h,w,c} - \mu_c)^2 \tag{4.3}$$

Then the data are normalized by

$$\tilde{x}_{n,h,w,c} = \frac{x_{n,h,w,c} - \mu_c}{\sqrt{\sigma_c^2 + \delta}} \tag{4.4}$$

where δ is a small constant for numerical stability. The normalized data $\tilde{x}$ follow a standard normal distribution. Learnable parameters γ and β are introduced to restore the representation power of the network and the output of the layer is

$$y_{n,h,w,c} = \gamma_c \tilde{x}_{n,h,w,c} + \beta_c \tag{4.5}$$

y are used instead of x for the later computation. BN can accelerate the convergence speed, avoid gradient vanishing and explosion and also has a slight regularization effect [145].

Softmax classifier

Softmax is a generalized version of Logistic regression to solve the classification problem for multi-classes. In such a problem, the labels representing the class of the sample can have different values. Let us assume that we have N training samples $\{(\mathbf{x}_1, y_1), (\mathbf{x}_2, y_2), \ldots, (\mathbf{x}_N, y_N)\}$ and labels $y_n \in \{1, 2, \ldots, Y\}$. For a certain input $\mathbf{x}_i$, the softmax function calculates the probability of the input belonging to each class as

$$h(\mathbf{x}_n) = \frac{1}{\sum_{l=1}^{Y} e^{\boldsymbol{\theta}_l^T \mathbf{x}_n}} [e^{\boldsymbol{\theta}_1^T \mathbf{x}_n} \; e^{\boldsymbol{\theta}_2^T \mathbf{x}_n} \cdots e^{\boldsymbol{\theta}_Y^T \mathbf{x}_n}]^T \tag{4.6}$$

where $\boldsymbol{\theta}$ is the trainable parameters. It is easy to find that the probability of $\mathbf{x}_n$ classified into class y is

$$Pr(y_n = y|\mathbf{x}_n;\boldsymbol{\theta}) = \frac{e^{\boldsymbol{\theta}_y^T\mathbf{x}_n}}{\sum_{l=1}^{Y} e^{\boldsymbol{\theta}_l^T\mathbf{x}_n}} \tag{4.7}$$

We wish to maximize the probability of correct classification while minimizing the probability of cases where the sample is misclassified. The cost function here is

$$Q(\boldsymbol{\theta}) = \frac{1}{N}\left[\sum_{n=1}^{N}\sum_{y=1}^{Y} t_n^y \log\frac{e^{\boldsymbol{\theta}_y^T\mathbf{x}_n}}{\sum_{l=1}^{Y} e^{\boldsymbol{\theta}_l^T\mathbf{x}_n}}\right] \tag{4.8}$$

with

$$t_n^y = \begin{cases} 1, \text{ sample } n \text{ belongs to class } y \\ 0, \text{ otherwise} \end{cases} \tag{4.9}$$

This cost function is similar with the one in logistic regression, yet the cost is summed over all classes. By minimizing the cost functional, proper values for parameter $\boldsymbol{\theta}$ can be obtained and the samples can be correctly classified.

4.1.2 Training of CNN

Let us suppose that we have N pairs of training samples $\{(\mathbf{x}_1,\mathbf{y}_1),\ldots,(\mathbf{x}_N,\mathbf{y}_N)\}$, the final cost function is a summation of the misfit between the predicted and ideal outputs and a regularization term imposed on the network parameters to overcome overfitting as

$$Q(\boldsymbol{\theta};\mathbf{x},\mathbf{y}) = \frac{1}{N}\sum_{n} Q_{\text{mis}}(\boldsymbol{\theta};\mathbf{x}_n,\mathbf{y}_n) + \lambda Q_{\text{reg}}(\boldsymbol{\theta}) \tag{4.10}$$

The network can be trained by minimizing the cost function. Based on chain rule, the error back-propagates from the last layer to the first layer such that the gradient of the cost function with each trainable parameter can be obtained.

Usually the bias is initialized as zero, while for the weights, some widely-used initialization methods are developed to avoid magnifying or reducing the magnitudes of the signal exponentially and to further avoid exploding or vanishing gradients, such as Xavier initializer [146], where the weights follow a uniform distribution in the range $(-\frac{\sqrt{6}}{m_j+m_{j+1}}, \frac{\sqrt{6}}{m_j+m_{j+1}})$, with m_j the number of inputs and m_{j+1} the number of outputs, and He initializer [143] where the initial weights follow a Normal distribution with zero mean and standard deviation of $\sqrt{\frac{2}{m_j}}$.

Usually the network is trained on mini-batch data to benefit from the vectorization which can speed up the calculation and to avoid large data sets which takes too much time. If we choose the batch size as N_b, the gradient of the cost function with respect to the parameter θ is

$$\mathbf{g}_\theta = \frac{1}{N_b}\sum_{n=1}^{N_b}\frac{\partial Q_{\text{mis}}(\boldsymbol{\theta};\mathbf{x}_n,\mathbf{y}_n)}{\partial\boldsymbol{\theta}} + \lambda\frac{\partial Q_{\text{reg}}(\boldsymbol{\theta})}{\partial\boldsymbol{\theta}} \tag{4.11}$$

A number of epochs is set for the training where in each epoch all the training samples are used to update the network parameters once.

Stochastic gradient descent (SGD) is the most widely-used way for network training. For the gradient with respect to the parameter $\mathbf{g}_\theta$, the parameter is updated simply by

$$\boldsymbol{\theta} = \boldsymbol{\theta} - \alpha\mathbf{g}_\theta \tag{4.12}$$

where α is the learning rate and usually set by the users. To achieve good results, α should decay as the training proceeds.

Adam [147] is another optimization algorithm used in deep learning which combines the advantages of Adagrad and RMSProp which includes the momentum estimation and bias correction. Hyperparameters β_1 and β_2 as the exponential decay rates for the moment estimates are introduced. The Adam algorithm is summarized below.

Algorithm 2 Adam Optimization

Input: α, β_1,β_2,
Initialization: θ, m, v
repeat
$n = n + 1$
Calculate the gradient $\mathbf{g}_\theta$
Update biased first moment estimate $\mathbf{m} = \beta_1 \cdot \mathbf{m} + (1 - \beta_1) \cdot \mathbf{g}_\theta$
Update biased second raw moment estimate $\mathbf{v} = \beta_2 \cdot \mathbf{v} + (1 - \beta_2) \cdot \mathbf{g}_\theta . \times \mathbf{g}_\theta$
Compute bias-corrected first moment estimate $\mathbf{m}^c = \mathbf{m}/(1 - \beta_1)$
Compute bias-corrected second raw moment estimate $\mathbf{v}^c = \mathbf{v}/(1 - \beta_2)$
Update parameter $\boldsymbol{\theta} = \boldsymbol{\theta} - \alpha \cdot \mathbf{m}^c/(\sqrt{\mathbf{v}^c} + \delta)$
until a stopping criterion is satisfied
Output: $\boldsymbol{\theta}$

Usually a decay learning rate improves the performance of Adam optimization. Though Adam usually converges faster, the result may lose some generalization capability [148].

With the components of CNN above, we can train a network to achieve inversion of one modality and fusion of multi-modality, which will be described in Chapter 7. In the next section we will introduce edge-preserving regularization which can be used to preserve edges in the inverse scattering problem. Meanwhile, employing its augmented half-quadratic criterion with additional edge variables, we can develop another joint inversion algorithm.

4.2 Inversion with edge-preserving regularization

Consider the inverse problem $\mathbf{y} = \mathbf{A}\mathbf{x}$ where a quadratic regularization can be used to smooth the solution such that the optimization criterion is

$$Q(x) = \|\mathbf{A}\mathbf{x} - \mathbf{y}\|^2 + \lambda \sum_{i,j} |x_{i,j} - x_{i-1,j}|^2 + \lambda \sum_{i,j} |x_{i,j} - x_{i,j-1}|^2 \tag{4.13}$$

Here $x_{i,j}$ is the value of pixel at (i, j) when $\mathbf{x}$ is arranged as an image. Note that for simplicity we impose the regularization on the gradients along two directions while the gradients along diagonal directions can be easily incorporated. Such a regularization will oversmooth the discontinuities thus edge-preserving regularization with non-quadratic potential functions have been widely investigated. In such methods, a potential function φ operates on the gradient of the estimated solution and φ increases more slowly than a parabola, so that large variations are less penalized at some points and the edges can be preserved. The criterion becomes

$$Q(x) = \|\mathbf{A}\mathbf{x} - \mathbf{y}\|^2 + \lambda \sum_{i,j} \varphi\left(x_{i,j} - x_{i-1,j}\right) + \lambda \sum_{i,j} \varphi\left(x_{i,j} - x_{i,j-1}\right) \tag{4.14}$$

The choice of the function φ should affect the result much. Various forms of φ have been proposed and they can be mainly classified into two classes [149].

L_2L_1 functions are even, non-constant, convex and asymptotically linear such as the function [150]

$$\varphi(u) = 2\sqrt{u^2+1} - 2 \tag{4.15}$$

Such functions can keep the convexity of the criterion Q thus there is a unique global minimum and the convergence towards the global minimizer is ensured with standard minimization algorithms.

Another group is L_2L_0 functions which are non-constant, even and asymptotically constant, such as the function [42]

$$\varphi(u) = \frac{u^2}{u^2+1} \tag{4.16}$$

Such functions are not convex thus there might exist local minima and the optimization may become more difficult. However, the boundaries obtained are clearer. With these regularization terms, if the function is differentiable, gradient-based optimization methods can be employed to get the inversion results. Yet, it can be also solved by exploiting the duality between non-quadratic and half-quadratic criteria.

Duality between non-quadratic and half-quadratic criteria

The half-quadratic (HQ) criterion is such a function which depends on two sets of variables $\mathbf{x}$ and $\mathbf{b}$ and is quadratic in $\mathbf{x}$ but not in $(\mathbf{x}, \mathbf{b})$. Blake and Zisserman [44] have observed that a HQ criterion with edge variables $Q^*(\mathbf{x}, \mathbf{b})$ can be considered as an augmented equivalent of a non-quadratic criterion $Q(\mathbf{x})$ with $\varphi(u) = \min(u^2, 1)$ in the sense

$$\min_{\mathbf{b}\in\{0,1\}^M} Q^*(\mathbf{x}, \mathbf{b}) = Q(\mathbf{x}) \tag{4.17}$$

Further researches have shown that many non-quadratic methods have an equivalent augmented HQ criterion in the sense

$$\inf_{b\in\mathcal{B}} Q^*(\mathbf{x}, \mathbf{b}) = Q(\mathbf{x}) \tag{4.18}$$

with a set $\mathcal{B}$ to be defined which can be continuous. If the potential function φ satisfies

- φ is even
- $\varphi(\sqrt{\cdot})$ is concave on R_+
- φ is continuous at zero and the first derivative is continuous on $\mathcal{R}\backslash\{0\}$

the duality relations can be found

$$\varphi(u) = \inf_{b\in R_+} \left(bu^2 + \psi(b)\right) \tag{4.19}$$

$$\psi(b) = \sup_{u\in R} (\varphi(u) - bu^2) \tag{4.20}$$

We can get the augmented HQ criterion for Equation (4.14) as

$$\begin{aligned} Q^*(\mathbf{x}, \mathbf{b}) = \|\mathbf{A}\mathbf{x} - \mathbf{y}\|^2 &+ \lambda \sum_{i,j} b^1_{i,j} \left(x_{i,j} - x_{i-1,j}\right)^2 + \psi(b^1_{i,j}) \\ &+ \lambda \sum_{i,j} b^2_{i,j} \left(x_{i,j} - x_{i,j-1}\right)^2 + \psi(b^2_{i,j}) \end{aligned} \tag{4.21}$$

By finding the augmented HQ criterion for the original non-quadratic criterion, new algorithmic tools can be developed for the optimization. A typical method is to minimize the criterion by considering sub-problems. With initial guess of $(\mathbf{x}, \mathbf{b})$, update $\mathbf{x}$ with fixed $\mathbf{b}$ by minimizing the augmented

criterion $Q^*(\mathbf{x}, \mathbf{b})$ which is quadratic in $\mathbf{x}$ and then update $\mathbf{b}$ with fixed $\mathbf{x}$ which has an explicit form as $b(u) = \varphi'(u)/2u$.

Based on such method, we have proposed a new joint inversion algorithm where the additional variable b is used as the link between two modalities to describe the presence of edges with the potential function $\varphi(u) = u^2/(1+u^2)$ and the corresponding function $\psi(b) = b-2\sqrt{b}+1$, described in Chapter 6. In the next section, we will introduce a widely used joint inversion algorithm.

4.3 Joint inversion with multi-modal data

A joint inversion algorithm based on structural similarity is investigated in this section. Many researchers have proposed various functions or operators to describe the structure of the distribution of parameters to be retrieved. Various forms of regularization based on such structure description are employed to impose similarity between parameters of different modalities. Here we take an example with two linear inverse problems $\mathbf{y}^\alpha = \mathbf{A}^\alpha\mathbf{x}^\alpha$ and $\mathbf{y}^\beta = \mathbf{A}^\beta\mathbf{x}^\beta$ ($\mathbf{y}^\alpha, \mathbf{y}^\beta \in \mathcal{R}^N$, $\mathbf{x}^\alpha, \mathbf{x}^\beta \in \mathcal{R}^M$ and $\mathbf{A}^\alpha, \mathbf{A}^\beta \in \mathcal{R}^{N\times M}$) and introduce a widely used algorithm to show how they can be jointly inverted.

Cross-gradients are proposed in [119], for joint inversion and widely used in geophysics. They are defined as the cross product of the gradients of two parameters x^α and x^β

$$\vec{t}(x^\alpha, x^\beta) = \nabla x^\alpha(\mathbf{r}) \times \nabla x^\beta(\mathbf{r}) \tag{4.22}$$

Consider the cross product $|\vec{c}| = |\vec{a} \times \vec{b}| = |\vec{a}||\vec{b}|\sin\theta_{<\vec{a},\vec{b}>}|$, if $\vec{c} = \vec{0}$, it means either $|\vec{a}| = 0$, $|\vec{b}| = 0$, $\theta_{<\vec{a},\vec{b}>} = 0$ or $\theta_{<\vec{a},\vec{b}>} = \pi$. By imposing the constraint $\vec{t}(x^\alpha, x^\beta) = \vec{0}$ everywhere in the region of interest, it is required that the spatial variations occurring in both parameters be aligned in the same or opposite direction irrespective of the amplitude. The cross-gradients constraint is also satisfied when either gradient vanishes in some part of the model, thus giving the models the possibility of admitting a boundary which has a significant change only in one modality. When we consider the two-dimensional case on $x-y$ plane, the cross-gradient only has a z component and we only focus on the amplitude of this component and denote it as t.

The gradient can be calculated with forward difference [119] as

$$\nabla_i x_{i,j} = x_{i+1,j} - x_{i,j}, \qquad \nabla_j x_{i,j} = x_{i,j+1} - x_{i,j} \tag{4.23}$$

or central difference [125] as

$$\nabla_i x_{i,j} = (x_{i+1,j} - x_{x-1,j})/2, \qquad \nabla_j x_{i,j} = (x_{i,j+1} - x_{x,j-1})/2 \tag{4.24}$$

We take the forward difference as an example, the cross-gradient is

$$t_{i,j} = (x^\alpha_{i+1,j} - x^\alpha_{i,j})(x^\beta_{i,j+1} - x^\beta_{i,j}) - (x^\alpha_{i,j+1} - x^\alpha_{i,j})(x^\beta_{i+1,j} - x^\beta_{i,j}) \tag{4.25}$$

Imposing the cross-gradient constraint, the objective function becomes

$$\begin{aligned} \min\, & Q(\mathbf{x}^\alpha, \mathbf{x}^\beta) = \|\mathbf{y}^\alpha - \mathbf{A}^\alpha\mathbf{x}^\alpha\|^2 + \|\mathbf{y}^\beta - \mathbf{A}^\beta\mathbf{x}^\beta\|^2 \\ & \text{subject to } t(\mathbf{x}^\alpha, \mathbf{x}^\beta) = 0 \end{aligned} \tag{4.26}$$

Note that in [119], other regularization terms to enforce smoothness and incorporate *a priori* model parameters are also applied, here they are not shown for simplicity.

To simplify the calculation, the cross-gradient constraint can be linearized with first-order Taylor expansion, as

$$t(\mathbf{x}^\alpha, \mathbf{x}^\beta) \cong t(\mathbf{x}^\alpha_0, \mathbf{x}^\beta_0) + \mathbf{B}[(\mathbf{x}^\alpha - \mathbf{x}^\alpha_0)^T, (\mathbf{x}^\beta - \mathbf{x}^\beta_0)^T]^T \tag{4.27}$$

where $\mathbf{x}_0^\alpha$ and $\mathbf{x}_0^\beta$ are reference models and change at every iteration as the result of last iteration. $\mathbf{B}$ gives the derivatives of t with respect to the parameters [120] as

$$\begin{aligned}
\frac{\partial t}{\partial x_{i,j}^\alpha} &= x_{i+1,j}^\beta - x_{i,j+1}^\beta, \ \frac{\partial t}{\partial x_{i,j}^\beta} = x_{i,j+1}^\alpha - x_{i+1,j}^\alpha, \\
\frac{\partial t}{\partial x_{i,j+1}^\alpha} &= x_{i,j}^\beta - x_{i+1,j}^\beta, \ \frac{\partial t}{\partial x_{i,j+1}^\beta} = x_{i+1,j}^\alpha - x_{i,j}^\alpha, \\
\frac{\partial t}{\partial x_{i+1,j}^\alpha} &= x_{i,j+1}^\beta - x_{i,j}^\beta, \ \frac{\partial t}{\partial x_{i+1,j}^\beta} = x_{i,j}^\alpha - x_{i,j+1}^\alpha
\end{aligned} \tag{4.28}$$

The solution of this constrained optimization problem can be obtained with Lagrange multipliers by solving a series of equations as below

$$\frac{\partial}{\partial x_m}\left\{Q(\mathbf{x}^\alpha, \mathbf{x}^\beta) + 2\sum_{l=1}^{M}\gamma_l\left[\sum_{k}^{2M} b_{l,k}(x_k - x_{0k}) + t(x_0)_l\right]\right\} = 0, m = 1, \ldots, 2M \tag{4.29}$$

$$\sum_{j=1}^{2M} b_{l,k}(x_k - x_{0k}) + t(x_0)_l = 0, l = 1, \ldots, M \tag{4.30}$$

where x_m, $m = 1, \ldots, M$ is element of $\mathbf{x}^\alpha$ and x_m, $m = M+1, \ldots, 2M$ element of $\mathbf{x}^\beta$. γ_l is the Lagrange multiplier and $b_{l,k}$ the elements in $\mathbf{B}$. These equations have an explicit solution to get the multipliers and the unknowns.

Other methods use cross-gradient as a regularization term incorporated into the objective function. For example, at nth iteration, the cost functions for two parameters are

$$Q^\alpha = \|\mathbf{y}^\alpha - \mathbf{A}^\alpha \mathbf{x}^\alpha\|^2 + \lambda \frac{\|t(\mathbf{x}^\alpha, \mathbf{x}^{\beta(n-1)})\|^2}{\|t(\mathbf{x}^{\alpha(n-1)}, \mathbf{x}^{\beta(n-1)})\|^2} \tag{4.31}$$

$$Q^\beta = \|\mathbf{y}^\beta - \mathbf{A}^\beta \mathbf{x}^\beta\|^2 + \lambda \frac{\|t(\mathbf{x}^{\alpha(n)}, \mathbf{x}^\beta)\|^2}{\|t(\mathbf{x}^{\alpha(n)}, \mathbf{x}^{\beta(n-1)})\|^2} \tag{4.32}$$

Similarly, the cross-gradient is approximated with the result of last iteration as the reference. For example, $t(\mathbf{x}^\alpha, \mathbf{x}^{\beta(n-1)})$ is approximated as

$$t(\mathbf{x}^\alpha, \mathbf{x}^{\beta(n-1)}) \cong t(\mathbf{x}^{\alpha(n-1)}, \mathbf{x}^{\beta(n-1)}) + \mathbf{B}[\mathbf{x}^\alpha - \mathbf{x}^{\alpha(n-1)}] \tag{4.33}$$

Note that here $\mathbf{B}$ is different from the above case with only the gradient with respect to $\mathbf{x}^\alpha$ being needed. With a gradient-based optimization algorithm and alternate minimization, the solution can be obtained easily.

So far we have introduced some techniques which can be used in inverse problem with a simple linear case. Next, we will present some typical inverse scattering algorithms. Here we use the microwave case as an example while these methods can also be applied to the acoustic case.

4.4 Non-iterative methods

The non-iterative methods are presented first. As described before, they cannot be used in complicated cases in practice. However, they can give a solution in a short time, thus they are used to provide us with the initial guess in our methods.

4.4.1 Born Approximation

If we have the prior information that the scatterer is weak, i.e., the contrast is low and the size is small, the Born Approximation (BA) can be applied to give the solution. Since the scattered field produced by the scatterer is weak compared with the incident field, it is possible to make the approximation that the total field E^t can be replaced by the incident field E^i and then we have

$$\mathbf{E^s} \approx \mathbf{G_s}(\mathbf{X}\mathbf{E^i}) \tag{4.34}$$

With 0th-order Tikhonov regularization, the original problem can then be cast into an optimization problem as

$$Q(\boldsymbol{\chi}) = \sum_{p=1}^{N_i} \|\mathbf{G_s}\mathbf{X}\mathbf{E}_p^{\mathbf{i}} - \mathbf{E}_p^{\mathbf{s}}\|^2 + \lambda\|\boldsymbol{\chi}\|^2 \tag{4.35}$$

The problem has an anlytical solution as

$$\boldsymbol{\chi} = (\mathbf{K}^\dagger\mathbf{K} + \lambda\mathbf{I})^{-1}\mathbf{K}^\dagger\mathbf{y} \tag{4.36}$$

where $\mathbf{K}$ is a $(N_iN_r) \times M$ matrix with the entry $\mathbf{K}(i + N_r(p-1), j) = \mathbf{G_s}(i,j)\mathbf{E}_p^{\mathbf{i}}(j)$ and $\mathbf{y}$ is a $(N_iN_r \times 1)$ vector with $\mathbf{y}(i + N_r(p-1)) = \mathbf{E}_p^{\mathbf{s}}(i)$

4.4.2 Backpropagation

In the back-propagation method, the inverse problem is decomposed into problems and each one is linear [151].

To evaluate the contrast, the contrast current is determined first, it is assumed to be proportional to the back-propagated field as

$$\mathbf{J}_p = \gamma\mathbf{G}_\mathbf{s}^\dagger\mathbf{E}_p^\mathbf{s} \tag{4.37}$$

γ is chosen to minimize the misfit between measured scattered field and the one produced by such a contrast current as

$$Q(\gamma) = \sum_p \|\mathbf{E}_p^\mathbf{s} - \mathbf{G_s}(\gamma\mathbf{G}_\mathbf{s}^\dagger\mathbf{E}_p^\mathbf{s})\|^2 \tag{4.38}$$

It has the analytical solution as

$$\gamma = \frac{\sum_p < \mathbf{E}_p^\mathbf{s}, \mathbf{G_s}(\mathbf{G}_\mathbf{s}^\dagger\mathbf{E}_p^\mathbf{s}) >}{\sum_p \|\mathbf{G_s}(\mathbf{G}_\mathbf{s}^\dagger\mathbf{E}_p^\mathbf{s})\|^2} \tag{4.39}$$

When γ is obtained, the contrast current can be calculated by Equation (4.37) and the total field can be obtained further by

$$\mathbf{E}_p^\mathbf{t} = \mathbf{E}_p^\mathbf{i} + \mathbf{G_d}\mathbf{J}_p \tag{4.40}$$

With $J_p(\mathbf{r}) = \chi(\mathbf{r})E_p^t(\mathbf{r})$, the contrast can be easily obtained with is mth entry as

$$\chi_m = \frac{\sum_p \mathbf{J}_p(m)\overline{\mathbf{E}_p^\mathbf{t}(m)}}{\sum_p |\mathbf{E}_p^\mathbf{t}(m)|^2} \tag{4.41}$$

4.5 Iterative methods

In this section we introduce some iterative methods which are valid for scatterers with high contrast and large dimension compared with the wavelength. Our fusion methods will be developed based on such algorithms.

4.5.1 Distorted Born Iterative Method

Consider the contrast $\boldsymbol{\chi}$ as a small perturbation $\delta\boldsymbol{\chi}$ w.r.t. an inhomogeneous background $\boldsymbol{\chi}_n$; one has $\boldsymbol{\chi} = \boldsymbol{\chi}_n + \delta\boldsymbol{\chi}$ [55]. The secondary incident field by this inhomogeneous background is

$$\mathbf{E}^{\text{bac}} = (\mathbf{I_M} - \mathbf{G_d}\mathbf{X}^{(n)})^{-1}\mathbf{E^i} \tag{4.42}$$

where $\mathbf{I_M}$ is the M-dimensional identity matrix, with this background, the scattered field is

$$\mathbf{E^s} = \mathbf{G_s}\mathbf{X^{(n)}}\mathbf{E}^{\text{bac}} + \mathbf{G_s^{\chi_n}}\delta\mathbf{X}\mathbf{E^t} \tag{4.43}$$

Here, $\mathbf{G_s^{\chi_n}}$ is the inhomogeneous background Green's function. The cost functional is the sum of the difference between measured and calculated data and a regularization term

$$Q(\delta\boldsymbol{\chi}) = \sum_{p=1}^{N_i} \left\| \mathbf{E}_p^{\mathbf{s}} - \mathbf{G_s}\mathbf{X}^{(n)}\mathbf{E}_p^{\mathbf{bac}} - \mathbf{G_s^{\chi_n}}\delta\mathbf{X}\mathbf{E}_p^{\mathbf{bac}} \right\|^2 + \lambda Q_r(\delta\boldsymbol{\chi}) \tag{4.44}$$

within which $\mathbf{E^t}$ is replaced by $\mathbf{E}^{\text{bac}}$ with the Born approximation. The optimization procedure is summarized below.

At each iteration, update $\mathbf{G_s^{\chi_n}}$ by

$$\mathbf{G_s^{\chi_n}} = \mathbf{G_s}(\mathbf{I_M} - \mathbf{X}^{(n)}\mathbf{G_d})^{-1} \tag{4.45}$$

Note that the inverse calculation is quite time consuming, so in practice, the reciprocity theorem is used where the source and receiver are exchanged and the solution is obtained by solving a forward problem. If the incident field produced by the sources located at the position of receivers is denoted as $[\mathbf{E^i}]'$, then we need to solve the forward problem to get $\mathbf{G_s^{\chi_n}}$ as

$$[\mathbf{G_s^{\chi_n}}]^T = [\mathbf{E^i}]' + \mathbf{G_d}\mathbf{X}^{(n)}[\mathbf{G_s^{\chi_n}}]^T \tag{4.46}$$

With the current contrast $\boldsymbol{\chi}_n$, we need to solve the forward problem

$$[\mathbf{E}_p^{\mathbf{bac}}]^{(n)} = \mathbf{E}_p^{\mathbf{i}} + \mathbf{G_d}\mathbf{X}^{(n)}[\mathbf{E}_p^{\mathbf{bac}}]^{(n)} \tag{4.47}$$

and get the scattered field

$$[\mathbf{E}_p^{\mathbf{s}}]^{(n)} = \mathbf{G_s}\mathbf{X}^{(n)}[\mathbf{E}_p^{\mathbf{bac}}]^{(n)} \tag{4.48}$$

Then the difference $\delta\chi$ is obtained by solving the optimization problem (0th-order Tikhonov regularization is chosen here)

$$\min : Q(\delta\boldsymbol{\chi}) = \sum_{p=1}^{N_i} \left\| \mathbf{E}_p^{\mathbf{s}} - [\mathbf{E}_p^{\mathbf{s}}]^{(n)} - \mathbf{G_s^{\chi_n}}\delta\mathbf{X}[\mathbf{E}_p^{\mathbf{bac}}]^{(n)} \right\|^2 + \lambda \left\|\delta\boldsymbol{\chi}\right\|^2 \tag{4.49}$$

It can be dealt directly as

$$\delta\boldsymbol{\chi} = [\mathbf{K}^\dagger\mathbf{K} + \lambda\mathbf{I}]^{-1}\mathbf{K}^\dagger\mathbf{y}, \tag{4.50}$$

$\mathbf{K}$ is a $(N_iN_r)\times M$ matrix and element $\mathbf{K}(i+N_r(p-1), j) = \mathbf{G_s^{\chi_n}}(i,j)[\mathbf{E}_p^{\mathbf{bac}}]^{(n)}(j)$ and $\mathbf{y}$ is a $(N_iN_r)\times 1$ vector with $\mathbf{y}(i+N_r(p-1)) = \mathbf{E}_p^{\mathbf{s}}(i) - [\mathbf{E}_p^{\mathbf{s}}]^{(n)}(i)$. Last the contrast is updated as

$$\boldsymbol{\chi}_{n+1} = \boldsymbol{\chi}_n + \delta\boldsymbol{\chi} \tag{4.51}$$

Algorithm 3 Distorted Born Iterative Method

Input: $\mathbf{E}_p^{\mathbf{s}}$, $\mathbf{E}_p^{\mathbf{i}}$, $p = 1, \ldots, N_i$
Initialization: $\boldsymbol{\chi}^{(0)}$, $n = 0$
repeat
$n = n + 1$
Update total field $\mathbf{E}^{\mathbf{bac}}$ and scattered field $[\mathbf{E}^{\mathbf{s}}]^{(n)}$ with $\boldsymbol{\chi}^{(n)}$ by solving forward problem Equation (4.47) and (4.48)
Update inhomogeneous Green's function $\mathbf{G}_{\mathbf{s}}^{\boldsymbol{\chi}_{\mathbf{n}}}$ with background $\boldsymbol{\chi}^{(n)}$ by solving forward problem Equation (4.46)
Calculate $\delta\boldsymbol{\chi}$ with Equation (4.50)
Update $\boldsymbol{\chi}$ with Equation (4.51)
until a stopping criterion is satisfied
Output: $\boldsymbol{\chi}$

4.5.2 Contrast Source Inversion Method

The contrast source inversion (CSI) method is based on source-type equations where the contrast source is regarded as an independent parameter. The objective function here is a linear combination of normalized mismatches in the data equation Q_d and the state equation Q_s.

$$Q(\mathbf{J}, \boldsymbol{\chi}) = Q_d + Q_s = \frac{\sum_{p=1}^{N_i} \|\mathbf{E}_p^{\mathbf{s}} - \mathbf{G}_{\mathbf{s}}\mathbf{J}_p\|^2}{\sum_{p=1}^{N_i} \|\mathbf{E}_p^{\mathbf{s}}\|^2} + \frac{\sum_{p=1}^{N_i} \|\mathbf{X}\mathbf{E}_p^{\mathbf{i}} + \mathbf{X}\mathbf{G}_{\mathbf{d}}\mathbf{J}_p - \mathbf{J}_p\|^2}{\sum_{p=1}^{N_i} \|\mathbf{X}\mathbf{E}_p^{\mathbf{i}}\|^2} \tag{4.52}$$

The CSI method proposes an iterative minimization scheme using an alternating method that first updates $\mathbf{J}_p$ and then updates $\boldsymbol{\chi}$. At the nth iteration, the contrast source $\mathbf{J}_p$ is updated by CG method as

$$\mathbf{J}_p^{(n)} = \mathbf{J}_p^{(n-1)} + \beta_J^{(n)} \mathbf{v}_{J_p}^{(n)} \tag{4.53}$$

with search direction

$$\mathbf{v}_{J_p}^{(n)} = \mathbf{g}_{J_p}^{(n)} + \frac{\Re < \mathbf{g}_{J_p}^{(n)}, \mathbf{g}_{J_p}^{(n-1)} >}{< \mathbf{g}_{J_p}^{(n-1)}, \mathbf{g}_{J_p}^{(n-1)} >} \mathbf{v}_{J_p}^{(n-1)} \tag{4.54}$$

and the gradient $\mathbf{g}_{J_p}^{(n)}$ evaluated at $\mathbf{J}_p^{(n-1)}$ and $\boldsymbol{\chi}^{(n-1)}$:

$$\mathbf{g}_{J_p}^{(n)} = -\frac{\mathbf{G}_{\mathbf{s}}^{\dagger}\boldsymbol{\rho}_p^{(n-1)}}{\sum_{p=1}^{N_i} \|\mathbf{E}_p^{\mathbf{s}}\|^2} - \frac{\mathbf{o}_p^{(n-1)} - \mathbf{G}_{\mathbf{d}}^{\dagger}[\mathbf{X}^{(n-1)}]^{\dagger}\mathbf{o}_p^{(n-1)}}{\sum_{p=1}^{N_i} \|\mathbf{X}^{(n-1)}\mathbf{E}_p^{\mathbf{i}}\|^2} \tag{4.55}$$

where the data equation error $\boldsymbol{\rho}_p^{(n)}$ and the state equation error $\mathbf{o}_p^{(n)}$ are defined as

$$\boldsymbol{\rho}_p^{(n)} = \mathbf{E}_p^{\mathbf{s}} - \mathbf{G}_{\mathbf{s}}\mathbf{J}_p^{(n)} \tag{4.56}$$

$$\mathbf{o}_p^{(n)} = \mathbf{X}^{(n)}\mathbf{E}_p^{\mathbf{i}} + \mathbf{X}^{(n)}\mathbf{G}_{\mathbf{d}}\mathbf{J}_p^{(n)} - \mathbf{J}_p^{(n)} \tag{4.57}$$

The stepsize $\beta_J^{(n)}$ is

$$\beta_J^{(n)} = \frac{-\sum_p < \mathbf{g}_{J_p}^{(n)}, \mathbf{v}_{\mathbf{J}_p}^{(n)} >}{\frac{\sum_p \|\mathbf{G}_{\mathbf{s}}\mathbf{v}_{J_p}^{(n)}\|^2}{\sum_p \|\mathbf{E}_p^{\mathbf{s}}\|^2} + \frac{\sum_p \|\mathbf{v}_{J_p}^{(n)} - \mathbf{X}^{(n-1)}\mathbf{G}_{\mathbf{d}}\mathbf{v}_{J_p}^{(n)}\|^2}{\sum_p \|\mathbf{X}^{(n-1)}\mathbf{E}_p^{\mathbf{i}}\|^2}} \tag{4.58}$$

When $\mathbf{J}_p$ is updated, the total field $\mathbf{E}_p^{\mathbf{t}}$ can be updated by

$$[\mathbf{E}_p^{\mathbf{t}}]^{(n)} = \mathbf{E}_p^{\mathbf{i}} + \mathbf{G_d}\mathbf{J}_p^{(n)} \tag{4.59}$$

The contrast $\boldsymbol{\chi}$ has an analytical solution as

$$\boldsymbol{\chi}^{(n)}(m) = \frac{\sum_{p=1}^{N_i} \mathbf{J}_p^{(n)}(m)[\overline{\mathbf{E}_p^{\mathbf{t}}}]^{(n)}(m)}{\sum_{p=1}^{N_i} \|[\mathbf{E}_p^{\mathbf{t}}]^{(n)}(m)\|^2} \tag{4.60}$$

Algorithm 4 Contrast Source Inversion Method

Input: $\mathbf{E}_p^{\mathbf{s}}$, $\mathbf{E}_p^{\mathbf{i}}$, $p = 1, \ldots, N_i$, $\mathbf{G_s}$, $\mathbf{G_d}$
Initialization: $\mathbf{J}^{(0)}$, $\boldsymbol{\chi}^{(0)}$, $n = 0$
repeat
  $n = n + 1$
  Calculate equation errors $\boldsymbol{\rho}_p^{(n-1)}$ and $\mathbf{o}_p^{(n-1)}$ with Equation (4.56) and (4.57)
  Update $\mathbf{J}$ with Equation (4.53), (4.54), (4.55) and (4.58)
  Update total field $\mathbf{E}^{\mathbf{t}}$ with Equation (4.59)
  Update $\boldsymbol{\chi}$ by Equation (4.60)
until a stopping criterion is satisfied
Output: $\boldsymbol{\chi}$

MR-CSI

In the CSI method, the state equation can be recognized as a regularization. Yet we can incorporate some *a priori* information on the contrast to improve the result. Here we introduce a widely-used regularization, based on the so-called weighted L2 total variation norm [50] and the developed method is named MR-CSI since this regularization is incorporated in a multiplicative way. The regularization term has been introduced in the previous section. To remind, at nth iteration, the TV-factor reads as

$$Q_{TV}^{(n)}(\boldsymbol{\chi}) = \sum_{i,j} \frac{|\chi_{i,j+1} - \chi_{i,j}|^2 + |\chi_{i+1,j} - \chi_{i,j}|^2 + \delta^{(n)}}{|\chi_{i,j+1}^{(n-1)} - \chi_{i,j}^{(n-1)}|^2 + |\chi_{i+1,j}^{(n-1)} - \chi_{i,j}^{(n-1)}|^2 + \delta^{(n)}} \tag{4.61}$$

$\delta^{(n)}$ is chosen as proportional to the normalized state equation cost or the total cost which is decreasing during the optimization process to enhance the effect of regularization. The cost function becomes

$$Q(\mathbf{J}, \boldsymbol{\chi}) = [Q_s(\mathbf{J}) + Q_d(\mathbf{J}, \boldsymbol{\chi})]Q_{TV}(\boldsymbol{\chi}) \tag{4.62}$$

The introduction of the TV term has no influence on the update of the contrast current $\mathbf{J}$ while the update of contrast $\boldsymbol{\chi}$ needs to be changed with a conjugate gradient method used. Here we follow the update procedure proposed in [152]. In this optimization strategy, the contrast is first updated by Equation (4.60). Denote the result as $\boldsymbol{\chi}_{pre}^{(n)}$, The contrast is updated by

$$\boldsymbol{\chi}^{(n)} = \boldsymbol{\chi}_{pre}^{(n)} + \beta_\chi^{(n)} \mathbf{v}_\chi^{(n)} \tag{4.63}$$

with the search direction

$$\mathbf{v}_\chi^{(n)} = \mathbf{g}_\chi^{(n)} + \frac{\Re < \mathbf{g}_\chi^{(n)}, \mathbf{g}_\chi^{(n-1)} >}{< \mathbf{g}_\chi^{(n-1)}, \mathbf{g}_\chi^{(n-1)} >} \mathbf{v}_\chi^{(n-1)} \tag{4.64}$$

where $\mathbf{g}_\chi$ is a preconditioned gradient estimated at $\boldsymbol{\chi}_{pre}$ where the gradient of the state equation with respect to changes around this point vanishes and it reads as

$$\mathbf{g}_\chi^{(n)} = \left(Q_d(\mathbf{J}^{(n)}) + Q_s(\mathbf{J}^{(n)}, \boldsymbol{\chi}_{pre}^{(n)})\right) \left(\mathbf{D_v}\mathbf{B}^{(n)}\mathbf{D_v} + \mathbf{D_h}\mathbf{B}^{(n)}\mathbf{D_h}\right) \boldsymbol{\chi}_{pre}^{(n)} \tag{4.65}$$

where $\mathbf{D_v}$ and $\mathbf{D_h}$ are matrices calculating the gradient of the contrast along vertical and horizontal directions. $\mathbf{B}$ is a diagonal matrix with its mth entry as

$$\mathbf{B}^{(n)}(m,m) = \frac{1}{|[\mathbf{D_v}\boldsymbol{\chi}^{(n-1)}]_m|^2 + |[\mathbf{D_h}\boldsymbol{\chi}^{(n-1)}]_m|^2 + \delta^{(n)}} \tag{4.66}$$

Algorithm 5 Contrast Source Inversion Method with weighted L2 TV (MR-CSI)

Input: $\mathbf{E}^{\mathbf{s}}_p$, $\mathbf{E}^{\mathbf{i}}_p$, $p = 1, \ldots, N_i$, $\mathbf{G_s}$, $\mathbf{G_d}$
Initialization: $\mathbf{J}^{(0)}$, $\boldsymbol{\chi}^{(0)}$, $n = 0$
repeat
  $n = n + 1$
  Calculate equation errors $\boldsymbol{\rho}_p^{(n-1)}$ and $\mathbf{o}_p^{(n-1)}$ with Equation (4.56) and (4.57)
  Update $\mathbf{J}$ with Equation (4.53), (4.54), (4.55) and (4.58)
  Update total field $\mathbf{E^t}$ with Equation (4.59)
  Estimate $\boldsymbol{\chi}$ with no regularization by Equation (4.60)
  Update $\boldsymbol{\chi}$ with Equation 4.63, (4.64) and (4.65)
until a stopping criterion is satisfied
Output: $\boldsymbol{\chi}$

Given the search direction, we can get the cost functional as a fourth-degree polynomial in β_χ. By letting the gradient with respect to β_χ equal to zero, one can get the solution of β_χ, i.e., by solving

$$2ZB\beta^3 + 3YB\beta^2 + (BX + AZ)\beta + AY = 0 \tag{4.67}$$

where

$$A = Q_d(\mathbf{J}^{(n)}) + Q_s(\mathbf{J}^{(n)}, \boldsymbol{\chi}^{(n)}_{pre}) \tag{4.68}$$

$$B = \frac{\sum_p \|\mathbf{v}_\chi^{(n)} . \times \mathbf{E}^{\mathbf{t}}_p\|^2}{\sum_p \|\mathbf{X}^{(n-1)}\mathbf{E}^{\mathbf{i}}_p\|^2} \tag{4.69}$$

$$X = \|\mathbf{R}^{(n)}[\mathbf{D_v}\boldsymbol{\chi}^{(n)}_{pre}]\|^2 + \|\mathbf{R}^{(n)}[\mathbf{D_h}\boldsymbol{\chi}^{(n)}_{pre}]\|^2 + \delta^{(n)}\|\mathbf{R}^{(n)}\|^2 \tag{4.70}$$

$$Y = \Re\left(< \mathbf{B}^{(n)}[\mathbf{D_v}\boldsymbol{\chi}^{(n)}_{pre}], \mathbf{D_v}\mathbf{v}^{(n)}_\chi > + < \mathbf{B}^{(n)}[\mathbf{D_h}\boldsymbol{\chi}^{(n)}_{pre}], \mathbf{D_h}\mathbf{v}^{(n)}_\chi >\right) \tag{4.71}$$

$$Z = \|\mathbf{R}^{(n)}[\mathbf{D}_v\mathbf{v}^{(n)}_\chi]\|^2 + \|\mathbf{R}^{(n)}[\mathbf{D}_h\mathbf{v}^{(n)}_\chi]\|^2 \tag{4.72}$$

Here $\mathbf{R}^{(n)}$ is also a diagonal matrix with the element being the square root of the corresponding entry in matrix $\mathbf{B}^{(n)}$. The above cubic equation has one real root and two complex conjugate roots. The real one is the choice for $\beta^{(n)}_\chi$. The above algorithm is summarized in Algorithm 5.

Chapter 5

Microwave imaging with prior information from ultrasound

This chapter is based on the journal paper *Microwave breast imaging with prior ultrasound information*, Y. Qin, T. Rodet, M. Lambert, and D. Lesselier, published in the *IEEE Open Journal of Antennas and Propagation, Special Section Direct and Inverse Electromagnetic Scattering Methods*, vol. 1, pp. 472-482, 2020, doi: 10.1109/OJAP.2020. 3019953. Some parts of the introduction, forward problem and description of inversion algorithm are found in previous chapters. Some notations have been changed. The Born Approximation and Backpropagation methods used for obtaining the initial guess are described in Chapter 4.

5.1 Introduction

Breast tumors are some of the most common tumors among women. Early detection is critical at an early stage of cancer progression [153]. Therefore, to develop technologies to image a small tumor at low cost and with low risk is an important issue. Currently, X-ray mammography is still the gold standard for this detection. Despite of the high-resolution of imaging result, X-ray mammography has a number of limitations including low sensitivity, ionizing radiation, discomfort from breast compression, and detection quite affected by breast density.

Microwave imaging has been investigated as an alternative or at least a complementary imaging modality. Several investigations on the electromagnetic (EM) properties in different types of tissue have been led, e.g., [131, 132]. Based on the difference in dielectric properties between tumorous and normal tissues, the contrast appears relatively higher than the one associated to X-ray. Also, microwave imaging is non-ionizing, low-cost, and enables easy examination. The techniques proposed for microwave imaging can be roughly divided into two groups: radar and tomography. Radar techniques [154–156] rely on ultrawide-band pulse illuminations to identify regions with high contrast from backscattered signals. This is efficient and indeed indicates the location of strongly scattering parts. However, less detailed information about the breast is made available [23]. To achieve a possibly better retrieval of the distribution of EM parameters within the breast, tomographic microwave imaging is widely used, refer to [52, 133, 157] among many others. In this approach, several transmitting and receiving antennas are set around the breast. The transmitting ones illuminate it sequentially and scattered fields[1] are acquired by the receiving ones. Simulation is usually needed to get the scattered field when breast geometry and EM parameters are known, which is a forward problem linear w.r.t. the incident field. To reconstruct the contrast given the scattered field is an inverse problem and it is as well-known nonlinear due to multiple scattering.

[1] In practice, one should extract them from total fields as collected, and also field values are not observed but antenna-related S-parameters.

This inverse problem can be cast into an optimization problem where the misfit between measurements and simulation results from a numerical model is minimized. Under some conditions, it can be solved without iteration, e.g., a weak scatterer the size of which is no much larger than the wavelength, within the framework of the Born approximation (the total field being replaced by the incident one). In practice, these assumptions are usually not valid and imaging results remain unsatisfactory. This can be overcome by correcting the misfit iteratively. The Born Iterative Method [54], Distorted Iterative Method (DBIM) [55], Contrast Source Inversion (CSI) method [58], and Subspace-based Optimization Method (SOM) and its several variants [59–61, 158], work this way. Recently, convolutional neural netwoks (CNN) has been investigated as a tool to solve the inverse scattering problem [83, 85, 159]. A well-trained network can provide the complex permittivity of the object given the scattered fields or the preliminary results of some traditional inversion algorithms.

It is also well-known that the inverse problem is ill-posed. To alleviate ill-posedness and stabilize the inversion, regularization is usually applied in additive or multiplicative fashion. In DBIM, Tikhonov regularization is standardly enforced to reach a robust estimation. Further, *a priori* information can be incorporated into the regularization term. Two-fold SOM (TSOM) confines the reconstruction within a low-dimension subspace. Huber regularization [51, 52] and weighted L2 total variation (TV) [160] smoothen small-scale noise while trying to preserve discontinuities. For piecewise constant profiles, value picking (VP) [53] regularization can be applied. Level set is also a regularization technique suitable for binary cases [161] though it now adresses a broad range of cases [162].

The main drawback of microwave imaging is the relative low resolution due to the long wavelength. To achieve higher spatial resolution, a higher frequency is needed [163]. However, the dimension of the scatterer gets correspondingly larger compared to this wavelength and the inverse problem more difficult to solve while the penetration depth may be affected also. Besides, tissue heterogeneity and the fact that geometries and EM parameters vary from person to person may render the challenge quite complicated. Then, additional model-specific information from other imaging modalities can be very useful.

The structural region information can be extracted from images provided by the high-resolution modality as prior information. As an example, in [102], MRI-derived horizontal and vertical boundaries are incorporated into a Bayesian framework for functional image reconstruction. In [113], different tissue clusters are extracted from ultrasound (US) images by K-means to get a better distribution of dielectric properties which results into more accurate tissue-specific time-delays in Delay and Sum algorithm in EM reconstruction. In [106], the structural information is extracted from MRI and Diffuse Optical Tomography (DOT) involving a finite element method (FEM) is considered. In [105], a smaller regularization parameter is distributed in a Tikhonov regularization scheme to pixels identified as part of tumor from X-ray images in DOT breast imaging. In [164], MRI images are segmented into different regions to provide a FEM mesh and a Laplacian-type regularization follows to minimize variation in each region in near infrared (NIR) tomography. In [114], the structural information is extracted from US reconstruction with K-means clustering algorithm. Tissue permittivity values are assigned to these regions to form an inhomogeneous background and assist the EM reconstruction by the FEM-CSI algorithm. In [112], high-resolution images are segmented into different regions and pixels in the same region are constrained to have similar dielectric parameters in EM reconstruction.

Considering US imaging can offer high-resolution images with interior tissue boundaries from reflection algorithms when the travel time of the acoustic signal is recorded and an average sound speed is assumed, being emphasized that US data can be acquired simultaneously with EM ones so that no registration is needed (the hypothesis is the one of a pending breast). US imaging is chosen to offer the additional information in the present work. The tissue boundary information is incorporated into a traditional method for microwave breast imaging with a regularization term, which imposes on two adjacent pixels that the EM properties are the same when not on the boundaries and only undergo changes at interfaces of tissues. Then, one incorporates the US-information-guided regularization term into DBIM and CSI. Besides, CSI with separate constraints on real and imaginary parts is developed.

For comparison, results of DBIM with Tikhonov regularization and CSI with Huber regularization are also shown. A synthetic breast model is used to validate the algorithm, then two anatomically-realistic MRI-derived numerical breast phantoms are considered.

The contribution is organized as follows. The forward problem is described in Section 5.2. Regularization as well as inversion algorithms are considered in Section 5.3. Experiments on breast phantoms are discussed in Section 5.4. One concludes about present results and outlines ways ahead involving fusion procedures in Section 5.5.

5.2 Forward problem

One henceforth considers a two-dimensional non-magnetic case with transverse magnetic (TM) polarization. Time-harmonic waves are assumed with dependence $\exp(-i\omega t)$. The breast is located inside a domain of interest (DoI) $\mathcal{D}$. The known background medium is characterized by a complex relative permittivity ϵ_b, permeability μ_b and wavenumber $k_b = \omega\sqrt{\epsilon_0\epsilon_b\mu_b}$. The unknown scatterers (of same permeability μ_b) have complex relative permittivity $\epsilon_r(\mathbf{r})$ and wavenumber $k(\mathbf{r})$ functions of position. N_i transmitters illuminate the DoI successively and the scattered fields are collected by N_r receivers evenly located on an exterior circle $\mathcal{S}$.

The problem can be associated to two integral equations

$$E^t(\mathbf{r}) = E^i(\vec{r}) + \int_{\mathcal{D}} (k^2(\mathbf{r}') - k_b^2) g(\mathbf{r}, \mathbf{r}') E^t(\mathbf{r}') \, \mathrm{d}\mathbf{r}', r \in \mathcal{D} \tag{5.1}$$

$$E^s(\mathbf{r}) = \int_{\mathcal{D}} (k^2(\mathbf{r}') - k_b^2) g(\mathbf{r}, \mathbf{r}') E^t(\mathbf{r}') \, \mathrm{d}\mathbf{r}', r \in \mathcal{S} \tag{5.2}$$

where incident field $E^i(\mathbf{r})$ and total field $E^t(\mathbf{r})$ represent the electric field inside $\mathcal{D}$, object absent or present, respectively. E^s is the scattered field collected by the receivers. The scalar Green's function is $g(\mathbf{r}, \mathbf{r}') = \frac{i}{4} \mathrm{H}_0^{(1)}(k_b|r - r'|)$, $\mathrm{H}_0^{(1)}$ 1st-kind 0th-order Hankel function. Denote the contrast as

$$\chi(\mathbf{r}) = \frac{k^2(\mathbf{r}) - k_b^2}{k_b^2} \tag{5.3}$$

and integral operators

$$G_d[x](\mathbf{r}) = k_b^2 \int_{\mathcal{D}} g(\mathbf{r}, \mathbf{r}') x(\mathbf{r}') \, \mathrm{d}\mathbf{r}', r \in \mathcal{D} \tag{5.4}$$

$$G_s[x](\mathbf{r}) = k_b^2 \int_{\mathcal{D}} g(\mathbf{r}, \mathbf{r}') x(\mathbf{r}') \, \mathrm{d}\mathbf{r}', r \in \mathcal{S} \tag{5.5}$$

The equations above simplify into

$$E^t(\mathbf{r}) = E^i(\mathbf{r}) + G_d[\chi E^t](\mathbf{r}), r \in \mathcal{D} \tag{5.6}$$

$$E^s(\mathbf{r}) = G_s[\chi E^t](\mathbf{r}), r \in \mathcal{S} \tag{5.7}$$

To handle the problem numerically, discrete forms of the equations have to be derived, here via a pulse-basis point-matching Method of Moments (MoM). The DoI is discretized into $M = N_x \times N_y$ subwavelength cells with centers at $\mathbf{r}_m$, $m = 1, 2, \ldots, M$. The dielectric properties are considered homogeneous in each cell. Every square cell is approximated by a small disk with same area and with equivalent radius R whether needed. The equations above become

$$\mathbf{E^t} = \mathbf{E^i} + \mathbf{G_d X E^t} \tag{5.8}$$

$$\mathbf{E^s} = \mathbf{G_s X E^t} \tag{5.9}$$

where $\mathbf{X} = \text{diag}\{\boldsymbol{\chi}\} = \text{diag}\{\chi(\mathbf{r}_1), \ldots, \chi(\mathbf{r}_M)\}$. The $M \times M$ matrix $\mathbf{G_d}$ is

$$\mathbf{G_d}(m, m') = \begin{cases} \dfrac{ik_b\pi R}{2} \mathrm{J}_1(k_b R)\, \mathrm{H}_0^{(1)}(k_b|\mathbf{r}_m - \mathbf{r}_{m'}|), m \neq m' \\ \dfrac{ik_b\pi R}{2} \mathrm{H}_1^{\{1\}}(k_b R) - 1, \text{otherwise} \end{cases} \tag{5.10}$$

where J_1 is the 1st-kind Bessel function and $\mathrm{H}_1^{(1)}$ the 1st-kind 1st-order Hankel function. The $N_r \times M$ matrix $\mathbf{G_s}$ is

$$\mathbf{G_s}(s, m) = \frac{ik_b\pi R}{2} \mathrm{J}_1(k_b R)\, \mathrm{H}_0^{(1)}(k_b|\mathbf{r}_s - \mathbf{r}_m|) \tag{5.11}$$

where $\mathbf{r}_s$ is the position of receiver s.

A source-type framework is widely used. Consider the contrast current $J(\mathbf{r}) = \chi(\mathbf{r}) E^t(\mathbf{r})$, the formulation becomes

$$J(\mathbf{r}) = \chi\left(E^i(\mathbf{r}) + G_d[J](\mathbf{r})\right), r \in \mathcal{D} \tag{5.12}$$

$$E^s(\mathbf{r}) = G_s[J](\mathbf{r}), r \in \mathcal{S} \tag{5.13}$$

The discrete form reads as

$$\mathbf{J} = \mathbf{X}\mathbf{E^i} + \mathbf{X}\mathbf{G_d}\mathbf{J} \tag{5.14}$$

$$\mathbf{E^s} = \mathbf{G_s}\mathbf{J} \tag{5.15}$$

5.3 Inversion algorithms

Due to the large wavelength, resolution in microwave imaging is expected to be poor. Ultrasound imaging with its high resolution is employed to assist it. An ultrasound-guided smoothness (UGS) regularization term is proposed to incorporate a priori information. This regularization is introduced first and then its implementation into DBIM and CSI is shown. DBIM with Tikhonov regularization and CSI with Huber regularization are presented in parallel.

5.3.1 Smoothness constraint

Assume that interior boundaries of the breast model follow from US imaging. For easier incorporation, the tissue boundaries are depicted via two images to show discontinuities in vertical and horizontal directions, respectively, where dielectric properties also change. The principle is quite intuitive, two vertically or horizontally adjacent pixels should exhibit similar parameters when none lies at the boundaries. Otherwise, regularization is imposed. This constraint is expressed as

$$Q_{\text{UGS}} = \sum_i \sum_j [b_h]_{i,j} |\chi_{i,j} - \chi_{i,j+1}|^2 + \sum_i \sum_j [b_v]_{i,j} |\chi_{i,j} - \chi_{i+1,j}|^2 \tag{5.16}$$

Notice that $\chi_{i,j}$ is the pixel located at (i, j) when $\boldsymbol{\chi}$ is rearranged as an $Nx \times Ny$ image. Same relation can be found in $[b_v]_{i,j}$ and $\mathbf{b}_v$, $[b_h]_{i,j}$ and $\mathbf{b}_h$. $\mathbf{b}_v$ and $\mathbf{b}_h$ are included in the prior information and indicate if the pixel is at a boundary as

$$[b_h]_{i,j} = \begin{cases} 0, & (i, j) \text{ on horizontal boundaries} \\ 1, & \text{else} \end{cases} \tag{5.17}$$

$$[b_v]_{i,j} = \begin{cases} 0, & (i, j) \text{ on vertical boundaries} \\ 1, & \text{else} \end{cases} \tag{5.18}$$

Similarly with other smoothness constraints, the regularization term is based on the module of the gradient of the contrast, coefficients $\mathbf{b}_v$ and $\mathbf{b}_h$ guiding the smoothness while preserving edges with US information. Compared with other methods of incorporating US prior into EM inversion, the boundary is directly used but not the tissue region from segmentation.

This regularization term can be written in matrix form as

$$Q_{\mathrm{UGS}}(\boldsymbol{\chi}) = \|\mathbf{D_v}\boldsymbol{\chi}\|^{\mathbf{2}} + \|\mathbf{D_h}\boldsymbol{\chi}\|^{\mathbf{2}} \tag{5.19}$$

with matrices $\mathbf{D_v}$ and $\mathbf{D_h}$ providing the difference of two adjacent pixels in vertical and horizontal directions. Take $\mathbf{D_v}$ as an example, it can be written as

$$\mathbf{D_v} = \begin{bmatrix} 1 & -1 & & & & & & \\ & 1 & -1 & & & & & \\ & & \ddots & \ddots & & & & \\ & & & 0 & 0 & & & \\ & & & & \ddots & \ddots & & \\ & & & & & 1 & -1 & \\ & & & & & & 1 & \end{bmatrix} \tag{5.20}$$

Notice that the diagonal elements are 1 only when corresponding to pixels not at the boundaries, otherwise the value is zero, no constraint is imposed, and a jump is allowed.

This regularization term is quadratic and incorporated in an additive way, thus it will not introduce additional nonlinearity.

5.3.2 Distorted Born Iterative Method

Consider the contrast $\boldsymbol{\chi}$ as a small perturbation $\delta\boldsymbol{\chi}$ w.r.t. an inhomogeneous background $\boldsymbol{\chi}^{(n)}$; one has $\boldsymbol{\chi} = \boldsymbol{\chi}^{(n)} + \delta\boldsymbol{\chi}$ [55]. The secondary incident field by this inhomogeneous background is

$$\mathbf{E}^{\mathrm{bac}} = (\mathbf{I_M} - \mathbf{G_d}\mathbf{X}^{(n)})^{-1}\mathbf{E^i} \tag{5.21}$$

where $\mathbf{I_M}$ is the M-dimensional identity matrix, with this background, the scattered field is

$$\mathbf{E^s} = \mathbf{G_s}\mathbf{X^{(n)}}\mathbf{E}^{\mathrm{bac}} + \mathbf{G_s^{\chi_n}}\delta\mathbf{X}\mathbf{E^t} \tag{5.22}$$

Here, $\mathbf{G_s^{\chi_n}}$ is the inhomogeneous background Green's function. The cost functional is the sum of the difference between measured and calculated data and a regularization term

$$Q(\delta\boldsymbol{\chi}) = \sum_{p=1}^{N_i} \left\| \mathbf{E_p^s} - \mathbf{G_s}\mathbf{X}^{(n)}\mathbf{E_p^{bac}} - \mathbf{G_s^{\chi_n}}\delta\mathbf{X}\mathbf{E_p^{bac}} \right\|^2 + \lambda Q_r(\delta\boldsymbol{\chi}) \tag{5.23}$$

within which $\mathbf{E^t}$ is replaced by $\mathbf{E}^{\mathrm{bac}}$ with the Born approximation. The optimization procedure is summarized below.

At each iteration, update $\mathbf{G_s^{\chi_n}}$ by

$$\mathbf{G_s^{\chi_n}} = \mathbf{G_s}(\mathbf{I_M} - \mathbf{X}^{(n)}\mathbf{G_d})^{-1} \tag{5.24}$$

Solve the forward problem

$$[\mathbf{E_p^{bac}}]^{(n)} = \mathbf{E_p^i} + \mathbf{G_d}\mathbf{X}^{(n)}[\mathbf{E_p^{bac}}]^{(n)} \tag{5.25}$$

Calculate the scattered field

$$[\mathbf{E_p^s}]^{(n)} = \mathbf{G_s}\mathbf{X}^{(n)}[\mathbf{E_p^{bac}}]^{(n)} \tag{5.26}$$

Solve the optimization problem with 0th-order Tikhonov regularization

$$\min : Q(\delta\boldsymbol{\chi}) = \sum_{p=1}^{N_i} \left\| \mathbf{E}_p^{\mathbf{s}} - [\mathbf{E}_p^{\mathbf{s}}]^{(n)} - \mathbf{G}_{\mathbf{s}}^{\boldsymbol{\chi}_\mathbf{n}} \delta\mathbf{X} [\mathbf{E}_p^{\mathbf{bac}}]^{(n)} \right\|^2 + \lambda \left\| \delta\boldsymbol{\chi} \right\|^2 \tag{5.27}$$

or with UGS regularization

$$\min : Q(\delta\boldsymbol{\chi}) = \sum_{p=1}^{N_i} \left\| \mathbf{E}_p^{\mathbf{s}} - [\mathbf{E}_p^{\mathbf{s}}]^{(n)} - \mathbf{G}_{\mathbf{s}}^{\boldsymbol{\chi}_\mathbf{n}} \delta\mathbf{X} [\mathbf{E}_p^{\mathbf{bac}}]^{(n)} \right\|^2 + \lambda \left(\left\| \mathbf{D_v} \delta\boldsymbol{\chi} \right\|^\mathbf{2} + \left\| \mathbf{D_h} \delta\boldsymbol{\chi} \right\|^\mathbf{2} \right) \tag{5.28}$$

It can be dealt with directly as

$$\delta\boldsymbol{\chi} = [\mathbf{K}^\dagger \mathbf{K} + \lambda \mathbf{D}]^{-\mathbf{1}} \mathbf{K}^\dagger \mathbf{y}, \tag{5.29}$$

$\mathbf{D} = \mathbf{I_M}$ for Tikhonov regularization, $\mathbf{D} = \mathbf{D}_\mathbf{h}^\dagger \mathbf{D_h} + \mathbf{D}_\mathbf{v}^\dagger \mathbf{D_v}$ for the UGS one. $\mathbf{K}$ is a $(N_i N_r) \times M$ matrix and element $\mathbf{K}(i + N_r(p-1), j) = \mathbf{G}_\mathbf{s}^{\boldsymbol{\chi}_\mathbf{n}}(i,j)[\mathbf{E}_p^{\mathbf{bac}}]^{(n)}(j)$ and $\mathbf{y}$ is a $(N_i N_r) \times 1$ vector with $\mathbf{y}(i + N_r(p-1)) = \mathbf{E}_p^{\mathbf{s}}(i) - [\mathbf{E}_p^{\mathbf{s}}]^{(n)}(i)$. $\mathbf{K}^\dagger$ is the conjugate transpose of $\mathbf{K}$. To conclude, update the contrast as

$$\boldsymbol{\chi}_{n+1} = \boldsymbol{\chi}_n + \delta\boldsymbol{\chi} \tag{5.30}$$

Considering the imaginary part of the contrast contributes less due to the high difference in magnitude with the real part; consequently, one can separate them and the UGS regularization term becomes

$$Q_{UGS}(\delta\boldsymbol{\chi}) = Q_{UGS}\left(\Re\{\delta\boldsymbol{\chi}\}\right) + \beta Q_{UGS}\left(\Im\{\delta\boldsymbol{\chi}\}\right) \tag{5.31}$$

A larger regularization parameter ($\beta > 1$) can be assigned to the imaginary part based on the prior information of the magnitude of real and imaginary parts of contrast. To update $\delta\boldsymbol{\chi}$, the linear equation

$$\begin{bmatrix} \mathbf{K_d} + \lambda_r \mathbf{D} & \mathbf{K_m} \\ -\mathbf{K_m} & \mathbf{K_d} + \lambda_i \mathbf{D} \end{bmatrix} \begin{bmatrix} \Re\{\delta\boldsymbol{\chi}\} \\ \Im\{\delta\boldsymbol{\chi}\} \end{bmatrix} = \begin{bmatrix} \mathbf{y}_r \\ \mathbf{y}_i \end{bmatrix} \tag{5.32}$$

needs to be solved, with $\mathbf{y}_r = \Re\{\mathbf{K}^\dagger \mathbf{y}\}$, $\mathbf{y}_i = \Im\{\mathbf{K}^\dagger \mathbf{y}\}$, $\mathbf{K_d} = \mathbf{K}_\mathbf{r}^\dagger \mathbf{K_r} + \mathbf{K}_\mathbf{i}^\dagger \mathbf{K_i}$, $\mathbf{K_m} = \mathbf{K}_\mathbf{i}^\dagger \mathbf{K_r} - \mathbf{K}_\mathbf{r}^\dagger \mathbf{K_i}$, $\mathbf{K_r} = \Re\{\mathbf{K}\}$ and $\mathbf{K_i} = \Im\{\mathbf{K}\}$. The regularization parameters are $\lambda_r = \lambda$ and $\lambda_i = \lambda\beta$.

5.3.3 Contrast Source Inversion

The Contrast Source Inversion Method is based on the source-type integral equations wherein the contrast source is regarded as an independent parameter. The cost function is a sum of normalized mismatches in data and state equations

$$\begin{aligned} Q(\mathbf{J}_1, \ldots, \mathbf{J}_{N_i}, \boldsymbol{\chi}) = & \frac{\sum_{p=1}^{N_i} \left\| \mathbf{E}_p^{\mathbf{s}} - \mathbf{G_s} \mathbf{J}_p \right\|^2}{\sum_{p=1}^{N_i} \left\| \mathbf{E}_p^{\mathbf{s}} \right\|^2} \\ & + \frac{\sum_{p=1}^{N_i} \left\| \mathbf{X} \mathbf{E}_p^{\mathbf{i}} + \mathbf{X} \mathbf{G_d} \mathbf{J}_p - \mathbf{J}_p \right\|^2}{\sum_{p=1}^{N_i} \left\| \mathbf{E}_p^{\mathbf{i}} \right\|^2} \end{aligned} \tag{5.33}$$

Note that in the classical CSI [58] the second term normalization is $\sum_{p=1}^{N_i} \left\| \mathbf{X} \mathbf{E}_p^{\mathbf{i}} \right\|^2$, one simplifies it as $\sum_{p=1}^{N_i} \left\| \mathbf{E}_p^{\mathbf{i}} \right\|^2$ [61]. To improve the quality of the reconstruction and incorporate high frequency components of the image, one introduces prior information. Inspired by [51, 52], one incorporates Huber regularization into CSI.

The Huber function can be expressed as

$$h(x) = \begin{cases} |x|^2, & |x| \leqslant \gamma \\ 2\gamma|x| - \gamma^2, & \text{else} \end{cases} \tag{5.34}$$

with γ as the threshold. This function is used to estimate the difference in dielectric properties between the pixel and its neighborhood. The total difference is measured by

$$Q_{\mathrm{HB}} = \sum_{v} \sum_{v' \in N_p} h(\chi_v - \chi_{v'}) \tag{5.35}$$

where N_v represents the neighborhood of v. Eight neighbors are used for one pixel.[2] The first derivative of Huber regularization w.r.t. the contrast is

$$\mathbf{g}_{\chi}^{\mathrm{HB}}(v) = \sum_{v' \in N_v} \omega_{v'} \tag{5.36}$$

with

$$\omega_{v'} = \begin{cases} \chi_v - \chi_{v'}, & |\chi_v - \chi_{v'}| \leqslant \gamma \\ \gamma(\chi_v - \chi_{v'})/|\chi_v - \chi_{v'}|, & \text{else} \end{cases} \tag{5.37}$$

Another regularization term is the smoothness constraint guided by US information described in Section 5.3.1. The first derivative of UGS regularization is

$$\mathbf{g}_{\boldsymbol{\chi}}^{\mathrm{UGS}} = (\mathbf{D}_{\mathbf{v}}^{\dagger}\mathbf{D}_{\mathbf{v}} + \mathbf{D}_{\mathbf{h}}^{\dagger}\mathbf{D}_{\mathbf{h}})\boldsymbol{\chi} \tag{5.38}$$

With these regularizations, the criterion becomes

$$\begin{aligned} Q(\mathbf{J}_1, \ldots, \mathbf{J}_{N_i}, \boldsymbol{\chi}) &= \frac{\sum_{p=1}^{N_i} \left\| \mathbf{E}_p^{\mathbf{s}} - \mathbf{G}_{\mathbf{s}}\mathbf{J}_p \right\|^2}{\sum_{p=1}^{N_i} \left\| \mathbf{E}_p^{\mathbf{s}} \right\|^2} \\ &+ \frac{\sum_{p=1}^{N_i} \left\| \mathbf{X}\mathbf{E}_p^{\mathbf{i}} + \mathbf{X}\mathbf{G}_{\mathbf{d}}\mathbf{J}_p - \mathbf{J}_p \right\|^2 + \gamma Q_r(\boldsymbol{\chi})}{\sum_{p=1}^{N_i} \left\| \mathbf{E}_p^{\mathbf{i}} \right\|^2} \end{aligned} \tag{5.39}$$

There is no need to solve the forward problem at each iteration, so it is more efficient. With function $Q(\mathbf{J}_1, \ldots, J_{N_i}, \boldsymbol{\chi})$, it is difficult to optimize contrast current and contrast simultaneously due to their dependence. Here one follows [49] to optimize them alternately by minimizing the cost functional w.r.t. $\mathbf{J}$, assuming known $\boldsymbol{\chi}$, and update $\boldsymbol{\chi}$, assuming known $\mathbf{J}$. The optimization procedure is in Algorithm.

Similarly, the regularization term can also be enforced on the real and imaginary parts separately as

$$Q_r(\boldsymbol{\chi}) = Q_r\left(\Re\{\boldsymbol{\chi}\}\right) + \beta q_r\left(\Im\{\boldsymbol{\chi}\}\right) \tag{5.40}$$

During update of the contrast, the gradients of the cost functional w.r.t. to real and imaginary parts are

$$\begin{aligned} \mathbf{g}_{\Re\{\boldsymbol{\chi}\}}^{(n)} &= \sum_{p} \Re\left\{ (\mathbf{X}^{(n-1)}[\mathbf{E}_p^{\mathbf{t}}]^{(n)} - \mathbf{J}_p^{(n)})\overline{[\mathbf{E}_p^{\mathbf{t}}]^{(n)}} \right\} + \lambda_r \mathbf{g}_{\Re\{\boldsymbol{\chi}\}}^{Q_r}\left(\Re\{\boldsymbol{\chi}\}\right) \\ \mathbf{g}_{\Im\{\boldsymbol{\chi}\}}^{n} &= \sum_{p} \Im\left\{ (\mathbf{X}^{(n-1)}[\mathbf{E}_p^{\mathbf{t}}]^{(n)} - \mathbf{J}_p^{(n)})\overline{[\mathbf{E}_p^{\mathbf{t}}]^{(n)}} \right\} + \lambda_i \mathbf{g}_{\Im\{\boldsymbol{\chi}\}}^{Q_r}\left(\Im\{\boldsymbol{\chi}\}\right) \end{aligned} \tag{5.41}$$

with $\lambda_r = \lambda$ and $\lambda_i = \beta\lambda$.

[2] In [52], there is a coefficient 0.5 since the difference between two neighboring pixels is calculated twice. Here it is in the regularization parameter.

Algorithm 6 CSI with HB/UGS regularization

Input: $\mathbf{E^s}$, $\mathbf{E^i}$, $\mathbf{G_s}$, $\mathbf{G_d}$
Output: $\boldsymbol{\chi}$

Initialize $\boldsymbol{\chi}_0$ and $\mathbf{J}$ by back propagation [151] with

$$\mathbf{J}_p^{(0)} = \frac{\left\|\mathbf{G_s^\dagger E_p^s}\right\|^2}{\left\|\mathbf{G_s G_s^\dagger E_p^s}\right\|^2}\mathbf{G_s^\dagger E_p^s} \text{ and } \boldsymbol{\chi}_0 = \frac{\sum_{p=1}^{N_i}\mathbf{J}_p^{(0)}\overline{[\mathbf{E}_p^\mathbf{t}]^{(0)}}}{\sum_{p=1}^{N_i}\left\|[\mathbf{E}_p^\mathbf{t}]^{(0)}\right\|^2}$$

for $n = 1 : iter_{\max}$ **do**

Calculate data equation error $\boldsymbol{\rho}_p^{(n-1)} = \mathbf{E_p^s} - \mathbf{G_s}\mathbf{J}_p^{(n-1)}$

Calculate state equation error $\mathbf{o}_p^{(n-1)} = \mathbf{X}^{(n-1)}[\mathbf{E}_p^\mathbf{t}]^{(n-1)} - \mathbf{J}_p^{(n-1)}$

Update contrast current:

Gradient $\mathbf{g}_{J_p}^{(n)} = -\frac{\mathbf{G_s^\dagger}\boldsymbol{\rho}_p^{(n-1)}}{\sum_p\left\|\mathbf{E_p^s}\right\|^2} - \frac{\mathbf{o}_p^{(n-1)} - \mathbf{G_d^\dagger}[\mathbf{X}^{(n-1)}]^\dagger\mathbf{o}_p^{(n-1)}}{\sum_{p=1}\left\|\mathbf{E_p^i}\right\|^2}$

Polak-Ribière conjugate gradient search direction

$$\mathbf{v}_{J_p}^{(n)} = \mathbf{g}_{J_p}^{(n)} + \frac{\Re < \mathbf{g}_{J_p}^{(n)}, \mathbf{g}_{J_p}^{(n)} - \mathbf{g}_{J_p}^{(n-1)} >}{< \mathbf{g}_{J_p}^{(n-1)}, \mathbf{g}_{J_p}^{(n-1)} >}\mathbf{v}_{J_p}^{(n-1)}$$

Update $\mathbf{J}_p$ by $\mathbf{J}_p^{(n)} = \mathbf{J}_p^{(n-1)} + \beta_J^{(n)}\mathbf{v}_{J_p}^{(n)}$

Update total field by $[\mathbf{E}_p^\mathbf{t}]^{(n)} = \mathrm{E}_p^i + \mathbf{G_d}\mathbf{J}_p^{(n)}$

Update contrast:

Gradient $\mathbf{g}_\chi^{(n)} = \sum_p(\mathbf{X}^{(n-1)}[\mathbf{E}_p^\mathbf{t}]^{(n)} - \mathbf{J}_p^{(n)})\overline{\mathbf{E}_p^\mathbf{t}]^{(n)}} + \lambda\mathbf{g}_{\boldsymbol{\chi}}^{\mathrm{HB/UGS}}(\boldsymbol{\chi})$

Polak-Ribière conjugate gradient search direction

$$\mathbf{v}_\chi^{(n)} = \mathbf{g}_\chi^{(n)} + \frac{\Re < \mathbf{g}_\chi^{(n)}, \mathbf{g}_\chi^{(n)} - \mathbf{g}_\chi^{(n-1)} >}{< \mathbf{g}_\chi^{(n-1)}, \mathbf{g}_\chi^{(n-1)} >}\mathbf{v}_\chi^{(n-1)}$$

Update $\boldsymbol{\chi}$ by $\boldsymbol{\chi}^{(n)} = \boldsymbol{\chi}^{(n-1)} + \beta_\chi^{(n)}\mathbf{v}_\chi^{(n)}$

end for

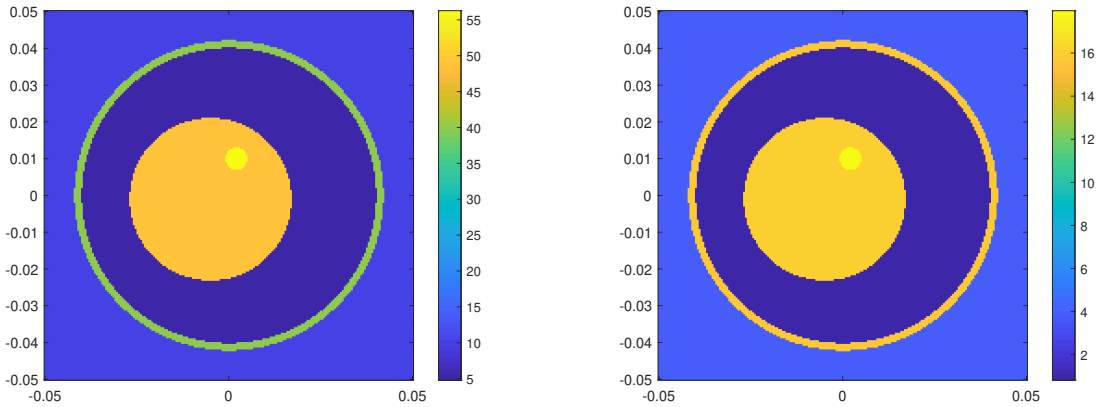

(a) (b)

Figure 5.1: Real (a) and imaginary (b) parts of synthetic Model 1.

5.4 Numerical simulations

In this section, one considers numerical experiments on three breast models: a synthetic one, Model 1, to validate algorithms, and two realistic breast phantoms, Models 2 and 3. As mentioned, in US imaging, reflective boundaries where acoustic impedance changes can be detected by reflection algorithms when the travel time t of acoustic signals is recorded and an average sound speed c assumed. Here, tissue boundary information is not derived from carrying out these methods in full but from simpler simulations: three sources are put around the object; each one emits ideal Gaussian-like ultrasonic pulses into different directions (from $-45°$ to $45°$ towards the center); the position of the boundary along each direction is calculated as $d = ct/2$; based on the angle of acoustic wave it is decided whether the boundary is vertical or horizontal and the images subsequently follow.

5.4.1 Reconstruction of synthetic breast model

This simple synthetic breast model consists of skin, fatty, fibroconnective/ glandular and tumorous tissues. Each tissue type is of regular shape and has uniform permittivity. The skin is 2 mm thick and the tumor of 6 mm-diameter. The experiments are conducted at a single frequency of 1 GHz. The immersion medium is chosen from [52], letting $\epsilon_b = 10 + 4i$. Relative permittivities of tissues at this 1 GHz frequency are $39.89 + 15.64i, 4.80 + 0.82i, 48.82 + 15.89i, 56.27 + 17.96i$, respectively. Figure 5.1 depicts the distribution of real and imaginary parts. The DoI is of size 0.1 m $\times$ 0.1 m. 40 antennas are distributed evenly on a circle of 0.057 m radius, operated as sources and receivers simultaneously. For the forward problem, the DoI is discretized into 200×200 pixels and the problem tackled by a conjugate-gradient fast Fourier transform (CG-FFT) algorithm. Additive Gaussian noise is added to the synthetic data with SNR = 30 dB.

For inversion, the domain is discretized into 80×80 pixels. One assumes that the breast is in a circle with 0.045 m radius (the radius of outer boundary of the breast model is 0.042 m). The reconstruction is confined within the region and pixels outside it restricted to same dielectric properties as the coupling medium. Retrieved real and imaginary parts of the relative permittivity are bounded by $1 \leqslant \Re\{\epsilon_r\} \leqslant 70$ and $0 \leqslant \Im\{\epsilon_r\} \leqslant 40$ at each iteration.

The regularization parameter λ can be chosen by L-curve [165], generalized cross-validation [166], or other methods. When it is determined, it can be chosen as λ_r in separate inversion. β, as the ratio of regularization parameter of imaginary part to real part, is chosen based on the relative magnitude of these two parts. γ in Huber regularization is the threshold below which a quadratic cost is used to smooth noise and above which a linearly-varying cost is added to penalize it in a lesser extent for

Table 5.1: Relative error with Model 1 with SNR = 30 dB

Method	DBIM-TK	DBIM-UGS	CSI	CSI-HB-S	CSI-UGS	CSI-UGS-S
$Err(\Re\{\epsilon_r\})$	0.385	0.335	0.370	0.345	0.342	0.322
$Err(\Im\{\epsilon_r\})$	0.674	0.483	0.596	0.389	0.469	0.385
$Err(\epsilon_r)$	0.4245	0.353	0.400	0.350	0.358	0.329

edge-preserving. It is selected as the smallest difference in the contrast (a margin can be left).

First, one experiments on DBIM with Tikhonov regularization (DBIM-TK) and CSI with separate Huber regularization (CSI-HB-S). The DBIM regularization parameter is $\lambda = 0.05$. With Huber, the threshold is $\gamma = 0.5$ and the regularization parameter $\lambda_i = 0.1$ for the imaginary part, $\lambda_r = 0.001$ for the real part. CSI with no regularization is run also in comparison and its results shown.

Results are in Figure 5.2. The glandular part is reconstructed as a ring with relatively higher relative permittivity but is still recognized. The contrast value of the center part is usually underestimated. Dielectric properties are not smooth in each region and the small tumor is not found. Now, one incorporates the prior information from US imaging by UGS regularization. The tissue boundary information incorporated is in Figure 5.3. As explained, these two images show the discontinuities in vertical and horizontal directions.

The regularization parameter is set to 1 in DBIM, 0.01 in CSI. Besides, one separates real and imaginary parts in DBIM-UGS (DBIM-UGS-S) and CSI-UGS algorithm (CSI-UGS-S). The regularization parameters are $\lambda_r = 1$ and $\lambda_i = 10$ for DBIM-UGS-S and $\lambda_r = 0.01$ and $\lambda_i = 10$ for CSI-UGS-S. Results are in Figure 5.4.

With this US information guided regularization, the results are smoother, while edges are well preserved with both algorithms. Besides, the tumor is well distinguished within the glandular part in the reconstruction of the real part. Upon separation of real and imaginary part reconstructions and assigning a large regularization parameter to the imaginary part, one sees obvious improvement in its retrieval.

To evaluate the imaging results quantitatively, one computes the relative error of the permittivity

$$Err(\boldsymbol{\zeta}) = \frac{\|\boldsymbol{\zeta}_{\text{est}} - \boldsymbol{\zeta}_{\text{true}}\|_2}{\|\boldsymbol{\zeta}_{\text{true}}\|_2} \tag{5.42}$$

where $\boldsymbol{\zeta}$ is the parameter to evaluate and subscripts "true" and "est" represent true value and estimation result, respectively. The errors with the algorithms above are in Table 5.1. Reconstructions are more accurate than those with the algorithms without prior information. Also, one sees a small decrease in the error result of the real part and a large one in the imaginary part when the two parts of contrast are retrieved separately.

The CPU time is also compared between the cases whether the real and imaginary parts are reconstructed separately. In average, it takes 13.89 seconds for one iteration in DBIM-UGS,14.38 in DBIM-UGS-S, 1.79 in CSI-UGS, and 0.73 in CSI-UGS-S, performed on Intel Core i7-8850H CPU (2.60 GHz) with 32 GByte memory. Considering both computation cost and imaging quality, DBIM-UGS and CSI-UGS-S are henceforth used to incorporate US information in the following experiments.

Robustness of the algorithm is tested based on DBIM-UGS. Here the reflective boundaries are assumed to have been obtained from some reflection mode imaging methods, however, in fact, those cannot be perfect. The acoustic signal may bounce between two interfaces so there will be artifacts and some boundaries may be missing due to a small variation in acoustic impedance. So, it is worthwhile to discuss the effects of inexact boundaries.

One has carried out several experiments with two kinds of inexact boundaries, which are shown in Figure 5.5. In the first kind, there is a fake tumor, and in the second one, interfaces between tumor and glandular part are incomplete. With these boundaries, retrievals are depicted in Figure 5.6. Since the regularization term is intended to suppress the discontinuity between two adjacent pixels not at

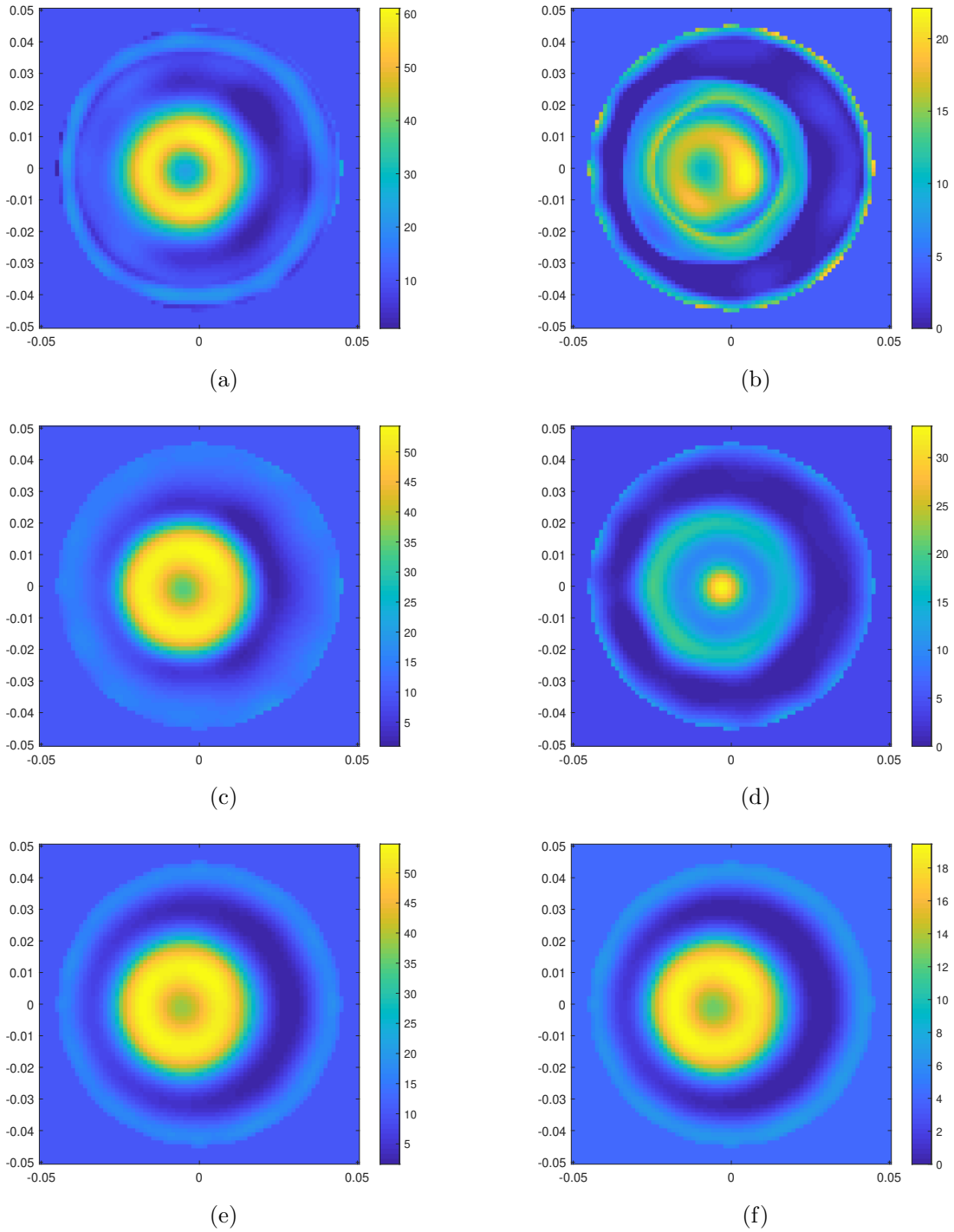

Figure 5.2: Retrieved real (left) and imaginary (right) parts of Model 1 with. (a),(b) DBIM-TK reconstruction; (c),(d) CSI reconstruction; (e),(f) CSI-HB-S reconstruction.

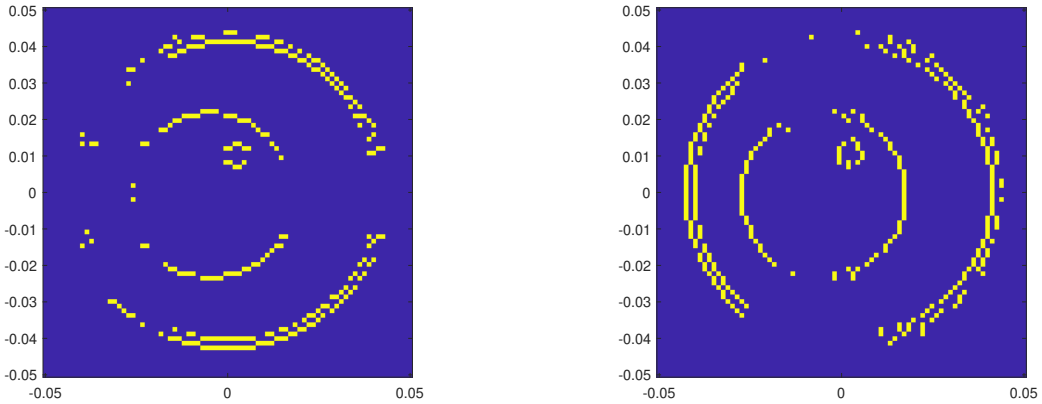

Figure 5.3: Boundary information in vertical (a) and horizontal (b) directions.

Table 5.2: Relative error with Model 1 with SNR = 10 dB

Method	DBIM-TK	DBIM-UGS	CSI-HB-S	CSI-UGS-S
$Err(\Re\{\epsilon_r\})$	0.436	0.351	0.352	0.325
$Err(\Im\{\epsilon_r\})$	0.857	0.584	0.4015	0.396
$Err(\epsilon_r)$	0.497	0.3825	0.358	0.333

a border, it has no constraint otherwise. That is more severe when boundaries are not complete. This is consistent with the experiments. If a fake tumor in the US information, it appears in the map with lower contrast, while the real one still has higher permittivity and one can detect it. When the boundaries are incomplete, the tumor has no evident border and is difficult to find. Thus, if the boundary information cannot yield the interface between tumor and other tissues, it is hard to image it with microwaves.

Now, a higher level of noise is considered with SNR = 10 dB. Experiments are conducted on DBIM-TK, DBIM-UGS, CSI-HB-S and CSI-UGS-S with the same regularization parameters. The relative errors are summarized in Table 5.2. Due to the high level of noise, the quality of the imaging is degraded for all algorithms yet the one proposed is affected to a lesser extent.

5.4.2 Reconstruction of realistic breast phantoms

To better validate the approach, one tests it on two more realistic breast phantoms as slices extracted from breast phantoms of the UWCEM repository [134], categorized in different classes according to radiographic density.

Class 2 breast phantom

Model 2 (ID 070604) has a scattered fibroglandular density. Debye parameters are from [133]. Figure 5.7 shows the phantom. The models and parameters are detailed in Section 3.7.1.

The cell size is 0.5 mm and one uses this grid to solve the forward problem. 40 antennas are set evenly on a circle of 0.08 m radius. Additive Gaussian noise of 30 dB is added to the data. For inversion, one adopts a 2 mm cell size, resulting in 88×77 pixels. Other configurations are the same as with experiments before. The reconstruction results of DBIM-TK and CSI-HB-S are in Figure 5.8. The regularization parameter is $\lambda = 0.05$ for DBIM and one sets $\lambda_r = 0.001$ and $\lambda_i = 0.1$ in CSI for Huber regularization, its threshold being $\gamma = 0.5$.

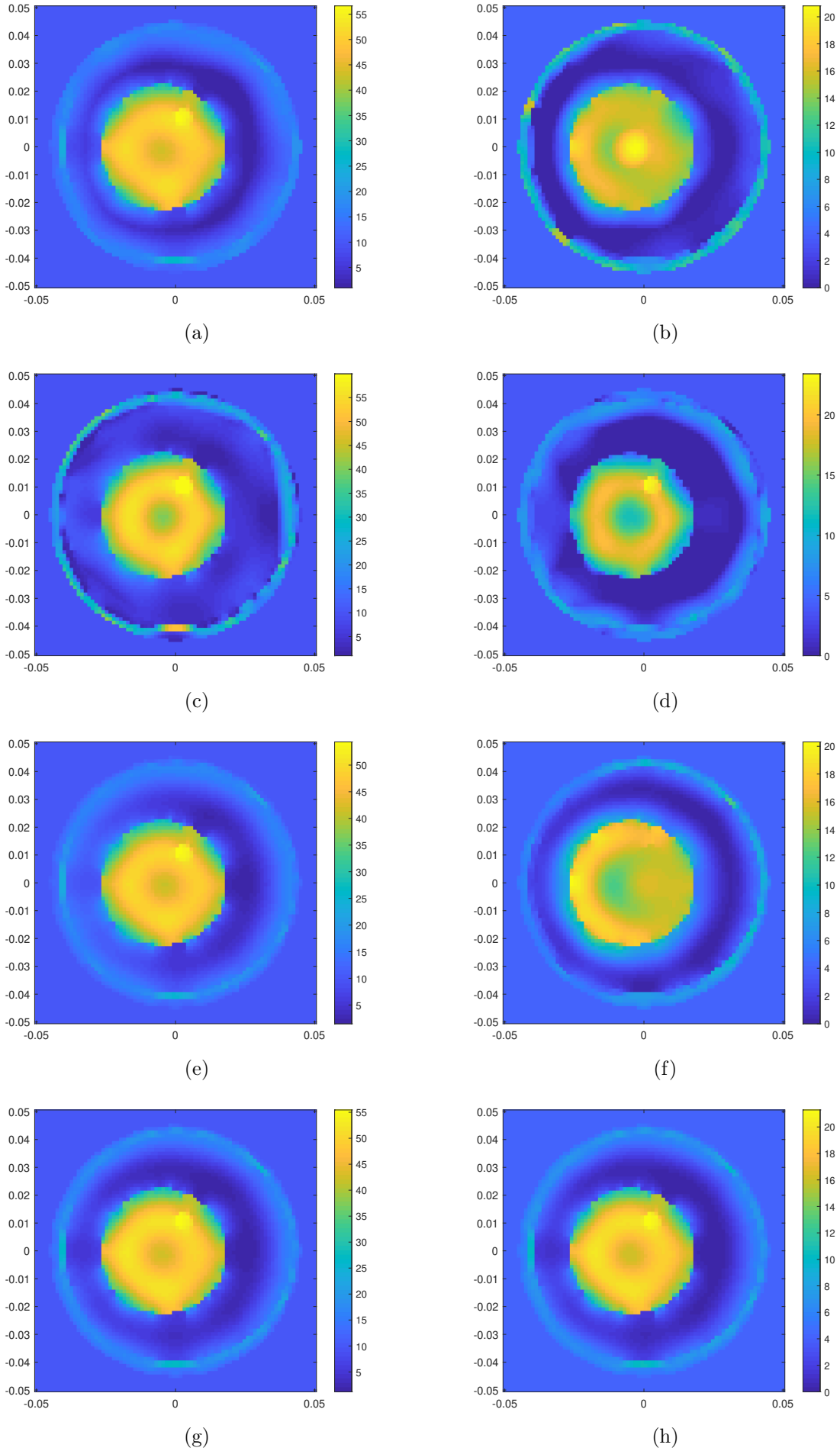

Figure 5.4: Retrieved real (left) and imaginary (right) parts of Model 1. (a),(b) DBIM-UGS; (c),(d) DBIM-UGS-S; (e),(f) CSI-UGS; (g),(h) CSI-UGS-S.

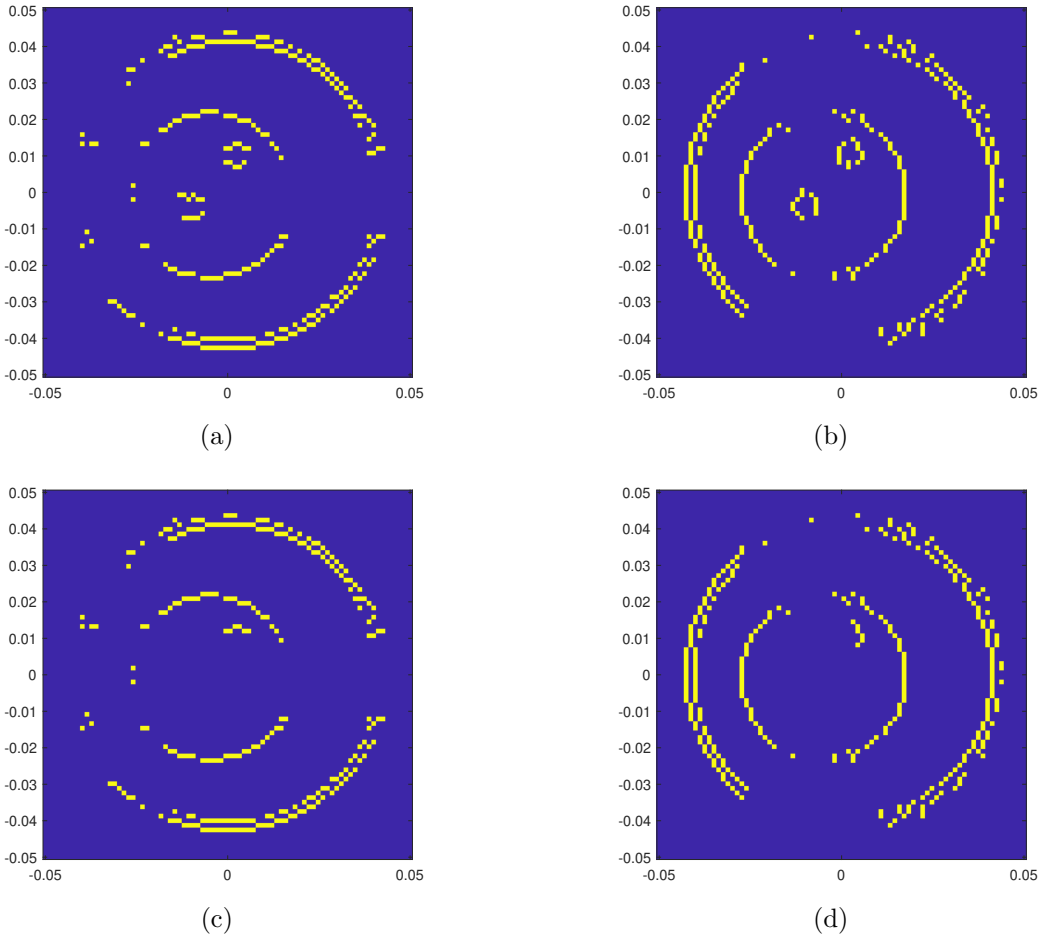

Figure 5.5: Inexact boundaries tested in experiments with Model 1: (a),(b) fake tumor; (c),(d) incomplete boundary.

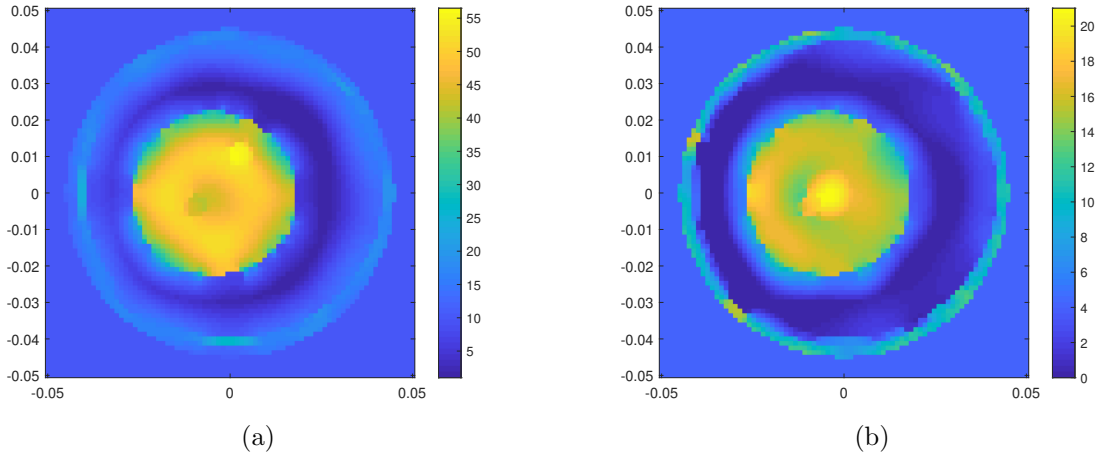

(a) (b)

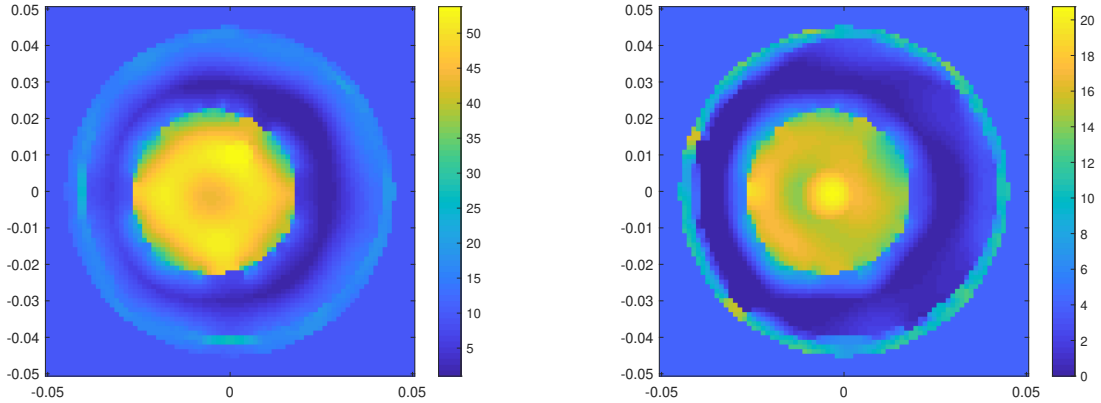

(c) (d)

Figure 5.6: Retrieved real (left) and imaginary (right) parts of Model 1. (a),(b) case with a fake tumor; (c),(d) case with incomplete boundary.

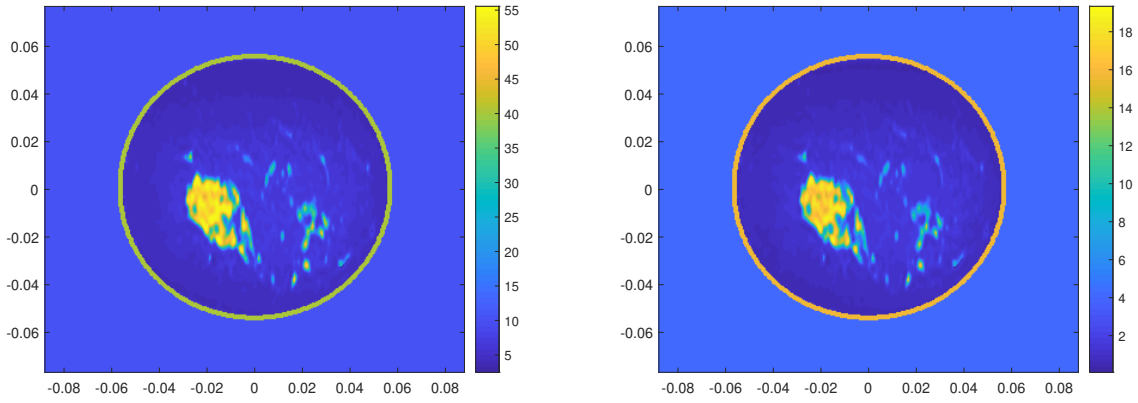

(a) (b)

Figure 5.7: Real (a) and imaginary (b) parts of Model 2.

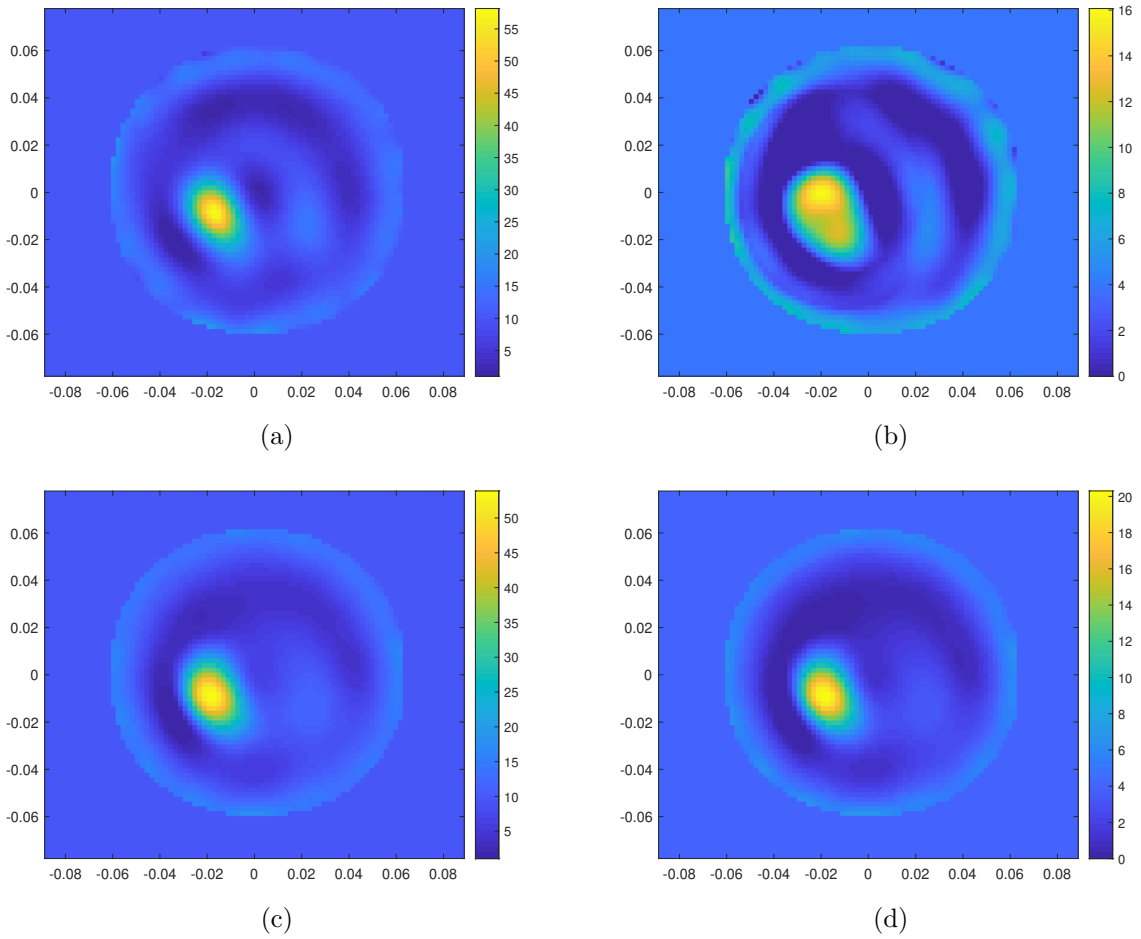

Figure 5.8: Retrieved real (left) and imaginary (right) parts of Model 2. (a),(b) DBIM-TK; (c),(d) CSI-HB-S.

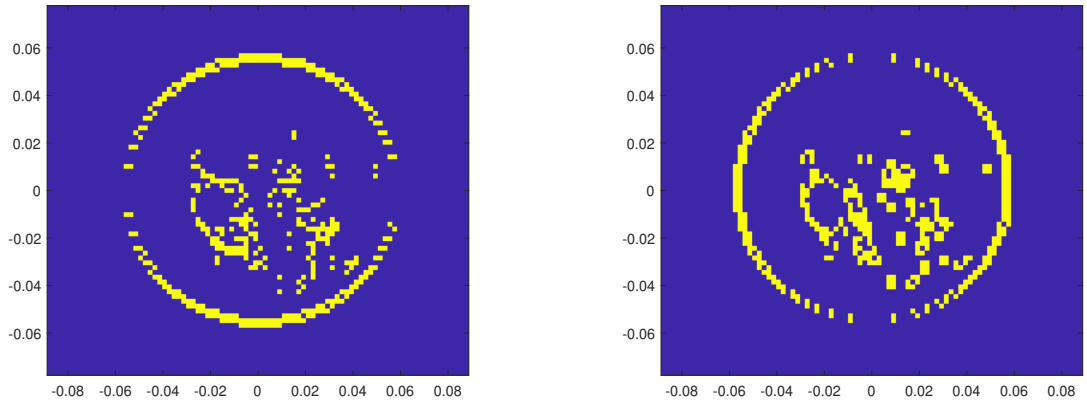

(a) (b)

Figure 5.9: Tissue boundaries of Model 2.

Table 5.3: Relative error with Model 2

Method	DBIM-TK	DBIM-UGS	CSI-HB-S	CSI-UGS-S
$Err(\Re\{\epsilon_r\})$	0.465	0.385	0.443	0.383
$Err(\Im\{\epsilon_r\})$	0.591	0.447	0.473	0.455
$Err(\epsilon_r)$	0.481	0.393	0.447	0.392

The main glandular part is well retrieved by both algorithms, though with a smaller size. Both fail in imaging the fine structure. Yet, imaging is satisfactory as one at sees the main structure.

Figure 5.9 shows the vertical and horizontal boundaries for the experiments next. As observed, discontinuities occur more frequently in the breast phantom and several points presenting discontinuities are adjacent in the same direction with null corresponding diagonal elements in $\mathbf{D}_\mathbf{h}^\dagger\mathbf{D}_\mathbf{v} + \mathbf{D}_\mathbf{p}^\dagger\mathbf{D}_\mathbf{v}$. As a result, in DBIM, the problem may remain ill-conditioned even with regularization $Q_{\text{UGS}} = \lambda\left(\| \mathbf{D}_\mathbf{v}\delta\boldsymbol{\chi} \|^\mathbf{2} + \| \mathbf{D}_\mathbf{h}\delta\boldsymbol{\chi} \|^\mathbf{2}\right)$.

This can be tackled by adding a small penalty term on the points where discontinuity shows in prior information. One sets $[b_{v/h}]_{i,j} = \gamma_t$ when the point is on a boundary and $\mathbf{D}_{\mathbf{v/h}}$ also changes accordingly. γ_t is chosen as a small value meanwhile keeping matrix $\mathbf{K}^\dagger\mathbf{K} + \lambda(\mathbf{D}_\mathbf{v}^\dagger\mathbf{D}_\mathbf{v} + \mathbf{D}_\mathbf{h}^\dagger\mathbf{D}_\mathbf{h})$ well-conditioned. Regularization parameters are chosen as $\lambda = 10$ and $\gamma_t = 0.1$ for UGS regularization in DBIM-UGS. In CSI-UGS-S, they are set as $\lambda_r = 0.01$ and $\lambda_i = 1$ for the real and imaginary parts.

Results of DBIM-UGS and CSI-UGS-S are in Figure 5.10. The results improve and finer structures are also imaged when the boundary information is incorporated. The relative errors of results above are in Table 5.3. From this error calculation, one observes that imaging quality is enhanced when US high-resolution information is indeed incorporated.

Class 3 breast phantom

Model 3 (ID 080304) is heterogeneously dense and its structure is quite complicated, see Figure 5.11. In Model 3, one inserts a synthetic 1 cm-diameter tumor at (1.2 cm, −0.5 cm). Its relative permittivity is $59.98 + 19.83i$, corresponding to the 75th percentile curve at 1 GHz in [132]. Configurations are as with Model 2. Cell size remains 2 mm for inversion and the DoI has 83×51 pixels.

One sets $\lambda = 0.001$ for the Tikhonov regularization, $\lambda_r = 0.001$ and $\lambda_i = 0.1$ for the Huber one. Figure 5.12 displays the reconstructions. Those by CSI-HB-S are smoother than those by DBIM-TK since the latter enforces no constraint on the spatial gradient of the contrast. Neither algorithm however can image the glandular part well and both fail in detecting the tumor.

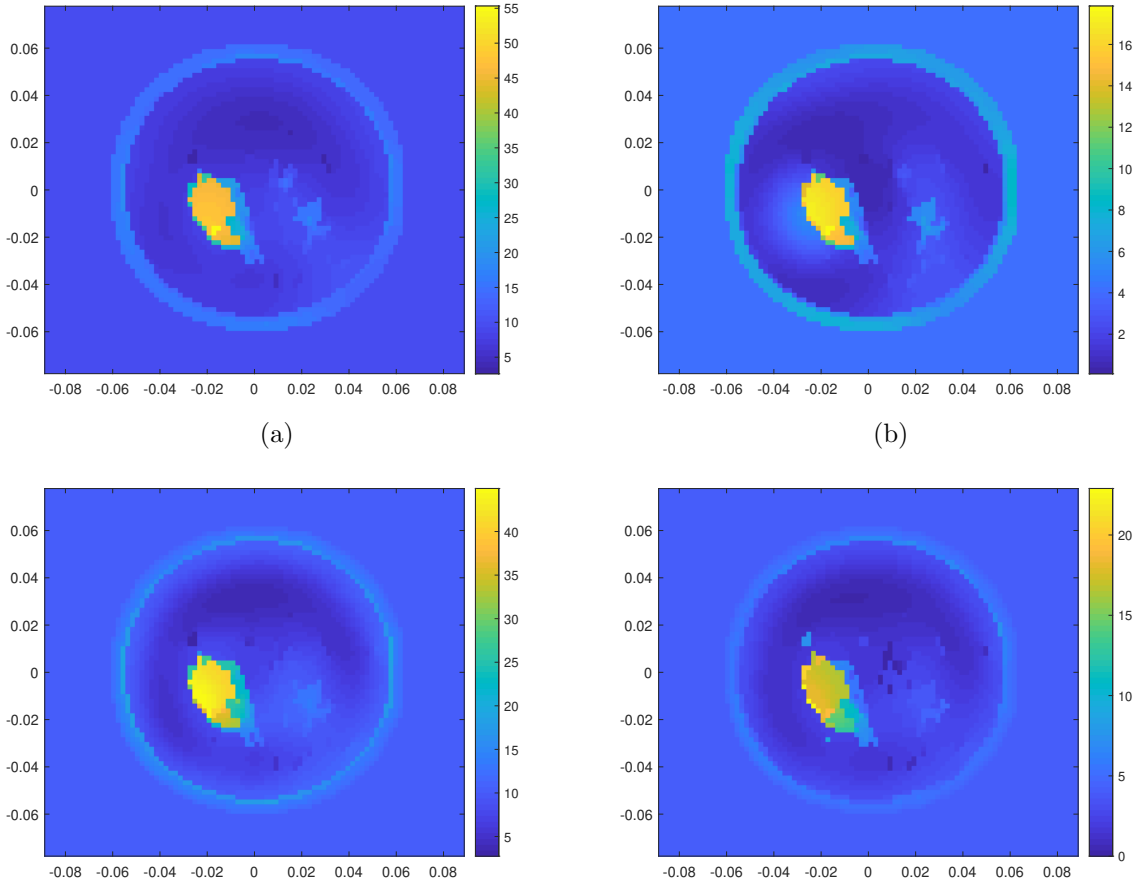

(a) (b)

(c) (d)

Figure 5.10: Retrieved real (left) and imaginary (right) parts of Model 2. (a),(b) DBIM-UGS; (c), (d) CSI-UGS-S.

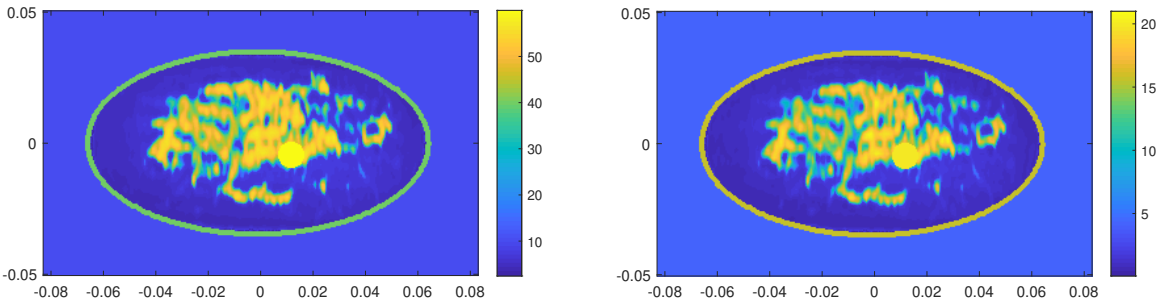

(a) (b)

Figure 5.11: Real (a) and imaginary (b) parts of Model 3.

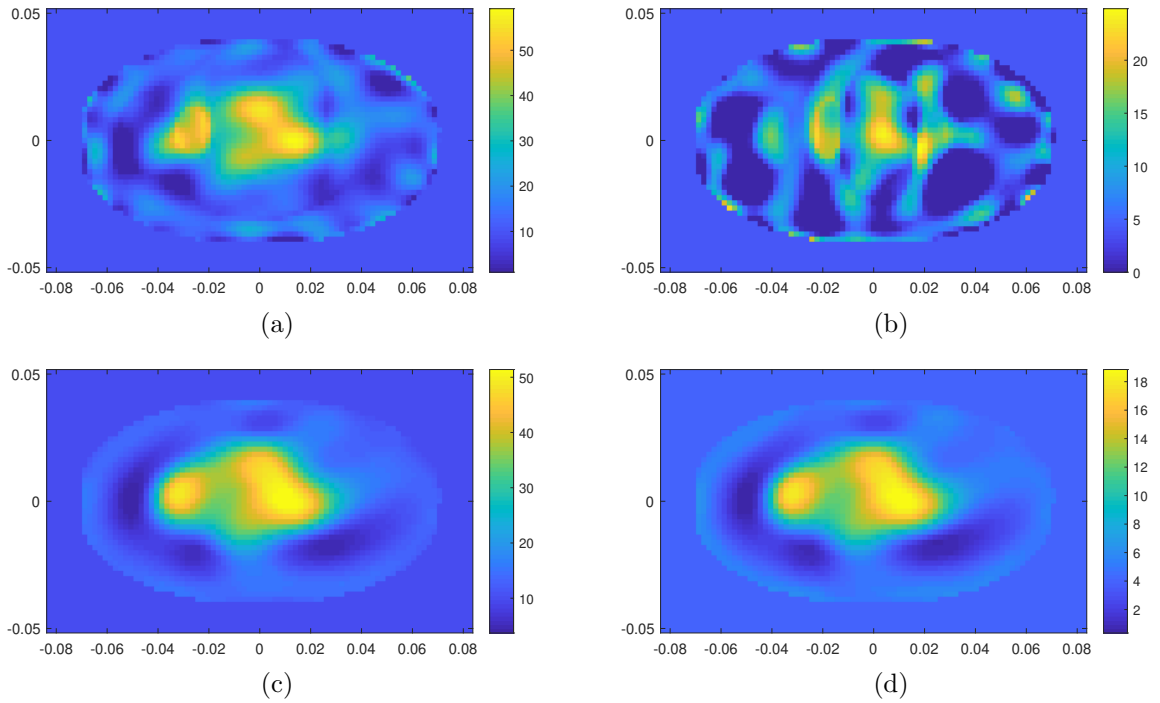

Figure 5.12: Retrieved real (left) and imaginary (right) parts of Model 3. (a),(b) DBIM-TK; (c),(d) CSI-HB-S.

Boundaries now used are shown in Figure 5.13. For DBIM, one sets $\gamma_t = 0.2$ and the other parameter values are like in the Model 2 experiment. When boundary information is incorporated, results improve, refer to Figure 5.14. Glandular and tumorous tissues are retrieved well. The small tumor can be distinguished from the glandular part, i.e., can be detected. Yet, singular points emerge with higher value. The regularization parameter γ_t must be properly chosen: too small, one may see those singular pixels, too large, the result may be too smooth to detect the tumor. The relative error of Model 3 is in Table 5.4, showing improvement of imaging.

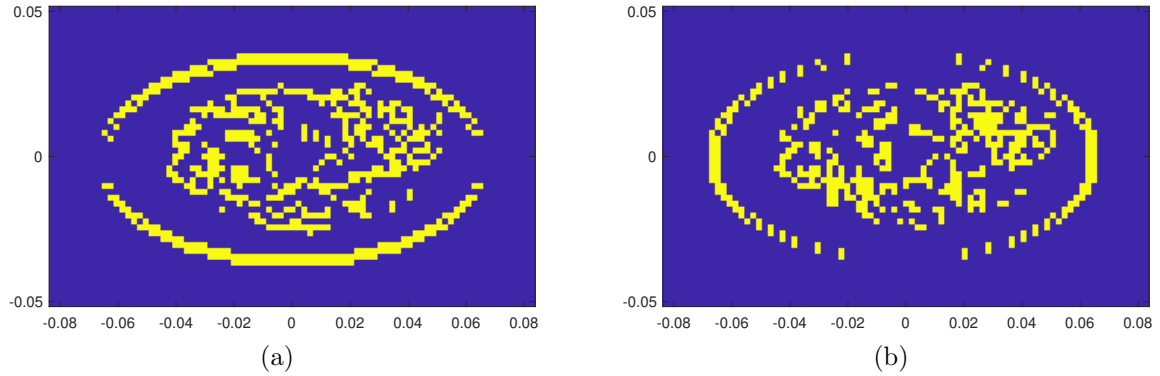

Figure 5.13: Tissue boundaries of Model 3

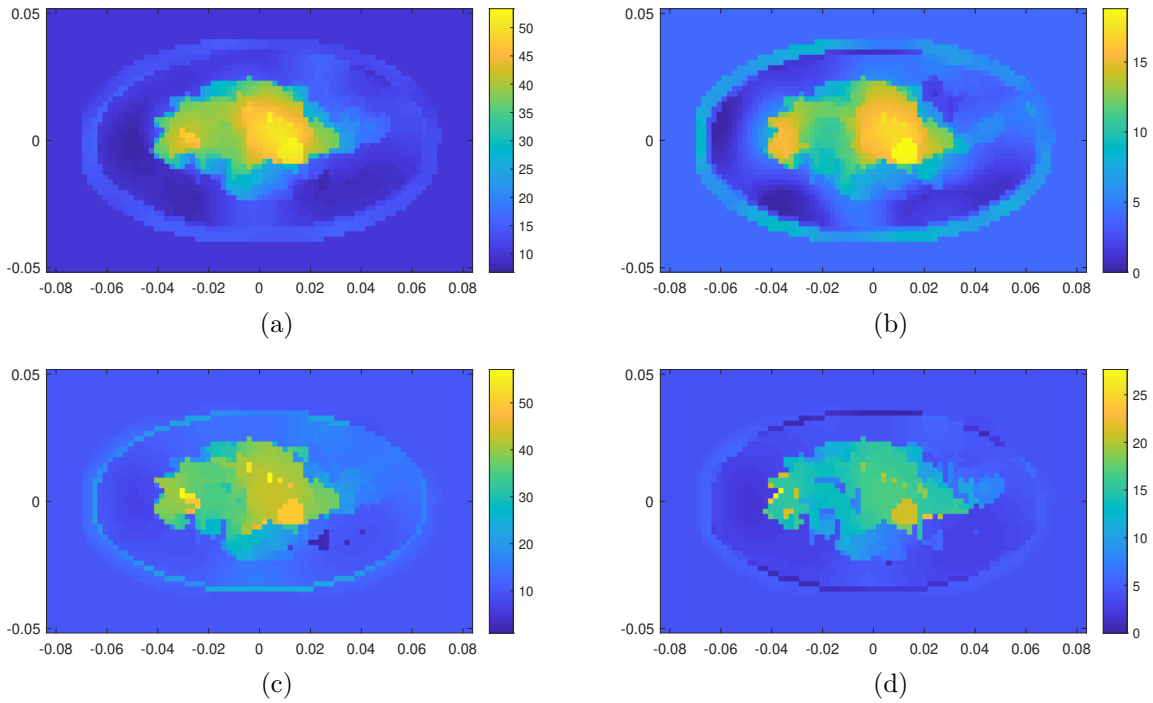

Figure 5.14: Retrieved real (left) and imaginary (right) parts of Model 3. (a),(b) DBIM-UGS; (c),(d) CSI-UGS-S.

Table 5.4: Relative error with Model 3

Method	DBIM-TK	DBIM-UGS	CSI-HB-S	CSI-UGS-S
$Err(\Re\{\epsilon_r\})$	0.486	0.427	0.4675	0.413
$Err(\Im\{\epsilon_r\})$	0.683	0.515	0.511	0.537
$Err(\epsilon_r)$	0.510	0.437	0.472	0.4275

5.5 Conclusion

In this chapter, one has proposed a regularization term to incorporate US information into microwave imaging. The regularizer tries to smoothen the dielectric properties between two adjacent pixels when none is on the tissue boundaries indicated by the US information, thus there is no need to segment US images to decide whether or not two pixels belong to the same tissue region, only tissue boundaries where reflection occurs in US imaging are used. Thus, it is easier to implement. One concludes that with microwave data only, it is quite difficult to image a small tumor inside the breast.

Adding high resolution information enables to well estimate its location and shape. One has also tested the robustness of the algorithm. Since the algorithm is imposed on pixels not on boundaries, this has more influence on the result when some boundaries are missing. If the interface of a small tumor and normal tissue is not detected by US imaging, it is hard to find it by microwave imaging. One has also shown that to retrieve real and imaginary parts in separate fashion can improve the results. Now, further attention should be on presentation of the boundary information from US imaging and attempting to find a way for a better exploitation.

As for joint (fused) inversion of electromagnetic and acoustic data for breast imaging, it is of good potential. Edge-preserving regularization [167] can be performed by introducing auxiliary variables indicating whether or not a pixel is on an edge. Edge markers could be obtained from the last

parameter profile and guide the next optimization as regularization term. Alternate minimization would be used to update acoustic contrast, edge markers and dielectric contrast. Also, increasingly popular convolutional neural netwoks (CNN), now involving a two-stream CNN [168], combining feature maps at a certain level, should produce tissue types, the last CNN layer being a classifier (this is expected to be easier than outputting EM and US parameters at each pixel).

Chapter 6

Joint inversion of microwave and ultrasound data with edge-preserving regularization

This chapter is based on the journal paper *Joint inversion of electromagnetic and acoustic data with edge-preserving regularization for breast imaging*, Y. Qin, T. Rodet, M. Lambert, and D. Lesselier, published in *IEEE Transactions on Computational Imaging*, vol. 7, pp. 349-360, 2021, doi: 10.1109/TCI.2021.3067158. There are some duplicate description in introduction and forward problem. Some notations and layout of the figures are changed. We compared our algorithm with MR-CSI and joint inversion with cross-gradient as regularization where the details can be found in Chapter 4.

6.1 Introduction

Breast cancer is common disease among females. X-ray mammography, as the standard for breast tumor detection, can provide high-resolution images. Yet, patients may suffer from ionizing radiation if too frequent examinations, and discomfort results from breast compression. Besides, the result is highly affected by breast density and exhibits low sensitivity.

Therefore, new imaging modalities with non-ionizing and low-cost features have been developed for breast tumor detection. Microwave imaging, due to the high contrast of the dielectric parameters between tumorous and normal tissues, has been investigated for breast imaging [37, 133]. However, images are of low resolution due to the long wavelength of the electromagnetic (EM) wave. In contrast, ultrasound (US) imaging, despite low contrast between different tissues, can provide high-resolution image and structure information [169,170]. To take advantage of both modalities, inversion of electromagnetic and ultrasonic data in simultaneouly- or sequentially-combined fashion is expected fruitful.

Yet such a combination appears to still lack application in the field, beyond recent investigations, like [114] and references therein —possibly at prototype stage [171], with special embedding since within a closed metal chamber.

One way to exploit the pros of each modality is to extract structure information from high-resolution image. The authors have proposed such an approach in [172] based on the edge information. A reflectometric acoustic analysis is run to get the boundaries (possibly blurred) between zones in the breast. This information is employed to guide the smoothness constraint at each pixel: constraint will only be imposed on the pixels which are not on the edges pointed by the ultrasound image. Prior information based on regions is also investigated. After segmentation of high-resolution images, regions of different tissues can be obtained. Such an information can provide a better initial guess of contrast at each pixel with parameters from literature and a finite element discretization for the reconstruction of dielectric parameters [113, 114].

Another way to combine multi-modalities is to invert the data simultaneously. To achieve joint inversion, the physical relation between different parameters can be used and this leads to a unique retrieval of the underlying physical parameter. In [116], petrophysical relation is used for joint inversion of EM and seismic data. However, this option which relies on much *a priori* is not pursued further.

Structure similarity can be employed for joint inversion also. In [118], a Laplacian operator and two thresholds to measure the magnitude of the changes in parameters and minimize the difference of such parameters is investigated. In [119, 120], cross-gradient constraints as the outer product of the gradients of different parameters to force the parameters to change into the same direction are proposed. This method is widely used in geophysics [122–125]. In [126], Joint Total Variation for joint inversion by combining spatial gradients of both parameters as the weighting factor in the regularization term is considered. In [127], a Total-Variation-like regularization operator is to achieve joint inversion of EM and US data by changing the weight factor associated with the variation of the other modality. A review of joint inversion is found, e.g., in [126].

Considering that acoustic and dielectric parameters share discontinuities at the tissue boundaries and vary relatively smoothly within each tissue region, it is possible to constrain smoothness in the same region yet preserve edges at same location for parameters of two modalities to achieve joint inversion. Different functions [48, 173, 174] with edge-preserving property have been used in image reconstruction [175, 176], image restoration [177], image fusion [178] and many other tasks. In edge-preserving regularization [167], usually a nonquadratic function [40–42] is introduced to less severely penalize a large gradient to preserve edges. Duality between nonquadratic criterion and a half-quadratic (HQ) criterion with additional variables is observed, first with binary edge variables [43, 44], then generalized to continuous ones [45, 46].

With the augmented HQ criterion, the nonlinear optimization problem is transformed into a quadratic problem with respect to the original image and a nonquadratic but separable criterion for the edge variables. The problem is optimized by solving a sequence of sub-optimization problems to get the estimate of original image and edge map alternately [150, 179, 180]. With such a regularization, joint inversion can be achieved by introducing the common edge variables for both modalities and the sub-optimization problems are easy to solve.

In the present work, a new joint inversion algorithm of EM and US data is developed in a contrast source inversion (CSI) [58] framework with edge-preserving regularization. Hidden variables to indicate the parameter discontinuities in different directions are introduced, which connects inversions of US and EM data. Edge maps can be computed from the last parameter distribution and help the optimization at the next step. Alternate minimization is used to update acoustic contrast, edge maps and electromagnetic contrast.

In the numerical experiments, a pending breast —again, underlining that this is in contrast with the demanding compressed breast of X-ray mammography— immersed within an unbounded coupling medium is assumed. Several acoustic frequencies in the sub-MHz range (then associated to mm local wavelengths) provide a better estimation of edges, while a single electromagnetic frequency (1 GHz associated to cm local wavelengths) takes advantage of the high contrast while achieving enough penetration into the breast.

A 4-zone 2-D model of breast (skin, fatty, fibroglandular and tumor tissues) and four MRI-derived models from the UWCEM Breast Phantom Repository [134] are used to validate the algorithm, with application of a standard Method of Moments (Fast Fourier Transform being implemented in both forward and inverse problems to speed up the computations).

The contribution is organized as follows. In Section 6.2 the formulation of the forward problem is presented. In Section 6.3, the joint inversion algorithm is detailed. In Section 6.4 numerical experiments on breast phantoms are proposed. A brief conclusion follows in 6.5.

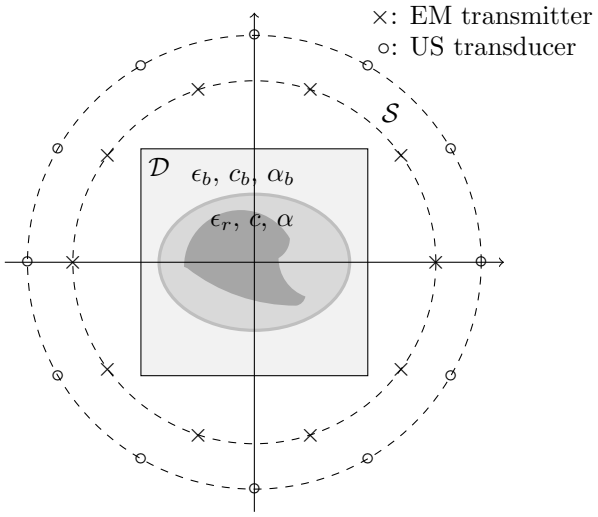

Figure 6.1: Schematic diagram of configuration of two modalities working in a multistatic way

6.2 Forward problem

One considers a two-dimensional case. Time-harmonic waves are assumed with time dependence $\exp(-i\omega t)$ for both acoustic and electromagnetic cases. The modeled breast is located inside a domain of interest (DoI) $\mathcal{D}$. The known background medium is characterized by its complex relative permittivity ϵ_b, permeability μ_b, and wavenumber $k_b^{\text{em}} = \omega\sqrt{\epsilon_0\epsilon_b\mu_b}$ in electromagnetics, and its speed of sound c_b, attenuation α_b, and wavenumber $k_b^{\text{ac}} = \omega/c_b + i\alpha_b$ in acoustics. Permeability and density are taken constant within the DoI. The unknown parameters are complex relative permittivity $\epsilon_r(\mathbf{r}) = \epsilon_r'(\mathbf{r}) + i\epsilon_r''(\mathbf{r})$, sound speed $c(\mathbf{r})$ and attenuation $\alpha(\mathbf{r})$. For each imaging modality, N_i probes are evenly located at $\mathbf{r}_v'$, $v = 1, 2, \ldots, N_i$ on a circle $\mathcal{S}$, as shown in Figure 6.1. Each illuminates the DoI and scattered fields are collected by all.

To solve the problem numerically, $\mathcal{D}$ is discretized into $M = N_x \times N_y$ small cells centered at $\mathbf{r}_m$, $m = 1, 2, \ldots, M$. A pulse-basis point-matching method of moments (MoM) is employed. Every square cell is approximated by a small disk with same area and with equivalent radius R. For the pth incidence, the fields inside $\mathcal{D}$ and on $\mathcal{S}$ can be described as

$$\mathbf{F}_p^{\mathbf{t}} = \mathbf{F}_p^{\mathbf{i}} + \mathbf{G_d X F}_p^{\mathbf{t}} \tag{6.1}$$

$$\mathbf{F}_p^{\mathbf{s}} = \mathbf{G_s X F}_p^{\mathbf{t}} \tag{6.2}$$

where F is the pressure field P or the electric field E. Superscripts "i" and "t" denote incident and total field, i.e., the field inside $\mathcal{D}$ without and with breast, respectively. In this case, $\mathbf{F}_p^{\mathbf{t/i}}$ is a $M \times 1$ vector with $\mathbf{F}_p^{\mathbf{t/i}} = [F_p^{t/i}(\mathbf{r}_1), \ldots, F_p^{t/i}(\mathbf{r}_M)]^T$ where superscript "T" denotes transpose. $\mathbf{F}_p^{\mathbf{s}}$ is a $N_i \times 1$ vector representing the scattered field collected by the receivers as $\mathbf{F}_p^{\mathbf{s}} = [F_p^s(\mathbf{r}_1'), \ldots, F_p^s(\mathbf{r}_{N_i}')]^T$. $\mathbf{X}$ is a matrix with diagonal entry representing the contrast at different location, as $\text{diag}(\mathbf{X}) = \boldsymbol{\chi}$. Acoustic and electromagnetic contrasts read as

$$\chi^{\text{ac}}(\mathbf{r}) = \frac{(k^{\text{ac}}(\mathbf{r}))^2 - (k_b^{\text{ac}})^2}{(k_b^{\text{ac}})^2} \tag{6.3}$$

$$\chi^{\text{em}}(\mathbf{r}) = \frac{(k^{\text{em}}(\mathbf{r}))^2 - (k_b^{\text{em}})^2}{(k_b^{\text{em}})^2} \tag{6.4}$$

$M \times 1$ vector $\boldsymbol{\chi}$ is the discrete form of χ as $\boldsymbol{\chi} = [\chi(\mathbf{r}_1), \ldots, \chi(\mathbf{r}_M)]^T$.

$\mathbf{G_d}$ is a $M \times M$ matrix with element

$$[\mathbf{G_d}]_{m,m'} = \begin{cases} \dfrac{ik_b\pi R}{2} \mathrm{J}_1(k_b R)\, \mathrm{H}_0^{(1)}(k_b|\mathbf{r}_m - \mathbf{r}_{m'}|), m \neq m' \\ \dfrac{ik_b\pi R}{2} \mathrm{H}_1^{(1)}(k_b R) - 1, \text{otherwise} \end{cases} \tag{6.5}$$

where J_1 is the 1st-kind Bessel function, $\mathrm{H}_1^{(1)}$ the 1st-kind 1st-order Hankel function and $\mathrm{H}_0^{(1)}$ the 1st-kind 0th-order one. The $N_i \times M$ matrix $\mathbf{G_s}$ is

$$[\mathbf{G_s}]_{v,m} = \frac{ik_b\pi R}{2} \mathrm{J}_1(k_b R)\, \mathrm{H}_0^{(1)}(k_b|\mathbf{r}'_v - \mathbf{r}_m|) \tag{6.6}$$

Letting the contrast source be

$$J_p(\mathbf{r}) = \chi(\mathbf{r}) F_p^t(\mathbf{r}) \tag{6.7}$$

and multiplying by χ on both sides of previous equations, source-type equations in the discrete form follow as

$$\mathbf{J}_p = \mathbf{X}\mathbf{F}_p^{\mathbf{i}} + \mathbf{X}\mathbf{G_d}\mathbf{J}_p \tag{6.8}$$

$$\mathbf{F}_p^{\mathbf{s}} = \mathbf{G_s}\mathbf{J}_p \tag{6.9}$$

Based on those, a contrast source inversion (CSI) method can be developed and used in the proposed imaging procedure.

6.3 Inversion algorithm

6.3.1 Deterministic edge-preserving regularization

Here, the edge-preserving regularization proposed in [167] is followed and only the main steps are shown (for further details and demonstrations, refer to the latter). Edge-preserving regularization enables to combine inversions of acoustic and electromagnetic data once assumed that discontinuities of corresponding properties occur at same locations. The regularization is imposed on the spatial gradients of the contrast. In this work, the first-order difference in horizontal, vertical and two diagonal directions are used and calculated as

$$[\mathbf{d}_1]_{i,j} = \chi_{i,j} - \chi_{i,j+1} \tag{6.10}$$

$$[\mathbf{d}_2]_{i,j} = \chi_{i,j} - \chi_{i+1,j} \tag{6.11}$$

$$[\mathbf{d}_3]_{i,j} = (\chi_{i,j} - \chi_{i+1,j+1})/\sqrt{2} \tag{6.12}$$

$$[\mathbf{d}_4]_{i,j} = (\chi_{i,j} - \chi_{x+1,y-1})/\sqrt{2} \tag{6.13}$$

with $[d_u]_{i,j}$, $u = 1, 2, 3, 4$, the spatial gradients for location (i, j). For convenience, the above equations are written in matrix vector form as

$$\mathbf{D}_u\boldsymbol{\chi} = \mathbf{d}_u \tag{6.14}$$

with $\mathbf{D}_u$, $u = 1, 2, 3, 4$, the difference operators. Regularization is enforced separately on the real and imaginary parts of the spatial gradients at all pixels as

$$Q_{\mathrm{EP}}(\boldsymbol{\chi}) = \lambda_r \sum_u \sum_m^M \varphi\left(\frac{[\mathbf{D}_u \Re\{\boldsymbol{\chi}\}]_m}{\delta_r}\right) + \lambda_i \sum_u \sum_m \varphi\left(\frac{[\mathbf{D}_u \Im\{\boldsymbol{\chi}\}]_m}{\delta_i}\right) \tag{6.15}$$

Here, λ_r and λ_i are regularization parameters, and δ_r and δ_i are scaling parameters to determine the value of the discontinuity that can be detected. $\varphi(\cdot)$ is the potential function.

To simplify the minimization process, half-quadratic regularization [46] is carried out by introducing some auxiliary variables and the problem is transformed into $\mathrm{Min}_{\boldsymbol{\chi}} Q_{\mathrm{EP}}(\boldsymbol{\chi}) = \mathrm{Min}_{\boldsymbol{\chi},\mathbf{b}} Q^*_{\mathrm{EP}}(\boldsymbol{\chi}, \mathbf{b})$, with

$$\begin{aligned} Q^*_{\mathrm{EP}}(\boldsymbol{\chi}, \mathbf{b}) = \lambda_r \sum_u \sum_m [b_u]_m \left(\frac{[\mathbf{D}_u \Re\{\boldsymbol{\chi}\}]_m}{\delta_r} \right)^2 + \psi\left([b_u]_m\right) \\ + \lambda_i \sum_u \sum_m [b_u]_m \left(\frac{[\mathbf{D}_u \Im\{\boldsymbol{\chi}\}]_m}{\delta_i} \right)^2 + \psi\left([b_u]_m\right) \end{aligned} \tag{6.16}$$

Additional variables $\mathbf{b} = [\mathbf{b}_1, \mathbf{b}_2, \mathbf{b}_3, \mathbf{b}_4]$ indicate if the point is at an edge in detecting directions and their values are continuous in $[0, 1]$ with a small value for large gradients and vice versa. For the real and imaginary parts, they share the same edge markers. $\psi(\cdot)$ is a function determined by the potential function $\varphi(\cdot)$. When the contrast $\boldsymbol{\chi}$ is fixed, the value of $\mathbf{b}$ can be calculated directly.

The potential function is chosen as $\varphi(t) = t^2/(1+t^2)$ [42] and correspondingly $\psi(t) = t - 2\sqrt{t} + 1$. Even though the potential function is not convex, it can give a satisfactory imaging result in our experiment, also observed in [167].

6.3.2 Inversion of electromagnetic data with edge-preserving regularization

To better illustrate the joint algorithm, separate inversion with edge-preserving regularization is presented, taking the EM case as an example. For simplicity, the superscript "em" is omitted and $\mathbf{J} = [\mathbf{J}_1, \ldots, \mathbf{J}_{N_i}]$ is used. Based on CSI, the cost function at the nth iteration is defined as

$$Q(\boldsymbol{\chi}, \mathbf{J}, \mathbf{b}) = Q_d(\mathbf{J}) + Q_s(\mathbf{J}, \boldsymbol{\chi}) + Q^*_{\mathrm{EP}}(\boldsymbol{\chi}, \mathbf{b}) \tag{6.17}$$

with the normalized data equation and state equation errors being

$$Q_d = \frac{\sum_{p=1}^{N_i} \|\mathbf{E}^{\mathbf{s}}_p - \mathbf{G}_{\mathbf{s}} \mathbf{J}_p\|^2}{\sum_{p=1}^{N_i} \|\mathbf{E}^{\mathbf{s}}_p\|^2} \tag{6.18}$$

$$Q_s = \frac{\sum_{p=1}^{N_i} \|\mathbf{X}\mathbf{E}^{\mathbf{i}}_p + \mathbf{X}\mathbf{G}_{\mathbf{d}}\mathbf{J}_p - \mathbf{J}_p\|^2}{\sum_{p=1}^{N_i} \|\mathbf{X}^{(n-1)}\mathbf{E}^{\mathbf{i}}_p\|^2} \tag{6.19}$$

where $\boldsymbol{\chi}^{(n-1)}$ is the reconstruction result at the $(n-1)$th iteration.

To solve the above, the optimization procedures in [167] and [49] are followed and alternate minimization is run. The optimization procedure is summarized in Algorithm 7.

Algorithm 7 Separate inversion with edge-preserving regularization

Input: $\mathbf{E}^{\mathbf{s}}_p$, $\mathbf{E}^{\mathbf{i}}_p$, $p = 1, \ldots, N_i$, $\mathbf{G}_{\mathbf{s}}$, $\mathbf{G}_{\mathbf{d}}$, regularization parameter λ_r, λ_i, δ_r, δ_i
Initialization: $\mathbf{J}^{(0)}$, $\boldsymbol{\chi}^{(0)}$, step $l = 0$, iteration $n = 0$
repeat
  $l = l + 1$
  repeat
    $n = n + 1$
    With $\boldsymbol{\chi}^{(n-1)}$ and $\mathbf{b}^{(l-1)}$, update $\mathbf{J}$ by Equation (6.21)
    With $\mathbf{J}^{(n)}$ and $\mathbf{b}^{(l-1)}$, update $\boldsymbol{\chi}$ by Equation (6.22, 6.23)
  until a stopping criterion is satisfied
  With $\mathbf{J}^{(n)}$ and $\boldsymbol{\chi}^{(n)}$, update $\mathbf{b}$ by Equation (6.27)
until a stopping criterion is satisfied
Output: $\boldsymbol{\chi}$, $\mathbf{b}_1$, $\mathbf{b}_2$, $\mathbf{b}_3$, $\mathbf{b}_4$, $\mathbf{J}$

update J

At lth step, nth iteration, $\mathbf{J}$ is updated by minimizing $Q = Q_d(\mathbf{J}) + Q_s(\mathbf{J}, \boldsymbol{\chi}^{(n-1)})$, which can be solved by gradient-based optimization methods. The partial gradient w.r.t. $\mathbf{J}_p$ is

$$\frac{\partial Q}{\partial \mathbf{J}_p} = -\frac{\mathbf{G}_\mathbf{s}^\dagger \boldsymbol{\rho}_p^{(n-1)}}{\sum_{p=1}^{N_i} \|\mathbf{E}_p^\mathbf{s}\|^2} - \frac{\mathbf{o}_p^{(n-1)} - \mathbf{G}_\mathbf{d}^\dagger [\mathbf{X}^{(n-1)}]^\dagger \mathbf{o}_p^{(n-1)}}{\sum_{p=1}^{N_i} \|\mathbf{X}^{(n-1)} \mathbf{E}_p^\mathbf{i}\|^2} \tag{6.20}$$

where superscript '†' denotes conjugate transpose. $\mathbf{o}_p^{(n-1)} = \mathbf{X}^{(n-1)} \mathbf{E}_p^\mathbf{i} + \mathbf{X}^{(n-1)} \mathbf{G}_\mathbf{d} \mathbf{J}_p^{(n-1)} - \mathbf{J}_p^{(n-1)}$, and $\boldsymbol{\rho}_p^{(n-1)} = \mathbf{E}_p^\mathbf{s} - \mathbf{G}_\mathbf{s} \mathbf{J}_p^{(n-1)}$.

With such a gradient, $\mathbf{J}_p$ is updated with the conjugate gradient method using the Polak-Ribière search direction as

$$\mathbf{J}_p^{(n)} = \mathbf{J}_p^{(n-1)} + \beta^{(n)} \mathbf{v}_{J_p}^{(n)} \tag{6.21}$$

where $\mathbf{v}_{J_p}^{(n)}$ is the search direction and $\beta^{(n)}$ the step size. More details are found in [49].

update $\boldsymbol{\chi}$

$\boldsymbol{\chi}$ is updated directly by minimizing $Q = Q_s(\mathbf{J}^{(n)}, \boldsymbol{\chi}) + Q_{EP}^*(\boldsymbol{\chi}, \mathbf{b}^{(l-1)})$. The solution can be obtained directly by letting $\partial Q / \partial \Re\{\boldsymbol{\chi}\} = 0$ and $\partial Q / \partial \Im\{\boldsymbol{\chi}\} = 0$, given as

$$\Re\{\boldsymbol{\chi}^{(n)}\} = (\mathbf{H}^{(n)} + \lambda_r \boldsymbol{\Delta}^{(l-1)} / \delta_r^2)^{-1} \Re\{\mathbf{z}^{(n)}\} \tag{6.22}$$

$$\Im\{\boldsymbol{\chi}^{(n)}\} = (\mathbf{H}^{(n)} + \lambda_i \boldsymbol{\Delta}^{(l-1)} / \delta_i^2)^{-1} \Im\{\mathbf{z}^{(n)}\} \tag{6.23}$$

where $\mathbf{H}$ is a diagonal matrix with mth diagonal entry

$$\mathbf{H}^{(n)}(m,m) = \frac{\sum_p \|[[\mathbf{E}_p^\mathbf{t}]^{(n)}]_m\|^2}{\sum_p \|\mathbf{X}^{(n-1)} \mathbf{E}_p^\mathbf{i}\|^2} \tag{6.24}$$

with total field $[\mathbf{E}_p^\mathbf{t}]^{(n)} = \mathbf{E}_p^\mathbf{i} + \mathbf{G}_\mathbf{d} \mathbf{J}_p^{(n)}$. $\mathbf{z}$ is a vector with mth entry

$$z_m^{(n)} = \frac{\sum_p \overline{([[\mathbf{E}_p^\mathbf{t}]^{(n)}]_m)} [\mathbf{J}_p^{(n)}]_m}{\sum_p \|\mathbf{X}^{(n-1)} \mathbf{E}_p^\mathbf{i}\|^2} \tag{6.25}$$

and $\boldsymbol{\Delta}$ is a matrix calculated by

$$\boldsymbol{\Delta}^{(l-1)} = \sum_u (\mathbf{D}_u)^T \operatorname{diag}(\mathbf{b}_u^{(l-1)}) \mathbf{D}_u \tag{6.26}$$

update b

At the end of lth step, $\mathbf{b}$ is updated by minimizing $Q = Q_{EP}^*(\boldsymbol{\chi}^{(n)}, \mathbf{b})$. To remind, the potential function is $\varphi(t) = t^2/(1+t^2)$ and correspondingly $\psi(t) = t - 2\sqrt{t} + 1$. Letting $\partial Q / \partial \bar{b}_u = 0$, every element of $\bar{b}_u$ is obtained by

$$[b_u^{(l)}]_m = \left(\frac{\lambda_r + \lambda_i}{\lambda_r + \lambda_i + [L_u]_m} \right)^2 \tag{6.27}$$

where $\mathbf{L}_u$ is a vector with mth element

$$[L_u]_m = \lambda_r \left(\frac{[\mathbf{D}_u \Re\{\boldsymbol{\chi}^{(n)}\}]_m}{\delta_r} \right)^2 + \lambda_i \left(\frac{[\mathbf{D}_u \Im\{\boldsymbol{\chi}^{(n)}\}]_m}{\delta_i} \right)^2 \tag{6.28}$$

In this work, initial guesses of $\mathbf{J}$ and $\boldsymbol{\chi}$ are obtained by backpropagation [151]. The above algorithm can be employed also in the acoustic case, by changing electric field E and dielectric contrast $\boldsymbol{\chi}^{\mathrm{em}}$ to pressure field P and acoustic contrast $\boldsymbol{\chi}^{\mathrm{ac}}$ and changing regularization parameters $\lambda_{r/i}^{\mathrm{em}}$, $\delta_{r/i}^{\mathrm{em}}$ to $\lambda_{r/i}^{\mathrm{ac}}$ and $\delta_{r/i}^{\mathrm{ac}}$ accordingly.

6.3.3 Joint inversion of electromagnetic and acoustic data

Based on the assumption that dielectric and acoustic parameters share the same distribution of discontinuity, $\mathbf{b}$ indicates edges for both parameters and is used to combine the modalities. The cost function for joint inversion is written as

$$\begin{aligned} Q = & Q_d(\mathbf{J}^{\mathrm{em}}) + Q_s(\mathbf{J}^{\mathrm{em}}, \boldsymbol{\chi}^{\mathrm{em}}) + Q^*_{\mathrm{EP}}(\boldsymbol{\chi}^{\mathrm{em}}, \mathbf{b}) \\ & + \gamma \left(Q_d(\mathbf{J}^{\mathrm{ac}}) + Q_s(\mathbf{J}^{\mathrm{ac}}, \boldsymbol{\chi}^{\mathrm{ac}}) + Q^*_{\mathrm{EP}}(\boldsymbol{\chi}^{\mathrm{ac}}, \mathbf{b}) \right) \end{aligned} \tag{6.29}$$

The regularization parameter γ is to balance the weight of acoustic and electromagnetic contrasts in calculating $\mathbf{b}$.

Similar with separate inversion, alternate minimization is employed. In the optimization procedure, the cost function w.r.t. acoustic data is minimized first to obtain an initial estimate of $\mathbf{b}$ to exhibit the discontinuities since acoustic imaging can indeed capture the fine structures. This value of $\mathbf{b}$ is then used to obtain the electromagnetic image. Due to the large wavelength, the retrieval will be smoother, thus edges denoted by acoustic parameters caused by noise can be eliminated. The new $\mathbf{b}$ is used in acoustic imaging again, and one works this way until convergence.

The joint inversion algorithm does not change the update of contrast current and contrast for both modalities compared with the separate inversion. Only the update of $\mathbf{b}$ needs modification. At each step, $\mathbf{b}$ is updated twice after the update of $\boldsymbol{\chi}^{\mathrm{ac}}$ and $\boldsymbol{\chi}^{\mathrm{em}}$, respectively. $\mathbf{b}$ is updated by minimizing $Q = Q^*_{\mathrm{EP}}(\boldsymbol{\chi}^{\mathrm{ac}}, \mathbf{b}) + \gamma Q^*_{\mathrm{EP}}(\boldsymbol{\chi}^{\mathrm{em}}, \mathbf{b})$. The solution is

$$[b_u]_m = \left(\frac{\gamma(\lambda_r^{\mathrm{em}} + \lambda_i^{\mathrm{em}}) + \lambda_r^{\mathrm{ac}} + \lambda_i^{\mathrm{ac}}}{\gamma \left(\lambda_r^{\mathrm{em}} + \lambda_i^{\mathrm{em}} + [L_u^{\mathrm{em}}]_m \right) + \lambda_r^{\mathrm{ac}} + \lambda_i^{\mathrm{ac}} + [L_u^{\mathrm{ac}}]_m} \right)^2 \tag{6.30}$$

where L_u is given in Equation (6.28) with corresponding regularization parameters and contrast.

Notice that $\gamma = 0$ for the first update of $\mathbf{b}$, which means that only acoustic parameters are used at the start.

The whole optimization procedure is sketched in Algorithm 8. One stops the update of contrast when the relative difference in contrast is less than some threshold θ and one stops the whole optimization when the change of electromagnetic contrast in two successive steps is less than θ, or when the maximum iteration number is reached.

Algorithm 8 Joint inversion with edge-preserving regularization

Input: $\mathbf{E}^{\mathbf{s}}_p$, $\mathbf{E}^{\mathbf{i}}_p$, $\mathbf{P}^{\mathbf{s}}_p$, $\mathbf{P}^{\mathbf{i}}_p$, $p = 1, \ldots, N_i$, $\mathbf{G}^{\mathrm{em}}_{\mathbf{s}}$, $\mathbf{G}^{\mathrm{em}}_{\mathbf{d}}$, $\mathbf{G}^{\mathrm{ac}}_{\mathbf{s}}$, $\mathbf{G}^{\mathrm{ac}}_{\mathbf{d}}$, regularization parameters γ, λ_r^{ac}, λ_i^{ac}, λ_r^{em}, λ_i^{em}, δ_r^{ac}, δ_i^{ac}, δ_r^{em}, δ_i^{em}
Initialization: $\boldsymbol{\chi}^{\mathrm{ac}(0)}$, $\boldsymbol{\chi}^{\mathrm{em}(0)}$, $\mathbf{J}^{\mathrm{ac}(0)}$, $\mathbf{J}^{\mathrm{em}(0)}$
repeat
  repeat
    Update $\mathbf{J}^{\mathrm{ac}}$ with Equation (6.21)
    Update $\boldsymbol{\chi}^{\mathrm{ac}}$ with Equations (6.22) and (6.23)
  until a stopping criterion is satisfied
  Update $\mathbf{b}_1$, $\mathbf{b}_2$, $\mathbf{b}_3$, $\mathbf{b}_4$, with Equation (6.30)
  repeat
    Update $\mathbf{J}^{\mathrm{em}}$ with Equation (6.21)
    Update $\boldsymbol{\chi}^{\mathrm{em}}$ with Equations (6.22) and (6.23)
  until a stopping criterion is satisfied
  Update $\mathbf{b}_1$, $\mathbf{b}_2$, $\mathbf{b}_3$, $\mathbf{b}_4$, with Equation (6.30)
until a stopping criterion is satisfied
Output $\boldsymbol{\chi}^{\mathrm{ac}}$, $\boldsymbol{\chi}^{\mathrm{em}}$, $\mathbf{b}_1$, $\mathbf{b}_2$, $\mathbf{b}_3$, $\mathbf{b}_4$, $\mathbf{J}^{\mathrm{ac}}$, $\mathbf{J}^{\mathrm{em}}$

6.4 Numerical experiments

In this section, numerical experiments are conducted on several breast models. First the algorithm is validated on a synthetic model with regular tissue shapes, then is investigated on three realistic breast models which have more complicated inner structures. All simulations are run on Matlab R2018b.

In the simulation, for the electromagnetic case, 40 antennas are evenly set on a circle, working as sources and receivers simultaneously at a single 1 GHz operation frequency. For the acoustic case, 64 transducers operate at three frequencies, namely 100, 150 and 200 kHz, to get a better estimate of the structure in the first step. This setting is in effect close to the one recently put forth in [181] save only a single US frequency and not three as of now. Considering the acoustic wavenumber $k^{\text{ac}} = \omega/c + i\alpha$ wherein attenuation $\alpha = \alpha_0 f$, α_0 the attenuation at frequency f =1 MHz (here a linear dependence is assumed [138]), the approximation can be made that the acoustic contrast does not change with frequency.

The DoI is discretized by MoM into a grid which is at least twice finer than the one used in inversion. The synthetic data are obtained by solving the forward problem with two steps: first, the contrast current is calculated by solving Equation 6.8 with a conjugate-gradient fast Fourier transform (CG-FFT) algorithm, then, the scattered field is obtained directly based on Equation 6.9.

Additive Gaussian noise is added to the data (in effect, to the scattered fields), which is frequently made by many authors and handy as a choice yet rather simple if to consider, e.g., laboratory-controlled experiments at a later stage possibly involving motions of sources and receivers (or the breast itself though pending freely) vs. nominal locations, misplacements, and obviously less simple radiation patterns of the devices —this is beyond our scope here, and other chapters, as emphasizing first and foremost proofs of concept and algorithmics.

For the inversion, the breast is assumed known to be in a given disk. The reconstruction is confined within this region and pixels outside it are restricted to have the same dielectric and acoustic properties as those of the coupling medium. Besides, the dielectric and acoustic parameters are bounded as $1 \leqslant \epsilon_r' \leqslant 70$, $0 \leqslant \epsilon_r'' \leqslant 40$, $1200 \leqslant c \leqslant 1800$, and $0 \leqslant \alpha \leqslant 5$ at each iteration by a projection method.

Two separate inversion algorithms and one joint inversion algorithms are run for comparison with the just derived JCSI-EP: CSI with deterministic edge-preserving regularization (CSI-EP) described in Section 6.3.2, CSI with multiplicative weighted L2 total variation (MR-CSI) [50, 152] and cross-gradient function [125] as a joint inversion method incorporated in CSI (JCSI-CG).

Imaging quality is evaluated in quantitative fashion via the relative error between reconstructed parameters $\boldsymbol{\zeta}$ and ground truth $\boldsymbol{\xi}$ calculated as

$$\text{Err} = \frac{\|\boldsymbol{\zeta} - \boldsymbol{\xi}\|_2}{\|\boldsymbol{\xi}\|_2} \tag{6.31}$$

and via the Structural Similarity (SSIM) Index [182]

$$\text{SSIM} = \frac{(2\mu_\zeta\mu_\xi + C_1)(2\sigma_{\zeta\xi} + C_2)}{(\mu_\zeta^2 + \mu_\xi^2 + C_1)(\sigma_\zeta^2 + \sigma_\xi^2 + C_2)} \tag{6.32}$$

where μ_ζ and σ_ζ are the mean and standard deviation of $\boldsymbol{\zeta}$, respectively. $\sigma_{\zeta\xi}$ is the covariance between $\boldsymbol{\zeta}$ and $\boldsymbol{\xi}$. $C_1 = (K_1 L)^2$ and $C_2 = (K_2 L)^2$ are used to avoid instability. In our calculation, $K_1 = 0.01$, $K_2 = 0.03$, $L = 70$, 40, 600 and 5 are set for ϵ_r', ϵ_r'', c and α respectively.

6.4.1 Reconstruction of synthetic breast model

Model 1 is a simple synthetic breast model which consists of skin, fatty, fibroconnective/glandular and tumorous tissues. Each tissue type has regular shape and uniform dielectric property. The skin thickness is 2 mm and the tumor is of 6 mm diameter. In this model, the DoI is 0.1 m × 0.1 m-sized.

Acoustic and dielectric parameters of tissue types [133,138,139] and coupling medium are in Table 6.1.

Table 6.1: Acoustic sound speed in m/s and attenuation in dB/MHz/cm, and relative dielectric permittivity ϵ_r at 1 GHz, for different tissues and background.

Tissue/Media	sound speed c	attenuation α_0	permittivity ϵ_r
skin	1615	0.35	$39.8816 + 15.6363i$
fatty	1478	0.48	$4.7950 + 0.8185i$
glandular	1510	0.75	$48.8218 + 15.8941i$
tumor	1548	1.45	$56.2672 + 17.9652i$
background	1568	0.056	$10 + 4i$

Figure 6.2 (1st column) shows the distribution of sound speed, attenuation, real and imaginary parts of the relative permittivity of this model.

The EM antennas are set on a circle of 0.057 m radius, the US transducers on one of 0.08 m radius. The DoI is discretized into 200×200 pixels for the electromagnetic case and 350×350 pixels for the acoustic one. Gaussian noise with SNR = 30 dB is added to the synthetic data.

For the inversion, the domain is discretized into 80×80 pixels. The breast is assumed within a disk of 0.045 m radius (the radius of the outer boundary of the model is 0.042 m).

The hyperparameter δ controls the discontinuity that can be detected, λ is to balance the trade-off between data and regularization terms, and γ to control the weight of acoustic and electromagnetic data when updating edge maps. Numerical experimentation provides their values as follows.

δ is chosen as $\delta_r^{\text{ac}} = \delta_i^{\text{ac}} = 5 \times 10^{-3}$, $\delta_r^{\text{em}} = 10^{-1}$ and $\delta_i^{\text{em}} = 10^{-2}$. $\delta_i^{\text{ac}} = \delta_r^{\text{ac}}$ is as such since the reconstruction of attenuation is usually not satisfactory and one attempts to decrease the effect of attenuation on calculating $\mathbf{b}$. $\lambda_r = \lambda_i$ is simply set for both acoustic and electromagnetic cases with $\lambda^{\text{ac}} = 5 \times 10^{-7}$ and $\lambda^{\text{em}} = 5 \times 10^{-7}$. $\gamma = 0.5$ is set to give comparable weights to electromagnetic and acoustic contrasts. As for the threshold θ in the stopping criterion, it must be small enough to maintain accuracy, yet not too small to avoid lengthy computations, and it is taken as 10^{-3}.

Let us recognize that choices of regularizers can be seen as rather ad hoc, yet they are based on thorough numerical experiments, and also they are expected to work in a broad window around the chosen values —the Bayesian solution, later one, is to free us from possibly arbitrarily chosen values.

Figure 6.2 (2nd and 3rd columns) shows the separate inversion results of two modalities by CSI-EP with the same regularization parameter values and MR-CSI. The speed of sound can be well retrieved by both algorithms, yet the dielectric parameters are more difficult to estimate while the tumor cannot be seen for either one.

Results of JCSI-CG and the presently proposed JCSI-EP are shown in the 4th and 5th columns. Compared with separate inversion, the tumor can be clearly seen in the real part of dielectric parameter profiles in both joint inversion algorithms and the quality of EM reconstruction is enhanced. Our algorithm also has a better reconstruction result of the imaginary part than JCSI-CG on this model. Besides, the noise is well smoothed.

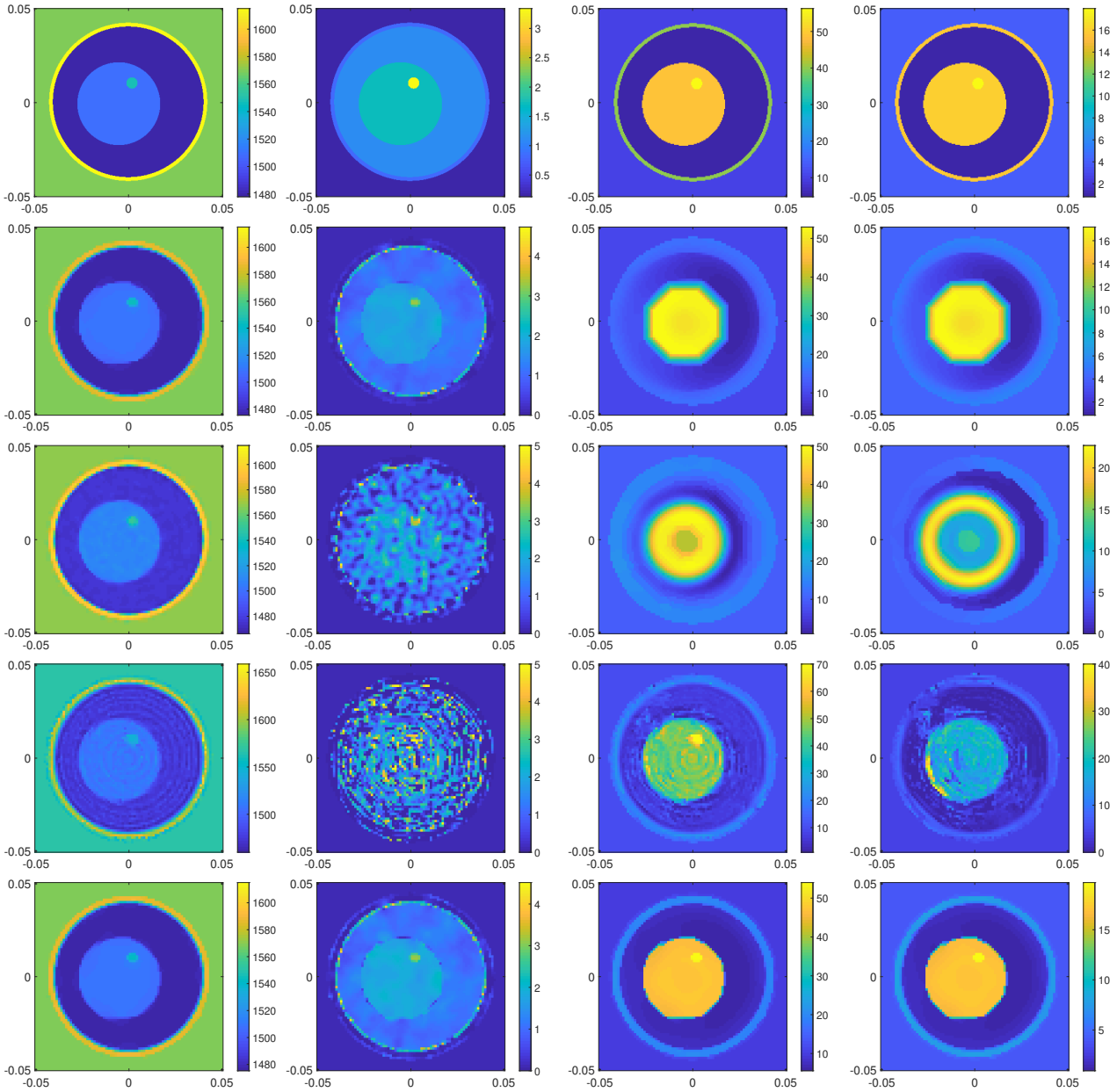

Figure 6.2: Model 1 – Ground truth (1st row), separate reconstruction results of CSI-EP (2nd), MR-CSI (3rd) and joint inversion results of JCSI-CG (4th) and JCSI-EP (5th) with speed of sound c (1st column), attenuation α (2nd), real part ϵ_r' (3rd) and imaginary part ϵ_r'' (4th) of relative permittivity.

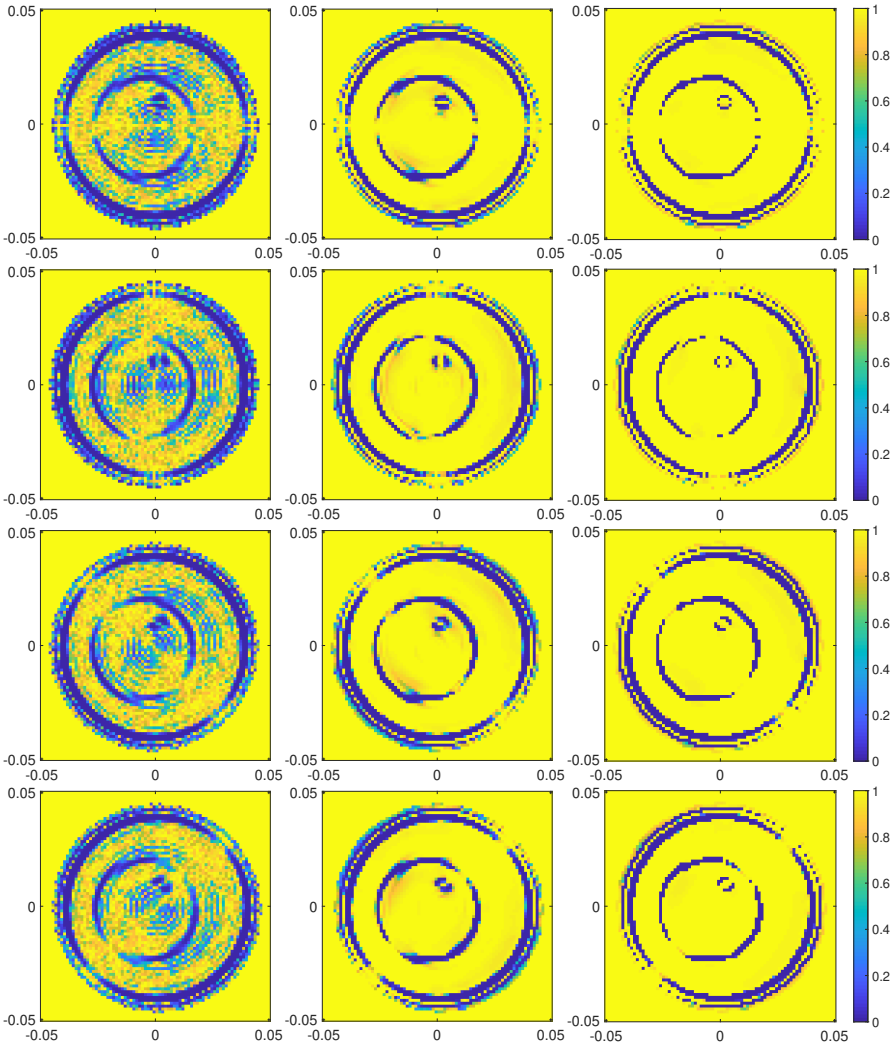

Figure 6.3: Model 1 – Joint reconstruction of edge variables b_1, b_2, b_3 and b_4 (from top to bottom) after 1st, 5th and 40th update (from left to right).

Table 6.2: Model 1 – Imaging quality assessment in reconstruction of acoustic and dielectric parameters

Index	Methods	acoustic parameter		dielectric parameter	
		c	α	ϵ_r'	ϵ_r''
Err	CSI-EP	0.0077	**0.3370**	0.3619	0.4004
	MR-CSI	**0.0061**	0.5653	0.3808	0.7233
	JCSI-CG	0.0080	0.8900	0.2971	0.4596
	JCSI-EP	0.0078	0.3406	**0.2664**	**0.3002**
SSIM	CSI-EP	0.9667	**0.8834**	0.8498	0.8163
	MR-CSI	**0.9794**	0.7237	0.8166	0.5097
	JCSI-CG	0.9649	0.5148	0.9001	0.8077
	JCSI-EP	0.9655	0.8798	**0.9198**	**0.9088**

Figure 6.3 displays the edge variables at different steps of JCSI-EP algorithm. The edges are well retrieved. After the first update, the edge map is not accurate but as the optimization proceeds, the

edges becomes sharper and the noise is smoothed.

The assessment results associated with the algorithms above are shown in Table 6.2. Though acoustic imaging benefits little from joint inversion, it appears that the quality of microwave imaging can be greatly improved. In particular, the proposed algorithm yields a smaller relative error and a higher SSIM value compared with cross-gradient method.

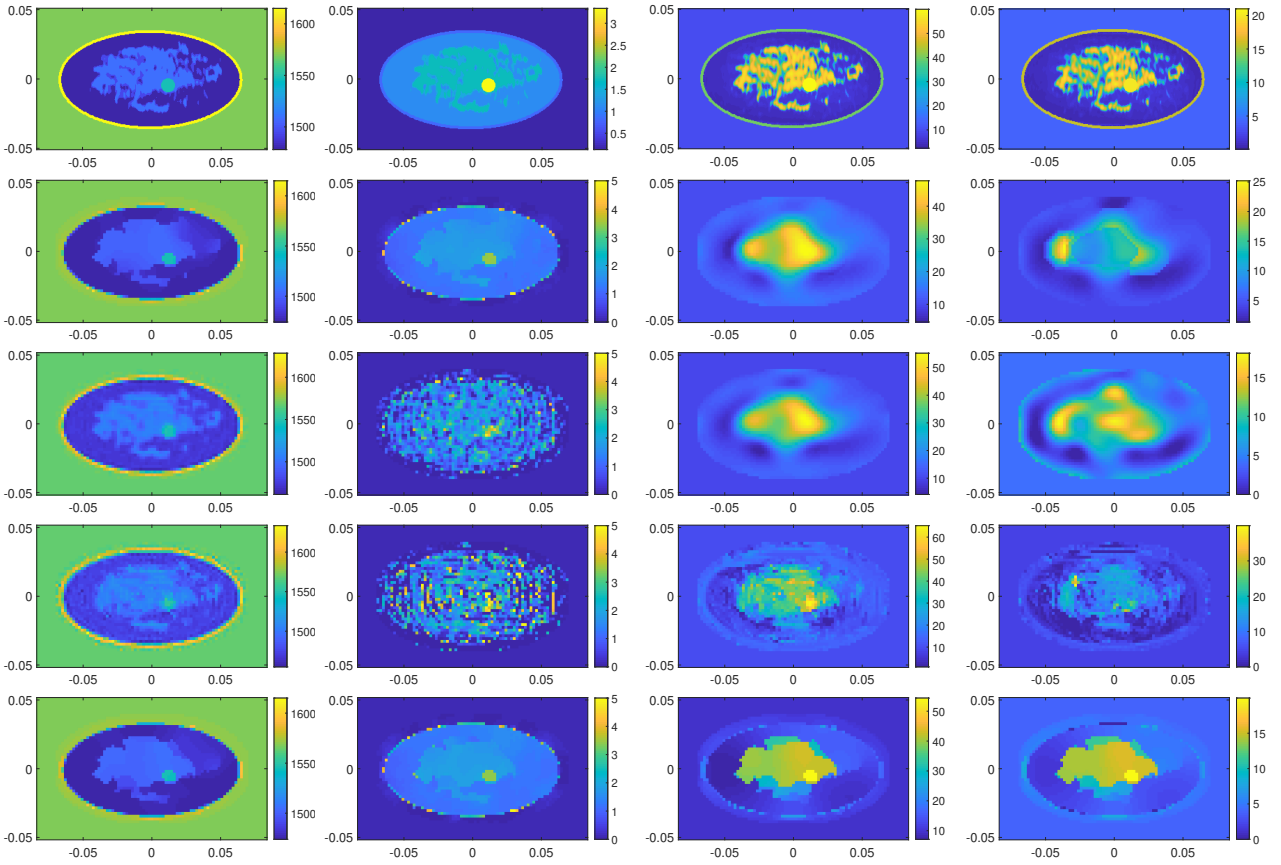

Figure 6.4: Model 2 – Ground truth (1st row), separate reconstruction results of CSI-EP (2nd), MR-CSI (3rd) and joint inversion results of JCSI-CG, JCSI-EP (5th) with speed of sound c (1st column), attenuation α (2nd), real part ϵ_r' (3rd) and imaginary part ϵ_r'' (4th) of relative permittivity.

6.4.2 Reconstruction of realistic breast phantoms

To better validate the proposed approach, experiments are conducted on several more realistic breast models, which are slices extracted from breast phantoms in the UWCEM repository [134] and are categorized in different classes according to radiographic density. The grid size is 0.5 mm and it is used in simulations for generation of synthetic data in both acoustic and electromagnetic cases. The thickness of skin is changed from 1.5 mm to 2 mm. The acoustic parameters are the same as with Model 1 and assigned vs. tissue type of each pixel and the type "transitional" is given the average value of fatty and glandular tissues. The Debye parameters of dielectric properties for normal tissues are from [133]. As for the hypothesized antennas, they are set on a circle of 0.08 m radius and the transducers on one of 0.1 m radius.

To test the resolution of the separate and joint procedures, a synthetic tumor is added into each model and the relative permittivity is chosen as the 75th percentile curve in [131].

For inversion, a cell size of 2 mm is adopted. Some columns or rows of pixels are added as background in the initial breast phantoms to have the numbers of columns and rows a multiple of 4. The

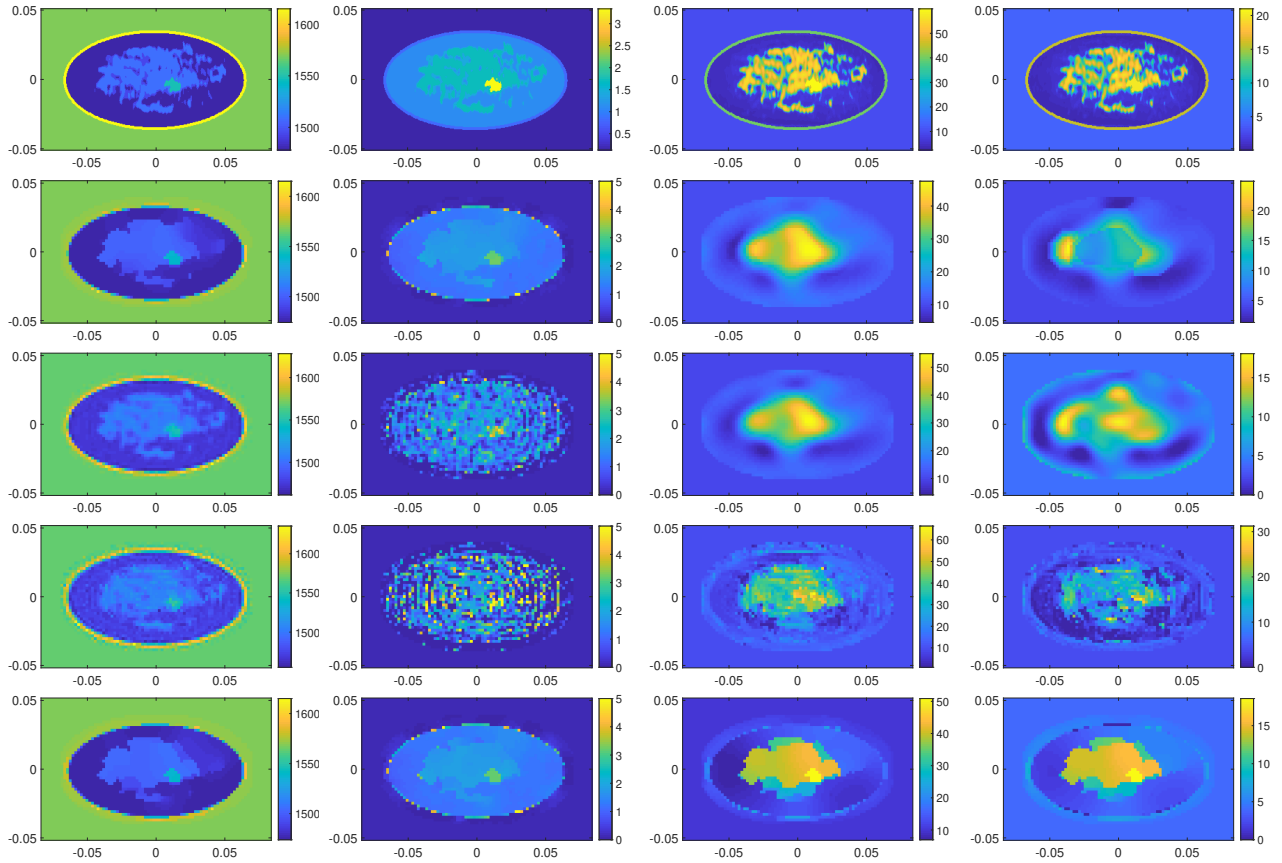

Figure 6.5: Model 3 – Ground truth (1st row), separate reconstruction results of CSI-EP (2nd), MR-CSI (3rd) and joint inversion results of JCSI-CG (4th) and JCSI-EP (5th) with speed of sound c (1st column), attenuation α (2nd), real part ϵ_r' (3rd) and imaginary part ϵ_r'' (4th) of relative permittivity.

region of the breast is also assumed known with a three-pixel margin left.

In this section, δ is kept unchanged as $\delta_r^{\text{ac}} = \delta_i^{\text{ac}} = 5 \times 10^{-3}$, $\delta_r^{\text{em}} = 10^{-1}$ and $\delta_i^{\text{em}} = 10^{-2}$. The regularization parameters are chosen as $\lambda^{\text{em}} = 2 \times 10^{-6}$ and $\lambda^{\text{ac}} = 2 \times 10^{-6}$ for all breast phantoms. The threshold in the stopping criterion is $\theta = 5 \times 10^{-4}$. Two levels of SNR are considered: 30 dB and 10 dB. The effect of γ is studied for different phantoms. Three values of γ are set as $\gamma = 0$, 0.5 and 5.

Class 3 model

The first phantom (ID 080304, slice s_1=150) is heterogeneously dense. Two models are developed from this phantom. The slice contains 332×204 pixels for simulation and 83×51 pixels for inversion. In Model 2, a synthetic 1 cm-diameter tumor at (1.2 cm, -0.5 cm) is inserted while in Model 3, a tumor with an irregular shape is considered at same location.

Figures 6.4 and 6.5 (1st column) show the distributions of acoustic and electromagnetic parameters of these two models. With noise of 30 dB, separate reconstruction results of CSI-EP, MR-CSI and joint inversion results of JCSI-CG and JCSI-EP with $\gamma = 0.5$ for these two models are also shown. Similarly, in separate imaging, the speed of sound can be retrieved well, while the results of dielectric parameters are unsatisfactory. The tumor cannot be identified and the results of these two models are quite similar.

JCSI-CG can image the tumor with a slight distortion in the real part of relative permittivity of Model 2, but in Model 3, the imaging result gets worse and the tumor is almost indistinguishable. Still, the imaginary parts are unsatisfactory and cannot estimate the tissue structures well. In contrast, the

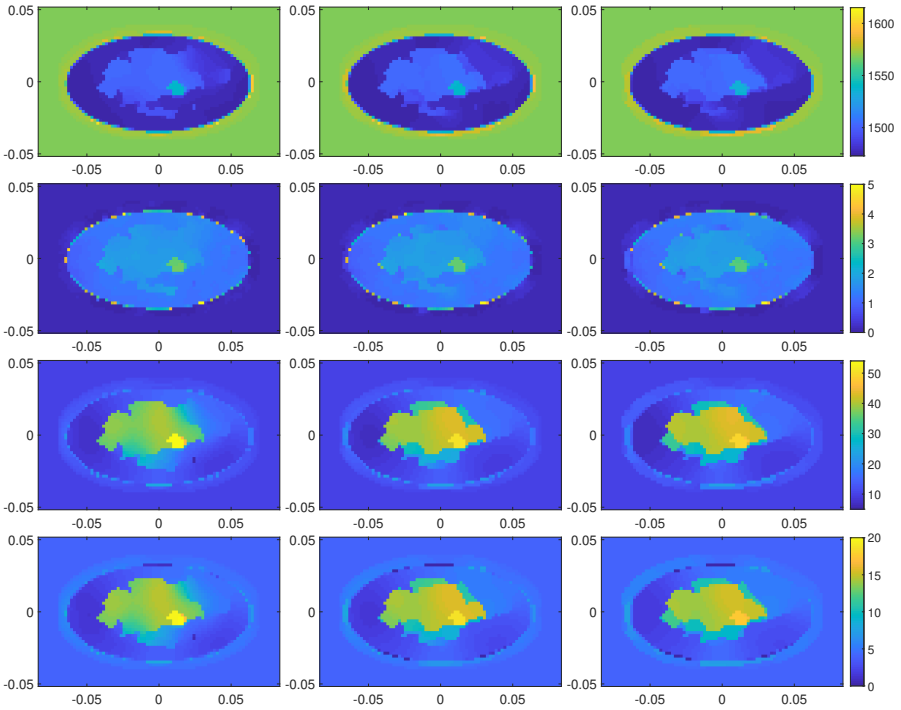

Figure 6.6: Model 3 – Joint reconstruction results of speed of sound c (1st row), attenuation α (2nd), real part ϵ_r' (3rd) and imaginary part ϵ_r'' (4th) of relative permittivity by JCSI-EP with $\gamma = 0$ (left), $\gamma = 0.5$ (middle) and $\gamma = 5$ (right).

tumor can be well identified in all parameters with JCSI-EP for both models. The skin is difficult to image since only one-pixel wide. The difference in the shape of tumor can also be seen when comparing the results of these two models, and the shapes fit the ground truth.

The effect of regularization parameter γ is also investigated. These two models have quite similar results and Figure 6.6 shows the results of Model 3 by JCSI-EP with $\gamma = 0$, 0.5 and 5. As γ increases, the contrast between the tumor and the background becomes lower. The tumor can still be seen in all cases and overall the results are satisfactory.

Table 6.3 and 6.5 show the quantitative assessment of the imaging quality. Joint inversion algorithms have a better reconstruction than separate ones in dielectric parameters. JCSI-CG has a higher SSIM value in the real part of the dielectric parameter but the smallest value in the imaginary part among all the joint inversion results. JCSI-EP with $\gamma = 0$ has the smallest relative error in dielectric parameters for both models which may be because the dielectric parameters are not uniform in each region and combining EM data may oversmooth the reconstruction result.

With $\gamma = 0.5$, imaging quality with different noise levels are in Tables 6.4 and 6.6. A decrease in SNR of acoustic data can result in a more severe degradation in quality than with electromagnetic data. Thus, a high quality of acoustic data is needed for a satisfactory result. Since the hyperparameters are fixed for all breast phantoms, this choice may be not optimal for each. Thus, as shown in Table 6.6, a lower SNR of electromagnetic data may lead to a better result than obtained with a higher SNR.

Class 4 model

The phantom (ID 012304, slice s_1=100) is very dense. The slice contains 328×212 pixels for the forward problem, 82×53 pixels for inversion. In Model 4, a synthetic tumor of irregular shape is added at (1.8 cm, 1.2 cm).

Figure 6.7 shows the distributions of acoustic and electromagnetic parameters and the reconstruction results of different algorithms and Figure 6.8 compares the results with different values of γ. The

Table 6.3: Model 2 – Imaging quality assessment in reconstruction of acoustic and dielectric parameters

Index	Methods	acoustic parameter		dielectric parameter	
		c	α	ϵ_r'	ϵ_r''
Err	CSI-EP	**0.0097**	0.3915	0.4808	0.5901
	MR-CSI	0.0098	0.6413	0.4715	0.5750
	JCSI-CG	0.0100	0.9070	0.4473	0.5619
	JCSI-EP ($\gamma = 0$)	0.0097	0.3915	**0.4406**	**0.4640**
	JCSI-EP ($\gamma = 0.5$)	0.0097	0.3977	0.4411	0.4771
	JCSI-EP ($\gamma = 5$)	0.0099	**0.3763**	0.4486	0.4856
SSIM	CSI-EP	0.9424	0.8718	0.6446	0.5323
	MR-CSI	**0.9426**	0.7113	0.6768	0.5414
	JCSI-CG	0.9404	0.5558	0.7164	0.6107
	JCSI-EP($\gamma = 0$)	0.9424	0.8718	0.7129	**0.7019**
	JCSI-EP($\gamma = 0.5$)	0.9420	0.8678	**0.7221**	0.6946
	JCSI-EP($\gamma = 5$)	0.9420	**0.8796**	0.7143	0.6777

Table 6.4: Model 2 – Imaging quality assessment in reconstruction of acoustic and dielectric parameters with different SNR

Index	SNR (dB)		acoustic parameter		dielectric parameter	
	AC	EM	c	α	ϵ_r'	ϵ_r''
Err	10	10	0.0131	1.0786	0.4770	0.5226
	10	30	0.0130	1.0697	0.4719	0.5157
	30	10	0.0098	**0.3934**	0.4436	0.4828
	30	30	**0.0097**	0.3977	**0.4411**	**0.4771**
SSIM	10	10	0.9002	0.0183	0.6844	0.6347
	10	30	0.9010	0.0212	0.6831	0.6380
	30	10	0.9410	**0.8707**	0.7218	0.6932
	30	30	**0.9420**	0.8678	**0.7221**	**0.6946**

Table 6.5: Model 3 – Imaging quality assessment in reconstruction of acoustic and dielectric parameters

Index	Methods	acoustic parameter		dielectric parameter	
		c	α	ϵ_r'	ϵ_r''
Err	CSI-EP	**0.0097**	0.3927	0.4805	0.5890
	MR-CSI	0.0098	0.6377	0.4712	0.5741
	JCSI-CG	0.0101	0.9620	0.4445	0.5822
	JCSI-EP ($\gamma = 0$)	0.0097	0.3927	**0.4421**	**0.4658**
	JCSI-EP ($\gamma = 0.5$)	0.0098	0.3983	0.4430	0.4811
	JCSI-EP ($\gamma = 5$)	0.0099	**0.3807**	0.4498	0.4894
SSIM	CSI-EP	0.9419	0.8708	0.6443	0.5325
	MR-CSI	**0.9425**	0.7141	0.6768	0.5415
	JCSI-CG	0.9394	0.5289	**0.7260**	0.5946
	JCSI-EP($\gamma = 0$)	0.9419	0.8708	0.7088	**0.6977**
	JCSI-EP($\gamma = 0.5$)	0.9411	0.8672	0.7172	0.6862
	JCSI-EP($\gamma = 5$)	0.9400	**0.8765**	0.7091	0.6685

Table 6.6: Model 3 – Imaging quality assessment in reconstruction of acoustic and dielectric parameters with different SNR

Index	SNR (dB) AC	SNR (dB) EM	acoustic parameter c	acoustic parameter α	dielectric parameter ϵ_r'	dielectric parameter ϵ_r''
Err	10	10	0.0126	1.0036	0.4689	0.5100
	10	30	0.0125	0.9991	0.4692	0.5145
	30	10	**0.0098**	**0.3962**	0.4432	**0.4767**
	30	30	0.0098	0.3983	**0.4430**	0.4811
SSIM	10	10	0.9081	0.0293	0.6868	0.6452
	10	30	0.9083	0.0294	0.6811	0.6384
	30	10	0.9408	**0.8685**	**0.7225**	**0.6944**
	30	30	**0.9411**	0.8672	0.7172	0.6862

Table 6.7: Model 4 – Imaging quality assessment in reconstruction of acoustic and dielectric parameters

Index	Methods	acoustic parameter c	acoustic parameter α	dielectric parameter ϵ_r'	dielectric parameter ϵ_r''
Err	CSI-EP	**0.0089**	0.3521	0.4505	0.5861
	MR-CSI	0.0090	0.5817	0.4391	0.5576
	JCSI-CG	0.0093	0.8499	0.4285	0.6591
	JCSI-EP ($\gamma = 0$)	0.0089	0.3523	0.4160	**0.4415**
	JCSI-EP ($\gamma = 0.5$)	0.0089	0.3513	**0.4157**	0.4523
	JCSI-EP ($\gamma = 5$)	0.0089	**0.3258**	0.4158	0.4544
SSIM	CSI-EP	0.9429	0.9056	0.6872	0.5449
	MR-CSI	**0.9433**	0.7739	0.7206	0.5813
	JCSI-CG	0.9398	0.6215	0.7423	0.5020
	JCSI-EP($\gamma = 0$)	0.9429	0.9056	0.7473	**0.7265**
	JCSI-EP($\gamma = 0.5$)	0.9432	0.9056	**0.7495**	0.7246
	JCSI-EP($\gamma = 5$)	0.9428	**0.9173**	0.7492	0.7192

quality assessment is given in Table 6.7. As before, in separate inversion, the speed of sound can be reconstructed well and fine structures can be identified in the acoustic case, but the reconstructions of dielectric parameters are not satisfactory and the tumor cannot be seen.

Joint inversion algorithms have improved the reconstruction of dielectric parameters. In detail, JCSI-CG can show the structure of glandular part but the tumor is not obvious in dielectric parameters, while JCSI-EP can give a better estimate of the location and shape of the tumor. According to the quantitative assessment, JCSI-EP performs best in the reconstruction of real part of relative permittivity when $\gamma = 0.5$, while for the imaginary part, $\gamma = 0$ gives the best result. When $\gamma = 5$, the images of JCSI-EP are oversmoothed and the tumor cannot emerge well from the dielectric parameters while in the other cases the tumor can be identified clearly and the overall results are satisfactory.

Table 6.8 provides the quality assessment with different levels of noise with $\gamma = 0.5$. As with the results above, the noise level of acoustic data has a higher influence on the final result. A relative low level of noise is needed for successful tumor detection.

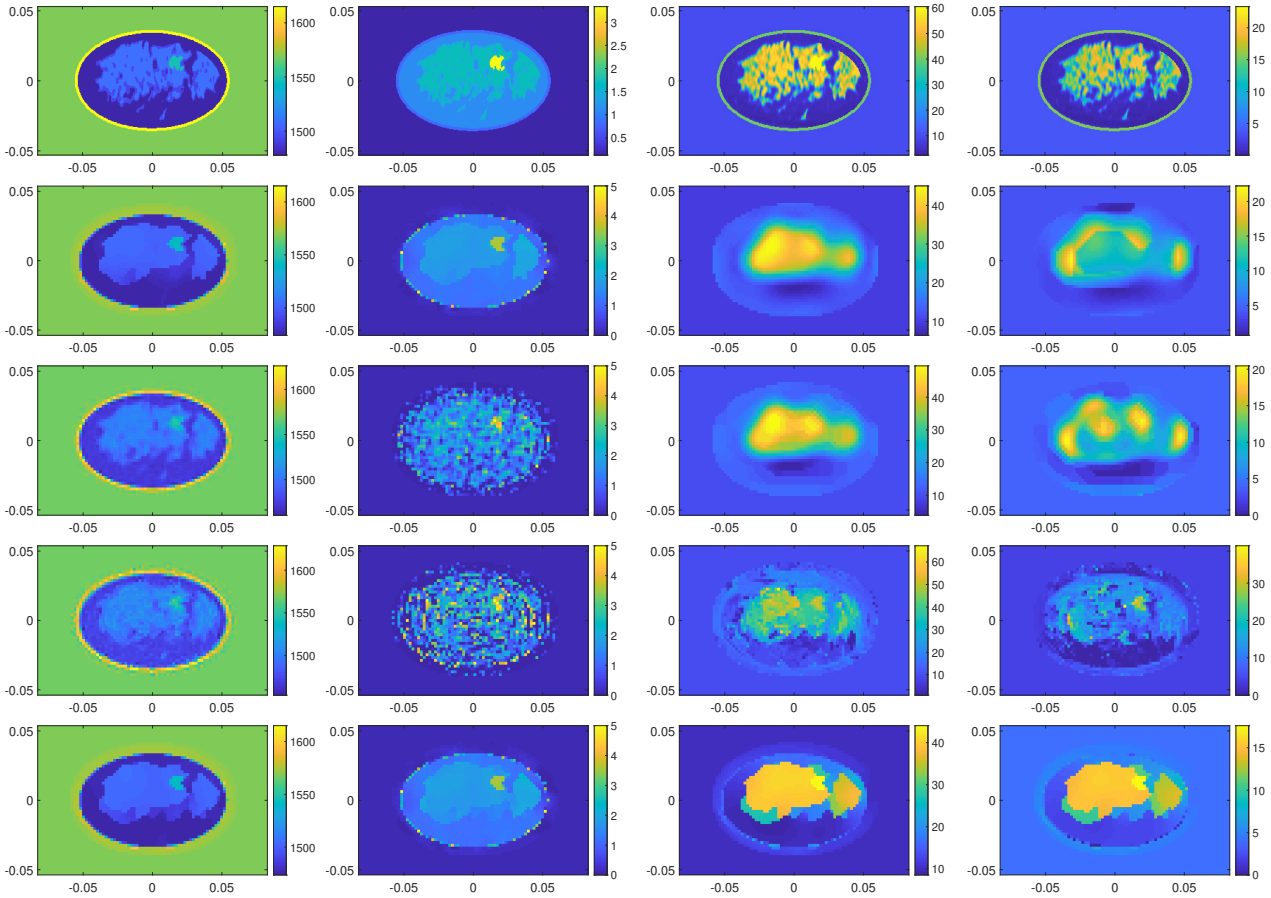

Figure 6.7: Model 4 – Ground truth (1st row), separate reconstruction results of CSI-EP (2nd), MR-CSI (3rd) and joint inversion results of JCSI-CG (4th) and JCSI-EP (5th) with speed of sound c (1st column), attenuation α (2nd), real part ϵ_r' (3rd) and imaginary part ϵ_r'' (4th) of relative permittivity.

Table 6.8: Model 4 – Imaging quality assessment in reconstruction of acoustic and dielectric parameters with different SNR

Index	SNR (dB) AC	SNR (dB) EM	acoustic parameter c	acoustic parameter α	dielectric parameter ϵ_r'	dielectric parameter ϵ_r''
Err	10	10	0.0108	1.0097	0.4427	0.4764
	10	30	0.0108	1.0262	0.4429	0.4817
	30	10	**0.0089**	**0.3502**	**0.4134**	**0.4473**
	30	30	0.0089	0.3513	0.4157	0.4523
SSIM	10	10	0.9189	0.1374	0.7356	0.6982
	10	30	0.9189	0.1335	0.7159	0.6813
	30	10	0.9412	0.8685	**0.7523**	**0.7361**
	30	30	**0.9432**	**0.9056**	0.7495	0.7246

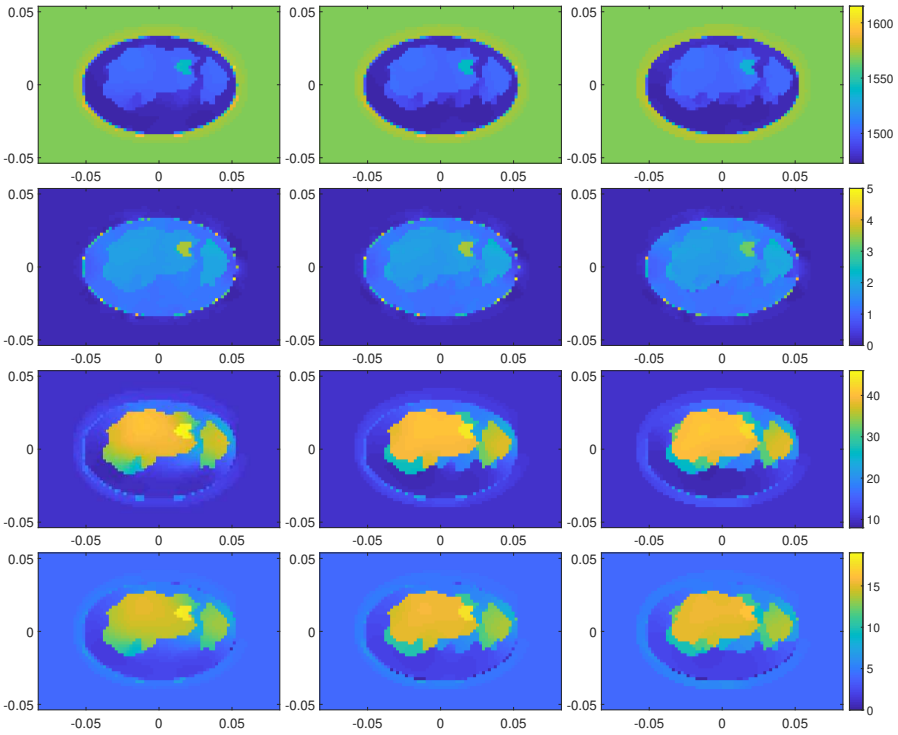

Figure 6.8: Model 4 – Joint reconstruction results of speed of sound c (1st row), attenuation α (2nd), real part ϵ_r' (3rd) and imaginary part ϵ_r'' (4th) of relative permittivity by JCSI-EP with $\gamma = 0$ (left), $\gamma = 0.5$ (middle) and $\gamma = 5$ (right).

6.5 Conclusion

In this chapter, a joint inversion algorithm of electromagnetic and acoustic data based on edge-preserving regularization has been proposed by introducing additional variables indicating the existence of an edge. Acoustic contrast, dielectric one and these edge markers are updated alternately.

Comprehensive numerical experiments, with due comparison with approaches involving total variation or cross-gradient, show that by joint inversion, electromagnetic imaging can gain from the high resolution of acoustic imaging and map out small tumors, which is very difficult when electromagnetic data are the only ones involved. A good quality of acoustic data is required to get a satisfactory joint inversion result.

For the three realistic models as introduced, increasing the weight of electromagnetic data in updating the edge variables may decrease the contrast between the tumor and the background. Overall, the electromagnetic imaging quality is much enhanced by joint inversion however. As for the choice of hyperparameters, here dealt with by thorough numerical experimentation beforehand, it still remains an open question. Forthcoming work should in particular focus onto a Bayesian methodology in order to estimate the hyperparameters jointly, so as to achieve a proper choice for each model under investigation.

Chapter 7

Joint inversion of microwave and ultrasound data by convolutional neural networks

This chapter is based on the paper *Breast imaging by convolutional neural networks from joint microwave and ultrasonic data*, Y. Qin, P. Ran, T. Rodet, and D. Lesselier, submitted to the *IEEE Transactions on Antennas and Propagation* and presently undertaking revision. Still there is some duplicate content in introduction and forward problem. We have changed some notations and the layout of the figures. Layers and optimization methods used to build and train the proposed network are detailed in Chapter 4.

7.1 Introduction

New imaging modalities with non-ionizing and low-cost features are being developed for breast tumor detection. Microwave imaging, due to the high contrast of the dielectric parameters between tumorous and normal tissues, has been investigated for breast imaging [37, 133]. However, images are of low resolution due to the long wavelength of the electromagnetic wave. In contrast, ultrasound imaging, despite low contrast between different tissues, can provide high-resolution image and structure information [169, 170]. Therefore, it is of good interest to fuse these two modalities to produce images exhibiting both high contrast and high resolution.

Fusion of multimodality data can be achieved by successive imaging with one modality used as prior. Usually structure information, like tissue interface or region, can be extracted from a high-resolution image. Such information can be used as regularization term to guide inversion with another modality [102, 105, 112] or give a better initial guess of unknown parameters [113]. Joint inversion is another way to fuse data where they are inverted simultaneously. Empirical or intrinsic physical relationship can be employed to achieve joint inversion [116]. Structural similarity can also be employed to combine the parameters of different modalities in the inversion procedure [118–120].

Such methods are based on iterative nonlinear inversion algorithms, like the Distorted Born Iterative Method (DBIM) [55], the Contrast Source Inversion (CSI) [58] method and the Subspace-based Optimization Method (SOM) [59], all under various guises and at different stages of sophistication, yet often requiring time-consuming iterations in order to get suitable reconstruction results, and as a matter of fact real-time imaging is difficult to achieve. As further examples breast microwave imaging with prior information on tissue boundaries yielded from ultrasound reflection data using regularized DBIM and CSI is dealt with by the authors and co-workers [183] while deterministic edge-preserving approaches, alternate minimization updating acoustic contrast, edge markers and dielectric contrast of the breast, incorporating the cost functional of CSI, is in [172].

Recently, convolutional neural networks (CNN) have shown to be successful in image recognition [76, 77], segmentation [78, 79], object detection [80, 81] and many other tasks, and have found their way in effect in a whole range of artificial-intelligence-based medical imaging as reviewed in [184], including diagnostic of lesions from ultrasound images, e.g., [185] — microwave breast imaging seems less investigated in that specific AI realm.

CNN has strong local modeling capability with few parameters. Once the network is well trained, it can give the result in real time. Such techniques have been investigated for inverse scattering problems and showed promising results.

As an example, in [82], a CNN structure is designed to use the measured fields as the input and to predict the scatterer map directly. Such a type of methods can provide reconstruction results in real time yet it benefits little of the physical knowledge available.

CNN can also be run in combination with traditional inversion algorithms. In [84], CNN is to estimate the total contrast current given the part in signal space calculated similarly to SOM as the input, then the noise subspace component of contrast current and contrast are optimized iteratively. In [85], the result of a backpropagation method is the input of a cascade of multi-layer complex-valued residual CNN networks in order to get a better reconstruction of the contrast. In [86], with the major part of the contrast current obtained from the scattered field and the corresponding total field as the input, the contrast current is predicted. A review of deep learning methods for the inverse scattering problem is found in [186].

In addition to the references above, CNNs have been applied in breast imaging [87, 88] where U-Net [79] is employed to refine the contrast obtained from CSI to get a better estimate. Though acoustic data are involved, fusion of these two modalities occurs within the CSI reconstruction procedure.

In the present study, convolutional neural networks are used to combine (collected at a single frequency) microwave data and (collected at two frequencies) ultrasonic data and to get the imaging results directly. Inspired by double-stream CNN [168], which is designed to fuse temporal and spatial information for video action recognition, in order to capture the complementary information and combine them within the last layer, a multi-stream structure is used to input data from the different modalities of exploration (in terms of the physics itself and the diverse operation frequencies).

To fully exploit the real-time feature of the network, its input consists of source and field quantities inside the domain of interest which are obtained by backpropagation from the measured data, and the output is chosen as the distribution of all parameters directly. Besides, multi-task learning strategy is used with an auxiliary classifier to classify each pixel to get a segmentation image where tissue types are shared by both modalities. Such an image can also help the diagnosis of tumors for physicians.

The contribution is organized as follows. In Section 7.2 the formulation of the forward problem is presented. In Section 7.3, the structure of the network is detailed. In Section 7.4 numerical experiments on breast phantoms are proposed. A brief conclusion follows in 7.5. Notice that recent works on breast imaging and data fusion by the authors and co-workers as mentioned before [183] [172] have been illustrated on phantoms and datasets like to those of now, yet going to tailored CNN stands in contrast to these earlier investigations.

7.2 Forward problem

In the investigation a two-dimensional geometry is considered. Time-harmonic waves are assumed with time dependence $\exp(-i\omega t)$ for both acoustic and electromagnetic cases. The breast is located within a domain of interest (DoI) $\mathcal{D}$.

The known background medium is characterized by its complex relative permittivity ϵ_b, permeability μ_b, and wavenumber $k_b^{\text{em}} = \omega\sqrt{\epsilon_0\epsilon_b\mu_b}$ in electromagnetics, and speed of sound c_b, attenuation α_b, and wavenumber $k_b^{\text{ac}} = \omega/c_b + i\alpha_b$ in acoustics. Permeability and density are set constant within the DoI. The unknown parameters are the space distributions of complex relative permittivity $\epsilon_r(\mathbf{r}) = \epsilon_r'(\mathbf{r}) + i\epsilon_r''(\mathbf{r})$, sound speed $c(\mathbf{r})$ and attenuation $\alpha(\mathbf{r})$.

For each modality, N_i probes are evenly located at $\mathbf{r}'_p$, $p = 1, 2, \ldots, N_i$ on a circle $\mathcal{S}$, as sketched in Fig. 7.1. Each one illuminates the DoI and scattered fields are collected by all.

To tackle the problem numerically, $\mathcal{D}$ is discretized into $M = H' \times W'$ small cells centered at $\mathbf{r}_m$, $m = 1, 2, \ldots, M$. A standard pulse-basis point-matching method of moments (MoM) is employed. Every square cell is approximated by a small disk with same area and with equivalent radius R.

Acoustic and electromagnetic contrasts are defined as

$$\chi^{\mathrm{ac}}(\mathbf{r}) = \frac{(k^{\mathrm{ac}}(\mathbf{r}))^2 - (k_b^{\mathrm{ac}})^2}{(k_b^{\mathrm{ac}})^2} \tag{7.1}$$

$$\chi^{\mathrm{em}}(\mathbf{r}) = \frac{(k^{\mathrm{em}}(\mathbf{r}))^2 - (k_b^{\mathrm{em}})^2}{(k_b^{\mathrm{em}})^2} \tag{7.2}$$

and the contrast source for the vth incidence

$$J_p(\mathbf{r}) = \chi(\mathbf{r}) F_p^t(\mathbf{r}) \tag{7.3}$$

where F is the pressure field P or the electric field E. Superscript "t" denotes total field. Source-type integral equations in discrete form can be derived as

$$\mathbf{J}_p = \mathbf{X}\mathbf{F}_p^{\mathbf{i}} + \mathbf{X}\mathbf{G}_{\mathbf{d}}\mathbf{J}_p \tag{7.4}$$

$$\mathbf{F}_p^{\mathbf{s}} = \mathbf{G}_{\mathbf{s}}\mathbf{J}_p \tag{7.5}$$

The $M \times 1$ vector $\mathbf{F}_p^{\mathbf{i}}$ represents the incident field with $\mathbf{F}_p^{\mathbf{i}} = [F_p^i(\mathbf{r}_1), \ldots, F_p^i(\mathbf{r}_M)]^T$ where superscript "T" denotes transpose. $\mathbf{F}_p^{\mathbf{s}}$ is a $N_i \times 1$ vector representing the scattered field collected by the receivers as $\mathbf{F}_p^{\mathbf{s}} = [F_p^s(\mathbf{r}'_1), \ldots, F_p^s(\mathbf{r}'_{N_i})]^T$. The $M \times 1$ vector $\boldsymbol{\chi}$ is the discrete form of χ as $\boldsymbol{\chi} = [\chi(\mathbf{r}_1), \ldots, \chi(\mathbf{r}_M)]^T$. $\mathbf{G}_{\mathbf{d}}$ is a $M \times M$ matrix with element

$$\mathbf{G}_{\mathbf{d}}(m, m') = \begin{cases} \dfrac{ik_b\pi R}{2} \mathrm{J}_1(k_b R)\, \mathrm{H}_0^{(1)}(k_b|\mathbf{r}_m - \mathbf{r}_{m'}|), m \neq m' \\ \dfrac{ik_b\pi R}{2} \mathrm{H}_1^{(1)}(k_b R) - 1, \text{otherwise} \end{cases} \tag{7.6}$$

J_1 is the 1^{st}-kind Bessel function, $\mathrm{H}_1^{(1)}$ the 1^{st}-kind 1^{st}-order Hankel function, $\mathrm{H}_0^{(1)}$ the 1^{st}-kind 0^{th}-order Hankel function. The $N_i \times M$ matrix $\mathbf{G}_{\mathbf{s}}$ is

$$\mathbf{G}_{\mathbf{s}}(v, m) = \frac{ik_b\pi R}{2} \mathrm{J}_1(k_b R)\, \mathrm{H}_0^{(1)}(k_b|\mathbf{r}'_v - \mathbf{r}_m|) \tag{7.7}$$

7.3 CNN scheme

A CNN structure with multi-stream input and multi-task learning strategy (CNN-MM) is proposed to achieve joint inversion of microwave and ultrasonic data in real-time.

7.3.1 CNN structure

As indicated, the structure is inspired by a two-stream CNN proposed in [168]. In the present work, microwave data at a single frequency and ultrasonic data at two frequencies are used, thus a three-stream architecture for input is designed, refer to Fig. 7.2.

To achieve real-time reconstruction, a network with input of scattered fields and with the distribution of parameters as the output is wished for. In this case, fully-connected layers are required

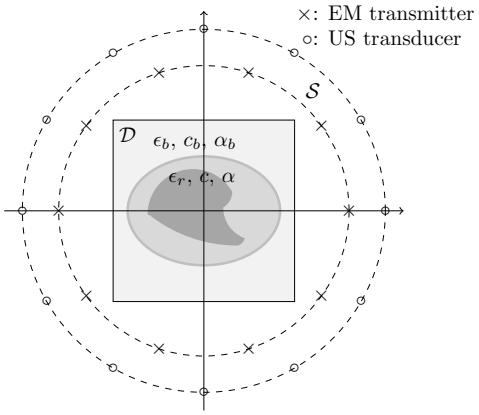

Figure 7.1: Sketch of configuration of two multistatic modalities.

since parameters at each pixel impact all scattered fields collected. However, fully-connected layers involving a large number of trainable parameters are the main cause of computational burden.

To overcome this hurdle and also introduce physical knowledge, the input of the proposed network is chosen as contrast-source and field quantities ω and f inside the DoI gotten from backpropagation

$$\boldsymbol{\omega}_p = \mathbf{G}_{\mathbf{s}}^{\dagger}\mathbf{F}_p^{\mathbf{s}} \tag{7.8}$$

$$\mathbf{f}_p = \mathbf{G}_{\mathbf{d}}\boldsymbol{\omega}_p \tag{7.9}$$

where $\mathbf{G}_{\mathbf{s}}^{\dagger}$ is the conjugate transpose of $\mathbf{G}_{\mathbf{s}}$ —notice that in back-propagation methods, a complex parameter is used in Equation (7.8) to minimize the quadratic error in the scattered field, here the parameter is simply set to 1.

Global relations between different pixels have been introduced via the Green's function. Given such input, focus can be concentrated on local spatial relation and connections between different channels.

For each modality at a given frequency, $\boldsymbol{\omega}_p$ and $\mathbf{f}_p$ are reshaped as $H \times W$ images. $\Re\{\boldsymbol{\omega}_p\}$, $\Im\{\boldsymbol{\omega}_p\}$, $\Re\{\mathbf{f}_p\}$ and $\Im\{\mathbf{f}_p\}$ obtained from all incidences are concatenated as input with size of $H \times W \times 4N_i$.

To achieve reconstruction, the network has an output of size $H \times W \times 4$ to give the prediction of electric parameters ϵ_r' and ϵ_r'', and acoustic parameters c and α simultaneously. To reduce the impact on the loss and gradient due to the difference in magnitude between different parameters, each parameter ζ is normalized to $[0, 1]$ given the corresponding range $[\zeta_{min}, \zeta_{max}]$ by $\widetilde{\zeta} = (\zeta - \zeta_{min})/(\zeta_{max} - \zeta_{min})$. Accordingly, the activation function of the last layer is the sigmoid function the output of which is between 0 and 1.

Apart from the regression task, an auxiliary classifier is added to provide a segmentation image. A softmax classifier is used to give the probability distribution over predicted output classes (tissue types and background medium) for each pixel and the pixel will be classified into the class with the highest score. This segmentation task is quite relevant to the regression task. Such multi-task learning can help training the network and improve the generalization capability [187].

Unlike the structure in [168] where fusion is achieved in the last layer, data from different modalities are combined earlier in the proposed network. After two sets of 1×1 convolutional layer with activation function of ReLU [76] and Batch Normalization (BN) [144], results of different streams are concatenated and convolved with a 3×3 convolutional layer. Separate convolution is chosen to reduce computational cost.

Six repeated residual units [188, 189] are cascaded as the main body of the structure. The details of the residual unit are illustrated in Fig. 7.3, it contains two convolutional layers and an identity shortcut with pre-activation [189] structure to help the training of the network. A 1×1 convolutional shortcut may be used to match dimensions.

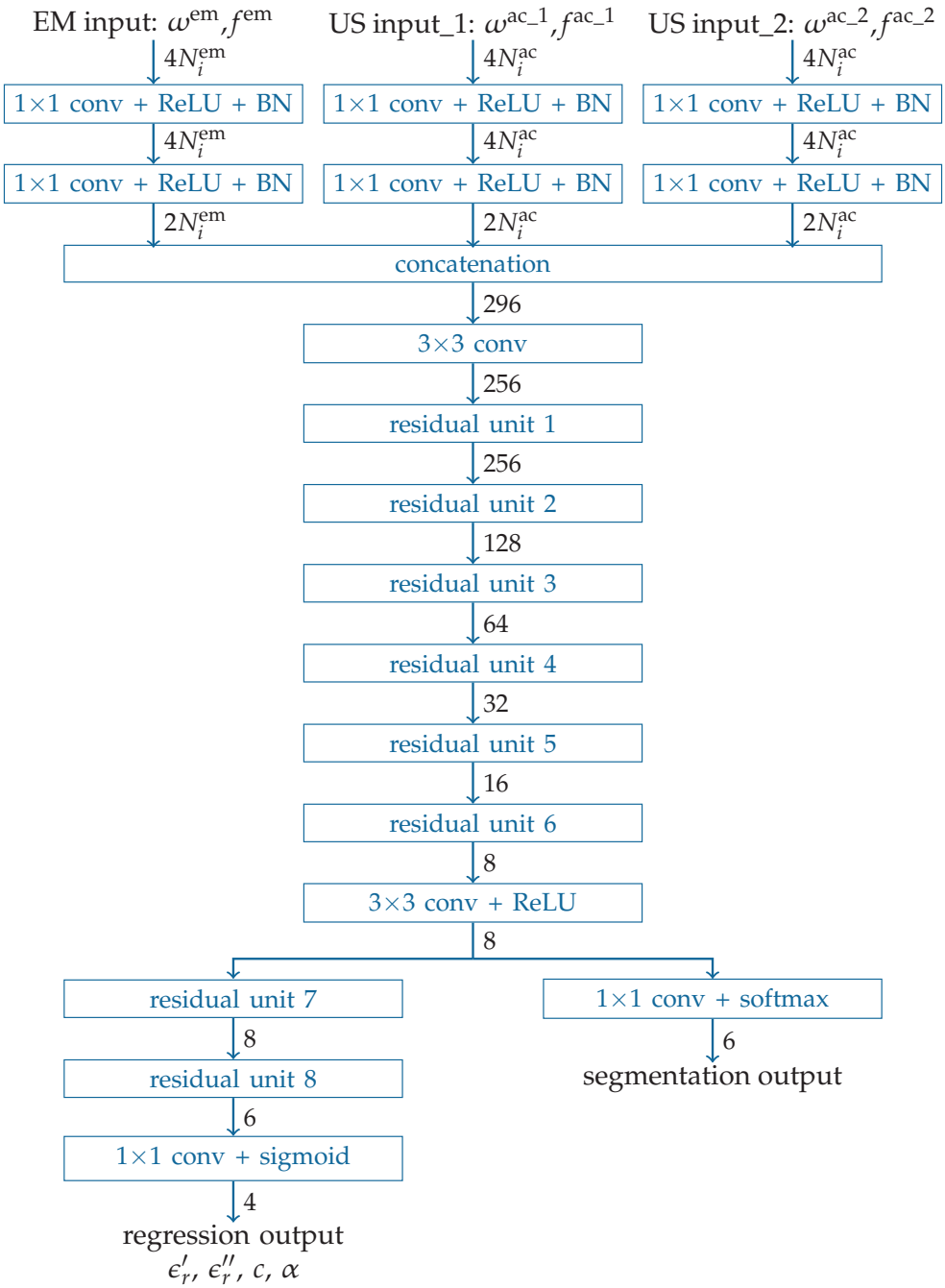

Figure 7.2: Structure of CNN-MM, with three streams to input microwave data at one frequency and ultrasonic data at two frequencies and two tasks to output the parameter values and tissue type image. Numbers beside the arrows are channel numbers. Height H and width W remain unchanged.

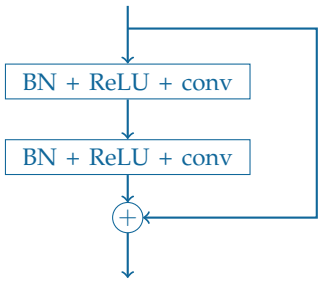

Figure 7.3: Residual unit with pre-activation.

To be mentioned, in the first two units, separate convolution with kernel size of 3×3 is used to model the connections in the spatial neighborhood and among different channels; the following three units are with a kernel of 1×1 to add nonlinearity for the data at the same position, and the last unit has a normal 3×3 convolution. Two other residual units are added before the output of distribution of parameters, each with two layers of 3×3 convolution and ReLU activation.

7.3.2 Loss function

The network gives the prediction of dielectric and acoustic parameters and the segmentation of the breast model simultaneously and different loss functions are employed.

In the regression task, dielectric and acoustic parameters at each pixel are predicted. The loss function is chosen as the mean of the absolute error and squared error as

$$L_{reg} = \frac{1}{2NHW} \sum_{n} \sum_{h,w} \left(|\hat{\tilde{\zeta}}^{n}_{h,w} - \tilde{\zeta}^{n}_{h,w}| + |\hat{\tilde{\zeta}}^{n}_{h,w} - \tilde{\zeta}^{n}_{h,w}|^2 \right) \tag{7.10}$$

for parameter ζ where $\hat{\tilde{\zeta}}^{n}_{h,w}$ is the predicted value of nth sample located at (h, w) and $\tilde{\zeta}^{n}_{h,w}$ is the groundtruth. N is the number of samples in a training batch.

In the segmentation task, each pixel is classified into a tissue type or background medium. Softmax classifier is used for this multi-class classification problem. The loss function is cross entropy as

$$L_{seg} = -\frac{1}{NHW} \sum_{n} \sum_{h,w} \sum_{k} t^{n}_{h,w;k} log(s^{n}_{h,w;k}) \tag{7.11}$$

with $t^{n}_{h,w;k}$ and $s^{n}_{h,w;k}$ the groundtruth and predicted probability of the pixel for Class k.

Considering that the tumor class should have a quite smaller number of pixels than other tissue types and that background has the most pixels, the class distribution is extremely imbalanced. The loss will be dominated by majority classes and minority classes will be ignored by the classifier.

To overcome this problem, a weight factor is introduced for each tissue type in order to balance the penalty especially when a tumor pixel is wrongly classified. In the present work, the weight for a class is proportional with the reciprocal of the square root of the number of pixels labeled as it.

7.3.3 Other structures

Apart from the network with multi-stream as input and multi-task learning described above, CNNs with other structures are built for comparison.

Two CNNs are used to test the performance with data from a single modality: CNN-US has two streams for ultrasonic data obtained at two frequencies and outputs the acoustic parameters and the tissue type image; CNN-EM has one stream for microwave data and outputs the dielectric parameters and also the tissue type images.

Another two CNNs have been built to test the effectiveness of multi-task learning: CNN-RG with both ultrasonic and microwave data to retrieve the distribution of dielectric and acoustic parameters, and CNN-SG with which one only tries to get the segmentation result.

The above four networks are constructed from the original network by removing the needless branches. Besides, CNN-OS with one stream where microwave and ultrasonic data are concatenated in different channels as the input is designed. The numbers of filters in the first two layers are 592 and 256, sum of the filters of the three streams in CNN-MM.

7.4 Numerical simulations

Here, numerical simulations are run to evaluate the performance of the networks. Several examples enable to compare the results of the networks above. Robustness is also tested on the proposed one.

7.4.1 Measurement setup and dataset

The networks are trained and tested with realistic breast phantoms available in the well-known on-line UWCEM repository [134], [190]. Breast composition varies from person to person and the phantoms in the repository are classified according to radiographic density into four classes: almost entirely fatty, scattered fibroglandular tissue, heterogeneously dense breast, and extremely dense tissue.

Since dense breasts have higher risk of cancers [137], phantoms categorized into the last two classes, Class 3 and 4, are used to generate the dataset. Each model is extracted along s1 axis from the 3D phantoms, including three phantoms in Class 3 and one phantom in Class 4. Several columns and rows with pixels of background are added to ensure that all samples have same size.

One tumor is added into the glandular part with random location. The size of this tumor is set randomly with a radius between 6 mm and 8 mm to add variability. In our work, one slice of the breast phantom generates three samples: one sample without tumor, another two with different tumors.

The Debye parameters of dielectric properties for normal tissues are from [133] and the relative permittivity of the tumor is set as the 75th percentile curve in [132]. The acoustic parameters are chosen from [138, 139]. A linear dependence between attenuation and frequency is assumed.

In the simulation, for the electromagnetic case, 20 antennas are evenly set on a circle with radius of 0.1 m, working as sources and receivers simultaneously at a single 1 GHz operation frequency. For the acoustic case, 64 transducers operate at 100 and 200 kHz, set on a 0.12 m-radius circle. The DoI for simulation has a resolution of 0.5 mm, with 300×300 pixels. Scattered fields are obtained by solving the forward problem. Corresponding calculations are run on Matlab.

To enlarge the dataset, data augmentation is employed. Different levels of noise are added to the scattered fields from 15 dB to 30 dB. The DoI is discretized into 75×75 pixels to calculate input data ω and f with Equations (7.8) and (7.9). Tissue type image and distribution of electric and acoustic parameters with the same discretization are used as the output. Rotation and flipping are operated on both input and output of a sample to generate new data. The whole data set contains 2180 samples, including 1920 training samples and 240 test samples. In the training set, 1296 samples are from Class 3 and 624 from Class 4, while in the test set, there are 144 samples from Class 3 and 96 from Class 4.

The ranges to normalize the parameters are $[1, 70]$, $[0, 30]$, $[1450, 1650]$ and $[0, 5]$ for ϵ_r', ϵ_r'', c and α, respectively. Here, attenuation at 200 kHz is predicted. In the segmentation task, pixels are classified into six categories according to tissue type in the repository, namely background medium, skin, fat, transitional, glandular and tumorous tissue.

7.4.2 Implementation details

All networks are implemented on Keras with Tensorflow backend, run on a laptop with NVIDIA GPU Quadro P600. The weights of segmentation and regression losses are set to 1 and 8, respectively. L2

regularization is chosen for all the networks with regularization parameter $\gamma = 0.01$. The weights in the convolutional layers are initialized by Xavier initialization [146]. The networks are trained with ADAM [147] solver with an initial learning rate of 0.001 which decays with a factor of 0.2 every 10 epochs. The batch size is 10 and 80 epochs are run in total. All the networks are trained on the same training set with the same configuration.

7.4.3 Quantitative assessment

The performance of the network is assessed by two metrics for different tasks. For the segmentation task, Intersection-over-Union (IoU) for Class i is calculated as

$$IoU_i = \frac{1}{N}\sum_n \frac{p_{ii}^n + 1}{\sum_{k=1}^K p_{ik}^n + \sum_{k=1}^K p_{ki}^n - p_{ii}^n + 1} \tag{7.12}$$

where p_{ik}^n is the number of pixels in test sample n labeled as Class i but predicted into Class k and K is the number of classes. Note that in the calculation, a smoothness number of 1 is used. For the regression task, the relative error is used for evaluation. Given the output of the network $\hat{\tilde{\zeta}}$ and ranges for normalization, the predicted parameter value $\hat{\zeta}$ can be calculated. The relative error between $\hat{\zeta}$ and groundtruth ζ is as

$$Err = \frac{1}{N}\sum_n \sqrt{\frac{\sum_{w,h} |\hat{\zeta}_{w,h}^n - \zeta_{w,h}^n|^2}{\sum_{w,h} |\zeta_{w,h}^n|^2}} \tag{7.13}$$

electromagnetic data (CNN-EM), single input of ultrasonic data (CNN-US), single output with tissue type (CNN-SG) and single output of parameter distribution maps (CNN-RG) are constructed by removing the needless branch. Besides, a network with one stream (CNN-OS) where electromagnetic and acoustic data are concatenated in different channels as the output is designed. The numbers of filters of first two layers are 592 and 256, sum of the filters of the three streams in CNN-MM. All the networks are trained on the same training set with the same training configuration. Quantitative assessment, IoU and Err on the test set are in Tables 7.1 and 7.2.

Table 7.1: IoU of different networks on test set.

Network	Medium	Skin	Fat	Transition	Gland	Tumor	Average
CNN-MM	0.9952	0.8363	0.8595	0.4176	0.6772	0.7168	0.7504
CNN-EM	0.9885	0.6270	0.7999	0.3242	0.5513	0.3231	0.6024
CNN-US	0.9960	0.8565	0.8538	0.3959	0.6480	0.7003	0.7418
CNN-SG	0.9956	0.8426	0.8430	0.3938	0.6595	0.6943	0.7381
CNN-OS	0.9945	0.8231	0.8516	0.3972	0.6616	0.6799	0.7347

Table 7.2: Err of different networks on test set.

Network	ϵ_r'	ϵ_r''	c	α
CNN-MM	0.2617	0.2652	0.0045	0.1356
CNN-EM	0.3575	0.3694	–	–
CNN-US	–	–	0.0042	0.1397
CNN-RG	0.2795	0.2826	0.0056	0.1572
CNN-OS	0.2731	0.2782	0.0045	0.1642

From the quantitative assessment, with both microwave and ultrasonic data, CNN-MM with outputs of both tissue type and parameter images works better on the test set than CNN-RG and CNN-SG which are trained with single task. Though the relative error in sound speed is slightly higher than with CNN-US, CNN-MM has higher score in segmentation task and works much better than CNN-EM in both regression and segmentation tasks. CNN-MM also outperforms CNN-OS with one stream for data of two modalities. Meanwhile, the proposed network can achieve real-time retrieval. In average, with FFT implemented, the network input data can be computed in 0.3477 second and it takes 0.2231 second to get the prediction results of one sample on Intel Core i7-8850H CPU (2.60 GHz).

7.4.4 Qualitative assessment

Reconstructions of two examples are shown to compare imaging quality. They are new slices extracted from models in Class 3 and Class 4 to compare the results of different modalities and network structures, respectively. Each example involves two cases to evaluate the tumor detection capability of the networks: one without tumor, another with a synthetic tumor. 30 dB noise is added to both data.

A breast model from Class 3 shows the reconstruction from different modalities. Groundtruth without and with tumor is in Figs. 7.4 and 7.5 (1^{st} row), respectively. Results yielded by CNN-MM, CNN-EM and CNN-US are in 2^{nd}, 3^{rd} and 4^{th} rows, respectively.

When only microwave data dealt with, several pixels in the segmentation image of CNN-EM are classified as tumor yet there is none. When a tumor, it cannot be identified from the distribution of the relative permittivity. Yet, both CNN-US and CNN-MM achieve a good reconstruction of parameters and segmentation images. The main structure is well estimated and the tumor detected in both parameter and tissue type images.

Their IoU and Err are in Tables 7.3, 7.4, 7.5 and 7.6. From the quantitative assessment, CNN-MM enjoys the best performance in both regression and segmentation tasks for both cases. Fusion of modalities has improved the imaging, especially if concerned with the microwave modality.

Table 7.3: IoU for example in Class 3 w/o tumor.

Network	Medium	Skin	Fat	Transition	Gland	Tumor	Average
CNN-MM	0.9949	0.8333	0.7885	0.4048	0.7049	1.0	0.7877
CNN-EM	0.9934	0.7021	0.7422	0.3452	0.6089	0.05	0.5736
CNN-US	0.9954	0.8118	0.7710	0.4015	0.6824	1.0	0.7770

Table 7.4: Err for example in Class 3 w/o tumor.

Network	ϵ'	ϵ''	c	α
CNN-MM	0.2626	0.2635	0.0046	0.1110
CNN-EM	0.3103	0.3125	–	–
CNN-US	–	–	0.0047	0.1091

Table 7.5: IoU for example in Class 3 w/ tumor.

Network	Medium	Skin	Fat	Transition	Gland	Tumor	Average
CNN-MM	0.9952	0.8286	0.7934	0.3894	0.6580	0.7586	0.7372
CNN-EM	0.9949	0.7213	0.75	0.3484	0.5549	0.4333	0.6338
CNN-US	0.9957	0.9082	0.7789	0.3861	0.6410	0.5667	0.7001

Table 7.6: Err for example in Class 3 w/ tumor.

Network	ϵ'	ϵ''	c	α
CNN-MM	0.2646	0.2633	0.0045	0.1562
CNN-EM	0.3160	0.3271	–	–
CNN-US	–	–	0.0047	0.1738

An example in Class 4 enables to evaluate the performance of CNNs with different structures with data of two modalities. Groundtruth and results of CNN-MM, CNN-OS, CNN-RG and CNN-SG are in Figs. 7.6 and 7.7 for no and one tumor. In segmentation, the tissue structure is well appraised and overall, results are satisfactory. All networks recognize presence/absence of tumor, though still little difference in size and shape vs. groundtruth. In regression, CNN-RG does not well distinguish if tumor in or not. Retrievals look alike.

CNN-MM and -OS with multi-task learning have better prediction on electric and acoustic parameters. There is higher contrast at location of the tumor whenever added. CNN-MM is better for attenuation than CNN-OS, which predicts lower attenuation for the tumor than the glandular part. Their IoU and Err are in Tables 7.7, 7.8, 7.9 and 7.10. CNN-MM with multi-task learning outperforms networks with single task of regression or segmentation. With multi-stream for different modalities, it is better than CNN-OS where data are combined at first layer.

7.4.5 Robustness experiment

The network is trained with 15 to 30 dB SNR and at most one tumor. Robustness tests are to see how CNN-MM performs with more noise and more tumors. Based on Class 3 example, 10 and 15 dB noise are added to data without/with tumor, Fig. 7.8. With 15 dB, the network performs well (2^{nd} and 4^{th} rows). The tumor is seen in parameters and segmentation results. With 10 dB, it is harder to detect. Only few pixels are classified as tumor, difficult to see in images (3^{rd} row). Their IoU and Err are in Tables 7.11, 7.12, 7.13 and 7.14. A new slice in Class 4 model is used to test if two tumors, with 30 dB noise. Ground truth and images are in Fig. 7.9. The tumors are localized, with higher contrast in parameters. Average IoU is 0.8103, Err are 0.2278 for ϵ'_r, 0.2316 for ϵ''_r, 0.0039 for c, 0.1480 for α.

7.5 Conclusion

A CNN structure is proposed to combine microwave and ultrasonic data and achieve real-time breast imaging. Apart from the regression task to predict parameter values, an auxiliary classifier is used to classify each pixel to get model segmentation. Such multi-task learning improves the reconstruction. Combination of two-modality data also performed better than with only one modality, especially for the microwave one, as further justification of the data fusion as operated herein. Though the network performs well on dense Class 3 and 4 models, it has a bad generalization capability for fatty breasts, due to lack of training samples from this group. Besides, loss weights for different tasks are set constant, which can be improved in adaptive fashion [191].

Table 7.7: IoU for example in Class 4 w/o tumor.

Network	Medium	Skin	Fat	Transition	Gland	Tumor	Average
CNN-MM	0.9969	0.8670	0.8978	0.4753	0.7547	1.0	0.8319
CNN-SG	0.9969	0.8483	0.8832	0.4564	0.7413	1.0	0.8210
CNN-OS	0.9961	0.8596	0.8989	0.4488	0.7206	1.0	0.8207

Table 7.8: Err for example in Class 4 w/o tumor.

Network	ϵ'	ϵ''	c	α
CNN-MM	0.2358	0.2418	0.0039	0.0960
CNN-RG	0.2585	0.2581	0.0052	0.0984
CNN-OS	0.2529	0.2540	0.0041	0.1036

Table 7.9: IoU for example in Class 4 w/ tumor.

Network	Medium	Skin	Fat	Transition	Gland	Tumor	Average
CNN-MM	0.9979	0.8935	0.9013	0.4844	0.7143	0.7045	0.7826
CNN-SG	0.9977	0.8693	0.8869	0.4767	0.7050	0.6458	0.7636
CNN-OS	0.9966	0.8786	0.8901	0.4337	0.6689	0.5682	0.7394

Table 7.10: Err for example in Class 4 w/ tumor.

Network	ϵ'	ϵ''	c	α
CNN-MM	0.2402	0.2428	0.0041	0.1363
CNN-RG	0.2547	0.2529	0.0054	0.1861
CNN-OS	0.2507	0.2586	0.0043	0.2081

Table 7.11: IoU for example in Class 3 w/o tumor vs. SNR.

SNR (dB)	Medium	Skin	Fat	Transition	Gland	Tumor	Average
10	0.9903	0.6580	0.6623	0.2628	0.4753	1.0	0.6748
15	0.9939	0.7809	0.7545	0.3548	0.6423	1.0	0.7544
30	0.9949	0.8333	0.7885	0.4048	0.7049	1.0	0.7877

Table 7.12: Err for example in Class 3 w/o tumor vs. SNR.

SNR (dB)	ϵ'	ϵ''	c	α
10	0.4233	0.4218	0.0067	0.1520
15	0.3216	0.3188	0.0054	0.1262
30	0.2626	0.2635	0.0046	0.1110

Table 7.13: IoU for example in Class 3 w/ tumor vs. SNR.

SNR (dB)	Medium	Skin	Fat	Transition	Gland	Tumor	Average
10	0.9911	0.6126	0.7030	0.3180	0.5	0.1034	0.5380
15	0.9949	0.7529	0.7520	0.3588	0.5947	0.5278	0.6338
30	0.9952	0.8286	0.7934	0.3894	0.6580	0.7586	0.7372

Table 7.14: Err for example in Class 3 w/ tumor vs. SNR.

SNR (dB)	ϵ'	ϵ''	c	α
10	0.3893	0.3909	0.0071	0.2113
15	0.3164	0.3137	0.0053	0.1698
30	0.2646	0.2633	0.0045	0.1562

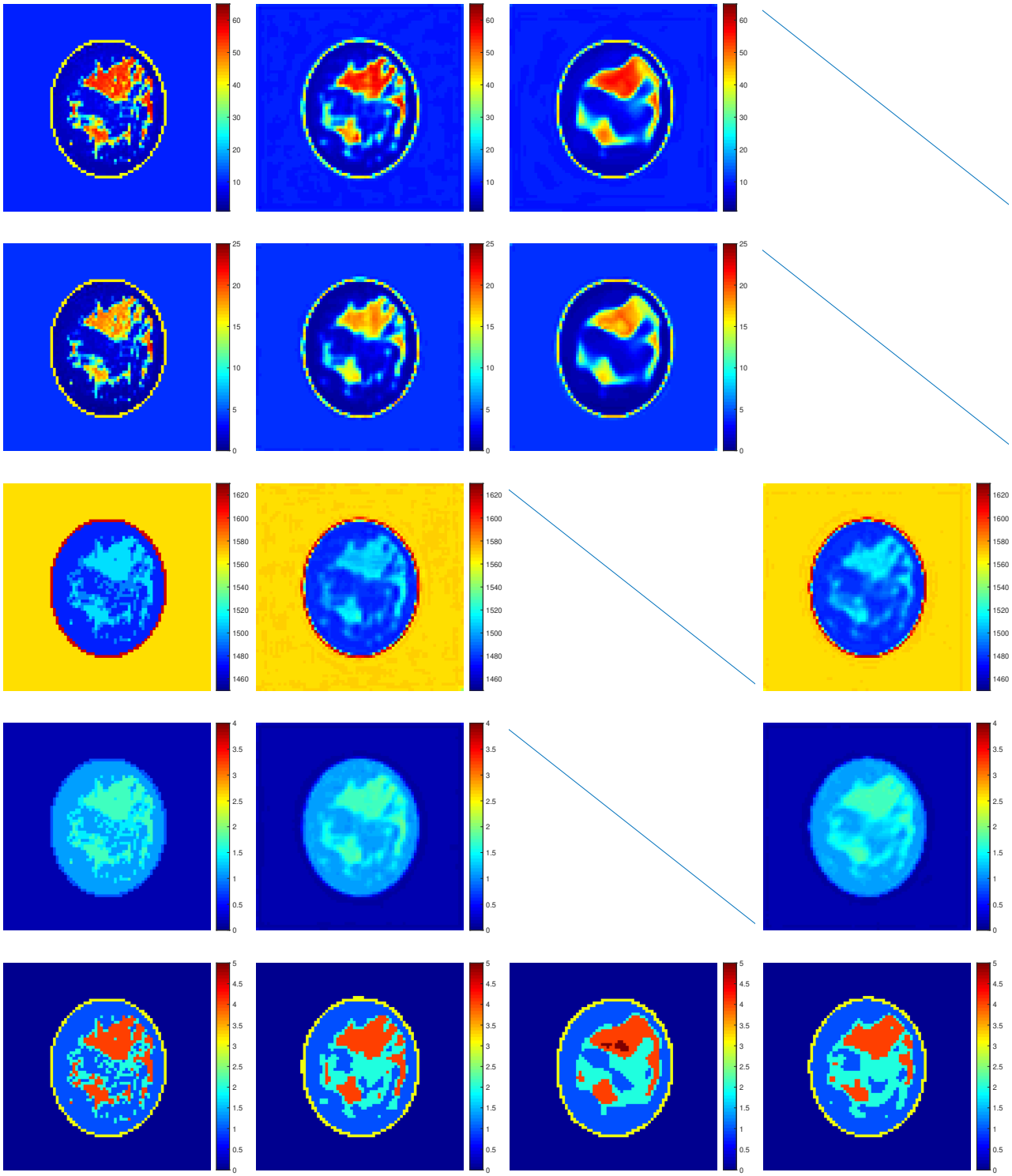

Figure 7.4: Example w/o tumor in Class 3: real ϵ' (1^{st} row) & imaginary parts ϵ'' (2^{nd}) of relative permittivity, sound speed c (3^{rd}), attenuation α (4^{th}), and tissue type image (5^{th}) of groundtruth (1^{st} column), CNN-MM (2^{nd}), CNN-EM (3^{rd}), CNN-US (4^{th}).

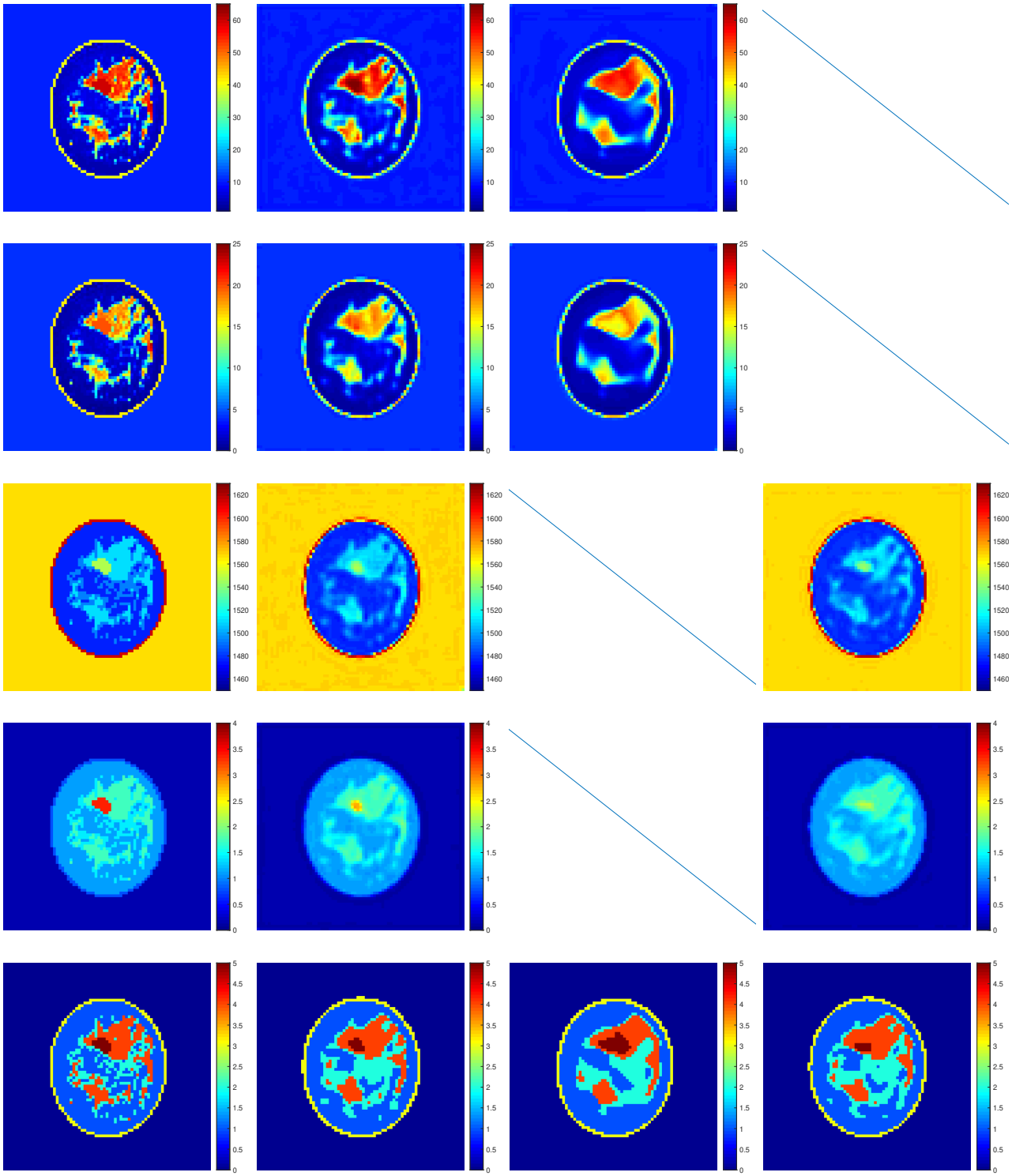

Figure 7.5: Example w/ tumor in Class 3: real ϵ' (1^{st} row) & imaginary parts ϵ'' (2^{nd}) of relative permittivity, sound speed c (3^{rd}), attenuation α (4^{th}) and tissue type image (5^{th}) of groundtruth (1^{st} column), CNN-MM (2^{nd}), CNN-EM (3^{rd}), CNN-US (4^{th}).

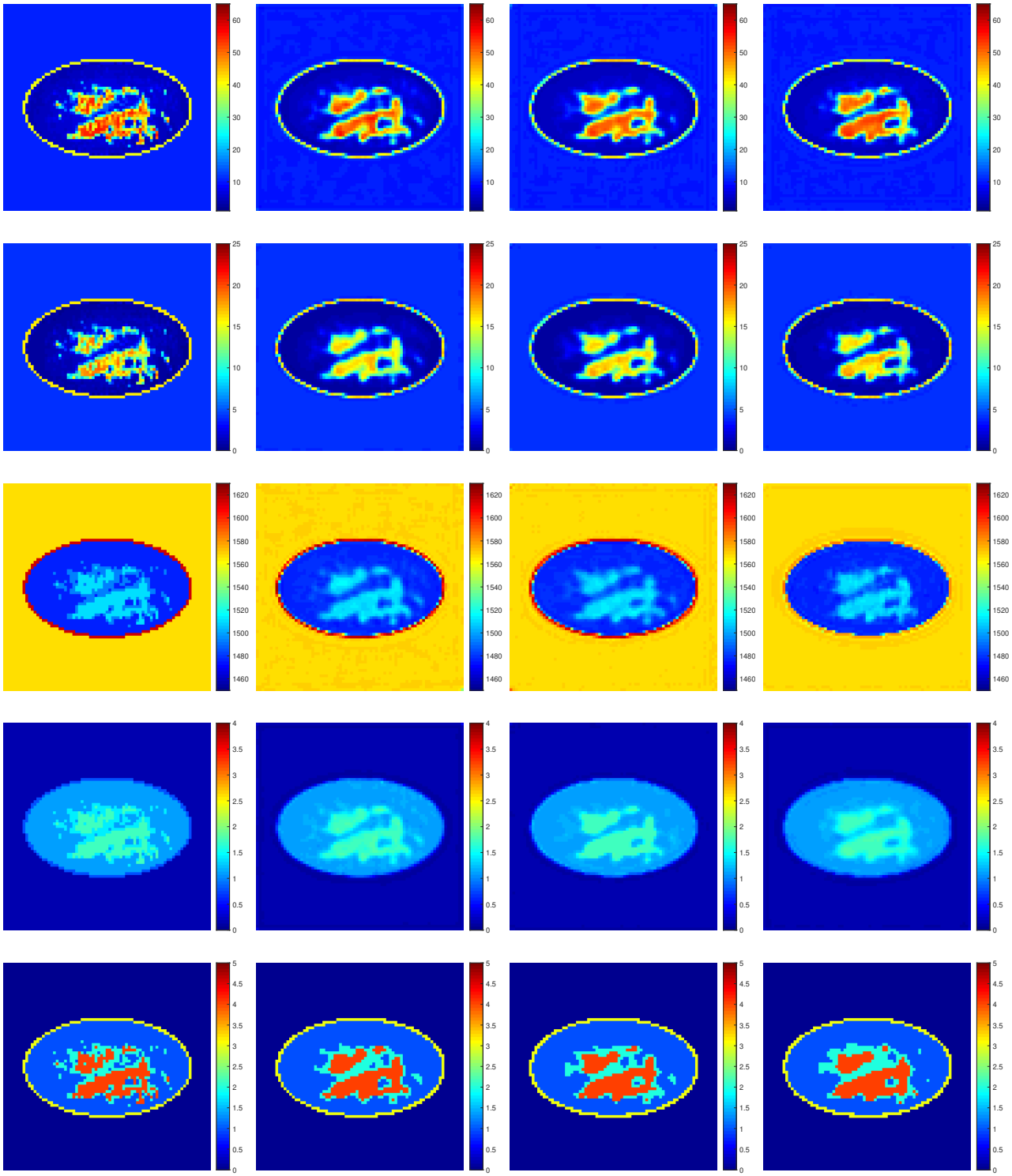

Figure 7.6: Example w/o tumor in Class 4: real ϵ' (1^{st} row) & imaginary parts ϵ'' (2^{nd}) of relative permittivity, sound speed c (3^{rd}), attenuation α (4^{th}) and tissue type image (5^{th}) of groundtruth (1^{st} column), CNN-MM (2^{nd}), CNN-OS (3^{rd}), CNN-RG (4^{th} column, first 4 figures), CNN-SG (4^{th} column, last figure).

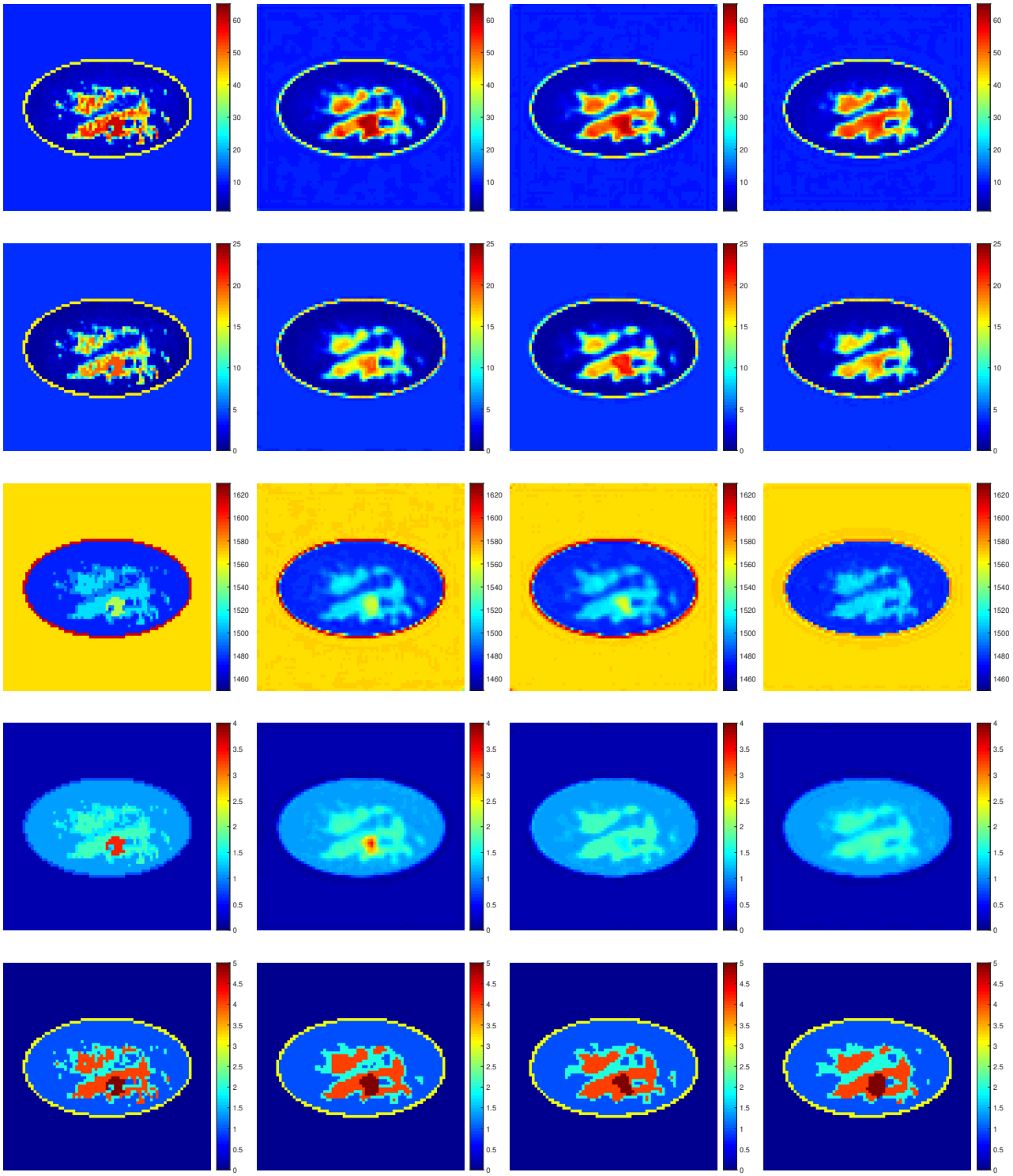

Figure 7.7: Example w/ tumor in Class 4: real ϵ' (1^{st} row) & imaginary part ϵ'' (2^{nd}) of relative permittivity, sound speed c (3^{rd}), attenuation α (4^{th}) and tissue type image (5^{th}) of groundtruth (1^{st} row), CNN-MM (2^{nd}), CNN-OS (3^{rd}), CNN-RG (4^{th} column, first 4 figures), CNN-SG (4^{th} column, last figure).

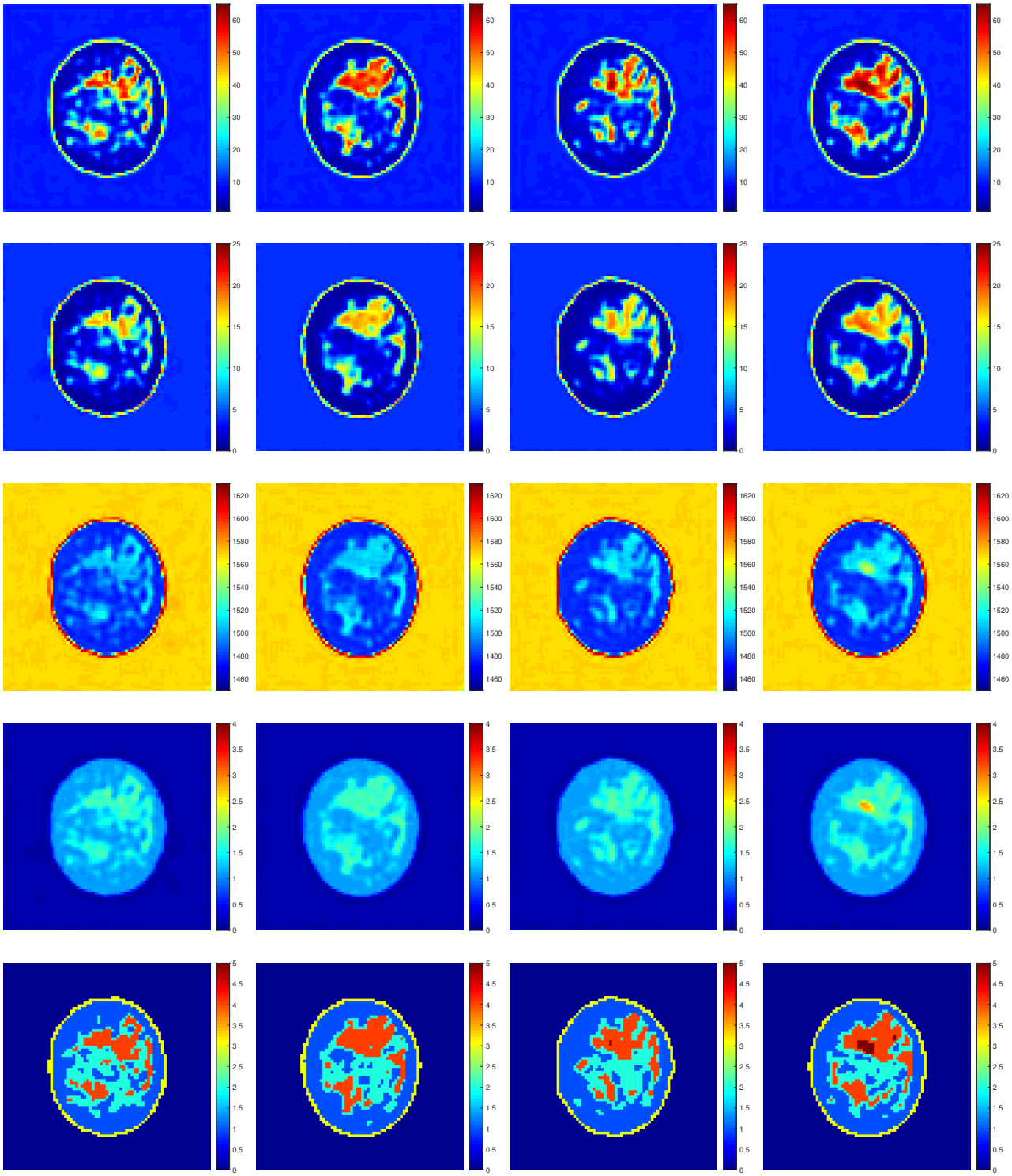

Figure 7.8: Example in Class 3 vs. SNR: CNN-MM w/o tumor and 10 dB noise (1st column), w/o tumor and 15 dB noise (2nd), w/ tumor and 10 dB noise (3rd column), 15 dB noise (4th).

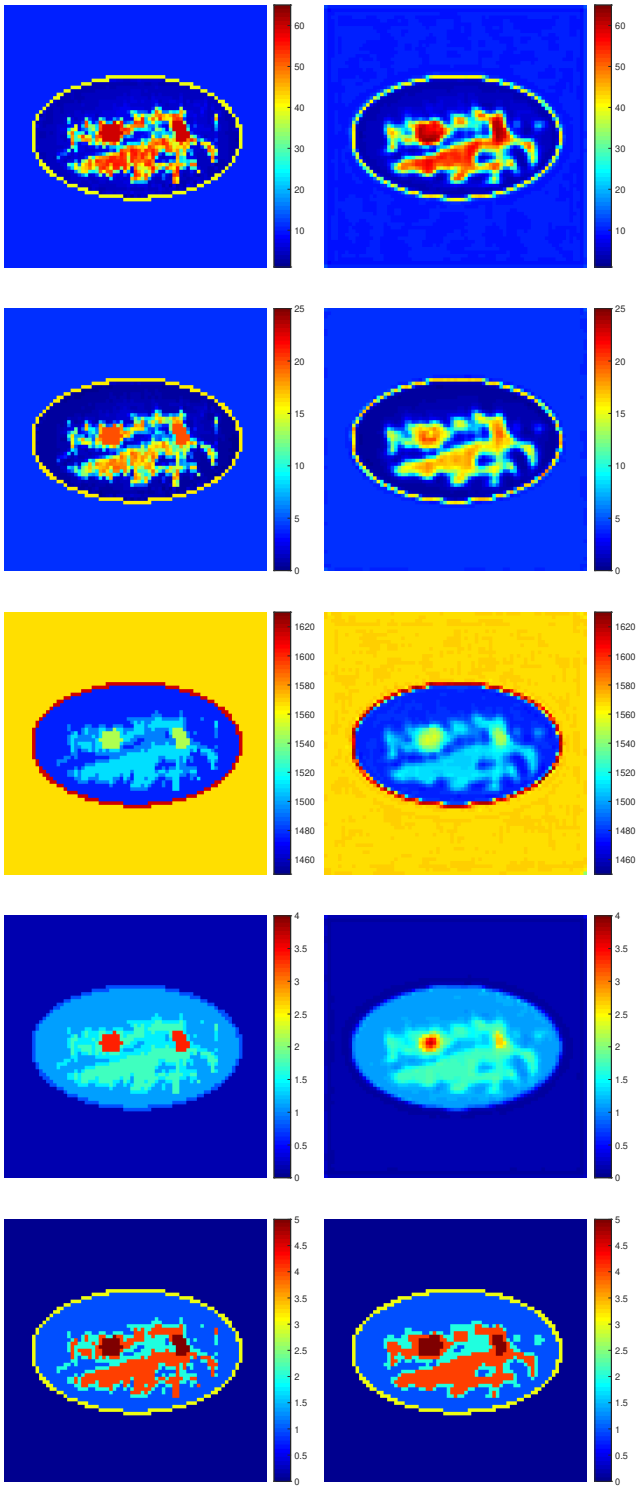

Figure 7.9: Example w/ 2 tumors in Class 4: real ϵ' (1^{st} row) & imaginary parts ϵ'' (2^{nd}) of relative permittivity, sound speed c (3^{rd}), attenuation α (4^{th}), tissue type image (5^{th}) of groundtruth (1^{st} column), result of CNN (2^{nd}).

Chapter 8

Joint inversion of electromagnetic and acoustic data with a variational Bayes method

This chapter is presently being developed as a journal paper to be submitted in due time. So there is some duplicate content in introduction and forward problem, as one is aiming at being comprehensive in that undergoing development.

8.1 Introduction

In Chapter 6 we have proposed a joint inversion algorithm with edge in different directions as the link between the two modalities. However, though the reconstruction results are improved for dielectric parameters, there are many hyperparameters that still need to be chosen. To avoid this problem, we employed CNN for inversion in Chapter 7 where hyperparameters are involved for the training of the network. When the network is trained, it can be used to give the imaging results without tuning hyperparameters for a certain sample. In the present chapter, we propose another method to solve this problem. We try to get the inversion result with a variational Bayesian method [63] and to estimate the hyperparameters automatically in the imaging process.

In a Bayesian framework, priors for the unknown object and the hyperparameters are assigned and a joint posterior distribution can be obtained. In VBA method, this joint posterior distribution is approximated by a free form separable distribution which minimizes the Kullback-Leibler divergence [192] between them. Classical approaches can provide the analytical approximation of the posterior. Such a method has been used as an example in image restoration [193, 194] and image reconstruction [195, 196], especially also in microwave breast imaging tasks [69, 70]. Here we follow our previous work and we use edges as hidden variables for both acoustic and dielectric parameters and estimate the hyperparameters jointly. The rest of this chapter is organized as follows: Section 8.2 describes the principle of the VBA method. The forward model is given in Section 8.3 and the algorithm to solve this problem is detailed in 8.4. Experiments are shown in Section 8.5 and the conclusion is drawn in Section 8.6.

8.2 Variational Bayesian Approximation (VBA) for inverse problem

In this section we take the inverse problem $\mathbf{y} = \mathbf{A}\mathbf{x}$ ($\mathbf{y} \in \mathcal{R}^N$, $\mathbf{x} \in \mathcal{R}^M$ and $\mathbf{A} \in \mathcal{R}^{N \times M}$) as an example to show how to use VBA to solve it.

8.2.1 Bayesian modeling

The principle of Bayesian inference is to determine a prior law $f(\mathbf{x})$ modeling the information that we have on the unknowns before taking the measurements. Then we update this information with the information from the measurements through the likelihood $f(\mathbf{y}|\mathbf{x})$. We determine the posterior law as follows:

$$f(\mathbf{x}|\mathbf{y}) = \frac{f(\mathbf{y}|\mathbf{x})f(\mathbf{x})}{f(\mathbf{y})} \tag{8.1}$$

where $f(\mathbf{y})$ is the normalization factor.

In a Bayesian framework, we consider additive noise in the data equation, and the problem becomes

$$\mathbf{y} = \mathbf{A}\mathbf{x} + \mathbf{n} \tag{8.2}$$

Usually we assume that $\mathbf{n}$ is independent, identically-distributed (iid) Gaussian noise with unknown but common variance γ_n^{-1} as

$$f(\mathbf{n}|\gamma_n) = \mathcal{N}(0, \gamma_n^{-1}\mathbf{I}) \tag{8.3}$$

γ_n is the inverse of variance and is called precision parameter. So we can get

$$f(\mathbf{y}|\mathbf{x}, \gamma_n) = \mathcal{N}(\mathbf{A}\mathbf{x}, \gamma_n^{-1}\mathbf{I}) \propto \gamma_n^{N/2} \exp\{-\frac{\gamma_n}{2}\|\mathbf{y} - \mathbf{A}\mathbf{x}\|^2\} \tag{8.4}$$

Suppose that we have a Gaussian prior model for the solution, thus we can assign an iid Gaussian distribution with mean $\mathbf{x}_0$ and inverse variance γ_x as

$$f(\mathbf{x}|\mathbf{x}_0, \gamma_x) = \mathcal{N}(\mathbf{x}_0, \gamma_x^{-1}\mathbf{I}) \propto \gamma_x^{M/2} \exp\{-\frac{\gamma_x}{2}\|\mathbf{x} - \mathbf{x}_0\|^2\} \tag{8.5}$$

Hierarchical Bayesian approach: To tune the compromise between information from the experiment (data) and prior information, we must tune the hyperparmeters γ_n and γ_x. These parameters are hidden and they cannot be directly observed. One major advantage of the Bayesian framework is that it can be an unsupervised approach where the hyperparameters are jointly estimated by assigning hyper-priors. Thus we can get a hierarchical Bayesian model and we call this problem, joint estimation of the unknown parameter $\mathbf{x}$ and the hidden parameters γ_n and γ_x, a hierarchical Bayesian problem.

To estimate the hyperparamters γ_n and γ_x jointly in our Bayesian framework, we assign a prior model to them. It is obvious that γ_n and γ_x are positive, thus we choose the Gamma distribution[1] to reflect the positivity of these parameters as

$$f(\gamma_n|\alpha_n, \beta_n) = \mathcal{G}_{\gamma_n}(\alpha_n, \beta_n) \propto (\gamma_n)^{\alpha_n - 1} \exp\{-\beta_n\gamma_n\} \tag{8.6}$$

$$f(\gamma_x|\alpha_x, \beta_x) = \mathcal{G}_{\gamma_x}(\alpha_x, \beta_x) \propto (\gamma_x)^{\alpha_x - 1} \exp\{-\beta_x\gamma_x\} \tag{8.7}$$

When we choose $\alpha_{n/x} \to 0$ and $\beta_{n/x} \to 0$, a non-informative law is obtained. In this particular case it is the Jeffrey's law.

Based on Bayes' rule, we can get the joint posterior distribution as

$$\begin{aligned} f(\mathbf{x}, \gamma_n, \gamma_x|\mathbf{y}, \mathbf{x}_0, \alpha_n, \beta_n, \alpha_x, \beta_x) \propto \\ f(\mathbf{y}|\mathbf{x}, \gamma_n)f(\mathbf{x}|\mathbf{x}_0, \gamma_x)f(\gamma_n|\alpha_n, \beta_n)f(\gamma_x|\alpha_x, \beta_x) \end{aligned} \tag{8.8}$$

which can be rewritten to express the posterior distribution of $\mathbf{x}$, $f(\mathbf{x}|\mathbf{y}, \mathbf{x}_0, \gamma_x, \gamma_n)$:

$$f(\mathbf{x}, \gamma_n, \gamma_x|\mathbf{y}, \mathbf{x}_0, \alpha_n, \beta_n, \alpha_x, \beta_x) = f(\mathbf{x}|\mathbf{y}, \mathbf{x}_0, \gamma_x, \gamma_n)f(\gamma_n|\alpha_n, \beta_n)f(\gamma_x|\alpha_x, \beta_x) \tag{8.9}$$

[1] it is a conjugate law with the likelihood of these parameters.

where the posterior law $f(\mathbf{x}|\mathbf{y}, \mathbf{x}_0, \gamma_x, \gamma_n)$ is a Gaussian law as:

$$f(\mathbf{x}|\mathbf{m}, \mathbf{\Sigma}) = (2\pi)^{-n/2}|\det(\mathbf{\Sigma})|^{-1/2} \exp\left(-\frac{1}{2}(\mathbf{x}-\mathbf{m})^t\mathbf{\Sigma}^{-1}(\mathbf{x}-\mathbf{m})\right) \tag{8.10}$$

where the covariance matrix $\mathbf{\Sigma} = (\gamma_n\mathbf{A}^T\mathbf{A} + \gamma_x\mathbf{I})^{-1}$ and the mean $\mathbf{m} = \gamma_n\mathbf{\Sigma}\left(\mathbf{A}^T\mathbf{y} + \mathbf{x}_0\right)$.

We can see in this very simple linear model with a Gaussian likelihood and with a Gaussian prior, that we can have an explicit form of the posterior law knowing the hyperparameters, but the dependency with respect of the hyperparameter is very complex due to the determinant and the inversion of the convariance matrix containing γ_n and γ_x. Thus it is relatively difficult to estimate jointly $\mathbf{x}$, γ_n and γ_x.

8.2.2 Variational Bayesian Approximation

The Variational Bayesian Approximation (VBA) is a way to solve the present problem. Unlike the classical approaches that determine a point estimator from the posterior distribution (maximum or expectation), the VBA approach seeks an approximate distribution. The principle is to determine a law that is simple to handle, in particular a separable law. Indeed, we have seen in the previous example that one of the major difficulties is the complicated dependence between the hyperparameters and the unknowns.

We define an approaching law $q(\mathbf{x}, \gamma_n, \gamma_x)$, which is separable as

$$q(\mathbf{x}, \gamma_n, \gamma_x) = q(\mathbf{x})q(\gamma_n)q(\gamma_x) \tag{8.11}$$

We are going to find the closest probability density function to the true posterior distribution in the sense of the Kullback-Leibler divergence. To that end we need to solve a constraint variational optimization problem:

$$\begin{aligned} q_{opt}(\mathbf{x}, \gamma_n, \gamma_x) &= \text{argmin}_{q\in L_1(\mathcal{R}^{M+2})}\text{KL}\{q(\mathbf{x}, \gamma_n, \gamma_x)\|p(\mathbf{x}, \gamma_n, \gamma_x|\mathbf{y}, \ldots)\} \\ &s.c \int q(\mathbf{x}, \gamma_n, \gamma_x)d\mathbf{x}d\gamma_n d\gamma_x = 1 \end{aligned} \tag{8.12}$$

where the space $L_1(\mathcal{R})$ is the space of the integrable function. If a function $h(t) \in L_1(\mathcal{R})$, the integral $\int h(t)dt$ exists.

The above optimization problem requires us to know the posterior probability density function. However, this density is often difficult to determine analytically due to the computation of the normalization coefficient. Thus, we use the following calculations in order to express our problem according to the joint law instead:

$$\begin{aligned} \log p(\mathbf{y}|\mathcal{M}) &= \log \frac{f(\mathbf{x}, \gamma_n, \gamma_x, \mathbf{y}|\mathcal{M})}{f(\mathbf{x}, \gamma_n, \gamma_x|\mathbf{y}, \mathcal{M})} \\ &= \log \frac{q(\mathbf{x}, \gamma_n, \gamma_x)f(\mathbf{x}, \gamma_n, \gamma_x, \mathbf{y}|\mathcal{M})}{q(\mathbf{x}, \gamma_n, \gamma_x)f(\mathbf{x}, \gamma_n, \gamma_x|\mathbf{y}, \mathcal{M})} \\ &= \int \log \frac{q(\mathbf{x}, \gamma_n, \gamma_x)f(\mathbf{x}, \gamma_n, \gamma_x, \mathbf{y}|\mathcal{M})}{q(\mathbf{x}, \gamma_n, \gamma_x)f(\mathbf{x}, \gamma_n, \gamma_x|\mathbf{y}, \mathcal{M})} q(\mathbf{x}, \gamma_n, \gamma_x)d\mathbf{x}d\gamma_n d\gamma_x \\ &= \int q(\mathbf{x}, \gamma_n, \gamma_x) \log\left(\frac{f(\mathbf{x}, \gamma_n, \gamma_x, \mathbf{y}|\mathcal{M})}{q(\mathbf{x}, \gamma_n, \gamma_x)}\right) d\mathbf{x}d\gamma_n d\gamma_x \\ &+ \int q(\mathbf{x}, \gamma_n, \gamma_x) \log\left(\frac{q(\mathbf{x}, \gamma_n, \gamma_x)}{f(\mathbf{x}, \gamma_n, \gamma_x|\mathbf{y}, \mathcal{M})}\right) d\mathbf{x}d\gamma_n d\gamma_x \\ &= \mathcal{F}(q, \mathbf{y}) + \text{KL}\{q(\mathbf{x}, \gamma_n, \gamma_x)\|f(\mathbf{x}, \gamma_n, \gamma_x|\mathbf{y}, \mathcal{M})\} \end{aligned} \tag{8.13}$$

It can be seen that minimizing the KL divergence is equivalent to maximize the free negative energy $\mathcal{F}(q, \mathbf{y})$. The problem becomes

$$q_{opt}(\mathbf{x}, \gamma_n, \gamma_x) = \text{argmax}_q \mathcal{F}(q, \mathbf{y}) \tag{8.14}$$

With the assuming separation form, the solution can be obtained with a fixed point method by proceeding in an alternate update scheme:

$$q^{(n+1)}(\mathbf{x}) = \text{argmax}_{q(\mathbf{x})} \mathcal{F}(q, \mathbf{y}) \quad \text{s.c.} \quad \int q(\mathbf{x}) d\mathbf{x} = 1 \tag{8.15}$$

$$= \frac{1}{Z_x} \exp\left[\langle \log f(\mathbf{y}, \mathbf{x}, \gamma_n, \gamma_x | \mathcal{M}) \rangle_{q^{(n)}(\gamma_n) q^{(n)}(\gamma_x)}\right] \tag{8.16}$$

$$q^{(n+1)}(\gamma_n) = \frac{1}{Z_{\gamma_n}} \exp\left[\langle \log f(\mathbf{y}, \mathbf{x}, \gamma_n, \gamma_x | \mathcal{M}) \rangle_{q^{(n+1)}(\mathbf{x}) q^{(n)}(\gamma_x)}\right] \tag{8.17}$$

$$q^{(n+1)}(\gamma_x) = \frac{1}{Z_{\gamma_x}} \exp\left[\langle \log f(\mathbf{y}, \mathbf{x}, \gamma_n, \gamma_x | \mathcal{M}) \rangle_{q^{(n+1)}(\mathbf{x}) q^{(n+1)}(\gamma_n)}\right] \tag{8.18}$$

with $\langle h(\mathbf{x}, \gamma_n, \gamma_x) \rangle_{q(\gamma_n) q(\gamma_x)} = \int h(\mathbf{x}, \gamma_n, \gamma_x) q(\gamma_n) q(\gamma_x) d\gamma_n d\gamma_x$.

To simplify the calculation of the approximate law q we can choose a prior law conjugate with the likelihood as described before. Then, we know that the posterior distribution is in a classical law. With this choice, we know that $\mathbf{x}$ follows a Gaussian law and γ_n and γ_x follow a Gamma law. Now for each iteration we only update the parameter of the approximate law:

$$q(\mathbf{x}) = \mathcal{N}(\mathbf{m}_x, \mathbf{\Sigma}_x) \tag{8.19}$$

$$q(\gamma_n) = \mathcal{G}(\alpha_n, \beta_n) \tag{8.20}$$

$$q(\gamma_x) = \mathcal{G}(\alpha_x, \beta_x) \tag{8.21}$$

With these shaping parameters, we can get the density distribution of each unknown and those can be estimated by choosing the mean of these distributions.

8.3 Forward problem

One considers as before the two-dimensional case. To remind, time-harmonic waves are assumed with time dependence $\exp(-i\omega t)$ for both acoustic and electromagnetic cases. The modeled breast is located inside a domain of interest (DoI) $\mathcal{D}$. The known background medium is characterized by its complex relative permittivity ϵ_b, permeability μ_b, and wavenumber $k_b^{\text{em}} = \omega\sqrt{\epsilon_0 \epsilon_b \mu_b}$ in electromagnetics, and its speed of sound c_b, attenuation α_b, and wavenumber $k_b^{\text{ac}} = \omega/c_b + i\alpha_b$ in acoustics. Permeability and density are taken constant within the DoI. The unknown parameters are the complex relative permittivity $\epsilon_r(\mathbf{r}) = \epsilon_r'(\mathbf{r}) + i\epsilon_r''(\mathbf{r})$, the sound speed $c(\mathbf{r})$ and the attenuation $\alpha(\mathbf{r})$. For each imaging modality, N_i probes are evenly located at $\mathbf{r}_v'$, $v = 1, 2, \ldots, N_i$ on a circle $\mathcal{S}$, see Figure 8.1. Each illuminates the DoI and scattered fields are collected by all.

To solve the problem numerically, $\mathcal{D}$ is discretized into $M = N_x \times N_y$ small cells centered at $\mathbf{r}_m$, $m = 1, 2, \ldots, M$. A pulse-basis point-matching method of moments (MoM) is employed. Every square cell is approximated by a small disk with same area and with equivalent radius R. The acoustic and dielectric contrasts are defined as

$$\chi^{\text{ac}}(\mathbf{r}) = \frac{(k^{\text{ac}}(\mathbf{r}))^2 - (k_b^{\text{ac}})^2}{(k_b^{\text{ac}})^2} \tag{8.22}$$

$$\chi^{\text{em}}(\mathbf{r}) = \frac{(k^{\text{em}}(\mathbf{r}))^2 - (k_b^{\text{em}})^2}{(k_b^{\text{em}})^2} \tag{8.23}$$

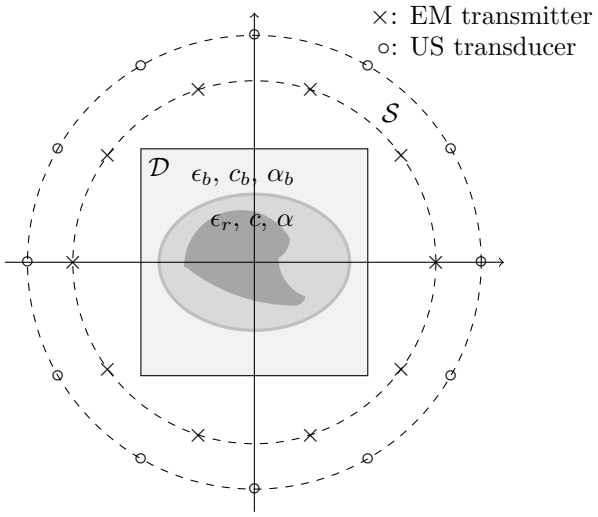

Figure 8.1: Schematic diagram of configuration of two modalities working in a multistatic way

The discrete form of χ is denoted as $\boldsymbol{\chi} = [\chi(\mathbf{r}_1), \ldots, \chi(\mathbf{r}_M)]^T$. We have source-type integral equations describing the relation between the fields and contrast for pth incidence as

$$\mathbf{J}_p = \mathbf{X}\mathbf{F}_p^{\mathbf{i}} + \mathbf{X}\mathbf{G}_{\mathbf{d}}\mathbf{J}_p \tag{8.24}$$

$$\mathbf{F}_p^{\mathbf{s}} = \mathbf{G}_{\mathbf{s}}\mathbf{J}_p \tag{8.25}$$

where F is the pressure field P or the electric field E. Superscripts "i" and "t" denote incident and total field, i.e., the field inside $\mathcal{D}$ without and with breast, respectively. In this case, $\mathbf{F}_p^{\mathbf{t/i}}$ is a $M \times 1$ vector with $\mathbf{F}_p^{\mathbf{t/i}} = [F_p^{t/i}(\mathbf{r}_1), \ldots, F_p^{t/i}(\mathbf{r}_M)]^T$ where superscript "T" denotes transpose. $\mathbf{F}_p^{\mathbf{s}}$ is a $N_i \times 1$ vector representing the scattered field collected by the receivers as $\mathbf{F}_p^{\mathbf{s}} = [F_p^s(\mathbf{r}'_1), \ldots, F_p^s(\mathbf{r}'_{N_i})]^T$. $\mathbf{X}$ is a matrix with diagonal entry representing the contrast at different location, as $\mathrm{diag}(\mathbf{X}) = \boldsymbol{\chi}$. J is the contrast current defined as

$$J(\mathbf{r}) = \chi(\mathbf{r})F^t(\mathbf{r}) \tag{8.26}$$

$\mathbf{G}_{\mathbf{d}}$ is a $M \times M$ matrix with element

$$[\mathbf{G}_{\mathbf{d}}]_{m,m'} = \begin{cases} \dfrac{ik_b\pi R}{2}\,\mathrm{J}_1(k_bR)\,\mathrm{H}_0^{(1)}(k_b|\mathbf{r}_m - \mathbf{r}_{m'}|), m \neq m' \\ \dfrac{ik_b\pi R}{2}\,\mathrm{H}_1^{(1)}(k_bR) - 1, \text{otherwise} \end{cases} \tag{8.27}$$

where J_1 is the 1st-kind Bessel function, $\mathrm{H}_1^{(1)}$ the 1st-kind 1st-order Hankel function and $\mathrm{H}_0^{(1)}$ the 1st-kind 0th-order one. The $N_i \times M$ matrix $\mathbf{G}_{\mathbf{s}}$ is

$$[\mathbf{G}_{\mathbf{s}}]_{v,m} = \frac{ik_b\pi R}{2}\,\mathrm{J}_1(k_bR)\,\mathrm{H}_0^{(1)}(k_b|\mathbf{r}'_v - \mathbf{r}_m|) \tag{8.28}$$

In a Bayesian framework, two variables $\mathbf{n}$ and $\boldsymbol{\vartheta}$ are introduced, representing the errors in the forward model, such as measurement noise and descritization error. The forward model becomes

$$\mathbf{J}_p = \mathbf{X}\mathbf{F}_p^{\mathbf{i}} + \mathbf{X}\mathbf{G}_{\mathbf{d}}\mathbf{J}_p + \mathbf{n} \tag{8.29}$$

$$\mathbf{F}_p^{\mathbf{s}} = \mathbf{G}_{\mathbf{s}}\mathbf{J}_p + \boldsymbol{\vartheta} \tag{8.30}$$

We assume that both $\mathbf{n}$ and $\boldsymbol{\vartheta}$ follow a normal distribution with zero means. Note that the errors are complex-valued, and here we assume that real and imaginary parts are independent and have the same variance, thus we have $\Re\{\mathbf{n}\}/\Im\{\mathbf{n}\} \sim \mathcal{N}(0, (\gamma_n/2)^{-1}\mathbf{I})$ and $\Re\{\boldsymbol{\vartheta}\}/\Im\{\boldsymbol{\vartheta}\} \sim \mathcal{N}(0, (\gamma_s/2)^{-1}\mathbf{I})$ where γ_n and γ_s are precision parameters that need to be estimated.

8.4 Bayesian framework

8.4.1 Bayesian modeling

Given the distributions of the errors, we can get the Gaussian likelihood of the data and prior law of the contrast current as

$$f(\mathbf{F}_p^{\mathbf{s}}|\mathbf{J}_p,\gamma_n) \propto (\gamma_n)^{N_i} \exp\{-\gamma_n \|\mathbf{F}_p^{\mathbf{s}} - \mathbf{G_s}\mathbf{J}_p\|^2\} \tag{8.31}$$

$$f(\mathbf{J}_p|\boldsymbol{\chi},\gamma_s,\mathbf{F}_p^{\mathbf{i}}) \propto (\gamma_s)^{M} \exp\{-\gamma_s \|\mathbf{J}_p - \mathbf{X}\mathbf{F}_p^{\mathbf{i}} - \mathbf{G_d}\mathbf{J}_p\|^2\} \tag{8.32}$$

The prior law of the contrast is a Gaussian law. We intend to introduce a smoothness information to limit the impact of the noise. Moreover, we aim at preserving the edge of the object. So we introduce a Gaussian law knowing the hidden edge variables $\mathbf{b}$.

$$\begin{aligned} f(\boldsymbol{\chi}|\gamma_b,\mathbf{b}) \propto (\gamma_b)^{4M} &\exp\left\{-\gamma_b(\mathbf{D}_1\boldsymbol{\chi})^\dagger \mathrm{diag}(\mathbf{b}_1)\mathbf{D}_1\boldsymbol{\chi}\right\} \\ &\times \exp\left\{-\gamma_b(\mathbf{D}_2\boldsymbol{\chi})^\dagger \mathrm{diag}(\mathbf{b}_2)\mathbf{D}_2\boldsymbol{\chi}\right\} \\ &\times \exp\left\{-\gamma_b(\mathbf{D}_3\boldsymbol{\chi})^\dagger \mathrm{diag}(\mathbf{b}_3)\mathbf{D}_3\boldsymbol{\chi}\right\} \\ &\times \exp\left\{-\gamma_b(\mathbf{D}_4\boldsymbol{\chi})^\dagger \mathrm{diag}(\mathbf{b}_4)\mathbf{D}_4\boldsymbol{\chi}\right\} \end{aligned} \tag{8.33}$$

where $\mathbf{D}_1$ is the horizontal discrete gradient, $\mathbf{D}_2$ the vertical, $\mathbf{D}_3$ the diagonal and $\mathbf{D}_4$ the second diagonal. Note that here we follow the work in Chapter 6, the gradient is normalized by a scaling parameter δ. Edge variable $\mathbf{b} = [\mathbf{b}_1, \mathbf{b}_2, \mathbf{b}_3, \mathbf{b}_4]$ is used to indicate the presence of a discontinuity in different directions. The prior law of $[\mathbf{b}_u]_m$ is a Bernoulli distribution $[\mathbf{b}_u]_m \sim \mathcal{BN}(p_b)$ as

$$Pr([\mathbf{b}_u]_m = 1|p_b) = p_b, \quad Pr([\mathbf{b}_u]_m = 0|p_b) = 1 - p_b \tag{8.34}$$

where p_b is a prior probability and is assumed to be known. These Bernoulli variables are the key point of our approach which are common to the two inverse problems. They allow to promote the solutions with the discontinuity in the same location in the two modality.

As we can see in Equations (8.31), (8.32) and (8.33), we have to tune three parameters γ per modality. Tuning of six parameters empirically is difficult. So we adopt a full Bayesian approach. where they are jointly estimated. To simplify the computation, we use the conjugate prior for the hyperparameters, i.e., the Gamma distribution, as follows

$$f(\gamma_n|\alpha_{n0},\beta_{n0}) = \mathcal{G}(\alpha_{n0},\beta_{n0}) \propto (\gamma_n)^{\alpha_{n0}-1} \exp\{-\beta_{n0}\gamma_n\} \tag{8.35}$$

$$f(\gamma_s|\alpha_{s0},\beta_{s0}) = \mathcal{G}(\alpha_{s0},\beta_{s0}) \propto (\gamma_s)^{\alpha_{s0}-1} \exp\{-\beta_{s0}\gamma_s\} \tag{8.36}$$

$$f(\gamma_b|\alpha_{b0},\beta_{b0}) = \mathcal{G}(\alpha_{b0},\beta_{b0}) \propto (\gamma_b)^{\alpha_{b0}-1} \exp\{-\beta_{b0}\gamma_b\} \tag{8.37}$$

where when $\alpha_{n0} \to 0$ and $\beta_{n0} \to 0$, we can get a non-informative prior for γ_n, and the same case for γ_s and γ_b. With the above distributions for both acoustic and electromagnetic cases, based on Bayes' rule, the joint posterior distribution can be expressed as

$$\begin{aligned} &f(\mathbf{J}^{\mathrm{ac}},\boldsymbol{\chi}^{\mathrm{ac}},\mathbf{J}^{\mathrm{em}},\boldsymbol{\chi}^{\mathrm{em}},\gamma_n^{\mathrm{ac}},\gamma_s^{\mathrm{ac}},\gamma_b^{\mathrm{ac}},\gamma_n^{\mathrm{em}},\gamma_s^{\mathrm{em}},\gamma_b^{\mathrm{em}},\mathbf{b}|\mathbf{E}^{\mathbf{s}},\mathbf{E}^{\mathbf{i}},\mathbf{P}^{\mathbf{s}},\mathbf{P}^{\mathbf{i}}) \propto \\ &\quad \prod_p f(\mathbf{E}_p^{\mathbf{s}}|\mathbf{J}_p^{\mathrm{em}},\gamma_n^{\mathrm{em}}) \prod_p f(\mathbf{J}_p^{\mathrm{em}}|\boldsymbol{\chi}^{\mathrm{em}},\gamma_s^{\mathrm{em}},\mathbf{E}_p^{\mathbf{i}}) f(\boldsymbol{\chi}^{\mathrm{em}}|\mathbf{b},\gamma_b^{\mathrm{em}}) \\ &\quad \times \prod_p f(\mathbf{P}_p^{\mathbf{s}}|\mathbf{J}_p^{\mathrm{ac}},\gamma_n^{\mathrm{ac}}) \prod_p f(\mathbf{J}_p^{\mathrm{ac}}|\boldsymbol{\chi}^{\mathrm{ac}},\gamma_s^{\mathrm{ac}},\mathbf{P}_p^{\mathbf{i}}) f(\boldsymbol{\chi}^{\mathrm{ac}}|\mathbf{b},\gamma_b^{\mathrm{ac}}) \\ &\quad \times f(\gamma_n^{\mathrm{em}}|\alpha_{n0}^{\mathrm{em}},\beta_{n0}^{\mathrm{em}}) f(\gamma_s^{\mathrm{em}}|\alpha_{s0}^{\mathrm{em}},\beta_{s0}^{\mathrm{em}}) f(\gamma_b^{\mathrm{em}}|\alpha_{b0}^{\mathrm{em}},\beta_{b0}^{\mathrm{em}}) \\ &\quad \times f(\gamma_n^{\mathrm{ac}}|\alpha_{n0}^{\mathrm{ac}},\beta_{n0}^{\mathrm{ac}}) f(\gamma_s^{\mathrm{ac}}|\alpha_{s0}^{\mathrm{ac}},\beta_{s0}^{\mathrm{ac}}) f(\gamma_b^{\mathrm{ac}}|\alpha_{b0}^{\mathrm{ac}},\beta_{b0}^{\mathrm{em}}) \prod_u \prod_m Pr([\mathbf{b}_u]_m|p_b) \end{aligned} \tag{8.38}$$

8.4.2 Variational Bayesian Approximation

As described before, with the variational Bayesian technique, an approximate distribution $q(\mathbf{x})$ ($\mathbf{x} = \{\mathbf{J}^{\text{ac}}, \mathbf{J}^{\text{em}}, \boldsymbol{\chi}^{\text{ac}}, \boldsymbol{\chi}^{\text{em}}, \mathbf{b}, \Theta\}$ with Θ the set of hyperparameters) consisting of a number of free-form separable distributions for each set of parameters to be estimated is to be found to approximate the true posterior distribution. $q(\mathbf{x})$ is chosen as

$$\begin{aligned} q(\mathbf{x}) = \prod_{p=1}^{N_i N_f} q(\mathbf{J}_p^{\text{ac}}) q(\boldsymbol{\chi}^{\text{ac}}) \prod_{p=1}^{N_i} q(\mathbf{J}_p^{\text{em}}) q(\boldsymbol{\chi}^{\text{em}}) q(\gamma_n^{\text{ac}}) q(\gamma_n^{\text{em}}) \\ \times q(\gamma_s^{\text{ac}}) q(\gamma_s^{\text{em}}) q(\gamma_b^{\text{ac}}) q(\gamma_b^{\text{em}}) \prod_{u}^{4} \prod_{m}^{M} q([\mathbf{b}_u]_m) \end{aligned} \tag{8.39}$$

where N_f is the number of frequencies employed in acoustic case which will be described in the experiment section.

The approximate laws are chosen as follows

$$\begin{aligned} q(\mathbf{J}_p^{\text{ac}}) = \mathcal{N}(\mathbf{m}_{J_p}^{\text{ac}}, \boldsymbol{\Sigma}_J^{\text{ac}}) \quad q(\boldsymbol{\chi}^{\text{ac}}) = \mathcal{N}(\mathbf{m}_\chi^{\text{ac}}, \boldsymbol{\Sigma}_\chi^{\text{ac}}) \\ q(\mathbf{J}_p^{\text{em}}) = \mathcal{N}(\mathbf{m}_{J_p}^{\text{em}}, \boldsymbol{\Sigma}_J^{\text{em}}) \quad q(\boldsymbol{\chi}^{\text{em}}) = \mathcal{N}(\mathbf{m}_\chi^{\text{em}}, \boldsymbol{\Sigma}_\chi^{\text{em}}) \\ q(\gamma_n^{\text{em}}) = \mathcal{G}(\alpha_n^{\text{em}}, \beta_n^{\text{em}}) \quad q(\gamma_s^{\text{em}}) = \mathcal{G}(\alpha_s^{\text{em}}, \beta_s^{\text{em}}) \\ q(\gamma_n^{\text{ac}}) = \mathcal{G}(\alpha_n^{\text{ac}}, \beta_n^{\text{ac}}) \quad q(\gamma_s^{\text{ac}}) = \mathcal{G}(\alpha_s^{\text{ac}}, \beta_s^{\text{ac}}) \\ q(\gamma_b^{\text{em}}) = \mathcal{G}(\alpha_b^{\text{em}}, \beta_b^{\text{em}}) \quad q(\gamma_b^{\text{ac}}) = \mathcal{G}(\alpha_b^{\text{ac}}, \beta_b^{\text{ac}}) \\ q([\mathbf{b}_u]_m = 1) = [\boldsymbol{\pi}_u]_m \end{aligned} \tag{8.40}$$

The shaping parameters are estimated during the optimization process as follows.

The parameters for the acoustic contrast source are updated as

$$\boldsymbol{\Sigma}_J^{\text{ac}} = \left\{ \tilde{\gamma}_n^{\text{ac}} (\mathbf{G}_{\mathbf{s}}^{\text{ac}})^\dagger \mathbf{G}_{\mathbf{s}}^{\text{ac}} + \tilde{\gamma}_s^{\text{ac}} \left[(\mathbf{G}_{\mathbf{d}}^{\text{ac}})^\dagger \text{diag}([\mathbf{m}_\chi^{\text{ac}}]^2) \mathbf{G}_{\mathbf{d}}^{\text{ac}} + \mathbf{I} - 2\Re((\mathbf{G}_{\mathbf{d}}^{\text{ac}})^\dagger \text{diag}(\overline{\mathbf{m}}_\chi^{\text{ac}})) \right] \right\}^{-1} \tag{8.41}$$

$$\mathbf{m}_{J_p}^{\text{ac}} = \boldsymbol{\Sigma}_J^{\text{ac}} \left(\tilde{\gamma}_n^{\text{ac}} (\mathbf{G}_{\mathbf{s}}^{\text{ac}})^\dagger \mathbf{P}_p^{\mathbf{s}} + \tilde{\gamma}_s^{\text{ac}} \left(\mathbf{m}_\chi^{\text{ac}} \mathbf{P}_p^{\mathbf{i}} - (\mathbf{G}_{\mathbf{d}}^{\text{ac}})^\dagger \text{diag}([\mathbf{m}_\chi^{\text{ac}}]^2) \mathbf{P}_p^{\mathbf{i}} \right) \right) \tag{8.42}$$

with $[\mathbf{m}_\chi^{\text{ac}}]^2 = \mathbf{m}_\chi^{\text{ac}}. \times \overline{\mathbf{m}}_\chi^{\text{ac}} + \text{diag}(\boldsymbol{\Sigma}_\chi^{\text{ac}})$ and $\overline{\mathbf{m}}_\chi^{\text{ac}}$ is the conjugate of $\mathbf{m}_\chi^{\text{ac}}$. Those s for the acoustic contrast are as

$$\boldsymbol{\Sigma}_\chi^{\text{ac}} = \left\{ \tilde{\gamma}_s^{\text{ac}} \text{diag}(\sum_p [\mathbf{P}_p^{\mathbf{t}}]^2) + \tilde{\gamma}_b^{\text{ac}} \sum_u (\mathbf{D}_u^T \text{diag}(\boldsymbol{\pi}_u) \mathbf{D}_u) \right\}^{-1} \tag{8.43}$$

$$\mathbf{m}_\chi^{\text{ac}} = \boldsymbol{\Sigma}_\chi^{\text{ac}} \left[\tilde{\gamma}_s^{\text{ac}} \sum_p \mathbf{m}_{J_p}^{\text{ac}}. \times \overline{\mathbf{P}}_p^{\mathbf{i}} + \text{diag}\left((\mathbf{m}_J^{\text{ac}} (\mathbf{m}_J^{\text{ac}})^\dagger + \boldsymbol{\Sigma}_J^{\text{ac}}) (\mathbf{G}_{\mathbf{d}}^{\text{ac}})^\dagger \right) \right] \tag{8.44}$$

with $[\mathbf{P}_p^{\mathbf{t}}]^2 = \mathbf{m}_{P_p^t}. \times \overline{\mathbf{m}}_{P_p^t} + \text{diag}(\boldsymbol{\Sigma}_{P_p^t})$ where $\mathbf{m}_{P_p^t} = \mathbf{P}_p^{\mathbf{i}} + \mathbf{G}_{\mathbf{d}}^{\text{ac}} \mathbf{m}_{J_p}^{\text{ac}}$ and $\boldsymbol{\Sigma}_{P_p^t} = \mathbf{G}_{\mathbf{d}}^{\text{ac}} \boldsymbol{\Sigma}_J^{\text{ac}} (\mathbf{G}_{\mathbf{d}}^{\text{ac}})^\dagger$.

$\tilde{\gamma}_n^{\text{ac}}$ is calculated as $\tilde{\gamma}_n^{\text{ac}} = \alpha_n^{\text{ac}} / \beta_n^{\text{ac}}$ with

$$\alpha_n^{\text{ac}} = \alpha_{n0}^{\text{ac}} + N_i N_r N_f \tag{8.45}$$

$$\beta_n^{\text{ac}} = \beta_{n0}^{\text{ac}} + \sum_p \left(\|\mathbf{G}_{\mathbf{s}}^{\text{ac}} \mathbf{m}_{J_p}^{\text{ac}}\|^2 + \|\mathbf{P}_p^{\mathbf{s}}\|^2 - 2\Re < \mathbf{G}_{\mathbf{s}}^{\text{ac}} \mathbf{m}_{J_p}^{\text{ac}}, \mathbf{P}_p^{\mathbf{s}} > + \text{tr}(\mathbf{G}_{\mathbf{s}}^{\text{ac}} \boldsymbol{\Sigma}_J^{\text{ac}} (\mathbf{G}_{\mathbf{s}}^{\text{ac}})^\dagger) \right) \tag{8.46}$$

$\tilde{\gamma}_s^{\text{ac}}$ is calculated as $\tilde{\gamma}_s^{\text{ac}} = \alpha_s^{\text{ac}} / \beta_s^{\text{ac}}$ with

$$\alpha_s^{\text{ac}} = \alpha_{s0}^{\text{ac}} + N_i N_f N_m \tag{8.47}$$

$$\beta_s^{\text{ac}} = \beta_{s0}^{\text{ac}} + \sum_p \left(\|\mathbf{m}_{J_p}^{\text{ac}}\|^2 + \|\mathbf{m}_\chi^{\text{ac}}\|^2 \|\mathbf{P}_p^{\mathbf{t}}\|^2 - 2\Re < \mathbf{m}_\chi^{\text{ac}}, \mathbf{m}_{J_p}^{\text{ac}} \overline{\mathbf{P}}_p^{\mathbf{t}} > \right) \tag{8.48}$$

with $\mathbf{m}_{J_p}^{\mathrm{ac}}\overline{\mathbf{P}}_p^{\mathbf{t}} = \mathbf{m}_{J_p}^{\mathrm{ac}}.\times\overline{\mathbf{P}}_p^{\mathbf{i}} + \mathrm{diag}\left((\mathbf{m}_{J_p}^{\mathrm{ac}}(\mathbf{m}_{J_p}^{\mathrm{ac}})^\dagger + \mathbf{\Sigma}_J^{\mathrm{ac}})(\mathbf{G}_{\mathbf{d}}^{\mathrm{ac}})^\dagger\right)$.

$\tilde{\gamma}_b^{\mathrm{ac}}$ is calculated as $\tilde{\gamma}_b^{\mathrm{ac}} = \alpha_b^{\mathrm{ac}}/\beta_b^{\mathrm{ac}}$ with

$$\alpha_b^{\mathrm{ac}} = \alpha_{b0}^{\mathrm{ac}} + 4N_m \tag{8.49}$$

$$\beta_b^{\mathrm{ac}} = \beta_{b0}^{\mathrm{ac}} + \sum_u \left(< \mathbf{D}_u\mathbf{m}_\chi^{\mathrm{ac}}, \mathrm{diag}(\boldsymbol{\pi}_u)(\mathbf{D}_u\mathbf{m}_\chi^{\mathrm{ac}}) > + \mathrm{tr}(\mathbf{D}_u\mathbf{\Sigma}_\chi^{\mathrm{ac}}\mathbf{D}_u^T.\times\mathrm{diag}(\boldsymbol{\pi}_u))\right) \tag{8.50}$$

Similarly, the parameters for the microwave case are updated as follows. For the parameters concerning the contrast source, we have

$$\mathbf{\Sigma}_J^{\mathrm{em}} = \left\{\tilde{\gamma}_n^{\mathrm{em}}(\mathbf{G}_{\mathbf{s}}^{\mathrm{em}})^\dagger\mathbf{G}_{\mathbf{s}}^{\mathrm{em}} + \tilde{\gamma}_s^{\mathrm{em}}\left[(\mathbf{G}_{\mathbf{d}}^{\mathrm{em}})^\dagger\mathrm{diag}([\mathbf{m}_\chi^{\mathrm{em}}]^2)\mathbf{G}_{\mathbf{d}}^{\mathrm{em}} + \mathbf{I} - 2\Re((\mathbf{G}_{\mathbf{d}}^{\mathrm{em}})^\dagger\mathrm{diag}(\overline{\mathbf{m}}_\chi^{\mathrm{em}}))\right]\right\}^{-1} \tag{8.51}$$

$$\mathbf{m}_{J_p}^{\mathrm{em}} = \mathbf{\Sigma}_J^{\mathrm{em}}\left(\tilde{\gamma}_n^{\mathrm{em}}(\mathbf{G}_{\mathbf{s}}^{\mathrm{em}})^\dagger\mathbf{E}_p^{\mathbf{s}} + \tilde{\gamma}_s^{\mathrm{em}}\left(\mathbf{m}_\chi^{\mathrm{em}}\mathbf{E}_p^{\mathbf{i}} - (\mathbf{G}_{\mathbf{d}}^{\mathrm{em}})^\dagger\mathrm{diag}([\mathbf{m}_\chi^{\mathrm{em}}]^2)\mathbf{E}_p^{\mathbf{i}}\right)\right) \tag{8.52}$$

with $[\mathbf{m}_\chi^{\mathrm{em}}]^2 = \mathbf{m}_\chi^{\mathrm{em}}.\times\overline{\mathbf{m}}_\chi^{\mathrm{em}} + \mathrm{diag}(\mathbf{\Sigma}_\chi^{\mathrm{em}})$ and $\overline{\mathbf{m}}_\chi^{\mathrm{em}}$ is the conjugate of $\mathbf{m}_\chi^{\mathrm{em}}$. The parameters for the dielectric contrast are calculated as

$$\mathbf{\Sigma}_\chi^{\mathrm{em}} = \left\{\tilde{\gamma}_s^{\mathrm{em}}\mathrm{diag}(\sum_p[\mathbf{E}_p^{\mathbf{t}}]^2) + \tilde{\gamma}_b^{\mathrm{em}}\sum_u(\mathbf{D}_u^T\mathrm{diag}(\boldsymbol{\pi}_u)\mathbf{D}_u)\right\}^{-1} \tag{8.53}$$

$$\mathbf{m}_\chi^{\mathrm{em}} = \mathbf{\Sigma}_\chi^{\mathrm{em}}\left[\tilde{\gamma}_s^{\mathrm{em}}\sum_p\mathbf{m}_{J_p}^{\mathrm{em}}.\times\overline{\mathbf{E}}_p^{\mathbf{i}} + \mathrm{diag}\left((\mathbf{m}_J^{\mathrm{em}}(\mathbf{m}_J^{\mathrm{em}})^\dagger + \mathbf{\Sigma}_J^{\mathrm{em}})(\mathbf{G}_{\mathbf{d}}^{\mathrm{em}})^\dagger\right)\right] \tag{8.54}$$

with $[\mathbf{E}_p^{\mathbf{t}}]^2 = \mathbf{m}_{E_p^t}.\times\overline{\mathbf{m}}_{E_p^t} + \mathrm{diag}(\mathbf{\Sigma}_{E_p^t})$ where $\mathbf{m}_{E_p^t} = \mathbf{E}_p^{\mathbf{i}} + \mathbf{G}_{\mathbf{d}}^{\mathrm{em}}\mathbf{m}_{J_p}^{\mathrm{em}}$ and $\mathbf{\Sigma}_{E_p^t} = \mathbf{G}_{\mathbf{d}}^{\mathrm{em}}\mathbf{\Sigma}_J^{\mathrm{em}}(\mathbf{G}_{\mathbf{d}}^{\mathrm{em}})^\dagger$.

$\tilde{\gamma}_n^{\mathrm{em}}$ is calculated as $\tilde{\gamma}_n^{\mathrm{em}} = \alpha_n^{\mathrm{em}}/\beta_n^{\mathrm{em}}$ with

$$\alpha_n^{\mathrm{em}} = \alpha_{n0}^{\mathrm{em}} + N_iN_r \tag{8.55}$$

$$\beta_n^{\mathrm{em}} = \beta_{n0}^{\mathrm{em}} + \sum_p\left(\|\mathbf{G}_{\mathbf{s}}^{\mathrm{em}}\mathbf{m}_{J_p}^{\mathrm{em}}\|^2 + \|\mathbf{E}_p^{\mathbf{s}}\|^2 - 2\Re < \mathbf{G}_{\mathbf{s}}^{\mathrm{em}}\mathbf{m}_{J_p}^{\mathrm{em}}, \mathbf{E}_p^{\mathbf{s}} > + \mathrm{tr}(\mathbf{G}_{\mathbf{s}}^{\mathrm{em}}\mathbf{\Sigma}_J^{\mathrm{em}}(\mathbf{G}_{\mathbf{s}}^{\mathrm{em}})^\dagger)\right) \tag{8.56}$$

$\tilde{\gamma}_s^{\mathrm{em}}$ is calculated as $\tilde{\gamma}_s^{\mathrm{em}} = \alpha_s^{\mathrm{em}}/\beta_s^{\mathrm{em}}$ with

$$\alpha_s^{\mathrm{em}} = \alpha_{s0}^{\mathrm{em}} + N_iN_m \tag{8.57}$$

$$\beta_s^{\mathrm{em}} = \beta_{s0}^{\mathrm{em}} + \sum_p\left(\|\mathbf{m}_{J_p}^{\mathrm{em}}\|^2 + \|\mathbf{m}_\chi^{\mathrm{em}}\|^2\|\mathbf{E}_p^{\mathbf{t}}\|^2 - 2\Re < \mathbf{m}_\chi^{\mathrm{em}}, \mathbf{m}_{J_p}^{\mathrm{em}}\overline{\mathbf{E}}_p^{\mathbf{t}} >\right) \tag{8.58}$$

with $\mathbf{m}_{J_p}^{\mathrm{em}}\overline{\mathbf{E}}_p^{\mathbf{t}} = \mathbf{m}_{J_p}^{\mathrm{em}}.\times\overline{\mathbf{E}}_p^{\mathbf{i}} + \mathrm{diag}\left((\mathbf{m}_{J_p}^{\mathrm{em}}(\mathbf{m}_{J_p}^{\mathrm{em}})^\dagger + \mathbf{\Sigma}_J^{\mathrm{em}})(\mathbf{G}_{\mathbf{d}}^{\mathrm{em}})^\dagger\right)$.

$\tilde{\gamma}_b^{\mathrm{em}}$ is calculated as $\tilde{\gamma}_b^{\mathrm{em}} = \alpha_b^{\mathrm{em}}/\beta_b^{\mathrm{em}}$ with

$$\alpha_b^{\mathrm{em}} = \alpha_{b0}^{\mathrm{em}} + 4N_m \tag{8.59}$$

$$\beta_b^{\mathrm{em}} = \beta_{b0}^{\mathrm{em}} + \sum_u\left(< \mathbf{D}_u\mathbf{m}_\chi^{\mathrm{em}}, \mathrm{diag}(\boldsymbol{\pi}_u)(\mathbf{D}_u\mathbf{m}_\chi^{\mathrm{em}}) > + \mathrm{tr}(\mathbf{D}_u\mathbf{\Sigma}_\chi^{\mathrm{em}}\mathbf{D}_u^T.\times\mathrm{diag}(\boldsymbol{\pi}_u))\right) \tag{8.60}$$

$[\boldsymbol{\pi}_u]_m$ is updated as

$$[\boldsymbol{\pi}_u]_m = \frac{\exp(l)p_b^2}{\exp(l)p_b^2 + (1-p_b)^2} \tag{8.61}$$

with $l = -\frac{\tilde{\gamma}_b^{\mathrm{ac}}}{2}\left(|[\mathbf{D}_u\mathbf{m}_\chi^{\mathrm{ac}}]_m|^2 + [\mathbf{D}_u\mathbf{\Sigma}_\chi^{\mathrm{ac}}\mathbf{D}_u^T]_m\right) - \frac{\tilde{\gamma}_b^{\mathrm{em}}}{2}\left(|[\mathbf{D}_u\mathbf{m}_\chi^{\mathrm{em}}]_m|^2 + [\mathbf{D}_u\mathbf{\Sigma}_\chi^{\mathrm{em}}\mathbf{D}_u^T]_m\right)$

The algorithm is summarized as follows:

Algorithm 9 Joint inversion with VBA (JVBA)

Input: $\mathbf{E}_p^{\mathbf{s}}$, $\mathbf{E}_p^{\mathbf{i}}$, $\mathbf{P}_p^{\mathbf{s}}$, $\mathbf{P}_p^{\mathbf{i}}$, $p = 1, \ldots, N_i$, $\mathbf{G}_{\mathbf{s}}^{\mathrm{em}}$, $\mathbf{G}_{\mathbf{d}}^{\mathrm{em}}$, $\mathbf{G}_{\mathbf{s}}^{\mathrm{ac}}$, $\mathbf{G}_{\mathbf{d}}^{\mathrm{ac}}$
Initialization: $\mathbf{J}^{\mathrm{ac}}$, $\boldsymbol{\chi}^{\mathrm{ac}}$, $\mathbf{J}^{\mathrm{em}}$, $\boldsymbol{\chi}^{\mathrm{em}}$, Θ
repeat
  Update the law $q(\mathbf{J}^{\mathrm{ac}})$ using (8.41) and (8.42)
  Update the law $q(\boldsymbol{\chi}^{\mathrm{ac}})$ using (8.43) and (8.44)
  Update the law $q(\gamma_n^{\mathrm{ac}})$ using (8.45) and (8.46)
  Update the law $q(\gamma_s^{\mathrm{ac}})$ using (8.47) and (8.48)
  Update the law $q(\gamma_b^{\mathrm{ac}})$ using (8.49) and (8.50)
  Update the law $q(\mathbf{J}^{\mathrm{em}})$ using (8.51) and (8.52)
  Update the law $q(\boldsymbol{\chi}^{\mathrm{em}})$ using (8.53) and (8.54)
  Update the law $q(\gamma_n^{\mathrm{em}})$ using (8.55) and (8.56)
  Update the law $q(\gamma_s^{\mathrm{em}})$ using (8.57) and (8.58)
  Update the law $q(\gamma_b^{\mathrm{em}})$ using (8.59) and (8.60)
  Update the law $q(\mathbf{b})$ using (8.61)
until a stopping criterion is satisfied
Output: $\boldsymbol{\chi}^{\mathrm{ac}}$, $\boldsymbol{\chi}^{\mathrm{em}}$

8.5 Numerical experiments

In this section, numerical experiments are conducted on several breast models. First the algorithm is validated on a synthetic model with regular tissue shapes, then is investigated on three realistic breast models which have more complicated inner structures. All simulations are run on Matlab R2018b.

In the simulation, for the electromagnetic case, 40 antennas are evenly set on a circle, working as sources and receivers simultaneously at a single 1 GHz operation frequency.

For the acoustic case, 64 transducers operate at three frequencies, namely 100, 150 and 200 kHz, to get a better estimate of the structure in the first step. Considering the acoustic wavenumber $k^{\mathrm{ac}} = \omega/c + i\alpha$ wherein attenuation $\alpha = \alpha_0 f$, α_0 the attenuation at frequency f =1 MHz (here a linear dependence is assumed [138]), the approximation can be made that the acoustic contrast does not change with frequency.

The DoI is discretized by MoM into a grid which is at least twice finer than the one used in inversion. Additive Gaussian noise of 30 dB is added to the data.

Relative error between reconstructed parameters $\boldsymbol{\zeta}$ and ground truth $\boldsymbol{\xi}$ is defined to evaluate the reconstruction results as

$$\mathrm{Err} = \frac{\|\boldsymbol{\zeta} - \boldsymbol{\xi}\|_2}{\|\boldsymbol{\xi}\|_2} \tag{8.62}$$

Before running the joint inversion algorithm, an initial guess of the acoustic reconstruction result is obtained by some nonlinear iterative inversion algorithm, such as CSI to get a better initial guess of the edge variables. During the first several iterations of the joint inversion, the edge variables are estimated only via the acoustic contrast. To save computation time, the update of parameters concerning the acoustic case stops when the relative difference of the acoustic contrast of two iterations is below the threshold and the whole optimization procedure stops when the relative difference of dielectric contrast is below the same threshold. To compare, reconstruction results by JCSI-EP with $\gamma = 0.5$ are also shown.

8.5.1 Synthetic breast model

The first breast model is a synthetic model where each tissue type has a regular shape. The prior probability p_b is chosen as 0.05 and the threshold used to stop the algorithm is 1×10^{-3}. The

Table 8.1: Model 1 – Relative error of acoustic and dielectric parameters

Methods	acoustic parameter		dielectric parameter	
	c	α	ϵ_r'	ϵ_r''
JCSI-EP	0.0078	0.3406	0.2664	0.3002
JVBA	0.0084	0.2634	0.3487	0.4282

groundtruth and the reconstruction results are shown in Figure 8.2. The relative error of parameters are shown in Table 8.1.

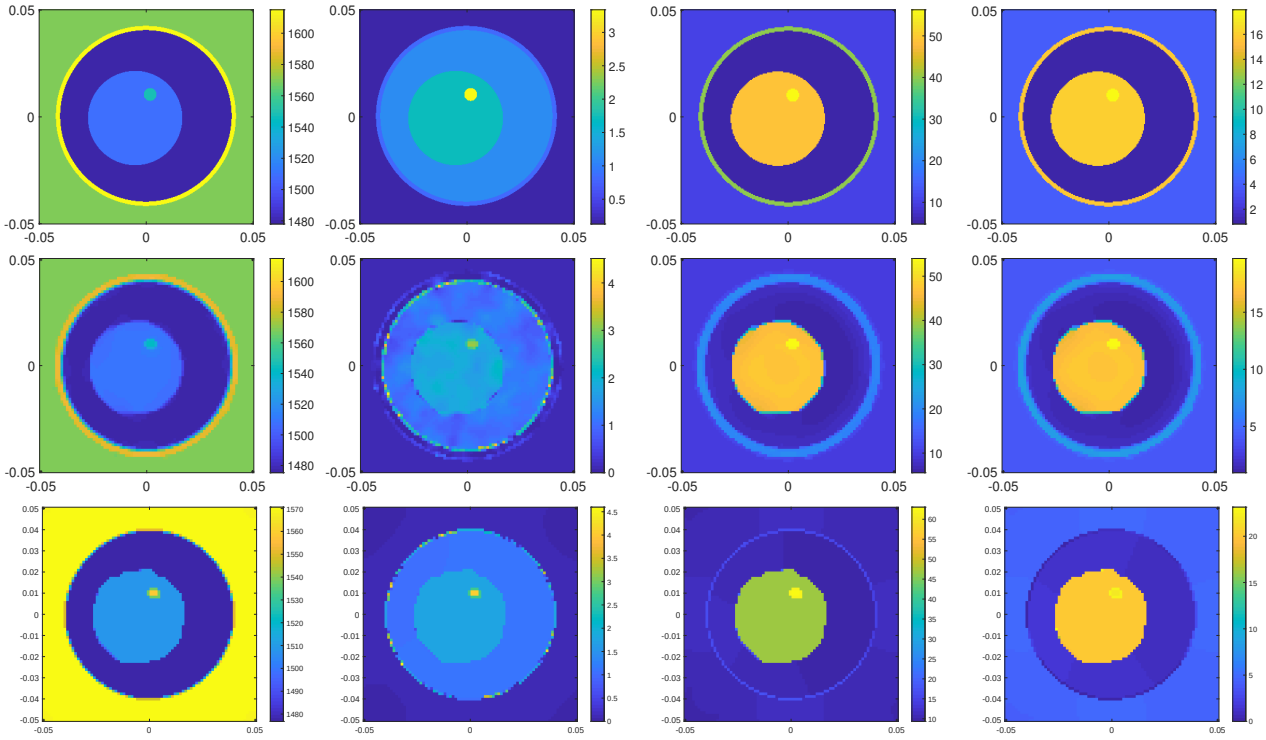

Figure 8.2: Model 1 – Ground truth (1st row), joint inversion results of JCSI-EP (2nd) and JVBA (3rd) with speed of sound c (1st column), attenuation α (2nd), real part ϵ_r' (3rd) and imaginary part ϵ_r'' (4th) of relative permittivity.

It can be seen that JVBA has a higher error than JCSI-EP. Compared with JCSI-EP, the skin is not well estimated by JVBA which is smoothed in the optimization process. Yet the tumor can still be seen clearly in the reconstruction results of all parameters with most of the hyperparameters estimated automatically.

Figure 8.3 shows the edge variables estimated by these two algorithms. It can be observed that the discontinuities between the tumor and the glandular part are finer in JCSI-EP while JVBA yields a better estimate on edges between glandular and fatty parts. We should also note that in JCSI-EP we have confined the region for reconstruction in a circle with a radius of 0.045 m, which is shown as the outer boundaries. However, we have no such restrictions in the JVBA. Considering that the cell size in inversion is 0.1 m/80=1.25 mm and that the thickness of the skin is 2 mm, the skin takes no more than 2 pixels in width and it is difficult to image.

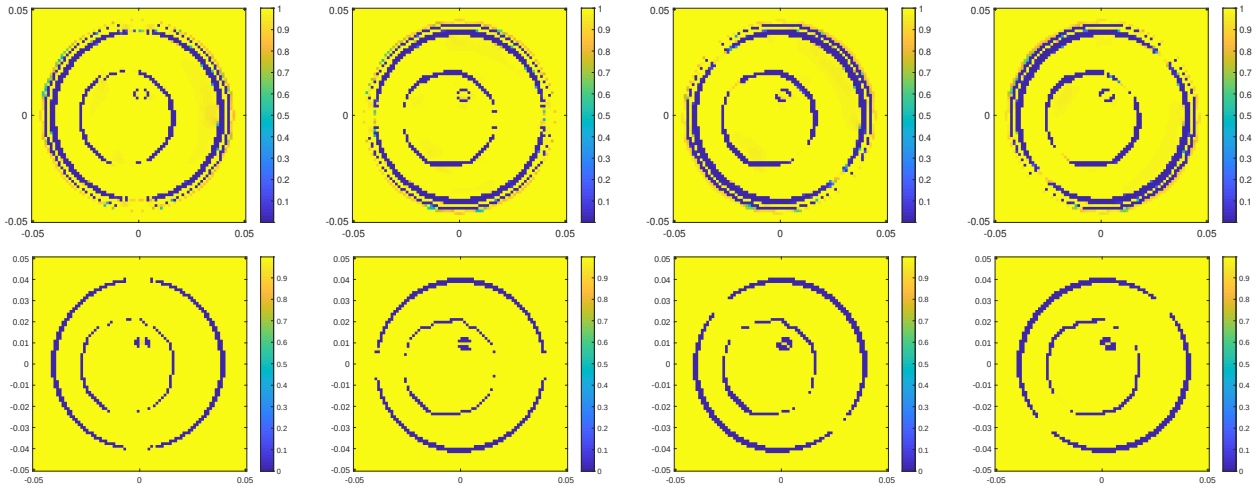

Figure 8.3: Model 1 – Reconstruction result of edge variables in four directions with JCSI-EP (1st row) and JVBA (2nd).

8.5.2 Realistic breast models

We validate our algorithm on three realistic breast models, with two models from Class 3 and one from Class 4. The prior probability p_b is chosen as 0.15 for all models. The threshold is 5×10^{-4} to stop the optimization procedure.

Class 3 Model

Two breast models are derived from the same breast phantom with a synthetic tumor located with the same position but with different shape. The first model has a regular-shaped tumor and the groundtruth and reconstruction results are shown in Figure 8.4. The tumor is visible with both inversion algorithms. The relative error is in Table 8.2. From the quantitative assessment, the reconstruction errors are quite similar. JVBA has a smaller error in the real part of the dielectric parameter while a higher error in the imaginary part.

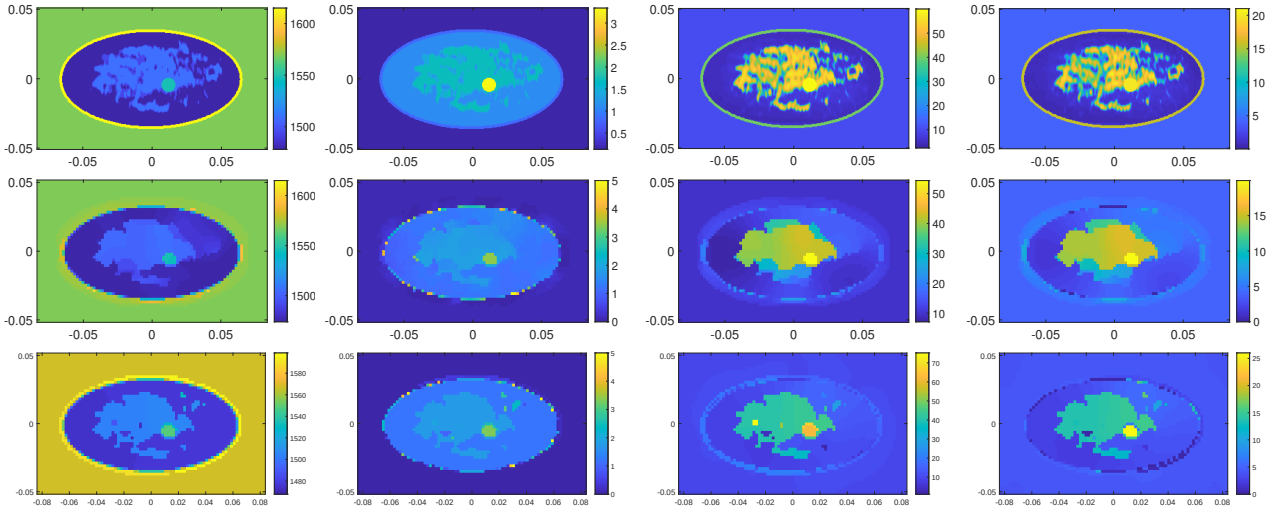

Figure 8.4: Model 2 – Ground truth (1st row) and reconstruction results of JCSI-EP (2nd) and JVBA (3rd) with speed of sound c (1st column), attenuation α (2nd), real part ϵ_r' (3rd) and imaginary part ϵ_r'' (4th) of relative permittivity.

Table 8.2: Model 2 – Relative error of acoustic and dielectric parameters

Methods	acoustic parameter		dielectric parameter	
	c	α	ϵ_r'	ϵ_r''
JCSI-EP	0.0097	0.3977	0.4411	0.4771
JVBA	0.0098	0.3516	0.4271	0.5104

Table 8.3: Model 2 – Estimation of hyperparameters

Modality	γ_n	γ_s	γ_b
AC	5.01×10^7	2.86×10^6	2.96×10^3
EM	2.59×10^7	4.46×10^3	10.51

An advantage of this algorithm is that the hyperparameters are automatically estimated. If there is only one hyperparameter, it can be chosen with the L-curve or another method, however, it is quite difficult when there are many parameters to choose. Table 8.3 gives the estimation result of hyperparameters at the last iteration. We can observe a higher precision parameter for the data equation γ_n than the parameter for the state equation γ_s in both acoustic and microwave cases. This may be a compensation for a smaller dimension in data compared with a higher dimension for unknowns. Meanwhile, γ_s in the microwave case is quite smaller than in the acoustic case which means a higher state equation error exists in the microwave case. Besides, the acoustic case also has a higher γ_b than in microwave. This can be inferred since the dielectric contrast is stronger even much stronger than the acoustic contrast.

The second model has an irregular-shaped tumor. The reconstruction results are shown in Figure 8.5 and relative errors are in Table 8.4. The shape of the tumor is well estimated by both algorithms. The comparison between these two algorithms is quite similar with Model 2.

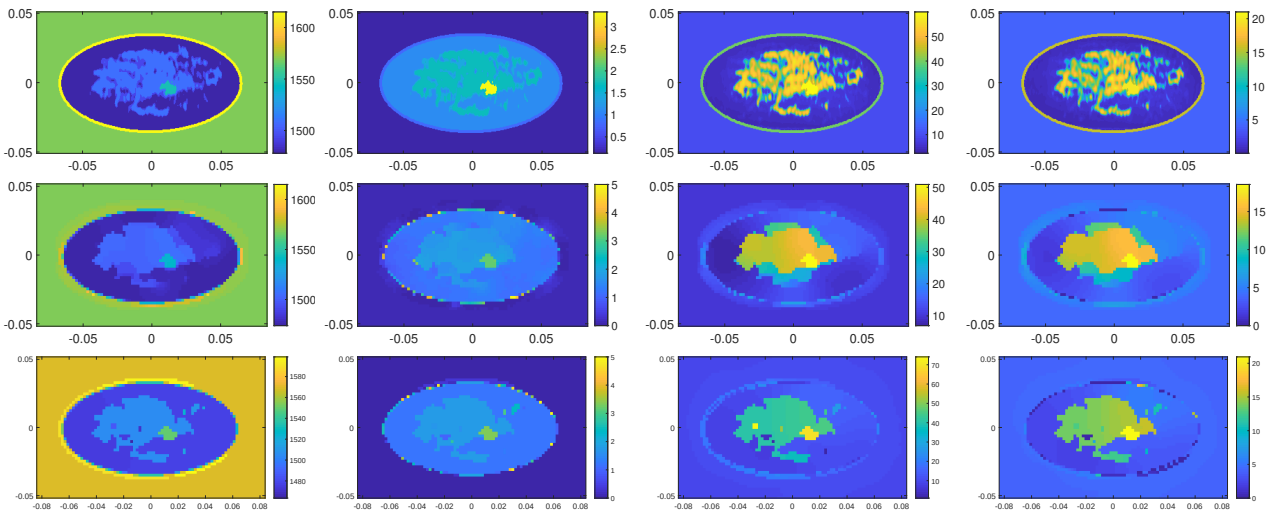

Figure 8.5: Model 3 – Ground truth (1st row) and reconstruction results of JCSI-EP (2nd) and JVBA (3rd) with speed of sound c (1st column), attenuation α (2nd), real part ϵ_r' (3rd) and imaginary part ϵ_r'' (4th) of relative permittivity.

Table 8.4: Model 3 – Relative error of acoustic and dielectric parameters

Methods	acoustic parameter		dielectric parameter	
	c	α	ϵ_r'	ϵ_r''
JCSI-EP	0.0098	0.3983	0.4430	0.4811
JVBA	0.0100	0.3643	0.4332	0.4948

Table 8.5: Model 4 – Relative error of acoustic and dielectric parameters

Methods	acoustic parameter		dielectric parameter	
	c	α	ϵ_r'	ϵ_r''
JCSI-EP	0.0089	0.3513	0.4157	0.4523
JVBA	0.0089	0.3051	0.3950	0.5511

Class 4 model

The reconstruction result and the relative error for the Class 4 model are shown in Figure 8.6 and Table 8.5. There are some small regions in the dielectric parameters that have a high contrast. If those could be removed, the imaging quality would be greatly enhanced.

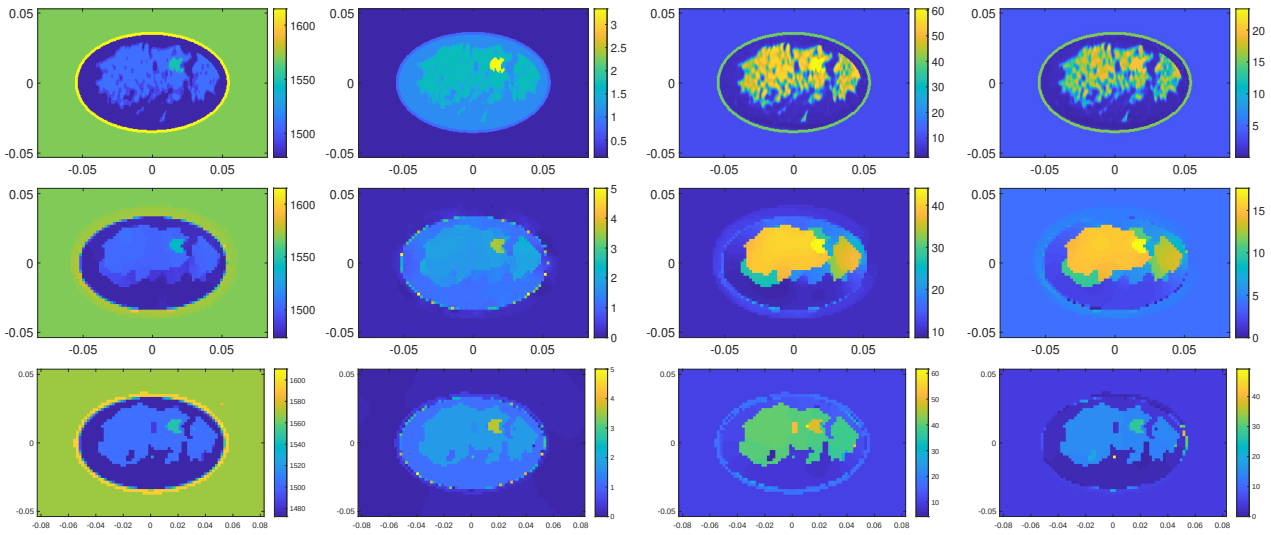

Figure 8.6: Model 4 – Ground truth (1st row) and reconstruction results of JCSI-EP (2nd) and JVBA (3rd) with speed of sound c (1st column), attenuation α (2nd), real part ϵ_r' (3rd) and imaginary part ϵ_r'' (4th) of relative permittivity.

8.6 Conclusion

In this part, we presented a joint inversion algorithm within a Bayesian framework to estimate the hyperparameters jointly. Like with the algorithm proposed in Chapter 6, we use edges toward different directions as hidden variables. Bernoulli distribution is employed to represent the presence of the edges at different positions. Gamma distributions are used for hyperparameters. Joint posterior distribution can be obtained according to Bayes' rule and an approximate law consisting of a number of separable distributions for the parameters is assumed to approximate the true distribution. From

the reconstruction, we conclude that the performance is similar with the one of JCSI-EP. Yet it is worth mentioning that in the present method, only one parameter p_b, the prior probability of the presence of the edge, is needed to be set based on the complexity of the breast models.

Chapter 9

Conclusion and perspectives

9.1 Conclusion

In this thesis, we have discussed early breast tumor detection with joint microwave and ultrasound modalities. The proposed methods can be classified into two classes and all of these methods are based on the assumption that the distributions of acoustic and electric parameters share the same structure, which is determined by tissue types.

The first class is model fusion, where successive imaging procedures are conducted and the result of one modality yields prior information for the inversion with the other modality. To detail somewhat, an image indicating the discontinuities is formed with ultrasound data. Such a procedure is similar with the B-mode scan, whereas only the traveling time of the pulse is recorded and used to find the distance between the reflection point and the transducer with a constant speed of sound being assumed. An ultrasound-guided smoothness regularization term is proposed given such images.

This regularization is like the first-order Tikhonov regularization while an additional parameter which can be 0 or 1 is introduced to indicate whether there is a tissue boundary or not. If no boundary, a smoothness constraint is imposed so as two adjacent pixels have similar parameters. In contrast, if a boundary, the value is 0 and a jump is allowed at this pixel.

Another class is joint fusion where acoustic data and microwave data are inverted simultaneously. Three methods are proposed in the above, which can be classified into this class. We see from the above result that given the position of edges, the imaging performance can be improved and therefore we have been developing some joint inversion algorithms based on edges.

Following such an idea, joint inversion with edge-preserving regularization is proposed. In this method edge variables as the hidden variables are introduced to combine the reconstruction of ultrasound and acoustic images. These edge variables indicating the presence and absence of the boundaries at each pixel are continuous between 0 and 1. Like with the UGS regularization, a value approaching 1 is for a discontinuity that should be preserved while a value closed to 0 for small gradients to be smoothed.

This regularization is incorporated into the CSI method and is imposed to both acoustic and electric parameters while the edge variables are shared by them. We have combined the optimization methods used in CSI and edge-preserving regularization, an alternate minimization being used to update the parameters in CSI cost of the acoustic case, acoustic contrast source and acoustic contrast, edge variables, and then parameters in the CSI cost associated to microwave.

To get rid of the problem of the choice of hyperparameters, we developed some other algorithms. The method is based on convolutional neural networks. We designed different streams to input data from different modalities and fused the feature maps after several layer such that the information of ultrasound and microwave are combined. After several residual bottlenecks the network outputs the acoustic and electric parameters to give the reconstruction images. Apart from such regression task, an auxiliary classifier is designed to classify each pixel into a tissue type or background medium. The

common structure of the breast for both modalities provides additional information for the network to learning the mapping from the data to the physical parameters. Such multi-task learning can help the training of the network and improve the generalization capability.

Another method is based on the Variational Bayesian Approximation. We use edges as the hidden variables to combine the acoustic and dielectric contrasts. A Bernoulli distribution is assigned to these variables. Hyperparameters are assigned with Gamma distribution for estimation. Based on Bayes' rule, we can get the joint posterior distribution of all variables to be estimated. Separable approximate laws are assumed for each set of parameters and are determined by approximating the true posterior distribution in the sense of Kullback-Leibler. The mean of these distributions is then used as the estimation result.

To summarize, we have developed and investigated a number of breast imaging methods with ultrasound and microwave modalities involved in the procedure. To combine different modalities, the relation between the parameters must be found. Usually structural similarity is a good choice since the parameters are related to the tissue type.

Structure information based on edge or region can be used. If region information is chosen, typically a segmentation of the image is needed while the boundary can be obtained in an easier way. Thus, most of the proposed algorithms are based on edges. In contrast, CNN learns the mapping itself thus the region information can be easily incorporated.

9.2 Perspectives

9.2.1 On the application in practice

In this investigation, we only consider a two-dimensional geometry, in the standard TM polarization case, which may be seen as quite a simplification in practice. In the future, one should try to solve such a problem in three dimensions, where the dyadic Green's function is needed in the microwave case (only the scalar one in acoustics, complexity is less) and more equations with more parameters are obviously faced with as the components along different axes need to be tackled. Also, one should be careful to consider real-world antennas, even if with a main polarization ensured, for which S-parameters are expected to be collected, also opening the door to not-so-simple calibration issues. The challenge by the way looks more critical in the microwave domain since ultrasonic transducers are readily available, used in standard breast imaging, and a lot of know-how is available there.

One point however, regarding 2D and 3D, once reminded that 3D electromagnetic probing of the breast has been considered with fair to good success by some authors already like [52, 88, 111], much work in the Ground Probing Radar research community still involves superimposition of 2D images of the subsoil, as is exemplified in the demanding situation of superficial tree root imaging by [197] and many references therein, and even if the breast is a challenge per se, assuming that superimposition may not go out-of-hand.

To reach such a goal, the full 3D situation, we could change the configuration used in the above joint inversion methods accordingly. That is, considering a third axis, z-axis, perpendicular to the plane, we could set the array of antennas and transducers along the z-axis. E.g., a set of antennas would be located on a circle at $z = z1$, and then an array of US transducers would be placed at $z = z2$. Such a placement could be repeated to collect more data.

The electric parameters considered in this thesis are obtained from *ex vivo* specimens between several minutes to hours after resection. Yet Haemmerich *et al.* [198] have reported that the largest change in the tissue property occurs immediately after the tissue removal, on the order of seconds to minutes. Thus these values differ from their *in vivo* counterparts. Halter *et al.* [199] have observed a fairly substantial decrease in both malignant decrease in both permittivity and conductivity of malignant tissue from the *in vivo* to *ex vivo* state. For example, the relative permittivity of *in vivo* tumor given by them is about 70 whereas this value in this work is about 60 at 1 GHz. Thus it is

reasonable to test the algorithms with different values. Meanwhile, the acoustic properties are uniform in each tissue type. Small variations should be added to model the complexity closer to reality.

9.2.2 On some potential improvement of algorithms

As for what concerns the convolutional neural network approach, the input of the network is high-dimensional (too many channels) and that makes it not practical in application to a 3D case. One way to overcome this problem can be that several networks are trained to get the imaging results at different locations. To add the spatial connection along the third direction, more sets of data with the central one representing the data for target position can be stacked along channels as the input of the network. Yet the input data still has a high dimension.

Another way is that one combines the data from different incidences before inputting them to the network. For example, many investigators use the reconstruction result of CSI or other inversion algorithms as input of the network [85, 87]. With this method, the input channel can be decreased to 2 (real and imaginary parts of the contrast) for one position. However, with a nonlinear iterative method, we may lose the real-time property of the imaging process while with a non-iterative method, the input of the network may lose some information. More investigation is still needed in that direction.

Otherwise, in this work, we have used edges as hidden variables in the Bayesian framework, yet some other priors with different hidden variables can be used. For example, with Potts prior we can get a segmentation of the breast models with the class of each pixel as a hidden variable. This prior has been employed in microwave breast imaging, e.g., [69]. In such a method, class label for each pixel $c(\mathbf{r})$ is the hidden variable and used for both acoustic and microwave cases. The model is expressed as

$$f(c|\lambda) = \frac{1}{T(\lambda)} \exp\{\lambda \sum_{r} \sum_{r' \in V_r} \delta(c(\mathbf{r}) - c(\mathbf{r}'))\} \tag{9.1}$$

where V_r is the neighborhood of $\mathbf{r}$ and λ is a parameter that determines the correlation between neighbors with $T(\lambda)$ as the normalization. The contrast is modeled as

$$f(\chi(\mathbf{r})|c(\mathbf{r}) = k) = \mathcal{N}(\chi(\mathbf{r})|m_k, v_k),\ k = 1, \ldots, K \tag{9.2}$$

Given the class of the pixel k, the contrast follows a Gaussian distribution with the mean m_k and variance v_k. Within this framework, the mean m_k and variance v_k for each class and for two modalities with the class label need to be estimated. The class number K is assumed to be known but can be set also with a higher value and then merge two classes when their means are quite close or remove one class if the pixel number is below a threshold.

Based on edge variables, some aspects can be considered also. In this work we have assumed these edge variables are independent. We may also assign a conditional prior, such as Ising model, to introduce some interactions between them, i.e., if there is an edge at a certain location, the probability will be higher that the discontinuity will occur in its neighborhood, thus we can get more continuous boundaries.

We may also consider the discretization. In this work, we use the same grid for two modalities with the method of moments. Since acoustic imaging has a higher resolution and that usually we get an acoustic image first to get the structure information, we may employ a grid for microwave based on this reconstruction result, with finer discretization on the borders and coarser one within the homogeneous region. For example, in [200], an adaptive discretization is proposed to solve the forward problem. Besides, FEM may be also investigated. In addition, the New Integral Equation approach, designed to tackle strong contrasts in inversion as introduced in [158] and further investigated or extended in subsequent works by its authors and a number of others, e.g., [201], [202], may also be a way forward in view of some indeed quite strong microwave contrasts to handle in the breast and its heterogeneity.

Bibliography

[1] J. Ferlay, M. Colombet, I. Soerjomataram, D. Parkin, M. Piñeros, A. Znaor, and F. Bray, "Cancer statistics for the year 2020: An overview," *Cancer Epidemiology*, vol. 149, no. 4, pp. 778–789, 2021.

[2] A. Modiri, S. Goudreau, A. Rahimi, and K. Kiasaleh, "Review of breast screening: Toward clinical realization of microwave imaging," *Medical Physics*, vol. 44, no. 12, pp. e446–e458, 2017.

[3] C. L. Carter, C. Allen, and D. E. Henson, "Relation of tumor size, lymph node status, and survival in 24,740 breast cancer cases," *Cancer*, vol. 63, no. 1, pp. 181–187, 1989.

[4] P. P. Rosen, S. Groshen, D. Kinne, and L. Norton, "Factors influencing prognosis in node-negative breast carcinoma: analysis of 767 T1N0M0/T2N0M0 patients with long-term follow-up.," *Journal of Clinical Oncology*, vol. 11, no. 11, pp. 2090–2100, 1993.

[5] P. C. Johns and M. J. Yaffe, "X-ray characterisation of normal and neoplastic breast tissues," *Physics in Medicine & Biology*, vol. 32, no. 6, p. 675, 1987.

[6] T. M. Kolb, J. Lichy, and J. H. Newhouse, "Comparison of the performance of screening mammography, physical examination, and breast us and evaluation of factors that influence them: an analysis of 27,825 patient evaluations," *Radiology*, vol. 225, no. 1, pp. 165–175, 2002.

[7] R. M. Mann, R. Hooley, R. G. Barr, and L. Moy, "Novel approaches to screening for breast cancer," *Radiology*, vol. 297, no. 2, pp. 266–285, 2020.

[8] M. L. Marinovich, K. E. Hunter, P. Macaskill, and N. Houssami, "Breast cancer screening using tomosynthesis or mammography: a meta-analysis of cancer detection and recall," *JNCI: Journal of the National Cancer Institute*, vol. 110, no. 9, pp. 942–949, 2018.

[9] P. Skaane, A. I. Bandos, L. T. Niklason, S. Sebu**o**deg**r**ard, B. H. Øster**r**as, R. Gullien, D. Gur, and S. Hofvind, "Digital mammography versus digital mammography plus tomosynthesis in breast cancer screening: the Oslo tomosynthesis screening trial," *Radiology*, vol. 291, no. 1, pp. 23–30, 2019.

[10] M. Bahl, S. Mercaldo, P. A. Dang, A. M. McCarthy, K. P. Lowry, and C. D. Lehman, "Breast cancer screening with digital breast tomosynthesis: are initial benefits sustained?," *Radiology*, vol. 295, no. 3, pp. 529–539, 2020.

[11] J. Y. Kim, H. J. Kang, J. K. Shin, N. K. Lee, Y. S. Song, K. J. Nam, and K. S. Choo, "Biologic profiles of invasive breast cancers detected only with digital breast tomosynthesis," *American Journal of Roentgenology*, vol. 209, no. 6, pp. 1411–1418, 2017.

[12] P. S. Tofts, B. Berkowitz, and M. D. Schnall, "Quantitative analysis of dynamic Gd-DTPA enhancement in breast tumors using a permeability model," *Magnetic Resonance in Medicine*, vol. 33, no. 4, pp. 564–568, 1995.

[13] R. M. Mann, N. Cho, and L. Moy, "Breast MRI: state of the art," *Radiology*, vol. 292, no. 3, pp. 520–536, 2019.

[14] L. Liberman, E. A. Morris, D. D. Dershaw, A. F. Abramson, and L. K. Tan, "MR imaging of the ipsilateral breast in women with percutaneously proven breast cancer," *American Journal of Roentgenology*, vol. 180, no. 4, pp. 901–910, 2003.

[15] S. P. Na and D. Houserkovaa, "The role of various modalities in breast imaging," *Biomed Pap Med Fac Univ Palacky Olomouc Czech Repub*, vol. 151, no. 2, pp. 209–218, 2007.

[16] C. M. Sehgal, S. P. Weinstein, P. H. Arger, and E. F. Conant, "A review of breast ultrasound," *Journal of Mammary Gland Biology and Neoplasia*, vol. 11, no. 2, pp. 113–123, 2006.

[17] W. A. Berg, J. D. Blume, J. B. Cormack, E. B. Mendelson, D. Lehrer, M. Böhm-Vélez, E. D. Pisano, R. A. Jong, W. P. Evans, M. J. Morton, *et al.*, "Combined screening with ultrasound and mammography vs mammography alone in women at elevated risk of breast cancer," *JAMA*, vol. 299, no. 18, pp. 2151–2163, 2008.

[18] R. Rella, P. Belli, M. Giuliani, E. Bufi, G. Carlino, P. Rinaldi, and R. Manfredi, "Automated breast ultrasonography (ABUS) in the screening and diagnostic setting: indications and practical use," *Academic Radiology*, vol. 25, no. 11, pp. 1457–1470, 2018.

[19] J. Zhan, X.-H. Diao, J.-M. Jin, L. Chen, and Y. Chen, "Superb microvascular imaging—a new vascular detecting ultrasonographic technique for avascular breast masses: a preliminary study," *European Journal of Radiology*, vol. 85, no. 5, pp. 915–921, 2016.

[20] T. A. Krouskop, T. M. Wheeler, F. Kallel, B. S. Garra, and T. Hall, "Elastic moduli of breast and prostate tissues under compression," *Ultrasonic Imaging*, vol. 20, no. 4, pp. 260–274, 1998.

[21] N. Duric, P. Littrup, and C. Kuzmiak, "Breast ultrasound tomography," *Breast Imaging*, vol. 6, 2018.

[22] L. Wang, "Early diagnosis of breast cancer," *Sensors*, vol. 17, no. 7, p. 1572, 2017.

[23] E. C. Fear, "Microwave imaging of the breast," *Technology in Cancer Research & Treatment*, vol. 4, no. 1, pp. 69–82, 2005.

[24] H. Schwan and K. Foster, "Dielectric properties of tissues and biological materials: a critical review," *Critical Reviews in Biomedical Engineering*, vol. 17, pp. 25–104, 1989.

[25] A. Campbell and D. Land, "Dielectric properties of female human breast tissue measured in vitro at 3.2 GHz," *Physics in Medicine & Biology*, vol. 37, no. 1, p. 193, 1992.

[26] A. J. Surowiec, S. S. Stuchly, J. R. Barr, and A. Swarup, "Dielectric properties of breast carcinoma and the surrounding tissues," *IEEE Transactions on Biomedical Engineering*, vol. 35, no. 4, pp. 257–263, 1988.

[27] S. Gabriel, R. Lau, and C. Gabriel, "The dielectric properties of biological tissues: Iii. parametric models for the dielectric spectrum of tissues," *Physics in Medicine & Biology*, vol. 41, no. 11, p. 2271, 1996.

[28] A. Barrett, P. Myers, and N. Sadowsky, "Detection of breast cancer by microwave radiometry," *Radio Science*, vol. 12, no. 6S, pp. 167–171, 1977.

[29] F. Bardati and S. Iudicello, "Modeling the visibility of breast malignancy by a microwave radiometer," *IEEE Transactions on Biomedical Engineering*, vol. 55, no. 1, pp. 214–221, 2008.

[30] S. C. Hagness, A. Taflove, and J. E. Bridges, "Two-dimensional FDTD analysis of a pulsed microwave confocal system for breast cancer detection: Fixed-focus and antenna-array sensors," *IEEE Transactions on Biomedical Engineering*, vol. 45, no. 12, pp. 1470–1479, 1998.

[31] X. Li and S. C. Hagness, "A confocal microwave imaging algorithm for breast cancer detection," *IEEE Microwave and Wireless Components Letters*, vol. 11, no. 3, pp. 130–132, 2001.

[32] E. J. Bond, X. Li, S. C. Hagness, and B. D. Van Veen, "Microwave imaging via space-time beamforming for early detection of breast cancer," *IEEE Transactions on Antennas and Propagation*, vol. 51, no. 8, pp. 1690–1705, 2003.

[33] R. Nilavalan, A. Gbedemah, I. Craddock, X. Li, and S. C. Hagness, "Numerical investigation of breast tumour detection using multi-static radar," *Electronics Letters*, vol. 39, no. 5, pp. 1787–1789, 2003.

[34] M. Shere, A. Preece, I. Craddock, L. Jones, A. Valencia, *et al.*, "Radar imaging of breast lesions–a clinical evaluation and comparison," in *Proceedings of the European Congress of Radiology 2016*, pp. C–0521, 2016.

[35] P. M. Meaney, M. W. Fanning, D. Li, S. P. Poplack, and K. D. Paulsen, "A clinical prototype for active microwave imaging of the breast," *IEEE Transactions on Microwave Theory and Techniques*, vol. 48, no. 11, pp. 1841–1853, 2000.

[36] D. Li, P. M. Meaney, and K. D. Paulsen, "Conformal microwave imaging for breast cancer detection," *IEEE Transactions on Microwave Theory and Techniques*, vol. 51, no. 4, pp. 1179–1186, 2003.

[37] A. E. Bulyshev, S. Y. Semenov, A. E. Souvorov, R. H. Svenson, A. G. Nazarov, Y. E. Sizov, and G. P. Tatsis, "Computational modeling of three-dimensional microwave tomography of breast cancer," *IEEE Transactions on Biomedical Engineering*, vol. 48, no. 9, pp. 1053–1056, 2001.

[38] A. Tikhonov and V. Arsenine, *Méthodes de Résolution des Problèmes Mal Posés*. Editions Mir, Moscow, 1976.

[39] P. C. Sabatier, "Past and future of inverse problems," *Journal of Mathematical Physics*, vol. 41, p. 4082, 2000.

[40] T. Hebert and R. Leahy, "A generalized EM algorithm for 3-D Bayesian reconstruction from Poisson data using Gibbs priors," *IEEE Transactions on Medical Imaging*, vol. 8, no. 2, pp. 194–202, 1989.

[41] C. Bouman and K. Sauer, "A generalized Gaussian image model for edge-preserving MAP estimation," *IEEE Transactions on Image Processing*, vol. 2, no. 3, pp. 296–310, 1993.

[42] S. Geman and D. E. McClure, "Bayesian image analysis: An application to single photon emission tomography," *Proceedings of the American Statistical Association*, pp. 12–18, 1985.

[43] S. Geman and D. Geman, "Stochastic relaxation, Gibbs distributions, and the Bayesian restoration of images," *IEEE Transactions on Pattern Analysis and Machine Intelligence*, no. 6, pp. 721–741, 1984.

[44] A. Blake and A. Zisserman, *Visual Reconstruction*. MIT Press, 1987.

[45] D. Geman and G. Reynolds, "Constrained restoration and the recovery of discontinuities," *IEEE Transactions on Pattern Analysis and Machine Intelligence*, vol. 14, no. 3, pp. 367–383, 1992.

[46] D. Geman and C. Yang, "Nonlinear image recovery with half-quadratic regularization," *IEEE Transactions on Image Processing*, vol. 4, no. 7, pp. 932–946, 1995.

[47] P. Lobel, L. Blanc-Féraud, C. Pichot, and M. Barlaud, "A new regularization scheme for inverse scattering," *Inverse Problems*, vol. 13, no. 2, p. 403, 1997.

[48] L. I. Rudin, S. Osher, and E. Fatemi, "Nonlinear total variation based noise removal algorithms," *Physica D: Nonlinear Phenomena*, vol. 60, no. 1-4, pp. 259–268, 1992.

[49] P. M. van den Berg, A. Van Broekhoven, and A. Abubakar, "Extended contrast source inversion," *Inverse Problems*, vol. 15, no. 5, p. 1325, 1999.

[50] P. M. Van den Berg and A. Abubakar, "Contrast source inversion method: State of art," *Progress in Electromagnetics Research*, vol. 34, pp. 189–218, 2001.

[51] F. Bai, A. Pi**v**zurica, A. Franchois, S. Van Loocke, D. De Zutter, and W. Philips, "Weakly convex discontinuity adaptive regularization for microwave imaging," *IEEE Transactions on Antennas and Propagation*, vol. 61, no. 12, pp. 6242–6246, 2013.

[52] F. Bai, A. Franchois, and A. Pizurica, "3D microwave tomography with Huber regularization applied to realistic numerical breast phantoms," *Progress In Electromagnetics Research*, vol. 155, pp. 75–91, 2016.

[53] J. De Zaeytijd, A. Franchois, and J.-M. Geffrin, "A new value picking regularization strategy-application to the 3-D electromagnetic inverse scattering problem," *IEEE Transactions on Antennas and Propagation*, vol. 57, no. 4, pp. 1133–1149, 2009.

[54] Y. Wang and W. C. Chew, "An iterative solution of the two-dimensional electromagnetic inverse scattering problem," *International Journal of Imaging Systems and Technology*, vol. 1, no. 1, pp. 100–108, 1989.

[55] W. C. Chew and Y.-M. Wang, "Reconstruction of two-dimensional permittivity distribution using the distorted Born iterative method," *IEEE Transactions on Medical Imaging*, vol. 9, no. 2, pp. 218–225, 1990.

[56] N. Zaiping, Y. Feng, Z. Yanwen, and Z. Yerong, "Variational Born iteration method and its applications to hybrid inversion," *IEEE Transactions on Geoscience and Remote Sensing*, vol. 38, no. 4, pp. 1709–1715, 2000.

[57] R. Kleinman and P. Van den Berg, "A modified gradient method for two-dimensional problems in tomography," *Journal of Computational and Applied Mathematics*, vol. 42, no. 1, pp. 17–35, 1992.

[58] P. M. Van Den Berg and R. E. Kleinman, "A contrast source inversion method," *Inverse Problems*, vol. 13, no. 6, p. 1607, 1997.

[59] X. Chen, "Subspace-based optimization method for solving inverse-scattering problems," *IEEE Transactions on Geoscience and Remote Sensing*, vol. 48, no. 1, pp. 42–49, 2009.

[60] Y. Zhong and X. Chen, "Twofold subspace-based optimization method for solving inverse scattering problems," *Inverse Problems*, vol. 25, no. 8, p. 085003, 2009.

[61] Y. Zhong and X. Chen, "An FFT twofold subspace-based optimization method for solving electromagnetic inverse scattering problems," *IEEE Transactions on Antennas and Propagation*, vol. 59, no. 3, pp. 914–927, 2011.

[62] C. Robert and G. Casella, *Monte Carlo Statistical Methods*. Springer, 2013.

[63] V. Smídl and A. Quinn, *The Variational Bayes Method in Signal Processing*. Springer Science & Business Media, 2006.

[64] C. Eyraud, A. Litman, A. Hérique, and W. Kofman, "Microwave imaging from experimental data within a Bayesian framework with realistic random noise," *Inverse Problems*, vol. 25, no. 2, p. 024005, 2009.

[65] D. Babacan, R. Molina, and A. Katsaggelos, "Variational Bayesian super resolution," *IEEE Transactions on Image Processing*, vol. 20, no. 4, p. 984–999, 2010.

[66] R. Autieri, G. Ferraiuolo, and V. Pascazio, "Bayesian regularization in nonlinear imaging: reconstructions from experimental data in nonlinearized microwave tomography," *IEEE Transactions on Geoscience and Remote Sensing*, vol. 49, no. 2, pp. 801–813, 2010.

[67] F.-C. Jeng and J. Woods, "Compound Gauss-Markov random fields for image estimation," *IEEE Transactions on Signal Processing*, vol. 39, no. 3, pp. 683–697, 1991.

[68] O. Féron, B. Duchêne, and A. Mohammad-Djafari, "Microwave imaging of inhomogeneous objects made of a finite number of dielectric and conductive materials from experimental data," *Inverse Problems*, vol. 21, no. 6, p. S95, 2005.

[69] L. Gharsalli, H. Ayasso, B. Duchêne, and A. Mohammad-Djafari, "Inverse scattering in a Bayesian framework: application to microwave imaging for breast cancer detection," *Inverse Problems*, vol. 30, no. 11, p. 114011, 2014.

[70] L. Gharsalli, H. Ayasso, B. Duchêne, and A. Mohammad-Djafari, "Variational Bayesian inversion for microwave breast imaging," *Computer Assisted Methods in Engineering and Science*, vol. 21, no. 3/4, pp. 199–210, 2017.

[71] M. Li, R. Guo, K. Zhang, Z. Lin, F. Yang, S. Xu, X. Chen, A. Massa, and A. Abubakar, "Machine learning in electromagnetics with applications to biomedical imaging: A review," *IEEE Antennas and Propagation Magazine*, vol. 63, no. 3, pp. 39–51, 2021.

[72] S. Caorsi and P. Gamba, "Electromagnetic detection of dielectric cylinders by a neural network approach," *IEEE Transactions on Geoscience and Remote Sensing*, vol. 37, no. 2, pp. 820–827, 1999.

[73] E. Bermani, A. Boni, S. Caorsi, and A. Massa, "An innovative real-time technique for buried object detection," *IEEE Transactions on Geoscience and Remote Sensing*, vol. 41, no. 4, pp. 927–931, 2003.

[74] I. T. Rekanos, "Neural-network-based inverse-scattering technique for online microwave medical imaging," *IEEE Transactions on Magnetics*, vol. 38, no. 2, pp. 1061–1064, 2002.

[75] E. Bermani, S. Caorsi, and M. Raffetto, "An inverse scattering approach based on a neural network technique for the detection of dielectric cylinders buried in a lossy half-space," *Progress In Electromagnetics Research*, vol. 26, pp. 67–87, 2000.

[76] A. Krizhevsky, I. Sutskever, and G. E. Hinton, "Imagenet classification with deep convolutional neural networks," *Advances in Neural Information Processing Systems*, vol. 25, pp. 1097–1105, 2012.

[77] K. Simonyan and A. Zisserman, "Very deep convolutional networks for large-scale image recognition," *arXiv preprint arXiv:1409.1556*, 2014.

[78] J. Long, E. Shelhamer, and T. Darrell, "Fully convolutional networks for semantic segmentation," in *Proceedings of the IEEE Conference on Computer Vision and Pattern Recognition*, pp. 3431–3440, 2015.

[79] O. Ronneberger, P. Fischer, and T. Brox, "U-net: Convolutional networks for biomedical image segmentation," in *International Conference on Medical Image Computing and Computer-Assisted Intervention*, pp. 234–241, Springer, 2015.

[80] R. Girshick, "Fast R-CNN," in *Proceedings of the IEEE International Conference on Computer Vision*, pp. 1440–1448, 2015.

[81] S. Ren, K. He, R. Girshick, and J. Sun, "Faster R-CNN: towards real-time object detection with region proposal networks," *IEEE Transactions on Pattern Analysis and Machine Intelligence*, vol. 39, no. 6, pp. 1137–1149, 2016.

[82] P. Ran, Y. Qin, D. Lesselier, and M. Serhir, "Subwavelength microstructure probing by binary-specialized methods: Contrast source and convolutional neural networks," *IEEE Transactions on Antennas and Propagation*, vol. 69, no. 2, pp. 1030–1039, 2021.

[83] H. M. Yao, E. Wei, and L. Jiang, "Two-step enhanced deep learning approach for electromagnetic inverse scattering problems," *IEEE Antennas and Wireless Propagation Letters*, vol. 18, no. 11, pp. 2254–2258, 2019.

[84] Y. Sanghvi, Y. Kalepu, and U. K. Khankhoje, "Embedding deep learning in inverse scattering problems," *IEEE Transactions on Computational Imaging*, vol. 6, pp. 46–56, 2019.

[85] L. Li, L. G. Wang, F. L. Teixeira, C. Liu, A. Nehorai, and T. J. Cui, "DeepNIS: Deep neural network for nonlinear electromagnetic inverse scattering," *IEEE Transactions on Antennas and Propagation*, vol. 67, no. 3, pp. 1819–1825, 2018.

[86] Z. Wei and X. Chen, "Physics-inspired convolutional neural network for solving full-wave inverse scattering problems," *IEEE Transactions on Antennas and Propagation*, vol. 67, no. 9, pp. 6138–6148, 2019.

[87] V. Khoshdel, A. Ashraf, and J. LoVetri, "Enhancement of multimodal microwave-ultrasound breast imaging using a deep-learning technique," *Sensors*, vol. 19, no. 18, p. 4050, 2019.

[88] V. Khoshdel, M. Asefi, A. Ashraf, and J. LoVetri, "Full 3D microwave breast imaging using a deep-learning technique," *Journal of Imaging*, vol. 6, no. 8, p. 80, 2020.

[89] K. Edwards, V. Khoshdel, M. Asefi, J. LoVetri, C. Gilmore, and I. Jeffrey, "A machine learning workflow for tumour detection in breasts using 3D microwave imaging," *Electronics*, vol. 10, no. 6, 2021.

[90] P. Mojabi, M. Hughson, V. Khoshdel, I. Jeffrey, and J. LoVetri, "CNN for compressibility to permittivity mapping for combined ultrasound-microwave breast imaging," *IEEE Journal on Multiscale and Multiphysics Computational Techniques*, vol. 6, pp. 62–72, 2021.

[91] F. E.-Z. A. El-Gamal, M. Elmogy, and A. Atwan, "Current trends in medical image registration and fusion," *Egyptian Informatics Journal*, vol. 17, no. 1, pp. 99–124, 2016.

[92] T.-M. Tu, P. S. Huang, C.-L. Hung, and C.-P. Chang, "A fast intensity-hue-saturation fusion technique with spectral adjustment for IKONOS imagery," *IEEE Geoscience and Remote Sensing Letters*, vol. 1, no. 4, pp. 309–312, 2004.

[93] H. R. Shahdoosti and H. Ghassemian, "Combining the spectral PCA and spatial PCA fusion methods by an optimal filter," *Information Fusion*, vol. 27, pp. 150–160, 2016.

[94] A. Ben Hamza, Y. He, H. Krim, and A. Willsky, "A multiscale approach to pixel-level image fusion," *Integrated Computer-Aided Engineering*, vol. 12, no. 2, pp. 135–146, 2005.

[95] F. Nencini, A. Garzelli, S. Baronti, and L. Alparone, "Remote sensing image fusion using the curvelet transform," *Information Fusion*, vol. 8, no. 2, pp. 143–156, 2007.

[96] S. Yang, M. Wang, L. Jiao, R. Wu, and Z. Wang, "Image fusion based on a new contourlet packet," *Information Fusion*, vol. 11, no. 2, pp. 78–84, 2010.

[97] E. Holupka, I. Kaplan, E. Burdette, and G. Svensson, "Ultrasound image fusion for external beam radiotherapy for prostate cancer," *International Journal of Radiation Oncology* Biology* Physics*, vol. 35, no. 5, pp. 975–984, 1996.

[98] A. Rastinehad, J. Kruecker, C. Benjamin, P. Chung, B. Turkbey, S. Xu, J. Locklin, S. Gates, C. Buckner, M. Linehan, *et al.*, "846 MRI/US fusion prostate biopsies: cancer detection rates," *The Journal of Urology*, vol. 185, no. 4S, pp. e340–e340, 2011.

[99] F. Lindseth, S. Ommedal, J. Bang, G. Unsgrard, and T. N. Hernes, "Image fusion of ultrasound and MRI as an aid for assessing anatomical shifts and improving overview and interpretation in ultrasound-guided neurosurgery," in *International Congress Series*, vol. 1230, pp. 254–260, Elsevier, 2001.

[100] C. P. Behrenbruch, K. Marias, P. A. Armitage, M. Yam, N. Moore, R. E. English, and J. M. Brady, "MRI-mammography 2D/3D data fusion for breast pathology assessment," in *International Conference on Medical Image Computing and Computer-Assisted Intervention*, pp. 307–316, Springer, 2000.

[101] G. M. Duarte, C. Cabello, R. Z. Torresan, M. Alvarenga, G. H. Telles, S. T. Bianchessi, N. Caserta, S. R. Segala, M. d. C. L. de Lima, E. C. S. de Camargo Etchebehere, *et al.*, "Fusion of magnetic resonance and scintimammography images for breast cancer evaluation: a pilot study," *Annals of Surgical Oncology*, vol. 14, no. 10, pp. 2903–2910, 2007.

[102] G. Gindi, M. Lee, A. Rangarajan, and I. G. Zubal, "Bayesian reconstruction of functional images using anatomical information as priors," *IEEE Transactions on Medical Imaging*, vol. 12, no. 4, pp. 670–680, 1993.

[103] X. Ouyang, W. H. Wong, V. E. Johnson, X. Hu, and C.-T. Chen, "Incorporation of correlated structural images in PET image reconstruction," *IEEE Transactions on Medical Imaging*, vol. 13, no. 4, pp. 627–640, 1994.

[104] J. E. Bowsher, V. E. Johnson, T. G. Turkington, R. J. Jaszczak, C. Floyd, and R. E. Coleman, "Bayesian reconstruction and use of anatomical a priori information for emission tomography," *IEEE Transactions on Medical Imaging*, vol. 15, no. 5, pp. 673–686, 1996.

[105] A. Li, E. L. Miller, M. E. Kilmer, T. J. Brukilacchio, T. Chaves, J. Stott, Q. Zhang, T. Wu, M. Chorlton, R. H. Moore, *et al.*, "Tomographic optical breast imaging guided by three-dimensional mammography," *Applied Optics*, vol. 42, no. 25, pp. 5181–5190, 2003.

[106] G. Gulsen, O. Birgul, M. B. Unlu, R. Shafiiha, and O. Nalcioglu, "Combined diffuse optical tomography (DOT) and MRI system for cancer imaging in small animals," *Technology in Cancer Research & Treatment*, vol. 5, no. 4, pp. 351–363, 2006.

[107] X. Intes, C. Maloux, M. Guven, B. Yazici, and B. Chance, "Diffuse optical tomography with physiological and spatial a priori constraints," *Physics in Medicine & Biology*, vol. 49, no. 12, p. N155, 2004.

[108] M. Guven, B. Yazici, X. Intes, and B. Chance, "Diffuse optical tomography with a priori anatomical information," *Physics in Medicine & Biology*, vol. 50, no. 12, p. 2837, 2005.

[109] P. M. Meaney, A. H. Golnabi, N. R. Epstein, S. D. Geimer, M. W. Fanning, J. B. Weaver, and K. D. Paulsen, "Integration of microwave tomography with magnetic resonance for improved breast imaging," *Medical Physics*, vol. 40, no. 10, p. 103101, 2013.

[110] A. H. Golnabi, P. M. Meaney, and K. D. Paulsen, "Tomographic microwave imaging with incorporated prior spatial information," *IEEE Transactions on Microwave Theory and Techniques*, vol. 61, no. 5, pp. 2129–2136, 2013.

[111] A. H. Golnabi, P. M. Meaney, and K. D. Paulsen, "3D microwave tomography of the breast using prior anatomical information," *Medical Physics*, vol. 43, no. 4, pp. 1933–1944, 2016.

[112] L. M. Neira, B. D. Van Veen, and S. C. Hagness, "High-resolution microwave breast imaging using a 3-D inverse scattering algorithm with a variable-strength spatial prior constraint," *IEEE Transactions on Antennas and Propagation*, vol. 65, no. 11, pp. 6002–6014, 2017.

[113] M. Omer, P. Mojabi, D. Kurrant, J. LoVetri, and E. Fear, "Proof-of-concept of the incorporation of ultrasound-derived structural information into microwave radar imaging," *IEEE Journal on Multiscale and Multiphysics Computational Techniques*, vol. 3, pp. 129–139, 2018.

[114] N. Abdollahi, D. Kurrant, P. Mojabi, M. Omer, E. Fear, and J. LoVetri, "Incorporation of ultrasonic prior information for improving quantitative microwave imaging of breast," *IEEE Journal on Multiscale and Multiphysics Computational Techniques*, vol. 4, pp. 98–110, 2019.

[115] G. M. Hoversten, F. Cassassuce, E. Gasperikova, G. A. Newman, J. Chen, Y. Rubin, Z. Hou, and D. Vasco, "Direct reservoir parameter estimation using joint inversion of marine seismic AVA and CSEM data," *Geophysics*, vol. 71, no. 3, pp. C1–C13, 2006.

[116] G. Gao, A. Abubakar, and T. M. Habashy, "Joint petrophysical inversion of electromagnetic and full-waveform seismic data," *Geophysics*, vol. 77, no. 3, pp. WA3–WA18, 2012.

[117] J. Zhang and F. D. Morgan, "Joint seismic and electrical tomography," in *Symposium on the Application of Geophysics to Engineering and Environmental Problems 1997*, pp. 391–396, Society of Exploration Geophysicists, 1997.

[118] E. Haber and D. Oldenburg, "Joint inversion: a structural approach," *Inverse Problems*, vol. 13, no. 1, p. 63, 1997.

[119] L. A. Gallardo and M. A. Meju, "Characterization of heterogeneous near-surface materials by joint 2D inversion of DC resistivity and seismic data," *Geophysical Research Letters*, vol. 30, no. 13, p. 1658, 2003.

[120] L. A. Gallardo and M. A. Meju, "Joint two-dimensional DC resistivity and seismic travel time inversion with cross-gradients constraints," *Journal of Geophysical Research: Solid Earth*, vol. 109, no. B3, 2004.

[121] L. A. Gallardo and M. A. Meju, "Joint two-dimensional cross-gradient imaging of magnetotelluric and seismic traveltime data for structural and lithological classification," *Geophysical Journal International*, vol. 169, no. 3, pp. 1261–1272, 2007.

[122] W. Hu, A. Abubakar, and T. M. Habashy, "Joint electromagnetic and seismic inversion using structural constraints," *Geophysics*, vol. 74, no. 6, pp. R99–R109, 2009.

[123] A. Abubakar, G. Gao, T. M. Habashy, and J. Liu, "Joint inversion approaches for geophysical electromagnetic and elastic full-waveform data," *Inverse Problems*, vol. 28, no. 5, p. 055016, 2012.

[124] T. Lan, H. Liu, N. Liu, J. Li, F. Han, and Q. H. Liu, "Joint inversion of electromagnetic and seismic data based on structural constraints using variational Born iteration method," *IEEE Transactions on Geoscience and Remote Sensing*, vol. 56, no. 1, pp. 436–445, 2017.

[125] Y. Zhang, Z. Zhao, Z. Nie, and Q. H. Liu, "Approach on joint inversion of electromagnetic and acoustic data based on structural constraints," *IEEE Transactions on Geoscience and Remote Sensing*, vol. 58, no. 11, pp. 7672–7681, 2020.

[126] E. Haber and M. H. Gazit, "Model fusion and joint inversion," *Surveys in Geophysics*, vol. 34, no. 5, pp. 675–695, 2013.

[127] X. Song, M. Li, F. Yang, S. Xu, and A. Abubakar, "Study on joint inversion algorithm of acoustic and electromagnetic data in biomedical imaging," *IEEE Journal on Multiscale and Multiphysics Computational Techniques*, vol. 4, pp. 2–11, 2019.

[128] O. Scherzer, *Handbook of Mathematical Methods in Imaging*. Springer Science & Business Media, 2010.

[129] P. M. Morse and K. U. Ingard, *Theoretical Acoustics*. Princeton University Press, 1986.

[130] J. Bakker, M. Paulides, I. Obdeijn, G. Van Rhoon, and K. Van Dongen, "An ultrasound cylindrical phased array for deep heating in the breast: theoretical design using heterogeneous models," *Physics in Medicine & Biology*, vol. 54, no. 10, p. 3201, 2009.

[131] M. Lazebnik, L. McCartney, D. Popovic, C. Watkins, M. Lindstrom, J. Harter, S. Sewall, A. Magliocco, J. Booske, M. Okoniewski, and S. Hagness, "A large-scale study of the ultrawideband microwave dielectric properties of normal breast tissue obtained from reduction surgeries," *Physics in Medicine & Biology*, vol. 52, no. 10, p. 2637, 2007.

[132] M. Lazebnik, M. Okoniewski, J. H. Booske, and S. C. Hagness, "Highly accurate Debye models for normal and malignant breast tissue dielectric properties at microwave frequencies," *IEEE Microwave and Wireless Components Letters*, vol. 17, no. 12, pp. 822–824, 2007.

[133] J. D. Shea, P. Kosmas, S. C. Hagness, and B. D. Van Veen, "Three-dimensional microwave imaging of realistic numerical breast phantoms via a multiple-frequency inverse scattering technique," *Medical Physics*, vol. 37, no. 8, pp. 4210–4226, 2010.

[134] E. Zastrow, S. Davis, M. Lazebnik, F. Kelcz, B. Van Veen, and S. Hagness, "Database of 3D grid-based numerical breast phantoms for use in computational electromagnetics simulations," tech. rep., Department of Electrical and Computer Engineering University of Wisconsin-Madison, 2008.

[135] M. J. Burfeindt, T. J. Colgan, R. O. Mays, J. D. Shea, N. Behdad, B. D. Van Veen, and S. C. Hagness, "MRI-derived 3-D-printed breast phantom for microwave breast imaging validation," *IEEE Antennas and Wireless Propagation Letters*, vol. 11, pp. 1610–1613, 2012.

[136] American College of Radiology and others, "Breast imaging reporting and data system," *BI-RADS*, 2003.

[137] V. A. McCormack and I. dos Santos Silva, "Breast density and parenchymal patterns as markers of breast cancer risk: a meta-analysis," *Cancer Epidemiology and Prevention Biomarkers*, vol. 15, no. 6, pp. 1159–1169, 2006.

[138] T. D. Mast, "Empirical relationships between acoustic parameters in human soft tissues," *Acoustics Research Letters Online*, vol. 1, no. 2, pp. 37–42, 2000.

[139] J. Nebeker and T. R. Nelson, "Imaging of sound speed using reflection ultrasound tomography," *Journal of Ultrasound in Medicine*, vol. 31, no. 9, pp. 1389–1404, 2012.

[140] M. Z. Alom, T. M. Taha, C. Yakopcic, S. Westberg, P. Sidike, M. S. Nasrin, M. Hasan, B. C. Van Essen, A. A. Awwal, and V. K. Asari, "A state-of-the-art survey on deep learning theory and architectures," *Electronics*, vol. 8, no. 3, p. 292, 2019.

[141] V. Nair and G. E. Hinton, "Rectified linear units improve restricted Boltzmann machines," in *ICML*, 2010.

[142] A. L. Maas, A. Y. Hannun, and A. Y. Ng, "Rectifier nonlinearities improve neural network acoustic models," in *Proceedings of the 30th International Conference on Machine Learning*, p. 3, Citeseer, 2013.

[143] K. He, X. Zhang, S. Ren, and J. Sun, "Delving deep into rectifiers: Surpassing human-level performance on imagenet classification," in *Proceedings of the IEEE International Conference on Computer Vision*, pp. 1026–1034, 2015.

[144] S. Ioffe and C. Szegedy, "Batch normalization: Accelerating deep network training by reducing internal covariate shift," in *International Conference on Machine Learning*, pp. 448–456, PMLR, 2015.

[145] S. Santurkar, D. Tsipras, A. Ilyas, and A. Madry, "How does batch normalization help optimization?," *arXiv preprint arXiv:1805.11604*, 2018.

[146] X. Glorot and Y. Bengio, "Understanding the difficulty of training deep feedforward neural networks," in *Proceedings of the Thirteenth International Conference on Artificial Intelligence and Statistics*, pp. 249–256, JMLR Workshop and Conference Proceedings, 2010.

[147] D. P. Kingma and J. Ba, "Adam: A method for stochastic optimization," *arXiv preprint arXiv:1412.6980*, 2014.

[148] A. C. Wilson, R. Roelofs, M. Stern, N. Srebro, and B. Recht, "The marginal value of adaptive gradient methods in machine learning," *arXiv preprint arXiv:1705.08292*, 2017.

[149] J. Idier, *Bayesian Approach to Inverse Problems*. John Wiley & Sons, 2013.

[150] P. Charbonnier, L. Blanc-Feraud, G. Aubert, and M. Barlaud, "Two deterministic half-quadratic regularization algorithms for computed imaging," in *Proceedings of 1st International Conference on Image Processing*, vol. 2, pp. 168–172, IEEE, 1994.

[151] K. Belkebir, P. C. Chaumet, and A. Sentenac, "Superresolution in total internal reflection tomography," *Journal of the Optical Society A*, vol. 22, no. 9, pp. 1889–1897, 2005.

[152] P. M. van den Berg, A. Abubakar, and J. T. Fokkema, "Multiplicative regularization for contrast profile inversion," *Radio Science*, vol. 38, no. 2, p. 8022, 2003.

[153] L. Tabar, M.-F. Yen, B. Vitak, H.-H. T. Chen, R. A. Smith, and S. W. Duffy, "Mammography service screening and mortality in breast cancer patients: 20-year follow-up before and after introduction of screening," *The Lancet*, vol. 361, no. 9367, pp. 1405–1410, 2003.

[154] S. K. Davis, B. D. Van Veen, S. C. Hagness, and F. Kelcz, "Breast tumor characterization based on ultrawideband microwave backscatter," *IEEE Transactions on Biomedical Engineering*, vol. 55, no. 1, pp. 237–246, 2007.

[155] W. C. Khor, M. E. Bialkowski, A. Abbosh, N. Seman, and S. Crozier, "An ultra wideband microwave imaging system for breast cancer detection," *IEICE Transactions on Communications*, vol. 90, no. 9, pp. 2376–2381, 2007.

[156] M. Klemm, J. A. Leendertz, D. Gibbins, I. J. Craddock, A. Preece, and R. Benjamin, "Microwave radar-based breast cancer detection: Imaging in inhomogeneous breast phantoms," *IEEE Antennas Wireless and Propagation Letters*, vol. 8, pp. 1349–1352, 2009.

[157] S. H. Zainud-Deen, W. M. Hassen, E. Ali, K. H. Awadalla, and H. Sharshar, "Breast cancer detection using a hybrid finite difference frequency domain and particle swarm optimization techniques," in *2008 National Radio Science Conference*, pp. 1–8, IEEE, 2008.

[158] Y. Zhong, M. Lambert, D. Lesselier, and X. Chen, "A new integral equation method to solve highly nonlinear inverse scattering problems," *IEEE Transactions on Antennas and Propagation*, vol. 64, no. 5, pp. 1788–1799, 2016.

[159] Z. Wei and X. Chen, "Deep-learning schemes for full-wave nonlinear inverse scattering problems," *IEEE Transactions on Geoscience and Remote Sensing*, vol. 57, no. 4, pp. 1849–1860, 2019.

[160] P. Mojabi and J. LoVetri, "Microwave biomedical imaging using the multiplicative regularized Gauss-Newton inversion," *IEEE Antennas and Wireless Propagation Letters*, vol. 8, pp. 645–648, 2009.

[161] A. Litman, D. Lesselier, and F. Santosa, "Reconstruction of a two-dimensional binary obstacle by controlled evolution of a level-set," *Inverse Problems*, vol. 14, no. 3, p. 685, 1998.

[162] O. Dorn and D. Lesselier, "Level set methods for inverse scattering," *Inverse Problems*, vol. 22, no. 4, p. R67, 2006.

[163] M. Slaney, A. C. Kak, and L. E. Larsen, "Limitations of imaging with first-order diffraction tomography," *IEEE Transactions on Microwave Theory and Techniques*, vol. 32, no. 8, pp. 860–874, 1984.

[164] B. A. Brooksby, S. Jiang, H. Dehghani, B. W. Pogue, K. D. Paulsen, J. B. Weaver, C. Kogel, and S. P. Poplack, "Combining near-infrared tomography and magnetic resonance imaging to study in vivo breast tissue: implementation of a Laplacian-type regularization to incorporate magnetic resonance structure," *Journal of Biomedical Optics*, vol. 10, no. 5, p. 051504, 2005.

[165] P. C. Hansen and D. P. O'Leary, "The use of the L-curve in the regularization of discrete ill-posed problems," *SIAM Journal on Scientific Computing*, vol. 14, no. 6, pp. 1487–1503, 1993.

[166] G. H. Golub, M. Heath, and G. Wahba, "Generalized cross-validation as a method for choosing a good ridge parameter," *Technometrics*, vol. 21, no. 2, pp. 215–223, 1979.

[167] P. Charbonnier, L. Blanc-Féraud, G. Aubert, and M. Barlaud, "Deterministic edge-preserving regularization in computed imaging," *IEEE Transactions on Image Processing*, vol. 6, no. 2, pp. 298–311, 1997.

[168] K. Simonyan and Z. Andrew, "Two-stream convolutional networks for action recognition in videos," in *Proceedings of the 27th International Conference on Neural Information Processing Systems (NIPS'14)*, vol. 1, pp. 568–576, 2014.

[169] N. Ozmen-Eryilmaz, L. Demi, E. J. Alles, M. D. Verweij, and K. W. A. van Dongen, "Modeling acoustic wave field propagation in 3D breast models," in *2011 IEEE International Ultrasonics Symposium*, pp. 1700–1703, Oct 2011.

[170] N. Ozmen, R. Dapp, M. Zapf, H. Gemmeke, N. V. Ruiter, and K. W. van Dongen, "Comparing different ultrasound imaging methods for breast cancer detection," *IEEE Transactions on Ultrasonics, Ferroelectrics, and Frequency Control*, vol. 62, no. 4, pp. 637–646, 2015.

[171] J. Asefi, A. Baran, and J. LoVetri, "An experimental phantom study for air-based quasi-resonant microwave breast imaging," *IEEE Transactions on Microwave Theory and Techniques*, vol. 67, no. 9, pp. 3946–3954, 2019.

[172] Y. Qin, T. Rodet, M. Lambert, and D. Lesselier, "Joint inversion of electromagnetic and acoustic data with edge-preserving regularization for breast imaging," *IEEE Transactions on Computational Imaging*, vol. 7, pp. 349–360, 2021.

[173] L. Xu, C. Lu, Y. Xu, and J. Jia, "Image smoothing via l 0 gradient minimization," in *Proceedings of the 2011 SIGGRAPH Asia Conference*, pp. 1–12, 2011.

[174] F. Zhu, Z. Liang, X. Jia, L. Zhang, and Y. Yu, "A benchmark for edge-preserving image smoothing," *IEEE Transactions on Image Processing*, vol. 28, no. 7, pp. 3556–3570, 2019.

[175] P. Lobel, C. Pichot, L. Blanc-Féraud, and M. Barlaud, "Microwave imaging: Reconstructions from experimental data using conjugate gradient and enhancement by edge-preserving regularization," *International Journal of Imaging Systems and Technology*, vol. 8, no. 4, pp. 337–342, 1997.

[176] C. Youzwishen and M. Sacchi, "Edge preserving imaging," *Journal of Seismic Exploration*, vol. 15, no. 1, p. 45, 2006.

[177] M. Belge, M. E. Kilmer, and E. L. Miller, "Wavelet domain image restoration with adaptive edge-preserving regularization," *IEEE Transactions on Image Processing*, vol. 9, no. 4, pp. 597–608, 2000.

[178] W. Gan, X. Wu, W. Wu, X. Yang, C. Ren, X. He, and K. Liu, "Infrared and visible image fusion with the use of multi-scale edge-preserving decomposition and guided image filter," *Infrared Physics & Technology*, vol. 72, pp. 37–51, 2015.

[179] P. Charbonnier, L. Blanc-Féraud, and M. Barlaud, "ARTUR: An adaptive deterministic relaxation algorithm for edge-preserving tomographic reconstruction," *Research Reports*, pp. 93–76, 1993.

[180] A. H. Delaney and Y. Bresler, "Globally convergent edge-preserving regularized reconstruction: an application to limited-angle tomography," *IEEE Transactions on Image Processing*, vol. 7, no. 2, pp. 204–221, 1998.

[181] N. Bayat, P. Mojabi, J. LoVetri, and P. Mojabi, "On microwave breast imaging with ultrasound spatial priors," in *2020 XXXIIIrd General Assembly and Scientific Symposium of the International Union of Radio Science*, pp. 1–4, 2020.

[182] Z. Wang, A. C. Bovik, H. R. Sheikh, and E. P. Simoncelli, "Image quality assessment: from error visibility to structural similarity," *IEEE Transactions on Image Processing*, vol. 13, no. 4, pp. 600–612, 2004.

[183] Y. Qin, T. Rodet, M. Lambert, and D. Lesselier, "Microwave breast imaging with prior ultrasound information," *IEEE Open Journal of Antennas and Propagation*, vol. 1, pp. 472–482, 2020.

[184] A. S. Panayides, A. Amini, N. D. Filipovic, A. Sharma, S. A. Tsaftaris, A. Young, D. Foran, N. Do, S. Golemati, T. Kurc, K. Huang, K. S. Nikita, B. P. Veasey, M. Zervakis, J. H. Saltz, and C. S. Pattichis, "AI in medical imaging informatics: Current challenges and future directions," *IEEE Journal of Biomedical and Health Informatics*, vol. 24, no. 7, pp. 1837–1857, 2020.

[185] M. H. Yap, G. Pons, J. Martí, S. Ganau, M. Sentís, R. Zwiggelaar, A. K. Davison, and R. Martí, "Automated breast ultrasound lesions detection using convolutional neural networks," *IEEE Journal of Biomedical and Health Informatics*, vol. 22, no. 4, pp. 1218–1226, 2018.

[186] X. Chen, Z. Wei, M. Li, and P. Rocca, "A review of deep learning approaches for inverse scattering problems (invited review)," *Progress In Electromagnetics Research*, vol. 167, pp. 67–81, 2020.

[187] R. Caruana, "Multitask learning," *Machine Learning*, vol. 28, no. 1, pp. 41–75, 1997.

[188] K. He, X. Zhang, S. Ren, and J. Sun, "Deep residual learning for image recognition," in *Proceedings of the IEEE Conference on Computer Vision and Pattern Recognition*, pp. 770–778, 2016.

[189] K. He, X. Zhang, S. Ren, and J. Sun, "Identity mappings in deep residual networks," in *European Conference on Computer Vision*, pp. 630–645, Springer, 2016.

[190] E. Zastrow, S. K. Davis, M. Lazebnik, F. Kelcz, B. D. V. Veen, and S. C. Hagness, "Development of anatomically realistic numerical breast phantoms with accurate dielectric properties for modeling microwave interactions with the human breast," *IEEE Transactions on Biomedical Engineering*, vol. 55, no. 12, pp. 2792–2800, 2008.

[191] A. Kendall, Y. Gal, and R. Cipolla, "Multi-task learning using uncertainty to weigh losses for scene geometry and semantics," in *Proceedings of the IEEE Conference on Computer Vision and Pattern Recognition*, pp. 7482–7491, 2018.

[192] S. Kullback and R. A. Leibler, "On information and sufficiency," *The Annals of Mathematical Statistics*, vol. 22, no. 1, pp. 79–86, 1951.

[193] A. C. Likas and N. P. Galatsanos, "A variational approach for Bayesian blind image deconvolution," *IEEE Transactions on Signal Processing*, vol. 52, no. 8, pp. 2222–2233, 2004.

[194] H. Ayasso and A. Mohammad-Djafari, "Joint ndt image restoration and segmentation using Gauss-Markov-Potts prior models and variational Bayesian computation," *IEEE Transactions on Image Processing*, vol. 19, no. 9, pp. 2265–2277, 2010.

[195] Y. Zheng, A. Fraysse, and T. Rodet, "Efficient unsupervised variational Bayesian image reconstruction using a sparse gradient prior," *Neurocomputing*, vol. 359, pp. 449–465, 2019.

[196] H. Ayasso, B. Duchêne, and A. Mohammad-Djafari, "Optical diffraction tomography within a variational Bayesian framework," *Inverse Problems in Science and Engineering*, vol. 20, no. 1, pp. 59–73, 2012.

[197] A. Aboudourib, M. Serhir, and D. Lesselier, "A processing framework for tree-root reconstruction using ground-penetrating radar under heterogeneous soil conditions," *IEEE Transactions on Geoscience and Remote Sensing*, vol. 59, no. 1, pp. 208–219, 2021.

[198] D. Haemmerich, O. R. Ozkan, J.-Z. Tsai, S. T. Staelin, S. Tungjitkusolmun, D. M. Mahvi, and J. G. Webster, "Changes in electrical resistivity of swine liver after occlusion and postmortem," *Medical and Biological Engineering and Computing*, vol. 40, no. 1, pp. 29–33, 2002.

[199] R. J. Halter, T. Zhou, P. M. Meaney, A. Hartov, R. J. J. Barth, K. M. Rosenkranz, W. A. Wells, C. A. Kogel, A. Borsic, E. J. Rizzo, and K. D. Paulsen, "The correlation of in vivo and ex vivo tissue dielectric properties to validate electromagnetic breast imaging: initial clinical experience," *Physiological Measurement*, vol. 30, p. S121–S136, 2009.

[200] S. Ambikasaran, C. Borges, L.-M. Imbert-Gerard, and G. L, "Fast, adaptive, high-order accurate discretization of the Lippmann-Schwinger equation in two dimensions," *SIAM Journal of Scientific Computing*, vol. 38, pp. A1770–A1787, 2016.

[201] K. Xu, Y. Zhong, X. Chen, and D. Lesselier, "A fast integral equation-based method for solving electromagnetic inverse scattering problems with inhomogeneous background," *IEEE Transactions on Antennas and Propagation*, vol. 66, no. 8, pp. 4228–4239, 2018.

[202] M. T. Bevacqua and T. Isernia, "Quantitative non-linear inverse scattering: A wealth of possibilities through smart rewritings of the basic equations," *IEEE Open Journal of Antennas and Propagation*, vol. 2, pp. 335–348, 2021.

Dissemination of research results

Journal papers (published or submitted)

Y. Qin, T. Rodet, M. Lambert, and D. Lesselier, "Microwave breast imaging with prior ultrasound information," *IEEE Open Journal of Antennas and Propagation, Special Section Direct and Inverse Electromagnetic Scattering Methods*, 1, 472-482, 2020, doi: 10.1109/OJAP.2020. 3019953.
Y. Qin, T. Rodet, M. Lambert, and D. Lesselier, "Joint inversion of electromagnetic and acoustic data with edge-preserving regularization for breast imaging," *IEEE Transactions on Computational Imaging*, 7, 349-360, 2021, doi: 10.1109/TCI.2021.3067158.
P. Ran, Y. Qin, D. Lesselier, and M. Serhir, "Subwavelength micro-structure probing by binary-specialized methods: contrast source and convolutional neural networks," *IEEE Transactions on Antennas and Propagation*, 69(2), 1030-1039, Feb. 2021, doi: 10.1109/TAP.2020.3016175.
Y. Qin, P. Ran, T. Rodet, and D. Lesselier, "Breast imaging by convolutional neural networks from joint microwave and ultrasonic data," under revision, Sept. 2021.

Conference papers

Oral presentations
Y. Qin, T. Rodet, M. Lambert, and D. Lesselier, "Nonlinearized electromagnetic imaging of complex biological structures - towards data fusion," *The 42nd PIERS, PhotonIcs & Electromagnetics Research Symposium, Special Session: Inverse Problems in Microwave and Optics*, Xiamen, Dec. 2019.
Y. Qin, P. Ran, and T. Rodet, "Convolutional neural networks and microwave-ultrasound data fusion for breast imaging," *XXXIII General Assembly and Scientific Symposium (GASS) of the International Union of Radio Science*, Rome, August-Sept. 2021.
Poster presentations
P. Ran, Y. Qin, D. Lesselier, and M. Serhir, "Retrieving missing elements of a 2-D micro-structure: joint-sparsity inversion and convolutional neural networks," *9th International Conference on New Computational Methods for Inverse Problems (NCMIP)*, Cachan, May 2019.
P. Ran, Y. Qin, and D. Lesselier, "Electromagnetic imaging of a dielectric micro-structure via convolutional neural network *27th European Signal Processing Conference (EUSIPCO)*, A Coruña, Sept. 2019, IEEE Conference Publication no. 8903073 (5pp), Nov. 2019.
Miscellaneous
Y. Qin, M. Lambert, T. Rodet, and D. Lesselier, "On nonlinearized inversion procedures and their application to breast imaging," *XXXIII General Assembly and Scientific Symposium (GASS) of the International Union of Radio Science*, Rome, August-Sept. 2020. Talk cancelled due to the pandemics, in Proc. B06-01, https://www.ursi.org/proceedings/procGA20/programme.html#B06.
P. Ran, Y. Qin, D. Lesselier, and M. Serhir, "Imaging of a micro-structure: binary contrast source inversion and convolutional neural networks," *XXXIII General Assembly and Scientific Symposium (GASS) of the International Union of Radio Science*, Rome, August-Sept. 2020. Talk cancelled due to the pandemics, in Proc. B06-02, https://www.ursi.org/proceedings/procGA20/programme.html#B06.

université PARIS-SACLAY

ÉCOLE DOCTORALE
Sciences et technologies de l'information et de la communication (STIC)

Titre: Détection précoce d'anomalies du sein à l'aide de modalités microondes et ultrasonores

Mots clés: imagerie du sein, micro-ondes, ultrasons, fusion de données, méthode itérative de Born distordue, inversion de source de contraste, régularisation bords préservés, solutions bayésiennes, réseaux de neurones double flux.

Résumé: L'imagerie du sein visant la détection précoce de tumeurs est étudiée en associant données micro-ondes (MW) et ultrasonores (US). Aucune inscription n'est imposée, un sein libre étant supposé. Une 1re approche utilise des informations antérieures sur les frontières des tissus venant de données de réflexion US. La régularisation intègre que deux pixels voisins présentent des propriétés MW similaires si hors frontière, un saut étant autorisé sinon. Ceci est appliqué au sein de la méthode itérative de Born distordue et la méthode d'inversion de source de contraste. Une 2de implique régularisation déterministe préservant les bords via variables auxiliaires indiquant si un pixel est ou non sur un bord, marqueurs partagés par les paramètres MW et US. Ceux-ci sont conjointement optimisés à partir de leurs derniers profils et guident la prochaine optimisation en coefficients du terme de régularisation. La minimisation alternative met à jour contraste US, marqueurs, et contraste MW. Une 3e implique réseaux de neurones convolutifs. Courant de contraste estimé et champ diffracté sont les entrées. Une structure multi-flux se nourrit des données MW et US. Le réseau produit les cartes des paramètres MW et US en temps réel. Outre la régression, une stratégie d'apprentissage multi-tâche est utilisée avec un classificateur qui associe chaque pixel à un type de tissu pour produire une image de segmentation. La perte pondérée attribue une pénalité plus élevée aux pixels dans les tumeurs si mal classés. Une 4e implique un formalisme bayésien où la distribution a posteriori jointe est obtenue via la règle de Bayes ; cette distribution est ensuite approximée par une loi séparable de forme libre pour chaque ensemble d'inconnues pour obtenir l'estimation. Ces méthodes de résolution sont illustrées et comparées à partir d'un grand nombre de données simulées sur des modèles synthétiques simples et sur des coupes transversales de fantômes numériques anatomiquement réalistes dérivés d'IRM où des tumeurs artificielles sont insérées.

Title: Early breast anomalies detection with microwave and ultrasound modalities

Keywords: breast imaging, microwave, ultrasound, data fusion, distorted Born iterative method, contrast source inversion, edge-preserving regularization, Bayesian solutions, 2-stream neural networks

Abstract: Imaging of the breast for early detection of tumors is studied by associating microwave (MW) and ultrasound (US) data. No registration is enforced since a free pending breast is tackled. A 1st approach uses prior information on tissue boundaries yielded from US reflection data. Regularization incorporates that two neighboring pixels should exhibit similar MW properties when not on a boundary, a jump allowed otherwise. This is enforced in the distorted Born iterative and the contrast source inversion methods. A 2nd one involves deterministic edge preserving regularization via auxiliary variables indicating if a pixel is on an edge or not, edge markers being shared by MW and US parameters. Those are jointly optimized from the last parameter profiles and guide the next optimization as regularization term coefficients. Alternate minimization is to update US contrast, edge markers and MW contrast. A 3rd one involves convolutional neural networks. Estimated contrast current and scattered field are the inputs. A multi-stream structure is employed to feed MW and US data. The network outputs the maps of MW and US parameters to perform real-time. Apart from the regression, a multi-task learning strategy is used with a classifier that associates each pixel to a tissue type to yield a segmentation image. Weighted loss assigns higher penalty to pixels in tumors when wrongly classified. A 4th one involves a Bayesian formalism where the joint posterior distribution comes from Bayes' rule; this true distribution is approximated by a free-form separable law for each set of unknowns to get the estimate sought. These solution methods are illustrated and compared from a wealth of simulated data on simple synthetic models and on 2D cross-sections of anatomically-realistic MRI-derived numerical phantoms in which artificial tumors are inserted.

Maison du doctorat de l'Université Paris-Saclay
2ème étage aile ouest, Ecole normale supérieure de Paris-Saclay
4 avenue des Sciences
91190 Gif-sur-Yvette, France